UNIVERSITY OF THE AEGEAN
SCHOOL OF ENGINEERING
Department of Financial and Management Engineering

DOCTORAL THESIS

INVESTIGATION OF CORROSION–INDUCED DEGRADATION OF AERONAUTICAL ALUMINUM–COPPER AND ALUMINUM–COPPER–LITHIUM ALLOYS

AUTHOR:
CHARALAMPIDOU Margarita Christina

SUPERVISOR:
Prof. Nikolaos D. ALEXOPOULOS

Chios, November 2022

Investigation of corrosion-induced degradation of aeronautical aluminum-copper and aluminum-copper-lithium alloys

By Charalampidou Margarita Christina

Examination Committee Members

1. **Alexopoulos D. Nikolaos,** Associate Professor, Department of Financial and Management Engineering, University of the Aegean, Supervisor
2. **Kourkoulis K. Stavros,** Professor, Department of Mechanics, National Technical University of Athens, Advisory committee member
3. **Papanikos Paraskevas,** Associate Professor, Department of Product and Systems Design Engineering, University of the Aegean, Advisory committee member
4. **Manolakos Dimitrios,** Professor, Department of Mechanical Engineering, National Technical University of Athens, Examiner
5. **Vosniakos George - Christopher,** Professor, Department of Mechanical Engineering, National Technical University of Athens, Examiner
6. **Papageorgiou Konstantinos,** Professor, Department of Financial and Management Engineering, University of the Aegean, Examiner
7. **Gkialas Ioannis,** Professor, Department of Financial and Management Engineering, University of the Aegean, Examiner

To the memory of my cousin Despoula and my grandpa Dimitris (μεγάλος παππούς)

Declaration of Authorship

I, Charalampidou Margarita Christina, declare that the research work presented in the present Thesis is my own. I confirm that:

- All the work was done entirely while I was a Ph.D. student at the University of Aegean;
- Where I have consulted the published work of others, this is always clearly attributed;
- Where I have quoted from the work of others, the source is always given. With the exception of such quotations, this Thesis is entirely my own work;
- I have acknowledged all main sources of help;
- This Thesis contains the author's original work published or submitted for publication to international journals, in accordance with the permission guidelines of the publishing houses. All the relevant publications are listed in the end of the present Thesis;

Signed: _____

Date: _____

Acknowledgements

In this section I would like to acknowledge those who have contributed to the present Thesis.

First of all, I would like to express my sincere gratitude to my supervisor Dr. Nikolaos Alexopoulos for trusting me to undertake such an interesting research project and for his mentoring during these years as well as his patience with me.

Besides my supervisor, I would like to thank Dr. Stavros Kourkoulis for his helpful and insightful advice and for the chance he gave me to perform part of my experiments at the venues of National Technical University of Athens. The above-mentioned experiments would have never been completed without the precious help from Dr. Noni Passiou and Dr. Aggelos Pikrakis regarding the experimental set-up and use of the apparatus and their patience which prevented them by locking me in the lab late at evenings. Additionally, I would like to thank Dr. Paraskevas Papanikos for all the hints and suggestions during my research work. I would also like to thank Dr. Mikhail Zeludkevich for the chance he gave me to perform part of the electrochemical experiments at the venues of Hereon Helmholtz-Zentrum in Geesthacht as well as for his very useful feedback and advice. His contribution regarding the electrochemical tests in the present study was fundamental for my research.

Furthermore, I feel really grateful to Dr. Blawert Carten and Dr. Maria Serdechnova from the Hereon Helmholtz-Zentrum in Geesthacht for their help regarding the electrochemical experiments and analysis of the results as well as to the technicians Volker Heitmann, Ulrich Burmester and Petra Fischer for the training and guidance regarding the experimental set-up and use of the apparatus as well as their humor that made this whole process enjoyable.

Also, I would like to acknowledge the precious help from Prof. Wenya Li, from the Northwestern University, for providing us the transmission electron microscopy (TEM) analysis results used in this Thesis and his valuable feedback. Additionally, I am very grateful to Dr. Roelf Mostert from the University of Pretoria and the Ph.D student Christiaan C.E. Pretorius for the performance of micro-X-ray tomography (XCT) and their feedback.

Regarding financial support, I would like to acknowledge the funding received for my Ph.D in the framework of the Research Project CorLi- Corrosion susceptibility, degradation and protection of advanced Al-Li aluminium alloys financed by H.F.R.I.

Besides all the above-mentioned academic and financial support, which is undoubtedly of imperative importance, the present Thesis would have never been completed without the appropriate emotional support. I am indebted to my family who have always supported me spiritually and sometimes financially and who have been by my side all these years. They helped me become the person I am today by encouraging me to follow my dreams − and not their expectations − and by respecting my decisions. My mother's optimism, patience, and dynamism helped me in this painful journey by teaching me to face the several problems with optimism and humor and made me not to quit. The unexpectedly troubles and (emotional) challenges caused by my father taught me that there are more significant problems and hard situations in life than completing a Ph.D, so I would like to thank him for making me stronger and independent. Additionally, I would like to acknowledge that working with my father taught me to pay attention to details and double-check everything. The way my brother deals with life − on some occasions − helped me in the stressful process of my thesis' defense and made me to "debunk" some people and situations. Finally, I have to give special thanks to my grandparents because they always advocated that my studies should be a priority.

I also feel really grateful about my friends, both those with whom I could share my thoughts and anxieties about work (Angela, Marilia) as well as those who could not understand exactly but were always there showing empathy and willingness to help with useful advice and happy moments (Matoyla, Gianna, Martha, Xrysa, Eva, Georgia).

Special thanks to my life partner George who endured my nagging and making me scream with laughter when I am anxious or sad. He always kept me in line and made sure I was not horsing around instead of working. I thank him for being a good and patient listener and advisor. His curiosity and knowledge about my topic made him to push me hard with challenging questions, while his way of thinking helped me to become more optimism and not to quit.

Last but not least, I would like to thank myself for my patience, passion, willingness, decisiveness and general my dynamism which made me reach the end without (completely) losing my mind.

Abstract

Corrosion is one of the major damage problems met in aircraft structures that can significantly affect its structural integrity. Accumulated corrosion damage on ageing aircrafts may lead to premature failure of the aircraft components due to interactions with other forms of damage such as fatigue cracks. The increasing demand of aeronautic industries for reduction of energy consumption and increase in payload led the material engineers to the development of light-weight materials with improved mechanical properties in several parts of the aircraft structure. Thus, the development of third generation Al-Cu-Li alloys took place. Some of their advantages that make them preferable than conventional Al-Cu aluminium alloys are the low density, improved specific strength, high stiffness to weight ratio and good corrosion resistance. However, it is of major importance for all aircraft structural components to withstand corrosive environments while continuing to perform at optimum levels after long-term operation (simulating natural ageing). The ageing-induced thermomechanical transformations in old aircrafts significantly influence their corrosion behaviour with the corrosion-induced degradation to be irreversible unlike mechanical properties degradation which can be reversible with special treatments. Hence, it is crucial to identify the corrosion degradation mechanisms on aircrafts in order to give feedback for the development of anti-corrosion protection methods and enhance aircrafts structural integrity.

The present Thesis aims to identify the corrosion-induced degradation mechanisms of Al-Cu and Al-Cu-Li alloys and correlate these mechanisms with corrosion-induced degradation of mechanical properties. Higher emphasis is given on ductility which is evaluated through elongation at fracture A_f. Comparison of Al-Cu against Al-Cu-Li alloys is performed during the whole Thesis in order to highlight the potential of Al-Cu-Li alloys and justify the replacement of Al-Cu alloys in aircraft structures. Towards these objectives exposure of specimens to different corrosive environments was performed and both the corrosion kinetics as well as the residual mechanical properties were investigated through immersion tests, electrochemical tests (electrochemical impedance spectroscopy-EIS, potentiodynamic polarization), microscopic examinations (*e.g.*, light optical microscopy, stereoscopical analysis, scanning electron microscopy-SEM, transmission electron microscopy-TEM, micro X-ray computed tomography-XCT) and mechanical tests (tensile, fatigue, fracture toughness).

Different embrittlement mechanisms were noticed for the different corrosive solutions for both Al-Cu and Al-Cu-Li alloys. Grain boundary embrittlement was evident at specimens exposed to EXCO solution, which lead to secondary cracking formation, while intergranular and transgranular corrosion were present at 3.5 *wt.* % NaCl solution. Corrosion degrades all aspects of the tensile behaviour of AA2024-T3 at a higher level and rate compared to the respective degradation of

AA2198-T8 at long exposure times, where pitting corrosion mechanism takes place. Regarding elongation at fracture, AA2024-T3 was found to degrade at much higher rates even at short exposure times where hydrogen embrittlement is possibly the dominant degradation mechanism.

Synergetic effect of micro-cracks and hydrogen embrittlement was revealed in Al-Cu 2024-T3 alloy. Hydrogen embrittlement on AA2024-T3 specimens corroded on both surfaces was found to contribute to approximately 27% of the ductility (A_f) decrease while micro-crack formations to the rest 73%. Different corrosion attack mechanisms were noticed for the different exposure times and the different surfaces of the alloys. Depth of micro-cracks increases with increasing exposure time to exfoliation corrosion (EXCO) solution and for the single-sided corroded specimens of AA2024-T3 this depth is essentially higher than for the respective half-corrosion exposure time for the both-sided corroded specimens. Pitting corrosion on both surfaces of Al-Cu-Li 2198-T351 alloy was noticed for the short exposure times while two cases of corrosion damage were noticed for long exposure time ($\geq$ 24 hours): a) the formation of corrosion-induced surface cracks on the small side-surfaces along with transition to exfoliation on the large surfaces due to grain boundaries delamination and b) the accumulated corrosion products on the large surfaces. Regarding Al-Cu 2024-T3 alloy, pitting corrosion within grain boundaries was evident for short exposure times, while connection of corrosion-attacked sites along with cracking between the grains, was the dominant corrosion degradation mechanism for long exposure times. AA2024 was found to be more sensitive to side-surfaces corrosion attack, where a contribution of approximately 60% to the total A_f decrease was noticed for short exposure times, while accumulated corrosion on large surfaces (L/LT) is more critical in ductility decrease regarding Al-Cu-Li 2198 alloy.

AA2024 showed high responsiveness to microstructural transformations due to artificial ageing heat-treatments since both the electrochemical behaviour and the mechanical properties of the different ageing tempers exhibited high differences, with the peak-aged (PA) specimens to be less susceptible to corrosion evolution. However, this was not the case for AA2198 where no notable differences between the different ageing tempers were observed regarding corrosion propagation. In general, the advanced Al-Cu-Li 2198 alloy seems to be more corrosion resistant than Al-Cu 2024 both in terms of charge transfer resistance and A_f reduction rates; however, this superiority is more intense in short exposure times where slight pitting formation takes place.

Περίληψη

Η διάβρωση είναι μία από τις σημαντικότερες βλάβες που συναντώνται στις δομές των αεροσκαφών, μειώνοντας σημαντικά την δομική τους ακεραιότητα. Η συσσωρευμένη διάβρωση στα γηράσκοντα αεροσκάφη μπορεί να οδηγήσει σε πρόωρη αστοχία των δομικών μερών τους λόγω της συνέργειάς της με άλλες μορφές βλαβών, όπως είναι οι ρηγματώσεις λόγω κόπωσης. Οι αυξανόμενες απαιτήσεις των αεροναυπηγικών βιομηχανιών για μείωση της κατανάλωσης ενέργειας και αύξηση του ωφέλιμου φορτίου οδήγησε τους μηχανικούς υλικών στην ανάπτυξη υλικών χαμηλού βάρους με βελτιωμένες μηχανικές ιδιότητες. Έτσι, πραγματοποιήθηκε η ανάπτυξη των κραμάτων Al-Cu-Li τρίτης γενιάς. Μερικά από τα πλεονεκτήματά τους που τα καθιστούν προτιμότερα από τα συμβατικά κράματα αλουμινίου Al-Cu είναι η χαμηλή πυκνότητα, η βελτιωμένη ειδική αντοχή, η υψηλή αναλογία ακαμψίας προς βάρος και η καλή αντοχή στη διάβρωση. Ωστόσο, είναι πολύ σημαντικό όλα τα δομικά στοιχεία του αεροσκάφους να αντέχουν σε διαβρωτικά περιβάλλοντα, ενώ συνεχίζουν να αποδίδουν στα βέλτιστα επίπεδα μετά από μακροχρόνια λειτουργία (προσομοίωση φυσικής γήρανσης). Οι θερμομηχανικοί μετασχηματισμοί που προκαλούνται από τη γήρανση των αεροσκαφών επηρεάζουν σημαντικά τη συμπεριφορά τους σε διάβρωση, με την υποβάθμιση λόγω διάβρωσης να είναι μη αναστρέψιμη σε αντίθεση με την υποβάθμιση των μηχανικών ιδιοτήτων που μπορεί να είναι αναστρέψιμη με ειδικές επεξεργασίες. Επομένως, είναι σημαντικό να εντοπιστούν οι μηχανισμοί υποβάθμισης λόγω διάβρωσης στα αεροσκάφη, ώστε να αναπτυχθούν μέθοδοι αντιδιαβρωτικής προστασίας και να ενισχυθεί η δομική ακεραιότητα των αεροσκαφών.

Η παρούσα διατριβή στοχεύει στον εντοπισμό των μηχανισμών υποβάθμισης λόγω διάβρωσης των κραμάτων Al-Cu 2024 και Al-Cu-Li 2198 και στην συσχέτιση τους με την επαγόμενη από τη διάβρωση υποβάθμιση των μηχανικών ιδιοτήτων. Μεγαλύτερη έμφαση δίνεται στην ολκιμότητα, η οποία προσδιορίζεται από την παραμόρφωση θραύσης A_f. Σύγκριση των κραμάτων Al-Cu με τα καινοτόμα κράματα Al-Cu-Li πραγματοποιείται σε όλη τη Διατριβή, προκειμένου να αναδειχθεί η υπεροχή των κραμάτων Al-Cu-Li και να δικαιολογηθεί η αντικατάσταση των συμβατικών κραμάτων Al-Cu από αυτά στις δομές των αεροσκαφών. Για την εξαγωγή αυτών των πληροφοριών πραγματοποιήθηκε έκθεση δειγμάτων σε διαφορετικά διαβρωτικά περιβάλλοντα και διερευνήθηκαν τόσο η κινητική της διάβρωσης όσο και οι εναπομένουσες μηχανικές ιδιότητες μέσω δοκιμών εμβάπτισης, ηλεκτροχημικών δοκιμών (φασματοσκοπία ηλεκτροχημικής εμπέδησης-EIS, ποτενσιοδυναμική πόλωση), μικροσκοπικών αναλύσεων, μεταλλογραφιών (π.χ οπτική μικροσκοπία, στερεοσκοπική ανάλυση, ηλεκτρονική μικροσκοπία σάρωσης-SEM, ηλεκτρονική μικροσκοπία μετάδοσης-TEM, μικροσκοπική τομογραφία ακτίνων Χ-XCT) καθώς και μηχανικών δοκιμών (εφελκυσμός, κόπωση, δυσθραυστότητα).

Διαφορετικοί μηχανισμοί ευθραυστότητας/ψαθυροποίησης παρατηρήθηκαν στα διαφορετικά διαβρωτικά διαλύματα τόσο για τα κράματα Al-Cu όσο και για τα κράματα Al-Cu-Li. Η ψαθυροποίηση των ορίων των κόκκων ήταν εμφανής σε δείγματα που εκτέθηκαν σε διάλυμα EXCO, το οποίο οδηγεί σε σχηματισμό δευτερογενών ρωγμών, ενώ περικρυσταλλική και ενδοκρυσταλλική διάβρωση παρατηρήθηκε στο διάλυμα 3,5 wt. % NaCl. Η διάβρωση υποβαθμίζει το κράμα 2024-T3 σε υψηλότερο επίπεδο και ρυθμό σε σύγκριση με το 2198-T8, όσον αφορά τις μηχανικές ιδιότητες εφελκυσμού, σε μεγάλους χρόνους έκθεσης όπου λαμβάνει χώρα ο μηχανισμός διάβρωσης με οπές. Όσον αφορά την παραμόρφωση θραύσης, το 2024-T3 βρέθηκε να υποβαθμίζεται με πολύ υψηλότερο ρυθμό ακόμη και σε μικρούς χρόνους έκθεσης όπου η ψαθυροποίηση λόγω διάχυσης υδρογόνου είναι ο κυρίαρχος μηχανισμός υποβάθμισης.

Στο κράμα 2024-T3 παρατηρήθηκε συνέργεια των μικρο-ρωγμών λόγω διάβρωσης και της ψαθυροποίησης λόγω διάχυσης υδρογόνου. Η ψαθυροποίηση λόγω διάχυσης υδρογόνου σε δείγματα 2024-T3 που διαβρώθηκαν και στις δύο επιφάνειες οδηγεί σε περίπου 27% μείωση της ολκιμότητας (A_f). Διαφορετικοί μηχανισμοί υποβάθμισης παρατηρήθηκαν στους διαφορετικούς χρόνους διάβρωσης και τις διαφορετικές επιφάνειες των κραμάτων. Το βάθος των μικρο-ρωγμών αυξάνεται με την αύξηση του χρόνου διάβρωσης και για τα διαβρωμένα δοκίμια μονής όψης (διάβρωση σε μία πλευρά/επιφάνεια) είναι ουσιαστικά υψηλότερο από τα διαβρωμένα δείγματα αμφίπλευρης όψης. Διάβρωση με οπές παρατηρήθηκε και στις δύο επιφάνειες του κράματος 2198-T351 στους μικρούς χρόνους έκθεσης, ενώ δύο περιπτώσεις βλάβης παρατηρήθηκαν στους μεγάλους χρόνους (≥ 24 ώρες): α) ο σχηματισμός επιφανειακών ρωγμών λόγω διάβρωσης στις μικρές πλευρικές επιφάνειες μαζί με διάβρωση αποφλοίωσης στις μεγάλες επιφάνειες λόγω αποκόλλησης των ορίων των κόκκων και β) συσσωρευμένα προϊόντα διάβρωσης στις μεγάλες επιφάνειες. Όσον αφορά το κράμα 2024-T3, διάβρωση με οπές εντός των ορίων των κόκκων εντοπίστηκε στους μικρούς χρόνους έκθεσης, ενώ η σύνδεση των μικρο-ρωγμών λόγω διάβρωσης ήταν ο κυρίαρχος μηχανισμός υποβάθμισης στους μεγάλους χρόνους έκθεσης. Το κράμα 2024 βρέθηκε να είναι πιο ευαίσθητο στη διάβρωση των πλευρικών επιφανειών, όπου παρατηρήθηκε συμβολή περίπου 60% στη συνολική μείωση της A_f για μικρούς χρόνους έκθεσης, ενώ η συσσωρευμένη διάβρωση στις μεγάλες επιφάνειες (L/LT) είναι πιο κρίσιμη στη μείωση της ολκιμότητας για το κράμα Al-Cu-Li 2198.

Το 2024 επηρεάζεται σημαντικά από τους μετασχηματισμούς της μικροδομής λόγω τεχνητής γήρανσης, καθώς τόσο η ηλεκτροχημική του συμπεριφορά όσο και οι εναπομένουσες μηχανικές ιδιότητες σε διαφορετικές καταστάσεις γήρανσης παρουσίασαν υψηλές διαφορές, με τα δείγματα στην κατάσταση μέγιστης γήρανσης (PA) να είναι λιγότερο ευαίσθητα στην εξέλιξη της διάβρωσης. Ωστόσο, αυτό δεν ισχύει για το 2198. Το κράμα 2198 φαίνεται να είναι πιο ανθεκτικό στη διάβρωση.

List of pictures

List of figures

List of tables

Table of contents

Chapter 1

1 General introduction

The present chapter introduces the theoretical background and the motivation for conducting this research. General information regarding aeronautical aluminium alloys, with emphasis on 2xxx series Al-Cu and Al-Cu-Li alloys, and the corrosion problem on these materials is also given through a brief literature review. Additionally, the research objectives as well as the outline of the present Thesis are presented in the end of this chapter.

1.1 Brief theoretical background

1.1.1 Aeronautical aluminium alloys

Due to the unique combinations of physical and mechanical properties, aluminium and its alloys are considered as adjustable and cost-effective metallic materials for use in a wide range of applications such as aviation industry, automotive industry, construction, electronic technology etc. Commercially pure aluminium (at least 99% aluminium) is considered as relatively soft metal for engineering applications; however, alloying with other metals significantly enhances its strength due to microstructural transformations. One of the most important characteristics for the selection of aluminium alloys as structural materials for aeronautic applications is the light weight. Additionally, some other properties such as increased formability, high specific mechanical properties, high strength to weight ratio, enhanced corrosion resistance, high electrical and thermal conductivity as well as the well-established design methods and reliable inspection techniques, make aluminium alloys the most attractive metals for the aircrafts [1].

Aluminium alloys are classified into two groups regarding the manufacturing procedure: wrought aluminium alloys and cast aluminium alloys, with the former being more often used since it can be formed by every known method (*e.g.*, rolling, extruding, forging etc.). Wrought aluminium alloys are further divided into non heat-treatable and heat-treatable. Heat-treatable alloys have improved mechanical properties (*e.g.*, hardness, yield stress) coming from the combined effects of solution heat-treatment and subsequent natural or controlled artificial ageing that induce precipitation hardening. Hardening by heat-treatment incorporates three basic steps: a) solution heat-treatment for the dissolution of soluble phases, b) quenching for the formation of supersaturated solid solution and c) artificial ageing for the precipitation of solute atoms. Aeronautical aluminium alloys of 2xxx (Al-Cu) series are heat-treatable since their mechanical properties can be significantly improved by heat-treatment. AA2024 is a 2xxx (Al-Cu-Mg) series aluminium alloy, with a copper content in the range of 3.9-4.9% *wt.*, which contains different nonequilibrium precipitate structures. These precipitates are formed during ageing at temperatures lower than the equilibrium solvus temperature (≈ 500°C for Cu content 3.9-4.9% *wt.*). At these temperatures the equilibrium state includes a solid solution, α (Al), along with a phase θ (Al_2Cu) for Al-Cu alloys or S (Al_2CuMg) for Al-Cu-Mg alloys. By heating the alloy above the solvus temperature and then suddenly quenching in temperatures much lower than solvus, supersaturated solid solution (SSS) is formed and the material needs the equilibrium two-phase condition; then, the second phase precipitates are encountered by solid-state precipitation. Hence, the requisition for the occurrence of precipitation hardening of supersaturated solid solutions includes the formation of finely dispersed precipitates during ageing heat-treatments. However, in

order to obtain maximum strengthening the temperature should also be lower than a metastable miscibility interval named as Guinier-Preston (GP) zones solvus. The precipitation hardening system of AA2024 follows the well-known sequence of [1]:

SSS → Guinier-Preston- Bagaryatsky (GPB) zone/S'' → S' → S (Al_2CuMg) phase.

The GPB zones are ordered solute-rich clusters of atoms in the form of disks. They are deformed regions of the matrix lattice which maintain its structure and are fully coherent with it. These zones are metastable and dissolve when precipitation of a more stable phase tales place, thus leading to a precipitate free zone around the stable phases. GPB zones is possible to be formed prior to the equilibrium phase and/or coexist with the equilibrium phase. The strain fields that formed around these particles, as a result of the discrepancy in size between the solvent and the solute atoms, contribute to an increase in materials strength by impeding the dislocations movement. With increasing artificial ageing time or temperature phase transformations take place that further increase the strength up to a maximum level (peak-ageing condition), where fully coherency of the precipitates with the matrix is evident; however, with further increase of ageing time or temperature semi-coherent phases are formed leading to the final stage of equilibrium S phase which is non-coherent with the matrix and as a consequence reduces the material's strength (over-ageing condition) [1].

The second-phase precipitates are divided into shearable and non-shearable with respect to the mechanism that blocks the dislocations movement. The shearable are those in fully coherency with the matrix where high strain fields are developed around them and contribute to dislocations movement retardation. As the dislocation shear the particle at the slip plane, it destroys the perfectly ordered crystal lattice structure of the particle. The affected deformed region that is created is called the anti-phase boundary (APB). The boundary energy is high so that the resulting strengthening is significant. The non-shearable precipitates are usually large and widely spaced phases incoherent with the matrix. These phases can be bypassed by dislocations through a mechanism called Orowan loop. The dislocations surround these phases and finally bypass them leaving loops around them. The yield strength of the alloy in this condition is low but the rate of work-hardening is high, and plastic deformation tends to be more uniformly distributed throughout the grains [2].

Regarding Al-Cu-Li alloys, that were developed to replace the conventional Al-Cu alloys due to higher specific strength and specific modulus of elasticity, the intermetallic particles which are formed during precipitation hardening include δ' (Al_3Li), θ' (Al_2Cu), S (Al_2CuMg) and T_1 (Al_2CuLi) as the major strengthening phases. The precipitation sequence for Al-Cu-Li alloys with Cu/Li = 2.5–4 follows the reactions:

α (SSS) → GP zones → GP zones + δ' → θ'' + θ' + δ' → δ' + T_1 → T_1.

[3]

During the first stages of ageing, the metastable δ' phase precipitates, and further increasing of ageing time or temperature results in the formation of the equilibrium δ (AlLi) phase. Some of the advantages in Al-Cu-Li alloys are caused by the fact that the coherent with the matrix δ' phase remain in this stage even after extensive ageing. However, the major strengthening phase of these alloys is the T_1 with a hexagonal crystal structure. It is preferably nucleated on dislocations, grain and sub-grain boundaries, GP zones, dispersoids such as Al_3Zr, as well as inside grains. The lower contribution of δ' phase to ductility and toughness, due to heterogeneous slip as well as creation of precipitate free zones (PFZs) caused by the presence of equilibrium δ phase, led to the development of third generation quaternary (Al-Li-Cu-Mg) alloys that promote the nucleation of semi-coherent/incoherent phases such as T_1 which lead to homogenized slip caused by dislocations [3].

Regarding the effect of ageing on the mechanical behaviour of aluminium alloys, several approaches have been used in laboratory scale − including artificial ageing heat-treatments [4]-[8] − in order to accelerate the microstructural kinetics and simulate natural ageing. Alexopoulos et *al.* [9] investigated the effect of artificial ageing conditions on the precipitation kinetics, tensile and work hardening behaviour of AA2024-T3; an essential increase on yield stress up to the peak-ageing condition along with a simultaneous decrease of elongation at fracture, due to precipitation of *S*-type particles, was noticed. Additionally, an essential effect on hardness is referred by Astika [10], where an improvement in hardness values with increasing ageing time was observed. The changes in strength and ductility were found to be a result of the S'' and S phase precipitation as well as the subsequent decrease in dislocation density in an Al-Cu-Mg-Mn alloy, *e.g.*, Wang et *al.* [11]. In recent years, many researchers have studied the strengthening mechanisms of Al alloys during solution and ageing treatments. Liang et *al.* [12] have shown a gradually increase on the mechanical properties of AA2024 with a 1070 coating as the solution temperature increases up to 510°C, while a further increase in temperature resulted to elongation at fracture degradation. More recent studies are focused on the effect of multistage-ageing and pre-deformation on the thermomechanical microstructural transformations on aluminium alloys. Yang et *al.* [13] investigated the effect of multistage-ageing process on the formation of GP zones and their effect on the mechanical properties in an Al-Zn-Mg-Cu alloy. Xu et *al.* [14] studied the effect of interrupted ageing on the mechanical properties and corrosion behaviour of Al-Mg-Si alloys, where the more densely dispersed precipitates as well as the less distance between them was found to be responsible for higher strength and elongation values. In Pakravan et. *al.* [15] the fracture behaviour of two different ageing conditions of AA2024 was investigated showing that the toughness was dominated by deformability compared to strengthening factor. Sun et *al.* [16] studied the microstructure, hardness, and phase transformation of AA7075 in the process of solution and double ageing; the *S* and θ phases' precipitation at the grain boundary was

found to be responsible for the hardness improvement. A transition to ductile mode fracture was noticed in cold rolled AA2024 after the application of solution and ageing treatment, *e.g.*, Sun et *al.* [17]; however, with increasing ageing time the dimples became shallower, and the quasi-intergranular fracture became more obvious. In another study of Sun et *al.* [18] the effect of ageing treatment and peripheral coarse grain on the exfoliation corrosion behaviour of AA2024 was investigated.

Apart from their contribution to mechanical properties the above-mentioned precipitations may influence also physical properties (*e.g.*, electrical, and thermal conductivities) as well as electrochemical properties (corrosion potential) of the alloys. Thus, it is of imperative importance to investigate the effect of artificial ageing on the corrosion nucleation and propagation mechanisms of these alloys.

1.1.2 Corrosion problem

It is generally accepted, that aluminium and its alloys are thermodynamically active metals (anodic), regarding the position of Al in the standard electromotive force (emf) series. However, under particular environmental conditions they passivate due to the formation of a highly adherent oxide film on their surface that, if damaged, reforms rapidly. Nevertheless, in the presence of highly corrosive environments aluminium alloys tend to corrode with a mechanism of localized attack. Localized corrosion on aluminium alloys is triggered by micro-galvanic corrosion phenomena, which take place in their microstructure, due to transformations in the alloys' composition. The ageing-induced microstructural transformations on 2xxx series aluminium alloys were found to affect their susceptibility to corrosion attack, due to heterogeneity of the strengthening Cu-rich second phase intermetallic particles (precipitates) to Al matrix, from the electrochemical point of view [19]-[22]. Formation of a galvanic cell between the Cu-rich grain boundary precipitates and/or intermetallic particles (IMs) with the Al-matrix or the adjacent Cu-depleted areas is responsible for corrosion in these alloys [23]-[24]. Additionally, galvanic cells due to creation of microscopic Cu particles deposited on the alloy's surface may lead to localized corrosion.

Localized corrosion starts in the form of pits. Pits may be initiated by mechanical or chemical surface heterogeneities which lead to breakdown of the oxide passive film, *e.g.*, localized surface defects such as scratches/flaws or by slight variations in alloy's composition such as IMs and dislocations [25]-[26]. As a consequence, contact of the metal with the corrosive medium leads to electrochemical interactions between the alloying elements and the medium. The oxide passive film is formed on aluminium alloys' surface during their contact with normal atmospheres, as a result of oxidation at the interface of metal and the respective environment. The oxidation reaction is characterized by the equation below [27]:

$$2Al + \frac{3}{2} O_2 \rightarrow Al_2O_3 \qquad (1\text{-}1)$$

The anodic dissolution of second-phase precipitates' surrounding matrix leads to another form of localized corrosion named as intergranular corrosion (IGC), as depicted in Figure 1-1. IGC is the most common form of metallurgically corrosion and refers to selective attack of grain boundaries or closely adjacent regions without appreciable attack of the grain's interior [28]. The intergranular corrosion attack (IGC) dominant mechanism is the formation of a galvanic cell between the Cu-rich grain boundaries precipitates, *e.g.*, θ- (Al_2Cu) and *S*-type (Al_2CuMg) in case of AA2024, and the matrix or the adjacent Cu-depleted particles [29]-[34]. This kind of corrosion usually leads to exfoliation corrosion (EXCO). EXCO is a particular form of intergranular corrosion which occurs on the corroded surfaces of aircraft structures where the grains are elongated in layers parallel to the surface [35]-[36]. The formed corrosion products are larger in volume than the parent metal and, due to internal stress formation, lead to layers' separation as shown in Figure 1-2.

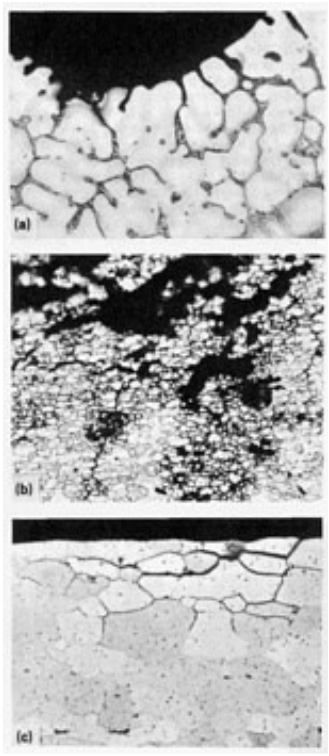

Figure 1-1: Various types of intergranular corrosion. (a) Interdendritic corrosion in a cast structure. (b) Interfragmentary corrosion in a wrought, unrecrystallized structure. (c) Intergranular corrosion in a recrystallized wrought structure. All etched with Keller's reagent. 500×[28].

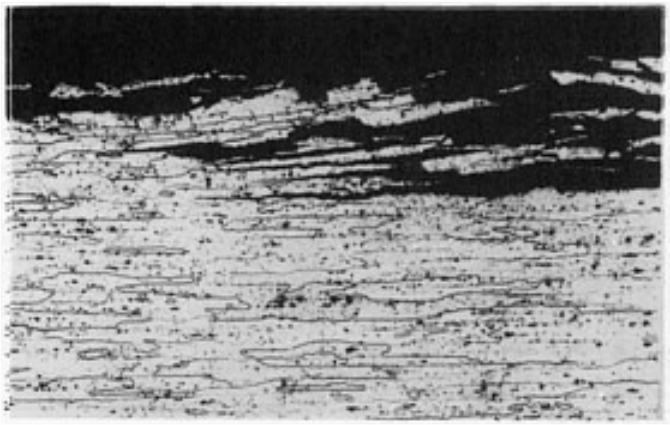

Figure 1-2: Exfoliation corrosion in an alloy 7178-T651 plate exposed to a seacoast environment. Cross section of the plate shows how exfoliation develops by corrosion along boundaries of thin, elongated grains [28].

In addition to the micro-galvanic corrosion associated with the grain boundary precipitates and its neighbouring regions, hydrogen embrittlement mechanisms have been reported to be contributing factors to the corrosion-induced degradation of mechanical properties in 2xxx aluminium alloys. Hydrogen is usually produced by surface corrosion reactions (cathodic reduction of water molecules, H_2O) and afterwards it can either be diffused into the aluminium matrix or react on the surface to form hydrogen gas (H_2) [37]; recently in-situ X-ray tomography was used to capture H_2 production at the corrosion surface of AA2024 and the networks of intergranular corrosion were found to extend into the material [38]-[39]. Grain and sub-grain boundaries, microstructural point defects, line-defects/dislocations, and precipitates (including matrix/precipitate interfaces) are preferential pathways for the diffusion of hydrogen, *e.g.*, Larignon et *al.* [40]. Several studies investigated the hydrogen trapping sites on AA2024; Scamans and Tuck [41] attributed the trapping site T3 to the formation of Mg hydride. Saitoh et *al.* [42] proved that the above microstructural features of the alloy can be used as hydrogen traps by employing tritium autoradiography. The presence of hydrogen atoms seems to increase the mobility of dislocations during plastic deformation, leading to high localized plastic deformation and fracture [43]. This phenomenon is called hydrogen enhanced localized plasticity (HELP) mechanism. Another mechanism of hydrogen embrittlement, called hydrogen enhanced decohesion (HEDE) is considered as a reduction in the bonding strength between the metal atoms due to the presence of hydrogen [44]. Despite of the fact that there is no universally accepted hydrogen embrittlement mechanism, some critical concentrations of atomic hydrogen have been reported to have an essential effect to the loss of tensile ductility of pre-corroded AA2024 [45]-[47]. In more recent work by Alexopoulos et *al.* [48] a synergistic effect of micro-cracking and hydrogen embrittlement was found on AA2024, with the total decrease in tensile ductility (represented by elongation at fracture) to be attributed to two different mechanisms: the first one consisted of the ¼ reduction of total elongation at fracture due to hydrogen embrittlement, while the

rest ¾ (actually 73%) was attributed to micro-crack formation and propagation. Similar results found in Alexopoulos and Papanikos [49], where they performed fracture toughness mechanical tests on the same alloy and for various exposure times to corrosive environment; the total reduction of almost 30% of the fracture toughness after 96 hours exposure to exfoliation corrosion solution was attributed primary to the reduction of the alloy's effective thickness (22%) and secondary to the hydrogen embrittlement (8%) mechanism. Additionally, in a recent study of Charalampidou et *al.* [50] the extent of secondary cracks ahead of the primary crack − after the exposure of AA2024-T3 C(T) specimens to EXCO solution and the subsequent crack-growth resistance evaluation − was found to correlate with the diameter of the plastically affected zone (≈3.78 ± 0.04mm). The depth of these cracks correlated well with the thickness of the intergranular fracture surface, giving evidence that they are a result of a grain boundary embrittlement mechanism. To assess the true hydrogen embrittlement effect, short exposure times should be selected to corrode the specimens so as to eliminate the formation of corrosion-induced surface pits that act as stress raisers and degrade the ductility of the alloy.

Regarding Al-Cu-Li alloys, corrosion initiation and propagation mechanisms are not well-defined. Signs of intergranular/intersubgranular corrosion susceptibility due to high grain stored energy (dislocations density per grain), *e.g.*, Figure 1-3, were reported to the articles of Ma et *al.* in [51]-[52] and Zhang et *al.* in [53], as well as transgranular and exfoliation corrosion attack found by Araujo et *al.* in [54]. T_1 precipitates lead in localized corrosion due to the anodic behaviour with respect to the adjacent Cu depleted zones and the matrix, *e.g.*, [55]-[58]. The higher corrosion potential of Li and Al elements leads to their preferential dissolution from the T_1 phase precipitates, promoting hydrolysis of water that leads to acidification of the solution and corrosion propagation [59]. Severe localized corrosion attack associated to micrometric precipitates [60] was evident at the slip bands in the interior of high energy grains, introduced by the stretching process in AA2198-T851 alloy [59]. Dispersed intermetallic (IMs) precipitates and subsequent pitting corrosion were observed after the exposure of AA2198-T3 to neutral sulphate and chloride solutions, *e.g.,* Balbo et *al.* in [61]; a rapid corrosion potential decrease was noticed at the early stages of corrosion exposure due to the pitting corrosion process. Severe localized corrosion on AA2198-T851 after only 1 hour of corrosion exposure as well as crystallographic propagation with increasing exposure time was revealed in [62], *e.g.*, Figure 1-4.

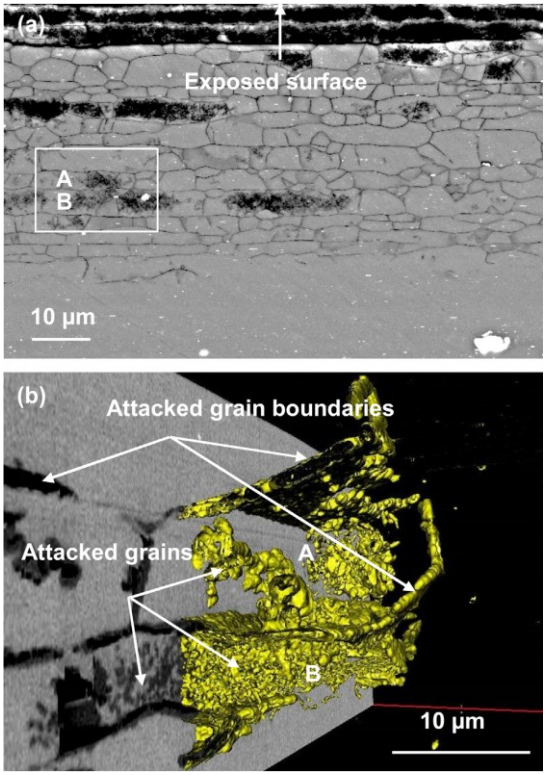

Figure 1-3: (a) A backscattered electron micrograph of the cross section of AA 2099-T83 alloy after polarization from −0.767 to 0.824 V(SCE) in 3.5% wt. NaCl solution; and (b) 3D volumetric reconstruction of the framed region in (a), with selective transparency applied to the aluminium matrix and yellow colour applied to corrosion product. The observed section corresponds to the long transverse section of the extrusion.(For interpretation of the references to colour in this figure legend, the reader is referred to the web version of this article) [51].

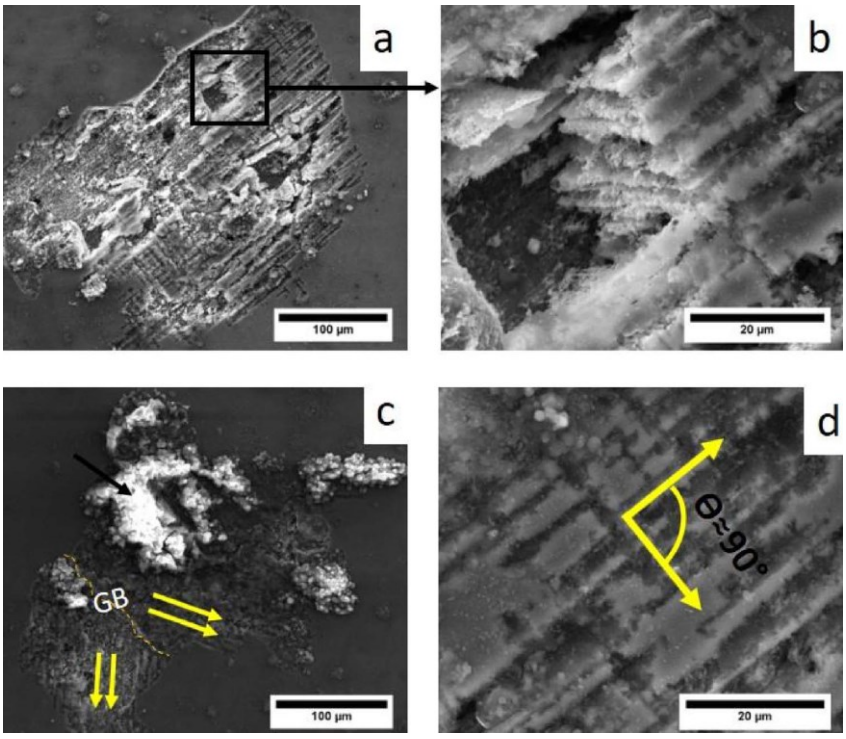

Figure 1-4: AA2198-T851 alloy surface after 13 h exposure to 0.01 mol L−1 NaCl solution showing pits with increased widths and crystallographic corrosion morphology [62].

In general, corrosion can be correlated to several types of materials' degradation. The most common corrosion phenomena on airframes are the following:

- localized pitting corrosion
- crevice corrosion (usually met in lap-joint regions)
- general surface deterioration caused by uniform or filiform corrosion
- intergranular and transgranular corrosion
- exfoliation corrosion

However, the deleterious effects of corrosion are caused by combination of corrosion with other forms of damage such as fatigue, wear, and stress that result to premature failure [28].

1.2 Motivation and research objectives

Although literature regarding corrosion initiation and propagation mechanisms of Al-Cu aeronautical alloys is very extended, information concerning corrosion behaviour of third generation Al-Cu-Li alloys is limited. Additionally, the correlation of electrochemical kinetics, especially at the first stages of corrosion exposure, with mechanical properties degradation of these alloys is not well-defined. For that reason, corrosion exposure of the innovative Al-Cu-Li 2198 alloy is performed under different corrosive environments and methods and the corrosion-induced degradation is directly compared against the respective of the conventional Al-Cu 2024 alloy.

The target of the present Thesis is tried to be reached through several specific objectives:

- **Investigation of the governing corrosion-induced degradation mechanisms under corrosive environments of different aggressiveness:** Exposure of specimens to different corrosive environments was performed, and the corrosion kinetics as well as the corrosion-induced degradation of mechanical properties were evaluated. A correlation between the different corrosive environments was attempted regarding the elongation at fracture decrease.
- **Investigation of the effect of corrosion-induced micro-cracking on the structural integrity of the alloys:** The contribution effect of corrosion-induced micro-cracks on the elongation at fracture decrease was evaluated through measurements of the depth of cracks. A quantitative evaluation was performed in order to isolate the effect of corrosion-induced micro-cracks and predict possible hydrogen embrittlement phenomena.
- **Investigation of the effect of microstructural changes coming from different artificial ageing heat-treatments on the corrosion behaviour of Al-Cu-Li alloys:** Exposure of specimens to different ageing tempers and subsequent corrosion was performed in order to

assess the effect of thermomechanical transformations on corrosion initiation and propagation mechanisms, as well as on corrosion-induced mechanical properties degradation.

1.3 Outline of the thesis

The outline of the present thesis is divided into the following chapters:

Chapter 2 refers to the investigation of corrosion behaviour under corrosive solutions of different aggressiveness. The effect of solution aggressiveness on the corrosion mechanism as well as on the corrosion-induced mechanical properties degradation is investigated through electrochemical techniques (electrochemical impedance spectroscopy) and mechanical testing (tensile, crack growth resistance test). Additionally, a correlation between the different solutions with regards to their effect on ductility decrease is attempted through a coefficient.

Chapter 3 deals with the effect of corrosion-induced micro-cracking on the structural integrity of alloys and the quantification of the contribution of these cracks to elongation at fracture decrease. Measurements of depth of cracks were performed and a statistical analysis was made in order to reveal their increasing trend on the different surfaces of the alloy with increasing exposure time. Additionally, different models for the calculation/simulation of the ”effective thickness” decrease due to micro-cracks propagation were developed.

Chapter 4 focuses on the effect of artificial ageing-induced microstructural transformations on corrosion kinetics and corrosion-induced mechanical properties degradation. The influence of artificial ageing is studied through both electrochemical techniques and tensile mechanical testing of artificial aged specimens which have been pre-exposed to exfoliation corrosion solution.

Chapter 5 includes the general concluding remarks of the present Thesis. The most important conclusions of each chapter are summarized in this final chapter.

Chapter 2

2 Investigation of corrosion behaviour on 2xxx series aeronautical aluminium alloys: The effect of solution aggressiveness

The current chapter deals with the corrosion attack mechanism of Al-Cu 2024-T3 and Al-Cu-Li 2198-T8 alloys under different corrosive solutions. The effect of solution aggressiveness on the corrosion attack mechanism as well as on the corrosion-induced mechanical properties degradation is investigated. Furthermore, a correlation between the different solutions is attempted with regards to the same corrosion-induced degradation of ductility, which is represented by elongation at fracture (A_f). Comparison between the two specimens is presented in the end of this chapter in order to prove the superiority of Al-Cu-Li alloys regarding corrosion resistance. The chapter starts with an extensive literature review on the corrosion problem of several aeronautical aluminium alloys, continues with the description of the experimental procedure and afterwards the experimental results are presented and briefly discussed in order to extract the main conclusions.

2.1 Introduction

During the last decades much attention has been paid by the aviation industries to the reduction of aircrafts' operational and maintenance costs. Due to the difficulty for direct intervention and reduction of operational costs, material engineers are focusing their activities on maintenance costs. Significant savings on maintenance costs can be achieved through damage tolerance evaluation and preservation. The aeronautical aluminium alloy 2024 is widely used in aircraft structures due to its high specific mechanical properties, enhanced damage tolerance capabilities (fatigue crack growth and fracture toughness) and increased corrosion resistance. However, the long-term usage of the conventional aluminium alloy 2024 in the aeronautical industry may lead to the degradation of the alloy's damage tolerance and mechanical performance during its service life. Degradation of the mechanical properties, such as tensile strength, fracture toughness, as well as elongation at fracture (ductility) may be brought on by several mechanisms, including natural ageing of the alloy, intergranular corrosion, and hydrogen embrittlement, as well as their combined effects [49], [63]-[64].

Among the greatest problems in maintenance and repair of aircraft structures from aluminium alloy 2024-T3 is corrosion [65], having a frequency of more than 30% of total repairs. The possibility that corrosion will interact with other forms of damage, *e.g.*, fatigue, impact etc., can result in significant loss of the damage tolerance capabilities and consequently of structural integrity that may lead to fatal consequences, *e.g.*, the Aloha Airlines accident. The synergetic interaction of corrosion and fatigue has a deteriorating effect on the mechanical performance of aeronautical aluminium alloys, mainly because of accelerated crack propagation [66]-[67]. The major damage mechanism on corroded surface is the formation of pitting [22]-[23], [68]. Localized corrosion in the form of pits initiates on materials' surface sites where breakdown of the protective oxide layer has occurred due to chemical or physical heterogeneities, such as intermetallic particles (IMs), dislocations or mechanical damage and flaws, *e.g.*, [24], [29]-[30] and [69]-[71]. Wrought aeronautical aluminium alloys contain numerous intermetallic particles and dispersoids which substantially increase their mechanical properties (*i.e.*, yield stress, hardness, fracture toughness etc.), nevertheless they play a pivotal role in the nucleation of pitting corrosion [24], [71]. Differences in the electrochemical corrosion potential between grain boundary precipitates and/or intermetallic particles with the Al-matrix or adjacent particles lead to localized galvanic corrosion [23], [71]. Intergranular corrosion attack (IGC) is also evident when corrosion is localized at grain boundaries; for instance, when a galvanic cell between Cu-rich grain boundaries' precipitates − *e.g.*, θ-type (Al_2Cu) and *S*-type (Al_2CuMg) in the case of 2xxx series aluminium alloys − and the matrix or the adjacent Cu-depleted particles is formed [30]-[34]. In the case of AA2024, corrosion was found to initiate with dealloying

of secondary phase particles, *e.g.*, *S*-type (Al_2CuMg) particles [25]-[26]. The anodic dissolution of *S* phase particles starts from the release of magnesium (Mg) into solution, which results in copper enrichment of the particles; therefore, Cu-rich remnants become nobler than matrix, which lead to anodic dissolution of surrounding matrix and pitting formation on their periphery [72]; thus, it assists the formation of sub-surface micro-cracks [73]-[75]. The occluded corrosive solution as well as the formed corrosion products inside pits raise internal stresses which promote stress concentration around them, and subsequent cracking formation. Cracking generally starts at local defects that act as stress concentrators, which may be microstructural features inside material, surface features (*e.g.*, notches) or arise from in-service damage process such as corrosion (*e.g.*, pitting) [76]-[77].

Additionally, accumulated corrosion damage can be noticed on ageing aircrafts due to corrosion-induced hydrogen embrittlement mechanisms that include hydrogen environment embrittlement, hydrogen stress cracking and loss in ductility [28]. It is well known that corrosion involves several electrochemical mechanisms; in acidified solutions, the basic anodic reaction is the metal dissolution while the cathodic reactions are oxygen and hydrogen reduction resulting from aluminium ions' hydrolysis [22]. Hydrogen embrittlement on aluminium alloys can lead to rapid failure of the materials due to enhanced localized plastic deformation caused by adsorbed hydrogen atoms, that are trapped at preferential lattice sites, as was mentioned in [37], [46], and [78]. Atomic hydrogen can be adsorbed at crack tips and/or notches or diffuse ahead of cracks [79], thus embrittles the material below the crack tip and lead to environmentally assisted cracking (EAC) and stress corrosion cracking (SCC) phenomena.

Among several types of localized corrosion on aeronautical aluminium alloys, the most common atmospheric corrosion attack is referred to as exfoliation corrosion (EXCO) and is caused by the exposure of these alloys to moist and/or corrosive environments. EXCO is considered as a particular form of intergranular corrosion attack that occurs on the corroded surfaces of aircraft structures comprising of elongated grain structures [35]-[36]. To face the issue of corrosion-induced degradation of aircrafts' structural integrity, available data usually refer to accelerated laboratory tests. The most common accelerated laboratory corrosion test − used for the assessment of exfoliation corrosion susceptibility in 2xxx and 7xxx series aluminium alloys − is the exfoliation corrosion (EXCO) test, according to ASTM G34 standard test method [80]. The ASTM G34 standard defines EXCO as corrosion that proceeds laterally along planes parallel to the surface, generally along grain boundaries, where it forms voluminous corrosion products that, due to internal stresses, forces the metal apart. It has been reported that 24 hours exposure of the aluminium alloy 2024-T4 to the EXCO solution corresponds to nearly 6 years of natural exposure of the same structural element, regarding its surface exfoliation [81]. Several studies in the open literature [62]-[64], [67] showed that

exfoliation corrosion can lead to significant material's degradation by reducing the ultimate tensile strength, fracture toughness, and fatigue endurance limit of Al-Cu alloys, as well as accelerate fatigue crack growth rate [82]-[83]. A moderate degradation of the material's mechanical strength properties, *e.g.,* yield stress and ultimate tensile strength, along with a significant reduction in tensile ductility (*e.g.*, elongation at fracture) was revealed from several studies regarding exfoliation corrosion of AA2024 [84]-[85]. The moderate reduction of tensile strength properties is a result of the reduction of specimens' load carrying capacity – "effective thickness" – as well as the notch effects caused by pitting formation [49], [86]. Important findings on the corrosion behaviour of AA2024 revealed a recovery of the residual strength after mechanical removal (*e.g.*, by milling) of the exfoliated corrosion layer; however, this was not the case for elongation at fracture [87]. This gave rise to the idea that the plasticity of the alloy is not only degraded by corrosion-induced cracking formation, but also by a corrosion-induced mechanism of hydrogen embrittlement, as was examined by Kamoutsi et *al.* [46].

As was already mentioned, the corrosion problem includes several types and degradation mechanisms, and the damage could be described and analyzed as the sum of several parameters downgrading the mechanical properties. In order to better interpret the corrosion-induced damage, various mechanisms involved in corrosion process should be taken into consideration; they may depend on material, temper, corrosive environment, and exposure time. The aggressiveness of the corrosive environment is a significant parameter influencing corrosion damage evolution as well as the underlying corrosion mechanism. Recent investigations [88] indicate that in-service obtained corrosion damage correlates well to the one caused by a 3.5 *wt.* % NaCl solution, with pitting density, depth and shape evolving with exposure time. Vasco et *al.* [89] performed correlations between corrosion damage from accelerated corrosion tests of varying aggressiveness by accounting for both, the metallographic features of corrosion damage and the mechanical properties of the corroded material. Correlations regarding geometrical metallographic features were found under dominance of pitting corrosion and up to 8 hours in EXCO solution; higher variations were presented after the occurrence of pit coalescence and transition to dominance of exfoliation corrosion.

In the present chapter the investigation of corrosion behaviour and corrosion-induced degradation mechanisms on the conventional AA2024-T3 as well as the innovative AA2198-T8 is attempted. The effect of corrosion on mechanical properties degradation as well as the corrosion mechanisms associated with exposure to the commonly used exfoliation corrosion solution (EXCO) are compared against milder solutions with the aim of studying the differences in the corrosion-induced degradation mechanisms.

2.2 Materials and experimental procedure

2.2.1 Materials

The materials used in the current research work were the conventional aeronautical aluminium alloy 2024 in T3 temper and the innovative 2198 in T8 temper, which were received in 3.2 mm nominal thickness. The chemical composition of AA2024 according to the sheet manufacturer is a mixture of the following elements as percentage by weight; 4.35% Cu, 1.50% Mg, 0.64% Mn, 0.50% Si, 0.50% Fe, 0.25% Zn, 0.15% Ti, 0.10% Cr, 92.01% Al, as shown in Table 2-1, while the chemical composition of AA2198 is a mixture of the following elements as percentage by weight; 2.9-3.5% Cu, 0.8-1.1% Li, ≤ 0.35% Zn, ≤ 0.5% Mn, 0.25-0.8% Mg, 0.04-0.18% Zr, ≤ 0.08% Si, 0.1-0.5% Ag, ≤ 0.01% Fe and Al rem., shown in Table 2-2. T3 condition includes solution heat-treatment at 495 °C, quenching in water at 0 °C, and natural age in room temperature (25 °C) to a substantially stable condition. The T8 temper corresponds to under-ageing condition for AA2198, since it does not possess among the highest tensile properties during artificial ageing (peak-ageing condition) and had an appropriate artificial ageing heat-treatment from the T3 temper.

Table 2-1: Chemical composition of AA2024 (percentage by weight).

Si	Fe	Cu	Mn	Mg	Zn	Cr	Ti	Al
0.5	0.5	3.9-4.9	0.64	1.5	0.25	0.1	0.15	92.5

Table 2-2: Chemical composition of AA2198 (percentage by weight).

Cu	Li	Zn	Mn	Mg	Zr	Si	Ag	Fe
2.9-3.5	0.8-1.1	≤ 0.35	≤ 0.5	0.25-0.8	0.04-0.18	≤ 0.08	0.1-0.5	≤ 0.01

Tensile and fracture toughness compact tension specimens (hereafter referred to as C(T)) were machined from the longitudinal (L) rolling direction of the sheet in accordance with ASTM E8 [90] and ASTM E561 [91] specifications, respectively. Additionally, small rectangular metallographic specimens were cut from the longitudinal (L) rolling direction of the sheet to be used for electrochemical as well as metallographic measurements. The geometrical dimensions of tensile specimens were 12.5 mm x 3.2 mm at the reduced cross section, with total length of 190 mm, as shown in Picture 2-1.

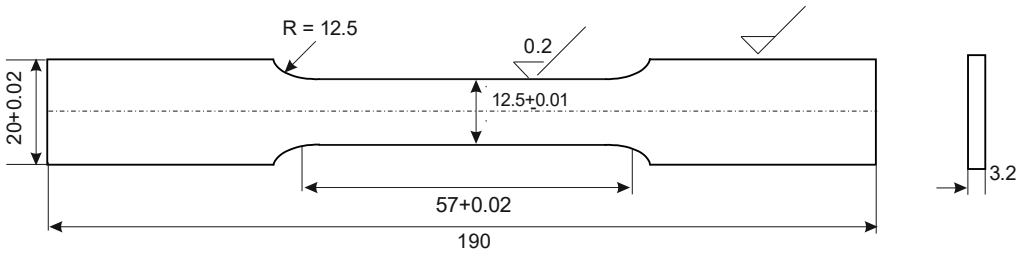

Picture 2-1: Schematic representation of tensile specimens according to ASTM E8 standard [90].

The C(T) specimens had a width (W) of 48 mm and an original crack/notch size (a_o) of approximately 16.70 mm in length. Further machining of the received C(T) specimens included the preparation of a fatigue starter notch with smaller radius (approximately 0.12 mm), that was machined at the tip of the pre-existing notch root through EDM, *e.g.,* Picture 2-2(b). Therefore, the original crack/notch size of machined C(T) specimens became $a_o \approx 22.50$ mm in length. Alteration of the notch root radius was performed in order to reduce the deleterious effect of large notch root radius on the initiation and propagation of fatigue pre-crack.

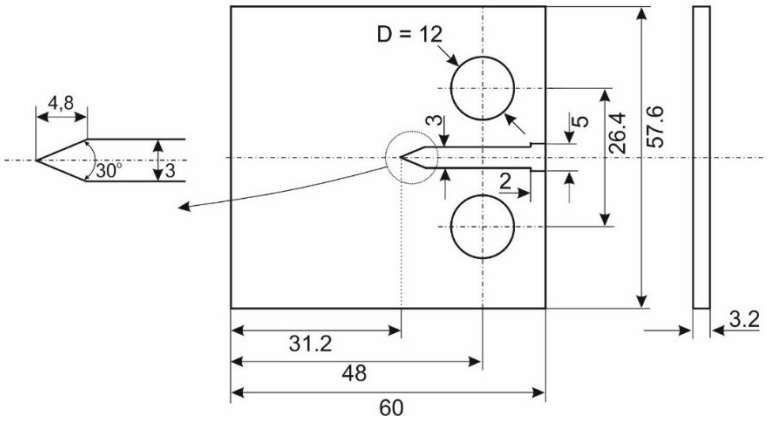

(a)

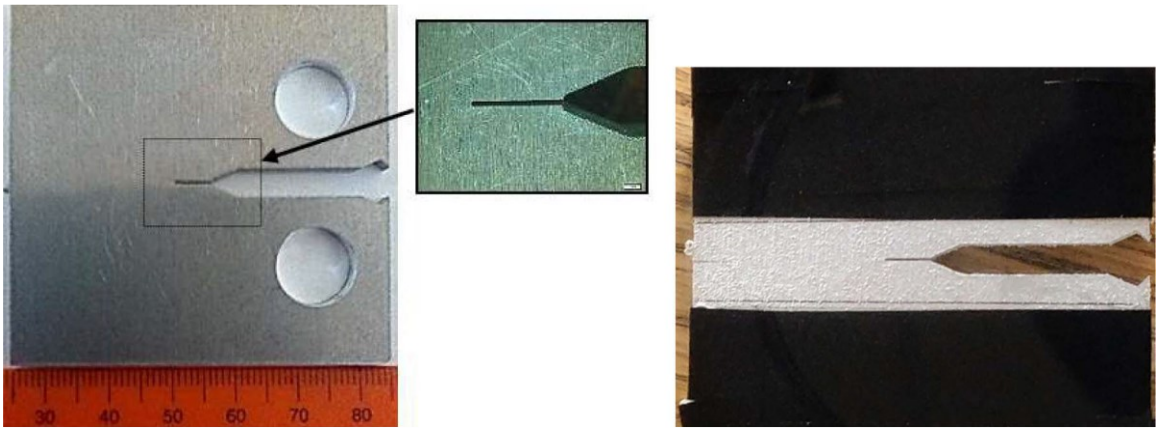

(b) (c)

Picture 2-2: (a) Schematic representation of the C(T) specimens' geometry according to ASTM E561 specification [91], (b) photograph of the machined notch extended by fatigue notch and (c) photograph of the shielded specimen.

The respective dimensions for the small rectangular specimens were 10 mm x 20 mm x 3.2 mm. Specimens shape and dimensions were designed with the aid of CorelDraw X7 software and they were sent to the machine shop in order to be cut via water-jet method. This method performs cutting with water and sand, with the water pressure equal to 3800 bar and its speed 2max. Water-jet process was chosen to limit the temperature increase during contact (friction) of material with the cutting tool, which can affect the mechanical properties of the metal. After cutting of the specimens, the samples were peeled off from the sheet, ground up and cleaned with alcohol according to ASTM G1 standard [92]. It is worth noting that grinding and cleaning are necessary processes in order to avoid heterogeneity on the materials surface and to remove any impurities, which accelerate corrosion in the micro- or macroscopic surface irregularities (claws).

2.2.2 Preparation of corrosive solutions

Exposure of test specimens to four different exposure environments were considered for this Thesis. That is:

(i) prior exposure to air for the baseline test results (reference),

(ii) prior exposure to a 0.6 M (or 3.5 *wt*. %) NaCl solution with a pH within the range of 6.4 to 7.2, according to ASTM G44 specification [93],

(iii) prior exposure to EXCO solution, according to ASTM G34 specification [80] and

(iv) prior exposure to Harrison's solution (diluted version), according to ASTM D5894 [94] specification.

The 0.6 M NaCl exposure environment was prepared by adding 35.0 g of sodium chloride (purity of 99.0% min) to 500 mL of distilled water and the pH measured after allowing enough time for the full dissolution of sodium chloride. To ensure that the pH value is between the established range of 6.4 to 7.2, a buffer solution containing hydrochloric acid with a pH value of 2.1 was prepared, according to ASTM G44 standard [93]. Thereafter, approximately 0.05 mL of the buffer solution was slowly added to sodium chloride solution for the adjustment of pH. An additional 500 mL of distilled water was added to the sodium chloride solution before transferring the solution into a storage container. The measured pH of solution stabilized at 6.5 after allowing sufficient time for equilibrium to set in. Thus, in total 35.0 g of sodium chloride added to 1000 mL distilled water.

The exfoliation corrosion (EXCO) exposure environment is a solution consisting of approximately 4.0 M sodium chloride (NaCl), 0.5 M potassium nitrate (KNO_3), and 0.1 M nitric acid (HNO_3). Preparation of the EXCO solution commenced with the addition of 50 g of potassium nitrate (reagent grade KNO_3 with 99% purity) and 234 g sodium chloride (reagent grade NaCl with 99.0% purity) to 1 L of distilled water. According to ASTM G34 standard [80], an additional 6.3 mL of 70%

concentrated nitric acid (HNO_3) should have been added to the solution. However, due to the unavailability of a 70% concentrated nitric acid solution in some cases, the volumetric addition of nitric acid was altered to make use of a 55% concentrated nitric acid solution. Therefore, 8.5 mL of the 55% concentrated nitric acid was added to solution in order to obtain the required HNO_3 molarity. The solution was then transferred to a proper storage container, and given sufficient time for equilibrium to set in. The final pH of the solution was measured at 0.27.

The Harrison's (diluted version) solution, often used to study the corrosion rates of Al-Cu-Li alloys, consisted of 0.35 g of ammonium sulfate ($(NH_4)_2SO_4$) and 0.05 g sodium chloride dissolved to 1 L of distilled water.

2.2.3 Electrochemical tests

The corrosion behaviour of the investigated aluminium alloys was assessed by electrochemical impedance spectroscopy (EIS) tests, which were carried out using a PalmSens® potentiostat at 25 ± 1 °C. The experiments were carried out in naturally aerated 3.5 *wt*. % NaCl solution at room temperature (25 ± 2) °C since the in-service obtained corrosion damage correlates well to the one caused by this solution [88]. However, for the case of AA2198-T8, the Harrison's solution [94] was also used in EIS tests since it better simulates the corrosion in industrial atmospheres − which are more aggressive due to the presence of soot, fly ash and sulfur compounds − that cause coating consumption. A typical three electrodes cell system that was composed of a platinum electrode as counter electrode, a silver chloride electrode Ag/AgCl as reference electrode and the small rectangular specimens (10 mm * 20 mm) of the investigated aluminium alloys as working electrodes was used, shown in Picture 2-3. A surface area of 0.5 cm^2 of the working electrode was exposed to the electrolyte. The voltage perturbation range used in the EIS measurements was 10 mV (rms), and the acquisition rate was 10 points per decade in a frequency range from 10^5 Hz down to 0.01 Hz. The measurements were repeated at fixed intervals of 0 (after 5 min immersion), 1, 3, 6, 12, 24, and 48 hours of immersion time. Each test was performed at least three times to evaluate the reproducibility of the results. The obtained data were fitted employing a PStrace5® analysis software. The set-up of the experiments is depicted in Picture 2-4.

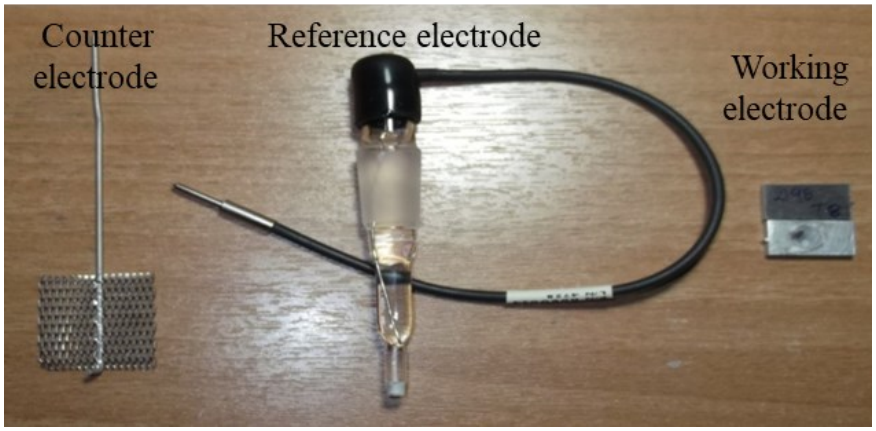

Picture 2-3: Electrodes used for the electrochemical impedance spectroscopy (EIS) measurements.

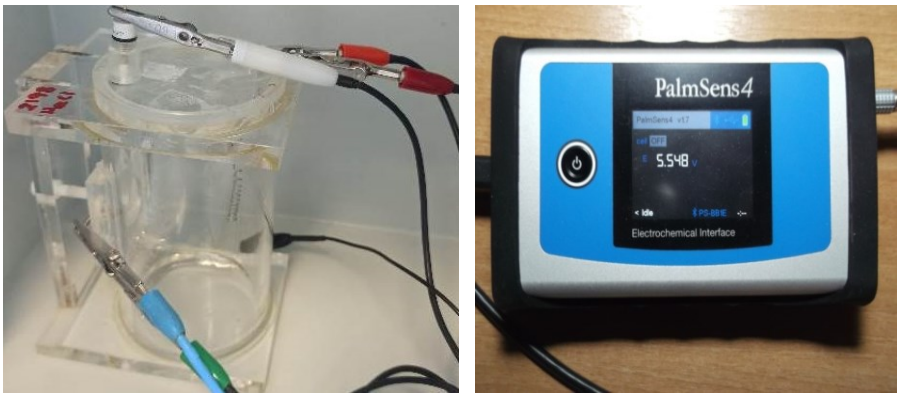

Picture 2-4: Set-up of EIS test.

2.2.4 Immersion tests

For the case of tensile specimens, further preparation was required prior to their immersion to the relevant exposure environments. The preparation included shielding of the specimens' surfaces so that only specific areas of interest (reduced cross-section) were exposed. Masking with appropriate insulating PVC tape (with excellent adherence) was performed in order to avoid crevice corrosion beneath the masking tape. The exposed area was within the reduced cross-section to ensure fracture within the gauge length, as indicated with grey colour in Picture 2-5. The solution volume was calculated per exposure area of the specimens and was 20 ml/cm^2 for all specimens, while solution temperature was 25 ± 1 °C, according to ASTM G34 specification [80]. The specimens were then placed into containers (Picture 2-6) and allowed to be exposed for several times to the different corrosive solutions, respectively. After corrosion exposure, the tensile specimens were immediately cleaned with acetone according to ASTM G34 specification [80] and then subjected to mechanical testing (tension). At least three specimens in each test series were used for the reproducibility of the results.

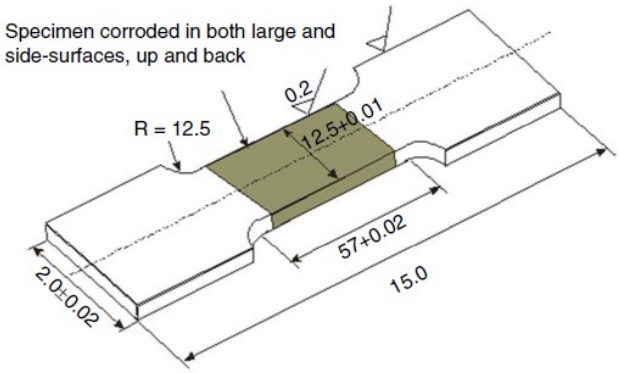

Picture 2-5: Schematic representation of shielded tensile specimens according to ASTM E8 specification [90].

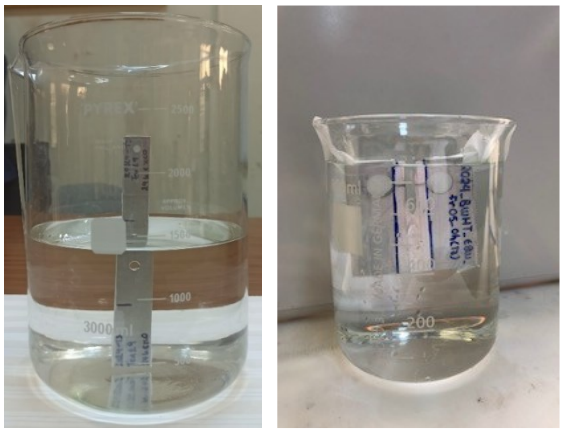

(a) (b)

Picture 2-6: Exposure of (a) tensile and (b) C(T) specimens to corrosive environment.

The C(T) specimens were shielded in such a way to ensure that only a 10 mm wide section near the specimen notch/pre-crack configuration would be exposed to the relevant exposure environments (see Picture 2-2(c)); in accordance with ASTM E1681 specification [95] the environmental chamber should enclose the portion of the specimen that contains the crack tip. The shielding procedure consisted of measuring the relevant specimen dimensions (*e.g.*, W, B and a_o) – according to ASTM E561 specification – before covering the surface areas with a layer of double-sided tape (refer to Picture 2-2(c)). Thereafter, the taped areas were covered again with a double layer of adherent PVC tape in order to avoid crevice corrosion beneath the masking tape. The specimens were then placed into containers (Picture 2-6) and allowed to be exposed to the relevant solutions. After completion of the exposure test, the specimens were removed from the containers and cleaned with acetone before performing mechanical testing (crack growth resistance). Throughout the duration of the exposure the solutions were kept in 25 ± 3°C temperature. At least three specimens in each test series were used for the reproducibility of the results.

2.2.5 Tensile tests

Tensile tests were carried out in a servo-hydraulic Instron 8801 100 kN testing machine according to ASTM E8 specification [90], as it is depicted in Picture 2-7. The software was programmed to apply a tensile strain to the specimen − under crosshead displacement control − and the rate was kept constant and equal to 0.7 mm/min. The relevant specimen dimensions (*i.e.*, the thickness t_0, width b_0, and gauge length L_0) were then taken and programed into the software. Thereafter, the specimens were individually installed into the machine's grips, ensuring good alignment with the loading axis. An external Instron extensometer with 50 mm ± 10 mm maximum travel was attached at the reduced cross-section gauge length of the specimens and zeroed before applying a 1 kN preload to the specimen. The test was then allowed to commence, with termination set to occur after the complete fracture of the specimens. A data logger was used during all tensile tests and the values of load, displacement and axial strain were recorded and stored in a computer. After termination of the tests, the relevant specimen dimensions were measured again and tabulated. The raw data from each test were then analyzed using a specially programmed Excel spreadsheet and edited with the aid of Microcal Origin© 8.5 software. More than three specimens were tested in each different case to get reliable average data. Afterwards, the fractured surfaces of the tensile specimens were examined in a Leica stereoscope as well as with the aid of scanning electron microscopy (SEM) in order to investigate the fracture mechanism. Furthermore, some specimens were sent for EDM in order to section out specimens for x-Ray computed microtomography imaging (micro-XCT). The micro-XCT specimens were then scanned to obtain 3D images of the specimens and cracks.

Picture 2-7: Experimental set-up of tensile testing.

2.2.6 Crack growth resistance tests

Fatigue pre-cracking commenced on the C(T) specimens, prior to corrosion exposure, using an Instron 1342 Servo-Hydraulic Testing Machine operating on Instron Crack Propagation Software. The specimens were installed into the testing machine using the prescribed grips and fixtures in accordance with ASTM E1820 standard [96]. The software was programmed to cyclically strain the specimens at a constant stress intensity range (ΔK) of between 15 and 27 MPa√m and a stress ratio (R) of 0.1. These cyclic loads were introduced until a fatigue pre-crack in the order of 2 mm was produced. This test step was force controlled and the maximum applied force did not exceed 1 kN, to avoid plastic yielding in the crack tip region of the specimen. However, for the calculation of fracture toughness a second experimental step followed the fatigue pre-cracking and subsequent corrosion exposure of specimens. The second step included quasi-static mechanical loading under displacement control, with a crosshead deformation rate of 0.01 mm/min applied to the specimen. A crack opening displacement (hereafter called COD) device/extensometer has been used to record the displacement of the mouth of the machined edge crack of the specimen and a data logger was used to record the data of the experiments, namely force, crosshead displacement and crack mouth opening displacement in a digital file. Test stopped when crack essentially increased and axial load took values lower than 2 kN, post to fracture of the specimens, as can be seen in Picture 2-8.

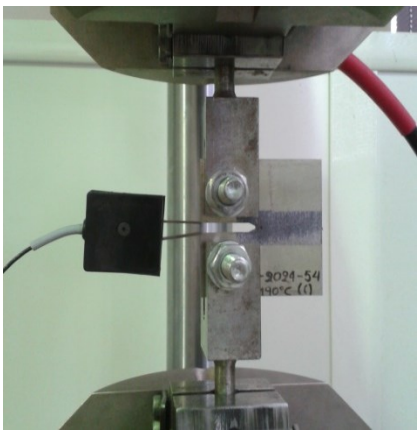

Picture 2-8: C(T) specimen at the grips of the testing machine with the COD device attached.

2.3 Results and discussion

2.3.1 AA2024-T3: Effect of exposure to 3.5 *wt*. % NaCl solution

2.3.1.1 Effect on corrosion mechanism

Electrochemical impedance spectroscopy (EIS) results for AA2024-T3, as a function of immersion time in 3.5 *wt.* % NaCl solution, are shown in the form of Bode diagrams in Figure 2-1. In Figure 2-1(a) two-time constants (peaks in the Theta phase – Frequency curve) are evident at low

(10^{-2}-10^{-1}) and medium (10^{0}-10^{3}) frequencies regime after above one hour of immersion. In contrast, at the initial period of immersion (black curve) the relaxation process at higher frequencies being responsible for the response from the passive film can also be evidenced. The presence of a time constant at higher frequencies – where the system is more kinetically – represents a capacitive behaviour instead of Ohmic behaviour, indicating the presence of an obstacle to charge transfer on the specimen. Time constants in medium frequencies are related to charge transfer processes coupled to the double layer capacitance, while the time constant at low frequencies is likely to be associated to diffusion-control. Slight fluctuations of the curves in 1 hour (shown in red curve) and 3 hours (shown in green curve) at low frequencies regime can be caused by non-stationarities of the system at this period resulted from the metastable pitting formation. However, after 6 hours (shown in blue curve) of exposure the pits seem to become more stable leading to much less scattering of the low-frequency impedance values. No essential differences in corrosion behaviour of AA2024-T3 are noticed with increasing immersion time, however, a slight decrease of the capacitive behaviour is evident with increasing exposure time and after 6 hours.

Impedance modulus shown in Figure 2-1(b) slightly increase for short exposure times and up to 3 hours at low frequencies regime (10^{-2}-10^{-1}) followed by a gradual decreasing trend for higher exposure times. Essential decrease is noticed between 6 and 12 hours (shown in cyan curve) of exposure while further corrosion exposure seems not to reduce impedance modulus essentially at low frequencies regime since by that time stable pits are formed, and the corrosion process is controlled by the diffusion limited cathodic oxygen reduction. Formation of voluminous corrosion products after long exposure times seal the pits and impede transport to/from the active areas.

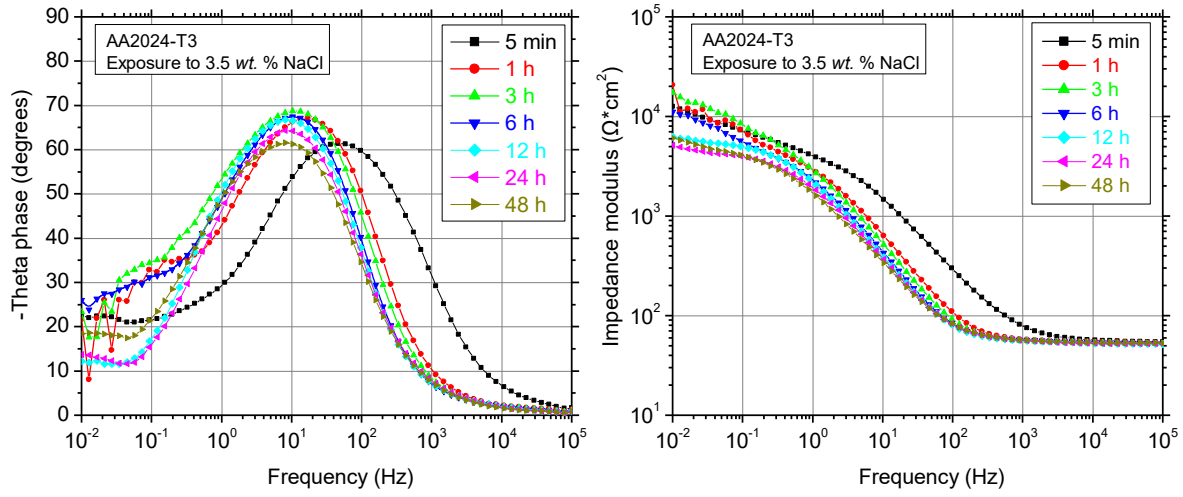

(a) (b)

Figure 2-1: Impedance spectra of AA2024-T3 measured in 3.5 wt. % NaCl solution.

Nyquist spectra shown in Figure 2-2 revealed the same change trend regarding corrosion behaviour of AA2024-T3. Capacitive arc (semi-circle diameter) tends to increase up to 3 hours

corrosion exposure time (represented by green curve), while a shrinkage is noticed after 6 hours which continues with increasing exposure time. One capacitive loop is noticed in high frequencies regime, for all exposure times, which corresponds to the flat surface oxide film according to [97] and [98], while a Warburg element is noticed in low frequencies regime. According to [99] when the resistance associated with diffusion becomes very large, the *R*//*CPE* element (time constant) may be replaced by a simple constant phase element (CPE) with the exponent "n" value of 0.5, which, in an ideal situation, is represented by a Warburg (*W*) element, as was the case for the present research work.

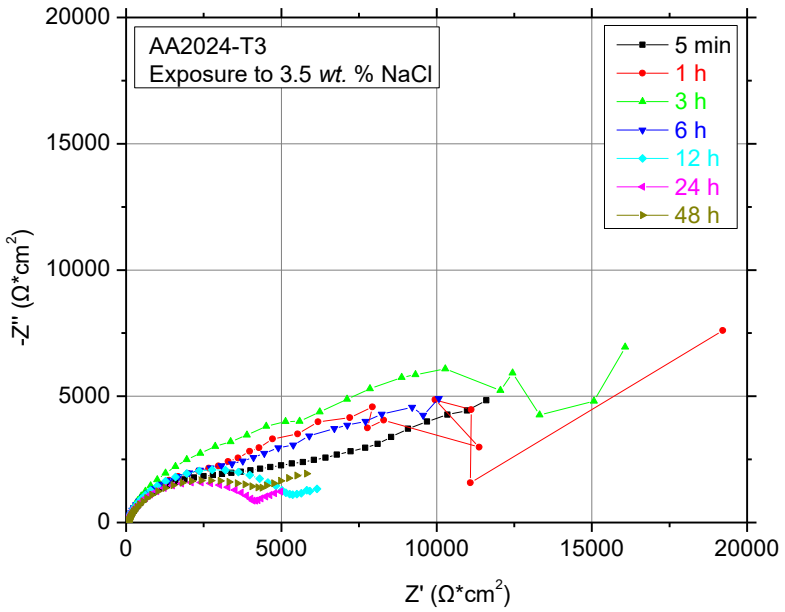

Figure 2-2: Nyquist plot of AA2024-T3 measured in 3.5 wt. % NaCl solution.

To gain a better insight into corrosion mechanisms, EIS response is modelled using equivalent electrical circuits, as shown in Figure 2-3. The R_1 element in circuit model represents the corrosive medium resistance. The pair R_2//Q_1 stands for the polarization resistance, *e.g.*, the resistance of electron flow through double layer, in parallel with capacitance of double layer, meaning the charge held in the double layer interface. A constant phase element (*CPE*) − that is denoted with *Q* in the present work − was used instead of an ideal capacitor to take into consideration the heterogeneity of the surface, as already mentioned in literature, *e.g.,* [20] and [100]. *W* element refers to Warburg impedance which is ascribed to the response at low frequencies being controlled by diffusion processes.

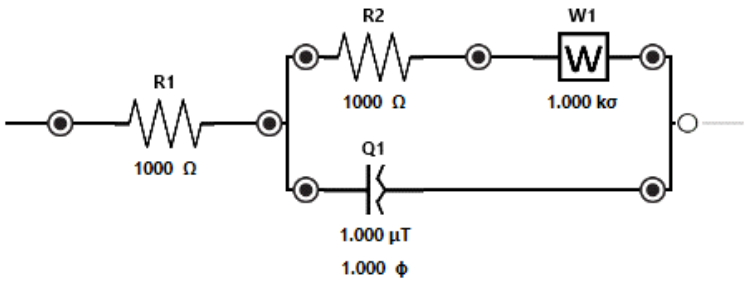

Figure 2-3: Equivalent circuit model of AA2024-T3 exposed to 3.5 wt. % NaCl solution.

The evolution of charge transfer resistance values of the circuit components (R_2 in this case) with increasing immersion time is depicted in Figure 2-4. Resistance was found to slightly decrease at the first stages of corrosion and then suddenly increase up to 1 hour of exposure. Fluctuations were noticed up to 12 hours of exposure while for higher exposure times the resistance tends to be stabilized due to the formation of stable pits.

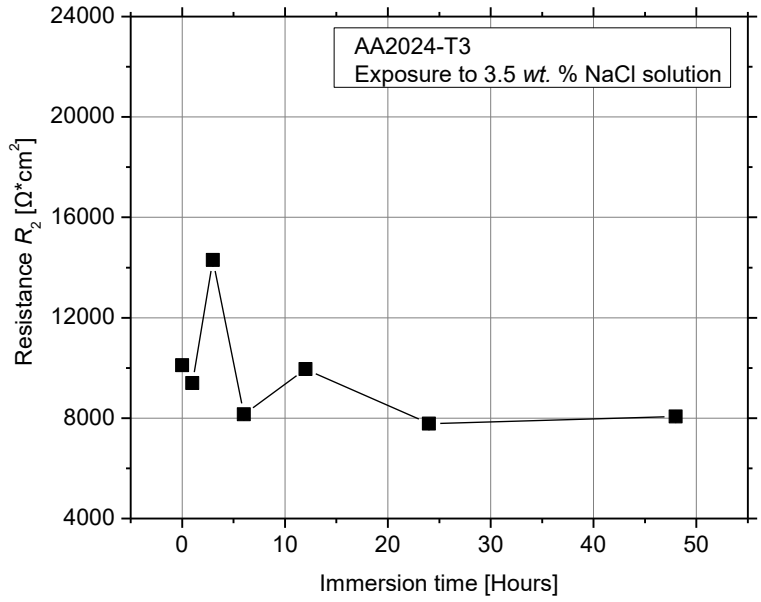

Figure 2-4: Variation of the charge transfer resistance R_2 as a function of immersion time to 3.5% wt. NaCl solution for AA2024-T3.

2.3.1.2 Effect on tensile mechanical performance

2.3.1.2.1 Surface characterization of pre-corroded specimens

Exposure of AA2024-T3 specimens to the corrosive environment (3.5 *wt.* % NaCl solution in the present case) results in deterioration of the specimens' surface due to the breakdown of the surface oxide passive film and the subsequent nucleation of corrosion-induced pits, as can be seen in Figure 2-5. The depicted corroded area has dimensions of 12.5 mm x 55 mm being the width and length of the exposed area of tensile specimens, respectively. Regarding the corrosion environment of 3.5 *wt.* % NaCl solution, it is evident that for the short exposure times surface deterioration remains limited since pits were not identified after 6 hours of exposure (Figure 2-5(a)); however, a significant amount

of precipitation in the form of a solid white layer of pustules was observed on the exposed surfaces. Nevertheless, the pitting density and size tend to increase with increasing exposure time; corrosion damage in the form of pits was observed after 168 hours of exposure (Figure 2-5(b)) while more pits of higher diameter as well as pit coalescence are evident after 720 hours exposure time (Figure 2-5(c)).

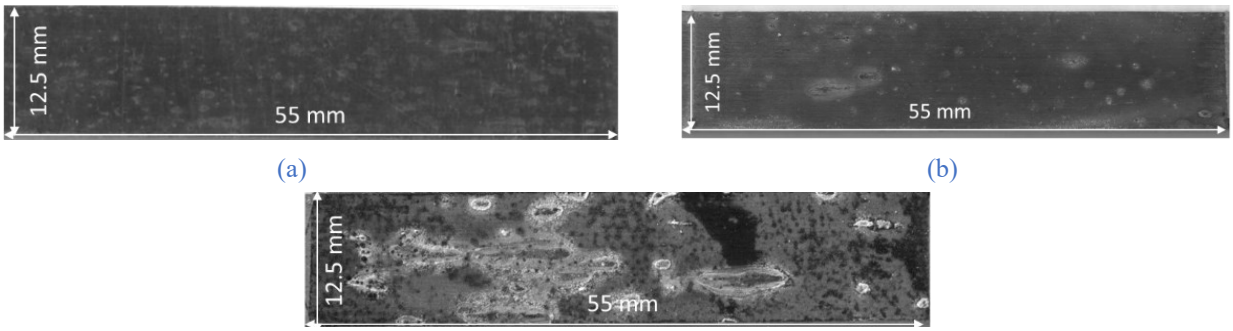

Figure 2-5: Typical photographs of AA2024-T3 pre-corroded tensile specimens exposed for (a)-(c) 6 h, 168 h and 720 h to 3.5 wt. % NaCl solution.

2.3.1.2.2 Mechanical evaluation of pre-corroded specimens

The typical nominal tensile stress-strain curves for the investigated exposure times of AA2024-T3 to 3.5 *wt.* % NaCl solution can be seen in Figure 2-6. The nominal stress calculation was based on the nominal cross-section of the tensile specimens, namely width x thickness = 12.5 mm x 3.2 mm. No essential decrease of the nominal axial stress was noticed even for the highest exposure time of 4200 hours. However, the nominal axial strain exhibited a significant degradation even for the very short exposure times, such as 6 hours, where the pitting corrosion mechanism was not identified (see Figure 2-5(a)). It is worth mentioning that higher ductility degradation was observed at the time range between 6 and 168 hours, where pitting incubation takes place since stable pits have started to form, as well as in the time range of 720 to 2184 hours, probably because of the change in the degradation mechanism, *e.g.,* pit growth and coalescence.

Figure 2-7 shows the experimental results, as average values, of elongation at fracture A_f (left y-axis) and conventional yield stress $Rp_{0.2\%}$ (right y-axis) with increasing immersion time to 3.5 *wt.* % NaCl solution. It is obvious that elongation at fracture decreases exponentially, and a significant degradation is evident even from the short exposure times, *e.g.*, approximately 16% after 6 hours of immersion. This degradation can be attributed to hydrogen diffusion into the material's crystal structure micro-voids and the subsequent embrittlement caused by the formation of strain fields, since pitting formation and subsequent sub-surface micro-cracking effect remains limited. In contrast, a degradation in the form of second degree polynomial can be noticed for the conventional yield stress. However, the remaining percentage of $Rp_{0.2\%}$ is approximately 90% after 2000 hours of immersion (≈ 3 months) while its degradation does not exceed 30% at maximum.

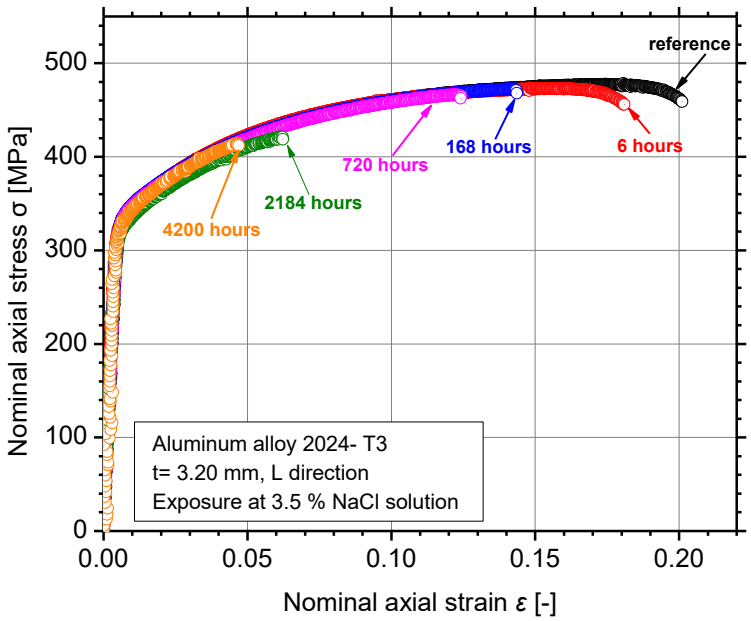

Figure 2-6: Typical tensile nominal stress-strain curves of AA2024-T3 after corrosion exposure to 3.5 wt. % NaCl solution for different exposure times.

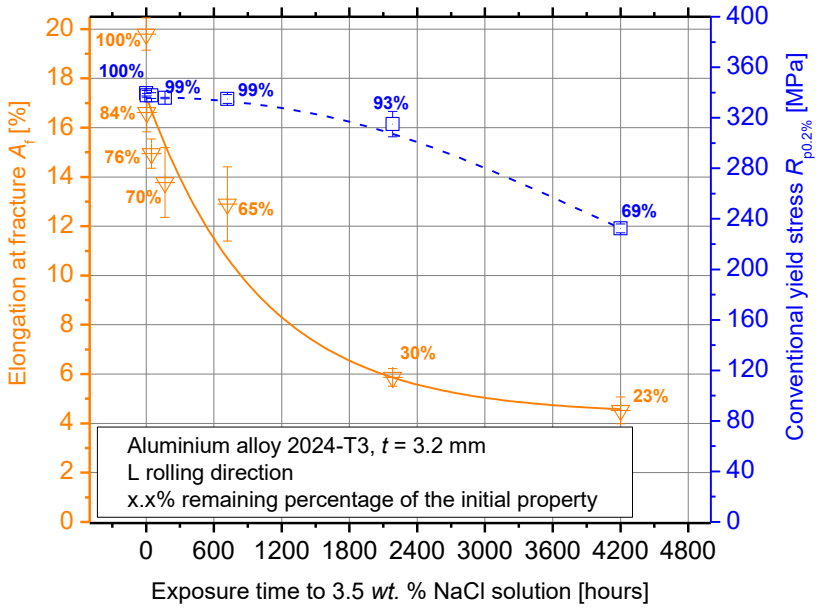

Figure 2-7: Experimental results of mechanical properties of AA2024-T3 after exposure to 3.5 wt. % NaCl solution for different exposure times.

2.3.1.2.3 Characterization of fractured pre-corroded specimens

Stereoscopical examination on the fractured, pre-corroded specimens of AA2024-T3 exposed to 3.5 *wt.* % NaCl solution are shown in Figure 2-8. The examination revealed that the pitting corrosion mechanism is limited for the very short corrosion exposure times and up to 168 hours (Figure 2-8(b)), while pitting density substantially increased for higher exposure times, *e.g.,* 720 hours (Figure 2-8(c)). Additionally, an increase in pits diameter in parallel with rolling direction as well as pit coalescence is noticed with increasing exposure time. Furthermore, a ductile fracture mechanism is evident from the 45° slope of the fracture surface that remains even after 720 hours of exposure.

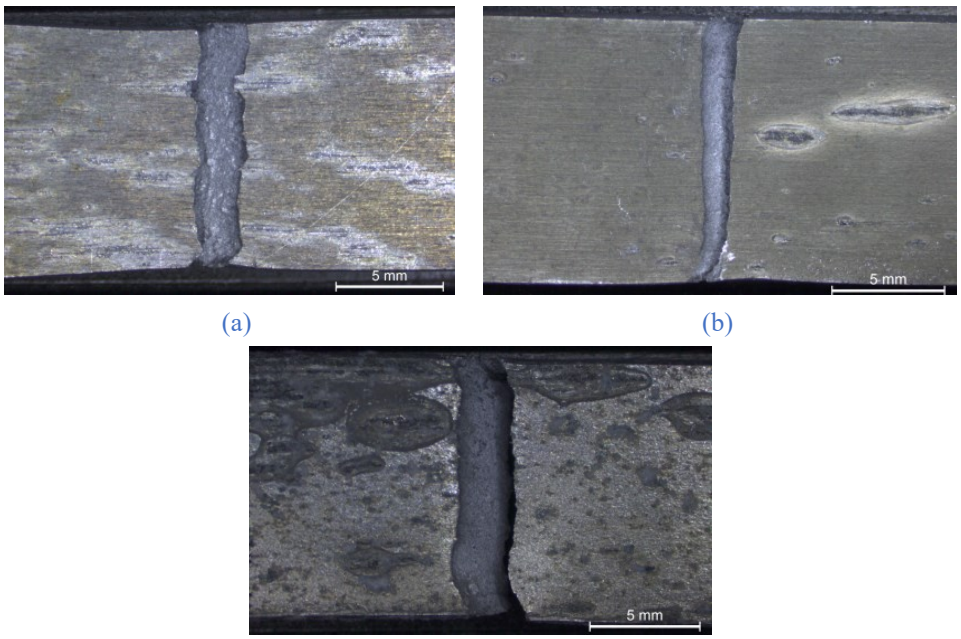

(a) (b)

(c)

Figure 2-8: Typical photographs of the fractured surfaces of AA2024-T3 pre-corroded tensile specimens exposed to 3.5 wt. % NaCl solution for (a)-(c) 6 h, 168 h and 720 h, respectively.

2.3.1.3 Effect on crack growth resistance

2.3.1.3.1 Macro- and microscopic features of pre-corroded specimens

Fracture toughness C(T) specimens exposed for 24 hours to 3.5 *wt.* % NaCl solution were used for the assessment of the corrosion effect on crack growth resistance. The 24 hours exposure to 3.5 *wt.* % NaCl solution were selected for further investigation because no essential stress decrease is noticed from the tensile flow curves, while a significant ductility decrease is evident even from the very short exposure times. Optical microscopy of the NaCl-exposed C(T) specimens − prior to the crack-growth resistance evaluation – revealed indications of localized corrosion attack in the form of pitting and intergranular corrosion. During the 24 hours exposure of the specimens to 3.5 *wt.* % NaCl solution, a significant amount of precipitation in the form of a solid white layer of pustules was observed on the exposed surfaces, as can be seen in Figure 2-9(a). In Figure 2-9(b) the observed localized corrosion attack appears to be more concentrated within the regions where the solid white layer of pustules has formed. Concerning the basic mechanism of pitting corrosion, Vargel [101] defines the overall reaction for pitting corrosion of aluminium alloys as:

$$2Al + 3H_2O + \frac{3}{2}O_2 \rightarrow 2Al(OH)_3 \qquad (2\text{-}1)$$

Therefore, the solid white layer is believed to be precipitation of aluminium-hydroxide $Al(OH)_3$, which results from corrosion of aluminium. Dissolution of aluminium at the pit's bottom leads to high concentration of Al^{3+}, which later diffuse toward the pit's opening. The half reaction concerned with the reduction of water or hydrogen (H^+) at the cathodic regions outside the pit is expected to

result in localized excess of OH^- at these sites, thereby increasing the pH (measured pH of 6.5) and, consequently, the alkalinity of the solution near these regions [101] giving rise to the precipitation of aluminium hydroxide. It is also observed that, once the specimen is moved, the solid white layer of pustules dissolves again. The dissolution of the white layer may be explained by the dissolution of aluminium-hydroxide after being exposed to the acidic environment (lower measured pH) of the bulk solution; this is in accordance with the findings of Gayer et *al.* [102].

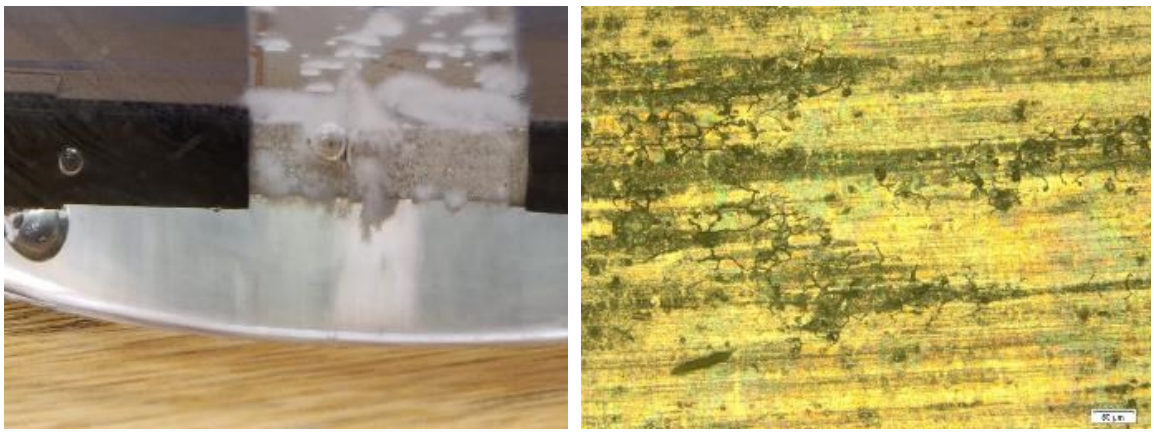

(a) (b)

Figure 2-9: (a) Photograph showing the white precipitate layer on the specimen's surface after 24 h immersion in 3.5 wt. % NaCl solution and (b) optical micrograph (200x magnification) showing significant pitting and intergranular corrosion attack within the area where white layer ($Al(OH)_3$) formation occurred.

2.3.1.3.2 Crack growth resistance behaviour of pre-corroded specimens

Figure 2-10(a) shows the load-crack mouth opening displacement (CMOD) curves and Figure 2-10(b) tabulates the evaluated critical stress intensity factor (K_{cr}) values (calculated from environmentally affected *R*-curves) of AA2024-T3 specimens exposed to 0.6 M-(or 3.5 *wt*. %) NaCl solution. As expected, the resistance curve is more recessive for the specimens exposed to corrosive environment (environmentally affected *R*-curve) regarding the maximum applied load and the associated critical crack extension values (Δa_c = 6.14 mm and 5.26 mm for the samples exposed to air and NaCl solution, respectively). However, no significant degradation of maximum applied load and crack mouth opening displacement (CMOD) at maximum load due to corrosion exposure is noticed. Specimens exposed to air were found to have a maximum load of approximately 4.0 kN while specimens exposed to NaCl solution exhibited a maximum applied force of 3.7 kN. Hence, it seems that the short corrosion exposure time investigated in this study does not essentially affect the maximum load capacity of specimens as well as the CMOD at the maximum load. Nevertheless, a considerable decrease in the material's ability to resist the propagation of a pre-existing crack is noticed from the K_{cr} values in Figure 2-10(b), as well as the critical values of crack extension leading to instability, quoted above. Specimens exposed to NaCl solution exhibited approximately 13% decrease of the K_{cr}.

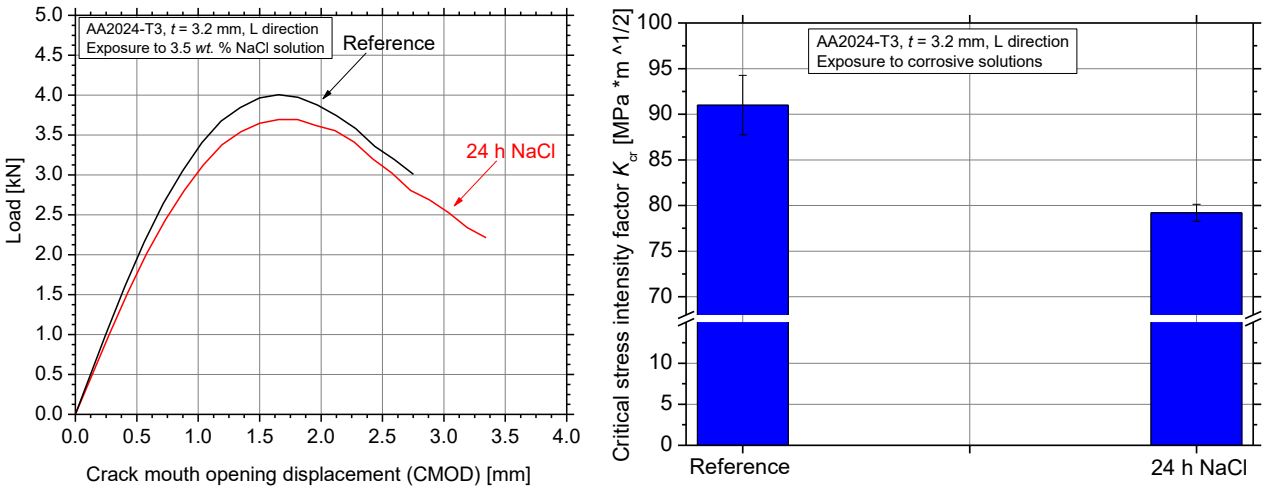

(a) (b)

Figure 2-10: (a) Load–crack mouth opening displacement (CMOD) curves and (b) evaluated critical stress intensity factor (K_{cr}) values of AA2024-T3 specimens after exposure to 3.5 wt. % NaCl corrosive solution.

Figure 2-11 shows the captured SEM images of the NaCl-exposed C(T) specimen after the crack-growth resistance evaluation. A ductile fracture surface, labeled with C in Figure 2-11(a), immediately adjacent to the specimen's outer surface (labeled with B) is evident from the dimples. Additionally, intergranular corrosion attack was revealed, as shown in the area labeled with D in Figure 2-11(a). It is evident from the dimpled fracture surface appearance, shown in higher magnification in Figure 2-11(b), that the crack propagated transgranularly. Furthermore, this transgranular crack propagation also persisted in the material near the intergranular attacked region. Similar observations have been reported in the literature [103]; revealing that intergranular corrosion attack is not restricted to the grain boundary itself, but tends to develop further in the interior of adjacent grains with high stored energy levels, thus becoming transgranular. This indicates that the type of corrosion mechanism brought on by the exposure of AA2024-T3 to a solution containing purely sodium-chloride does not result in the significant grain-boundary embrittlement of the bulk material; as was the case for the specimens exposed to EXCO solution shown by Posada et *al*. in [35].

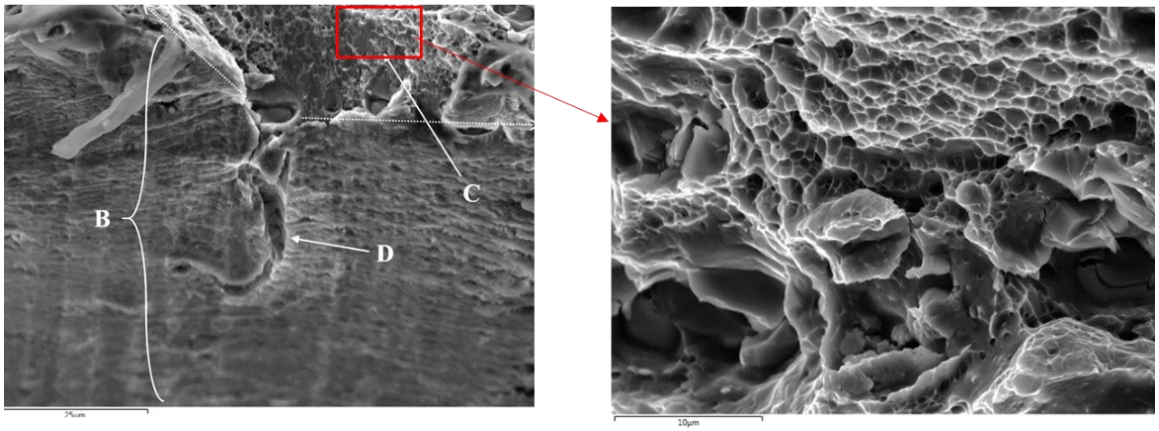

(a) (b)

Figure 2-11: (a) SEM image near the surface (B until dashed lines) of the NaCl exposed specimen, showing the ductile (dimpled) fracture surface (C) immediately adjacent to the specimen's surface, with (D) the point where intergranular corrosion has occurred and (b) higher magnification of area (C).

2.3.2 AA2024-T3: Effect of exposure to EXCO solution

2.3.2.1 Effect on tensile mechanical performance

2.3.2.1.1 Surface characterization of pre-corroded specimens

The exposure of AA2024-T3 specimens to the corrosive environment (EXCO solution in the present case) results in deterioration of the specimens' surface due to nucleation of corrosion-induced surface pits, as can be seen in Figure 2-12. The depicted corroded area has dimensions of 12.5 mm x 55 mm being the width and the length of the exposed area of the tensile specimens, respectively. For short exposure times to exfoliation corrosion solution and up to 2 hours (Figure 2-12(a)), pitting formation on the corroded surfaces remains rather limited. With increasing exposure time to EXCO solution, an increase in pitting density is evident (black spots), *e.g.*, Figure 2-12(b) and Figure 2-12(c). Corrosion damage initiates in the form of surface corrosion pits and evolves to the formation of micro-cracks and exfoliation areas in extreme exposure times due to the presence of intergranular corrosion (IGC).

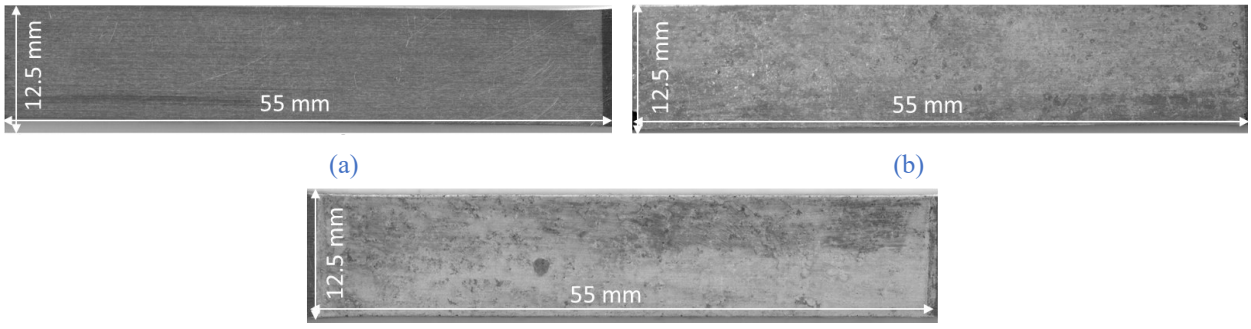

(a) (b)

(c)

Figure 2-12: Typical photographs of AA2024-T3 pre-corroded tensile specimens exposed for (a)-(c) 2 h, 4 h and 24 h to EXCO solution.

2.3.2.1.2 Mechanical evaluation of pre-corroded specimens

The typical nominal tensile stress-strain curves for the investigated exposure times of AA2024-T3 to EXCO solution can be seen in Figure 2-13. The nominal stress calculation was based on the nominal cross-section of the tensile specimens, namely width x thickness = 12.5 mm x 3.2 mm. It is obvious that the corrosion-induced degradation mechanism of the tensile curves is different from the respective in 3.5 *wt.* % NaCl solution (see Figure 2-6). It can be noticed that for the short corrosion exposure times to EXCO solution and up to 2 hours (shown in blue curve), the values of nominal axial stress are not essentially influenced by corrosion exposure. However, for higher exposure times, *e.g.,* after 4 hours, a significant sudden stress drop is noticed [63]. This stress drop is attributed to the decrease of specimen's cross-section – due to formation of corrosion-induced micro-cracks – that withstand the applied mechanical loading, referred as "effective thickness" in [49]. These results are in accordance with the observations from the corroded surface characterization (see Figure 2-12) where pitting corrosion was limited up to 2 hours of exposure. On the contrary, an essential decrease of tensile ductility, represented by nominal axial strain, is evident even for the very short exposure times, *e.g.,* 0.5 hours (shown in red curve), that can be attributed to hydrogen embrittlement phenomenon since pitting corrosion is extremely small in such short exposure times. For even higher exposure times, both the nominal axial stress and the nominal axial strain are essentially decreased. The above-mentioned results are depicted in Figure 2-14 as average values of elongation at fracture (left y-axis) and conventional yield stress (right y-axis) versus exposure time to EXCO solution. It can be noticed that the conventional yield stress (represented by the blue dashed curve) decreases linearly with increasing exposure time while the elongation at fracture (represented by the solid orange curve) decreases exponentially, and an essential degradation is noticed even after only 2 hours of exposure.

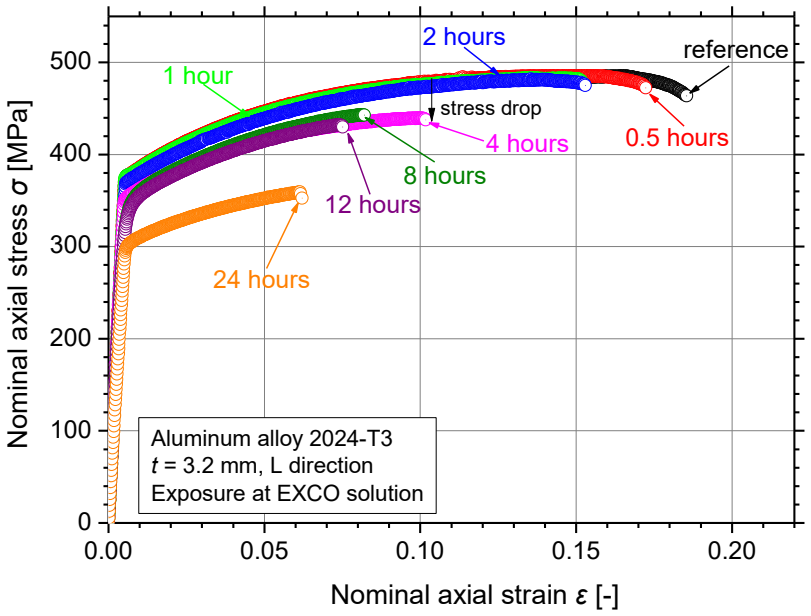

Figure 2-13: Typical tensile nominal stress-strain curves of AA2024-T3 after corrosion exposure to EXCO solution.

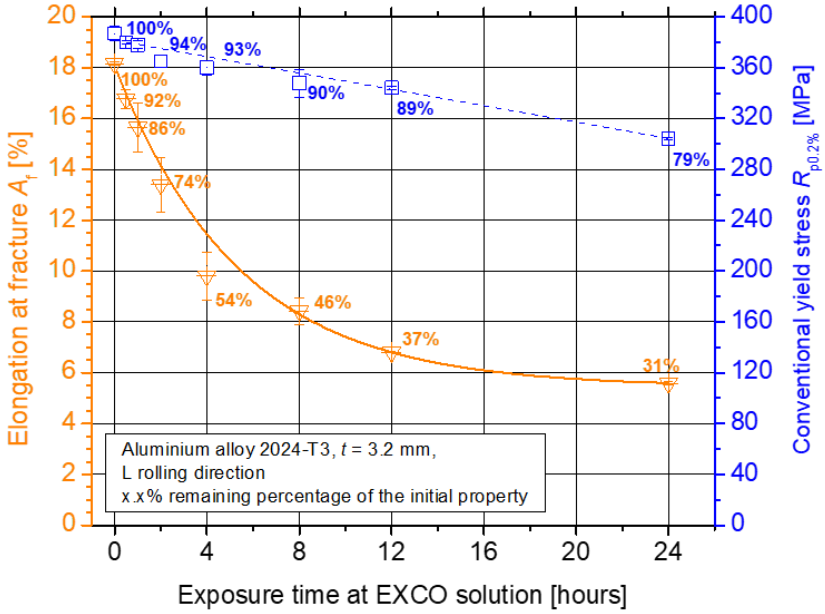

Figure 2-14: Experimental results of mechanical properties of AA2024-T3 after exposure to EXCO solution for different exposure times.

2.3.2.1.3 Characterization of fractured pre-corroded specimens

Stereoscopical examination on the fractured, pre-corroded specimens of AA2024-T3 exposed to EXCO solution are shown in Figure 2-15. It is obvious that pitting corrosion mechanism is extremely limited for the very short corrosion exposure times, *e.g.,* up to 2 hours (Figure 2-15 (a)). Nevertheless, with increasing exposure time, the pitting density tends to increase. A ductile fracture mechanism is evident from the 45° slope of the fracture surface, as can be seen in Figure 2-15 (a, b). However, for higher exposure times, *e.g.*, 24 hours shown in Figure 2-15 (c), it seems that the fracture path follows a non-linear pattern and definitely propagates from pit to pit.

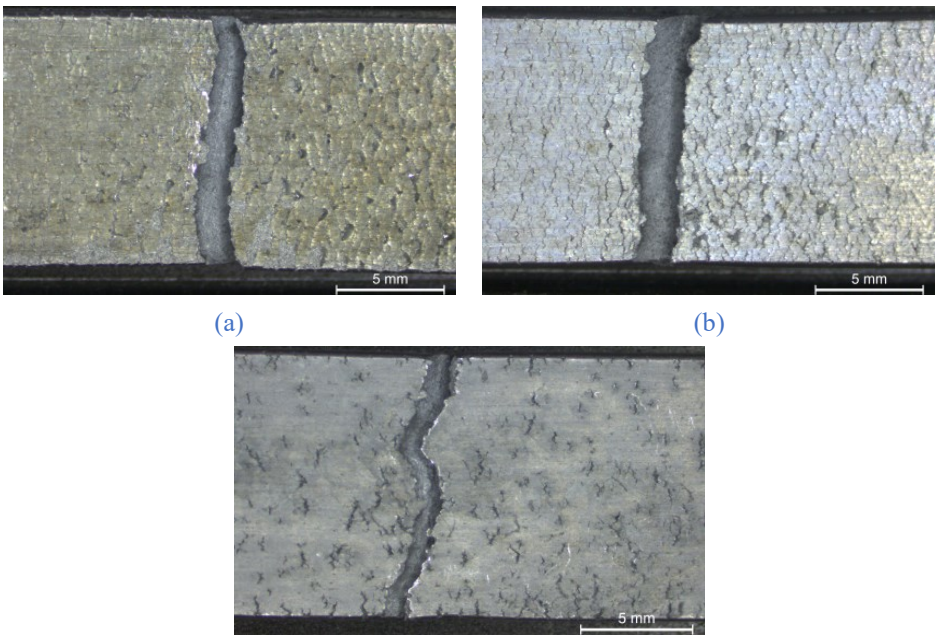

(a) (b)

(c)

Figure 2-15: Typical photographs of the fractured surfaces of AA2024-T3 pre-corroded tensile specimens exposed to EXCO solution for (a)-(c) 2 h, 4 h and 24 h, respectively.

A significant amount of intergranular tearing was observed by the micro-XCT imaging on the surfaces of post-test tensile specimens exposed for 2 hours to EXCO solution, as can be seen in Figure 2-16. Several secondary cracks (intergranular tears) have formed perpendicular to the loading direction due to grain boundary embrittlement. The corrosion products between grain layers tend to expand with corrosion evolution and act as wedges that introduce a stress field, thereby accelerating the formation of in-plane intergranular cracks [35]. Formation of some surface pits after 2 hours exposure to EXCO solution is evident from the cross-section in Figure 2-16(c), where the pits seem not to propagate deeply into the core of the material, but parallel to the surface. Furthermore, higher pitting density is noticed in the L/ST direction (z-y plane axis), providing evidence that the side-surfaces of the specimens are more prone to corrosion attack, as was experimentally observed by Kamoutsi [78] and Pantelakis et *al.,* [104], thus playing a pivotal role in the elongation at fracture A_f degradation at these short exposure times as was revealed by Charalampidou et *al.* [105].

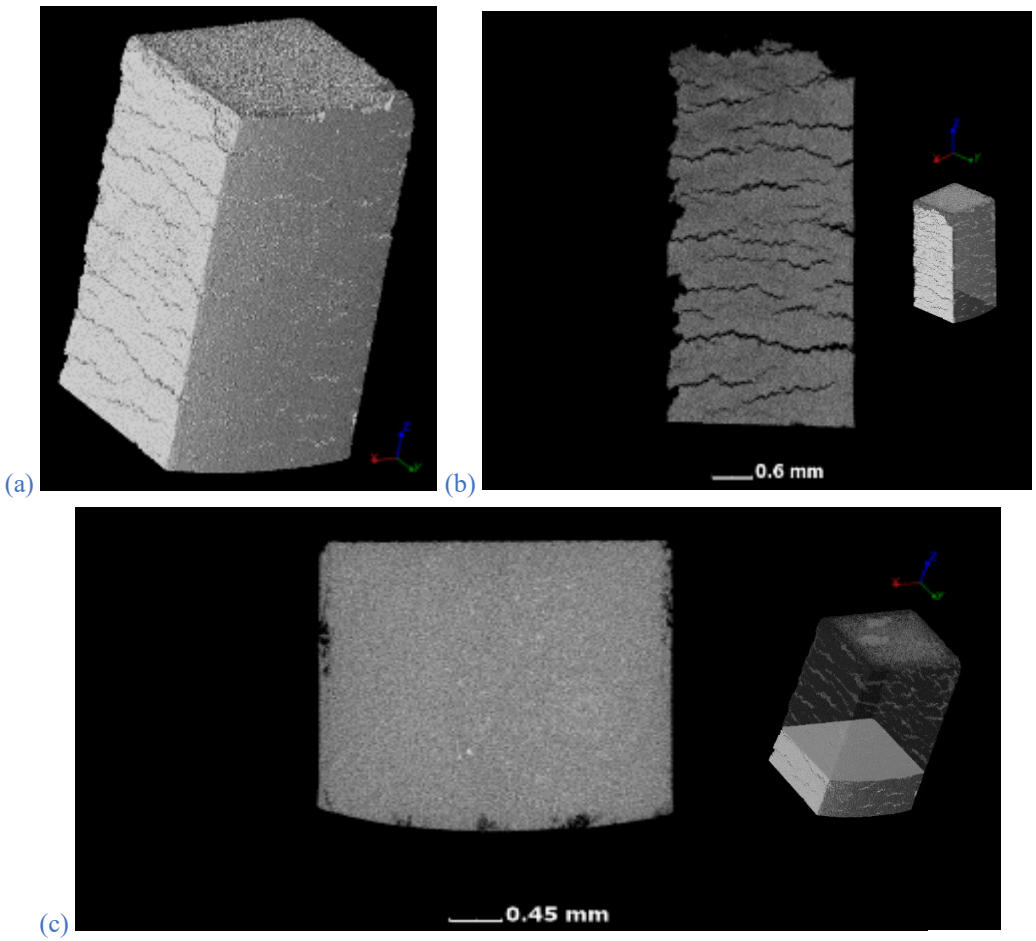

Figure 2-16: Post tensile test micro-XCT images of the EXCO-exposed specimens for 2 h, with (a) full volume micro-XCT specimen, (b) a section near the exposed surface showing intergranular tearing due to grain-boundary embrittlement, and (c) the cross-sectioned area shown in the right image included.

In order to develop an understanding regarding the development of these cracks, micro-XCT imaging was also performed on a tensile tested specimen, in which the test was interrupted after the application of 2% engineering strain. The micro-XCT image shown in Figure 2-17(a) reveals that, even at these low engineering strains, intergranular cracking is present with an approximate depth of 0.05 mm (50 µm) into the specimen (refer to Figure 2-17 (b)). Similar intergranular corrosion penetration was found in Hughes et *al*. [73] after 2 hours exposure of AA2024-T3 to 0.1 M NaCl solution. Additionally, approximately 40 µm depth of cracks was noticed in Alexopoulos et *al.* [63] after 4 hours exposure to EXCO solution and without the application of prior engineering strain. Notable intergranular cracking was observed to propagate deep into the metal prior to the formation of any substantial surface pitting. The same was noticed in the work of Luo et *al.* [106] where the intergranular corrosion attack of AA2024-T351 was microscopically examined after immersion in 0.1 M NaCl aqueous solution.

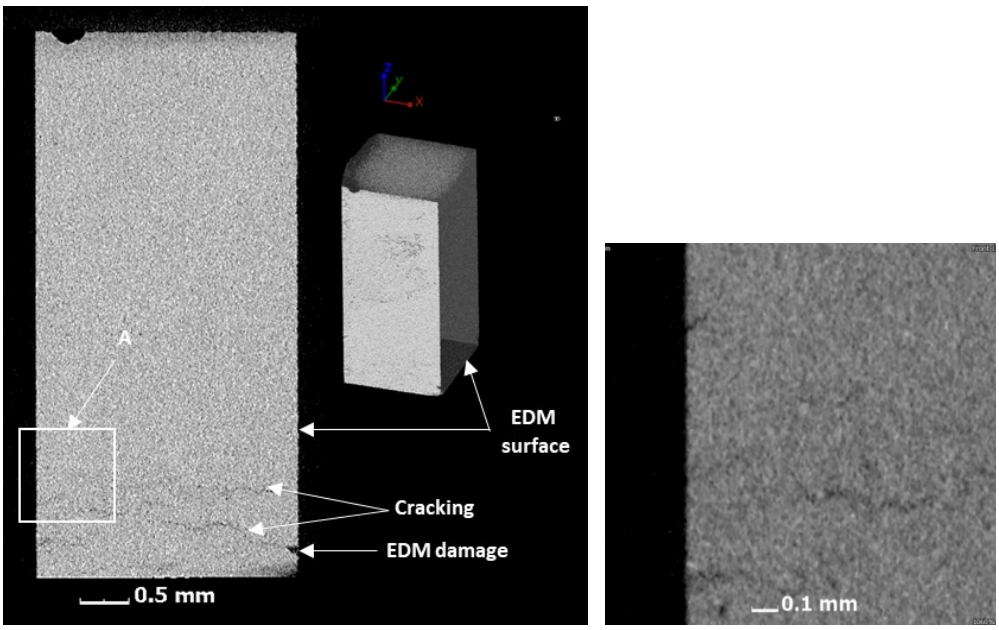

(a) (b)

Figure 2-17: (a) Micro-XRCT image of 2 h EXCO-exposed AA2024-T3 tensile specimen after the application of 2% engineering strain and (b) higher magnification of section A, showing that the secondary cracking extends to an approximate depth of 0.05 mm from the exposed surface.

2.3.2.2 Effect on crack growth resistance

2.3.2.2.1 Macro- and microscopic features of pre-corroded specimens

In order to investigate the effect of EXCO exposure on crack growth resistance of AA2024-T3, C(T) specimens exposed for 2 hours to exfoliation corrosion solution. The 2 hours exposure to EXCO solution were selected for further investigation because no essential stress decrease is noticed from the tensile flow curves, while a significant ductility decrease is evident according to Alexopoulos et *al.* [63]. During the 2 hours exposure of AA2024-T3 C(T)-specimens to the EXCO solution, extensive bubble formation could be observed on the exposed surfaces, as presented in Figure 2-18. Considering the measured pH of the solution (0.27) and the basic model for pitting corrosion of aluminium [101] the gas bubbles are believed to be hydrogen that forms as a result of the reduction of protons (H^+) in acidic solution according to reaction below in Equation (2-2):

$$6H^+ + 6e^- \rightarrow 3H_2 \qquad (2\text{-}2)$$

The necessary electrons for the formation of hydrogen gas (H_2) are provided by the oxidation of aluminium according to the reaction below in Equation (2-3):

$$2Al \rightarrow 2Al^{3+} + 6e^- \qquad (2\text{-}3)$$

The hydrogen gas-bubble formation was also accompanied by the precipitation of a large amount of small, cubic-shaped salt crystals with a white coloration which can be attributed to precipitation of sodium-chloride (NaCl) or aluminium-chloride ($AlCl_3$). However, optical microscopy evaluation of

the specimen surfaces after the exposure to EXCO solution revealed no visual signs of significant pitting nor intergranular corrosion (refer to Figure 2-19).

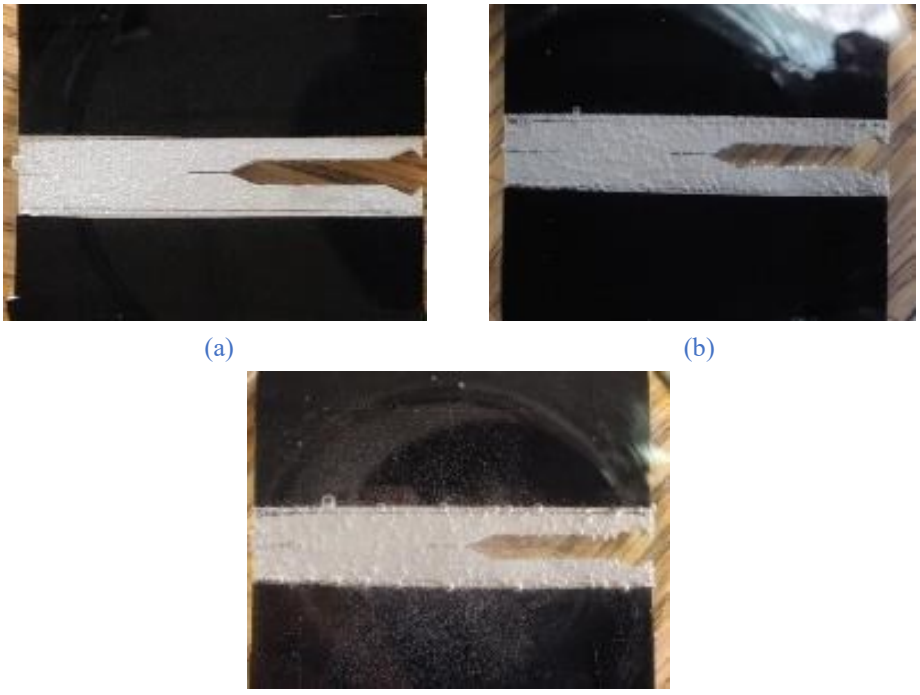

(a) (b)

(c)

Figure 2-18: Hydrogen bubble formation during EXCO exposure after (a) 15 minutes, (b) 30 minutes and (c) 90 minutes.

Figure 2-19: High magnification (1000x) optical micrograph of the C(T) (L-T) specimen surface after 2 h exposure to EXCO solution, showing no signs of significant pitting or intergranular corrosion.

2.3.2.2.2 Crack growth resistance behaviour of pre-corroded specimens

Figure 2-20(a) shows the load-crack mouth opening displacement (CMOD) curves and Figure 2-20(b) tabulates the evaluated critical stress intensity factor (K_{cr}) values (calculated from environmentally affected *R*-curves) of AA2024-T3 specimens exposed to three different exposure environments, that is (i) prior exposure to air for the reference test results, (ii) prior exposure to 0.6 M-(or 3.5 *wt*. %) NaCl solution and (iii) prior exposure to EXCO solution, for comparison purposes. As expected, the resistance curve is more recessive for the specimens exposed to corrosive environments regarding the maximum applied load and the associated critical crack extension values

(Δa_c = 6.14 mm, 5.52 mm and 5.26 mm for samples exposed to air, EXCO and NaCl solution, respectively). However, no significant difference in maximum applied load is noticed between the two corrosive environments. Higher difference is evident when comparing the specimens exposed in air against the specimens exposed to corrosive solutions, than comparing the results in two corrosive solutions. Specimens exposed in air were found to have a maximum load of approximately 4.0 kN while specimens exposed to EXCO as well as to NaCl solution exhibited a maximum applied force of 3.8 kN and 3.7 kN, respectively. Regarding the crack mouth opening displacement (CMOD) at maximum load, no considerable difference is noticed between the three investigated cases. Hence, it seems that the short corrosion exposure times investigated in this study does not essentially affect the maximum load capacity of specimens as well as the CMOD at the maximum load. Nevertheless, a considerable decrease in the material's ability to resist the propagation of a pre-existing crack is noticed from the K_{cr} values in Figure 2-20(b). Exposure of specimens to EXCO solution decrease the critical stress intensity factor K_{cr} by approximately 11% while the respective decrease for NaCl-exposed specimens is approximately 13%. Nevertheless, no signs of significant pitting nor intergranular corrosion observed in the surfaces of EXCO-exposed specimens for such a short exposure time, when evaluated with the aid of optical microscopy as shown in Figure 2-19.

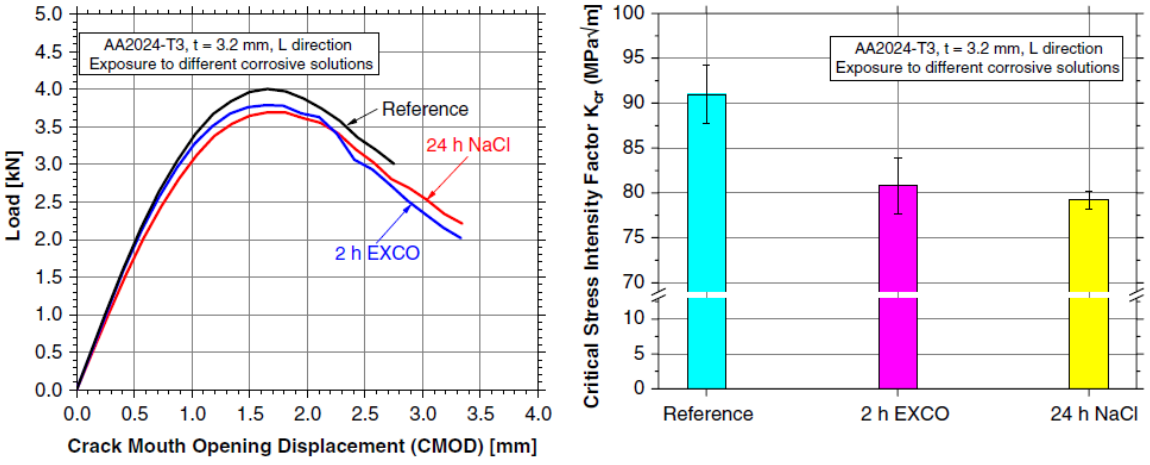

(a) (b)

Figure 2-20: (a) Load–crack mouth opening displacement (CMOD) curves and (b) evaluated critical stress intensity factor (K_{cr}) values of AA2024-T3 specimens after prior exposure to different corrosive solutions.

The fracture surface appearance of a specimen exposed to EXCO solution and after the crack-growth resistance evaluation is shown in Figure 2-21. As can be seen from the figure, the fracture surface can be divided into four (4) different stages. That is the fatigue pre-crack perpendicular to the applied load marked with (A), the stable crack extension fracture surface perpendicular to the applied load (B), the shear-lip (ductile) fracture surface with an orientation of ± 45 ˚ to the applied load marked with (C), and (D) an intergranular type of fracture near the edge of the specimen. It is worth noticing that the fracture surface types (A) to (C) are repeated in all exposure conditions considered for this

investigation. However, only the EXCO-exposed specimens reveal the type (D) fracture surface appearance, corresponding to intergranular cracking.

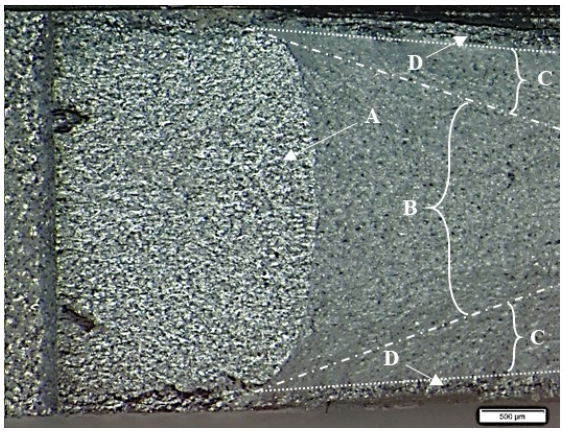

Figure 2-21: Optical micrograph showing the typical fracture surface of the EXCO-exposed specimens, with (A) the fatigue pre-crack, (B) the stable crack extension, (C) shear-lip (ductile) fracture, and (D) intergranular fracture.

The SEM image in Figure 2-22 more clearly shows the intergranular fracture (D) of the material near the exposed surface (E) of the EXCO-exposed AA2024-T3 specimen. The presence of intergranular fracture surface indicates the weakening of grain boundary strength, as was revealed in previous studies (*e.g.,* Posada et *al.* [35]). It is also noteworthy to mention that the embrittlement appears to be more severe during exposure conditions in which the hydrogen gas do not evolve from exposed surface as readily. It has been noticed that exposure conditions in which the hydrogen bubbles remain adsorbed to the specimen surface reveal less pitting corrosion, higher concentration of precipitated salt, and a significant increase in the thickness of intergranular fracture surface.

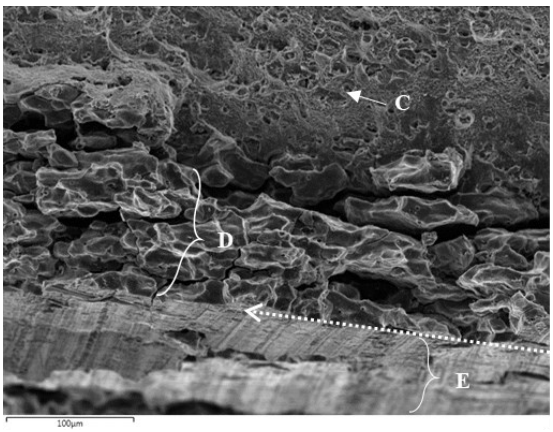

Figure 2-22: SEM image of the post crack-growth resistance evaluation fracture surface (D) near the exposed surface (E) of the EXCO-exposed C(T) specimens.

Significant secondary crack formation − adjacent to the primary crack − is also observed after the crack-growth resistance evaluation of the EXCO-exposed specimens, as can be seen in Figure 2-23. These secondary cracks do not form in the full width of the exposed region but are limited to approximately 2 mm on either side of the main crack plane. Moreover, at a position of approximately

4 mm ahead of the extended primary crack front, no secondary cracks are observed. It is also important to note that the secondary cracks were not visible immediately after the exposure to the EXCO-solution (refer to Figure 2-19), but only formed after the crack-growth resistance testing, that is, after the loading of the specimens. Considering the plastic-zone size (r_y) calculated during the crack-growth resistance procedure (according to ASTM E561 specification [91]), it appears that the final calculated diameter of the plastically affected zone ($\approx 3.78 \pm 0.04$ mm) correlates well with the area in which secondary crack formation is observed. Furthermore, according to the scale in Figure 2-24, the secondary cracks – indicated with the red arrow (b) – were measured through Image Analysis software and found to extend up to an approximate depth of 0.115 mm from the exposed surface. This corresponds well with the thickness of the intergranular fracture surface – labelled (D) in Figure 2-22 – which was calculated to be 0.12 mm in depth. The comparability between the depth of the secondary cracks evident in the EXCO-exposed specimens and the thickness of the intergranular fracture surface indicates that the secondary cracks form due to some form of grain boundary embrittlement. Whether this is induced by hydrogen embrittlement (HEDE model), or by the formation of some intergranular compound (*e.g.,* AlH_3) during the exposure of the specimen, is yet to be determined. However, the cohesion strength of grain boundaries near the exposed surface is significantly reduced for the specimens exposed to EXCO solution.

The mechanism of embrittlement for EXCO-exposed specimens appears to deviate from that of the NaCl-exposed specimens. The grain boundary weakening in NaCl-exposed specimens appears to be limited to the regions where localised corrosion has occurred; with the grain boundary strength of the material in the direct vicinity of attacked regions not being affected fundamentally. Thus, the transition from intergranular to transgranular attack seems to be responsible for the higher degradation of K_{cr} in the case of NaCl solution noticed from the mechanical tests in Figure 2-10(b). This behaviour can be attributed to the easier crack propagation in the case of transgranular attack; the crack front changes direction from grain to grain. These results are in accordance with the findings of Donatus et *al.* [62] where intergranular corrosion attack in AA2024-T3 was found to be less severe than transgranular attack occurred in AA2198-T851.

Furthermore, the loss in strength of the surface material also reduces the volume fraction of material with the ability to absorb the applied energy by yielding plastically. That is, the actual thickness of the specimen is reduced, and is smaller than the measured thickness used in the K_{cr} calculations.

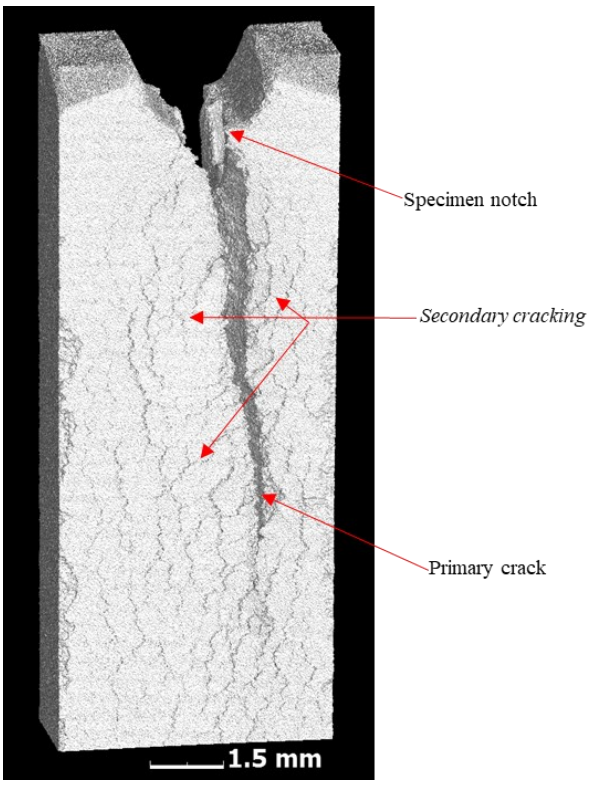

Figure 2-23: Post crack-growth resistance XCT image of the Exco-exposed specimen, showing the secondary cracks that formed within the plastic zone near the primary crack front.

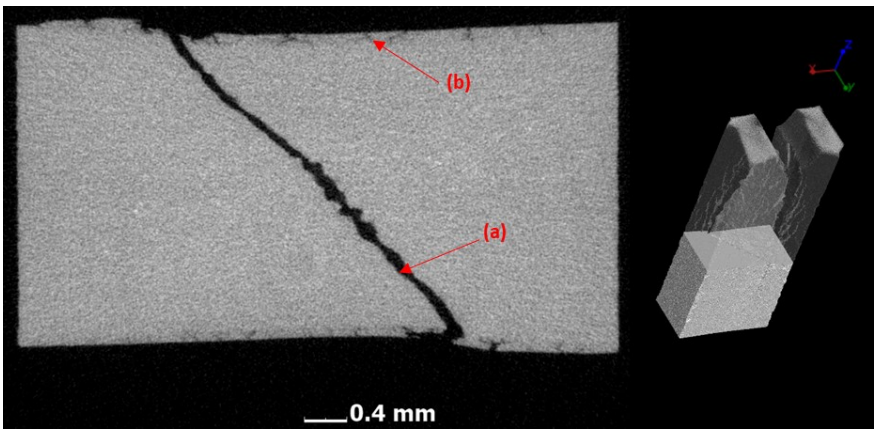

Figure 2-24: Post crack-growth resistance XCT images of the Exco-exposed specimen, with the left image showing the primary (a) and secondary (b) cracks and the cross-sectioned area shown in the right image.

2.3.3 AA2024-T3: Correlation and comparison of the corrosive environments

2.3.3.1 Effect of solution aggressiveness on mechanical properties

The experimental test results of the conventional yield stress $R_{p0.2\%}$ (nominal values) for the exposure times to EXCO and to 3.5 *wt.* % NaCl solution are presented in Figure 2-25(a). The results are presented in decreasing normalized average values (y-axis) from the initial value of the conventional yield stress for comparison purposes. The black circles and dotted line represent the experimental results and fitting line of exposure to EXCO solution and are linked to the bottom x-

axis, while the orange triangles and line corresponds to the fitting results of exposure to 3.5 *wt.* % NaCl solution and are linked to the upper x-axis of the figure. Regarding the comparison of conventional yield stress decrease between the two investigated corrosive environments, it is evident that the more aggressive solution (EXCO) leads to higher decrease of conventional yield stress up to 12 hours of exposure. For the very short exposure times, stress decrease seems to be almost the same for both investigated solutions; however, specimens exposed to the mild corrosive solution (3.5 *wt.* % NaCl) needed more hours for the same degradation percentage, *e.g.*, approximately 99% remaining percentage of $R_{p0.2\%}$ can be noticed after 168 hours of exposure to NaCl solution as well as after 1 hour of exposure to EXCO solution (Figure 2-25(a)). It is worth to mention that the 3.5 *wt.* % NaCl solution does not reveal any exfoliation of the corrosion attacked material surfaces which could represent a more pronounced notch effect reducing the specimens' cross-sectional area. However, the decrease of conventional yield stress, remains limited for all the investigated corrosion exposure times of both investigated environments and does not exceed 40% at maximum and for the investigated exposure times. The highest decrease of normalized $R_{p0.2\%}$ was approximately 32% (≈ 68% remaining value) for the specimens exposed to 3.5 *wt.* % NaCl solution and 21% (≈79% normalized value) for the specimens exposed to EXCO solution.

The results of the residual elongation at fracture A_f values can be seen in Figure 2-25(b) for the two investigated environments, namely the EXCO exposure and NaCl exposure. The results are presented in the form of normalized A_f with double X-axis for comparison reasons. Corrosion exposure has a deleterious effect on tensile ductility (elongation at fracture in the present case) even from the short exposure times to both investigated corrosive solutions. The normalized decrease of elongation at fracture A_f is almost the same for both solutions at short exposure times where the pitting formation remains limited; approximately 75% remaining percentage of the initial mechanical property was observed after only 1 hour of exposure to EXCO solution while the same decrease was noticed for the case of exposure to 3.5 *wt.* % NaCl solution after 24 hours (Figure 2-25(b)). The same was observed for 2 hours at EXCO and 168 hours at 3.5 *wt.* % NaCl with a normalized value of approximately 68%. Nevertheless, higher exposure times are needed for the 3.5 *wt.* % NaCl solution in order to result in the same degradation percentage with the respective specimens exposed to EXCO solution. It should also be taken into consideration that the hydrogen embrittlement phenomenon takes place in this case, especially at the short exposure times in EXCO solution.

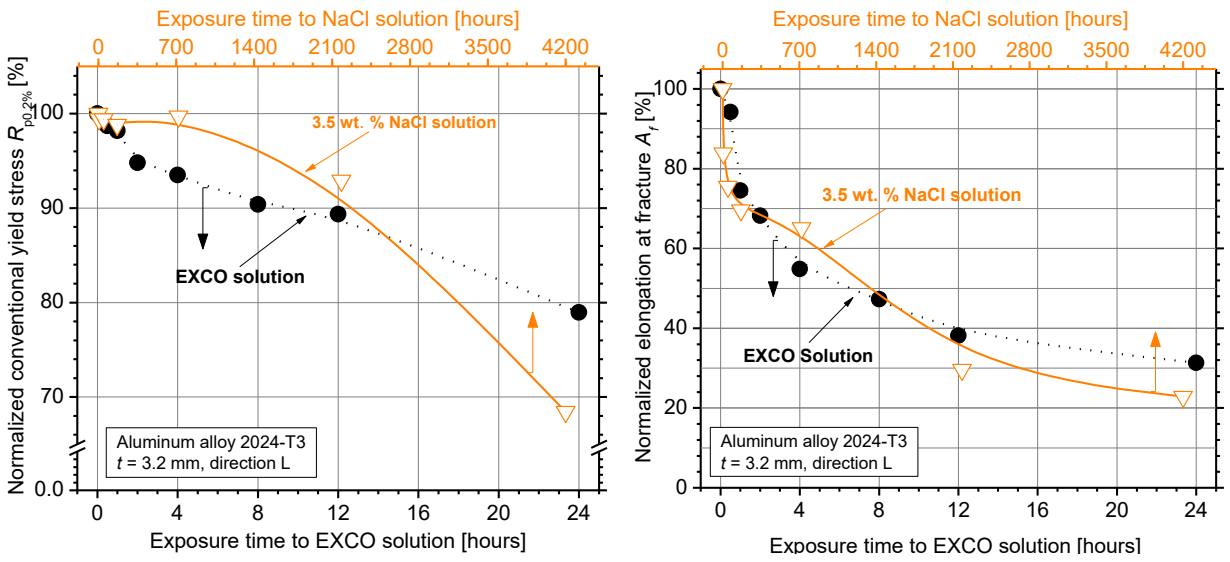

Figure 2-25: Normalized (a) conventional yield stress ($R_{p0.2\%}$) and (b) elongation at fracture (A_f) values of AA2024-T3 for the various exposure times to EXCO solution compared against 3.5 wt. % NaCl solution.

Figure 2-26 presents the correlation results of the effect of two corrosive environments, *e.g.,* EXCO and 3.5 *wt.* % NaCl solutions, with regard to the same corrosion-induced tensile ductility decrease. To this end, for the conversion of exposure times to EXCO solution to the respective times of exposure to NaCl solution, an empirical coefficient was devised. The *n* coefficient in [-] is formulated as shown below, in Equation (2-4):

$$n_{EXCO\ to\ NaCl} = \frac{exposure\ time\ to\ NaCl\ (h)}{exposure\ time\ to\ EXCO\ (h)} \qquad (2\text{-}4)$$

The best calculation results were found by using the value $n = 92$ for the empirical coefficient and for the simulation of the tensile ductility decrease curve of the investigated specimens for short exposure times regime. The same rate decrease is evident between the two different corrosive solutions at the short exposure times where slight pitting formation is the dominant degradation mechanism. By using this coefficient value, is obvious that the results of exfoliation corrosion are very close to the experimental values of exposure to 3.5 *wt.* % NaCl up to 1 hour of exposure and 14% elongation at fracture. Thus, it can be concluded that 1 hour of exposure to EXCO solution is equivalent to 92 hours of exposure to 3.5 *wt.* % NaCl solution regarding the A_f degradation. For higher exposure times, there is no correlation between the corrosive environments regarding the ductility decrease since the corrosion-induced degradation mechanism is different.

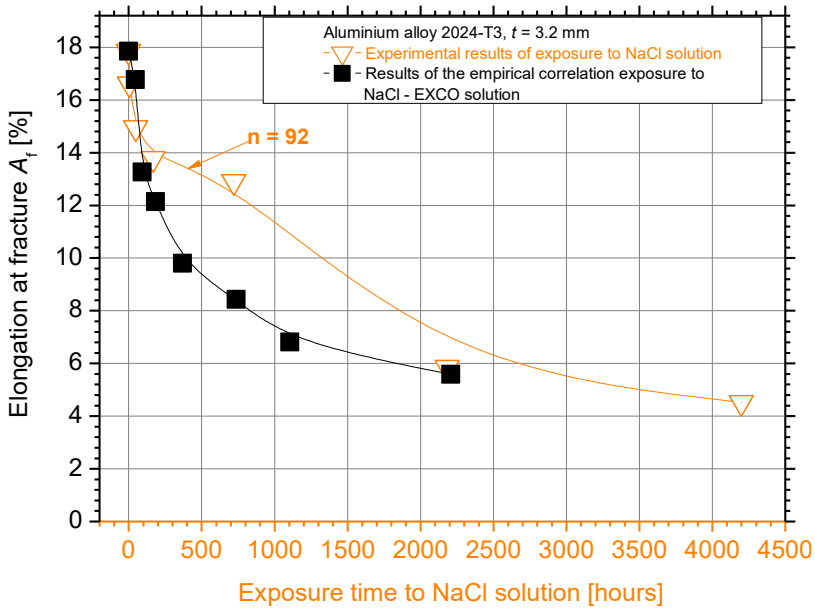

Figure 2-26: Correlation of the elongation at fracture A_f decrease due to exposure to EXCO solution as well as to 3.5 wt.% NaCl solution.

2.3.4 AA2198-T8: Effect of exposure to 3.5 *wt.* % NaCl solution

The increasing interest in Al-Cu-Li based alloys arises from the lithium addition-induced advantages such as the decrease in density (almost 3% for 1 *wt.* % lithium added), increase in elastic modulus (approximately 6% for 1 *wt.* % lithium added), the high strength-to-weight ratio as well as the high damage tolerance and corrosion resistance [107]-[108]. Third generation Al-Cu-Li alloys were developed to replace the conventional alloys such as AA2024-T3 in aircraft structures, where damage tolerance is the critical design factor [109]-[110]. However, Al-Cu-Li alloys were found to be highly susceptible to localized corrosion, especially to selective attack of certain grains or grain boundaries, due to their complex precipitation hardening system, according to [51]-[53].

The addition of Li introduces precipitation hardening due to the formation of several strengthening precipitates, including δ' (Al_3Li), θ' (Al_2Cu) and T_1 (Al_2CuLi). Other precipitates such as β (Al_3Zr) and $Al_{20}Cu_2Mn_3$ are formed by the addition of other alloying elements that control the recrystallization and grain refinement of the metal, *e.g.,* Proton et *al.* [56]. Corrosion susceptibility of aluminium alloys is strongly influenced by the strengthening intermetallic phases due to micro-galvanic processes between the intermetallic phases and the matrix, as described in [19]-[21]. In the case of Al-Cu-Li alloys, the T_1 precipitates contribute to localized corrosion due to the anodic behaviour with respect to the adjacent Cu depleted zone and the matrix, as was described by Kertz et *al*. [57]. In [111] it was found that in the presence of aggressive chloride solutions, aluminium alloys are subjected to localized corrosion by pitting, intergranular attack, or exfoliation corrosion that severely shorten the aircrafts service life due to stress concentration in the area next to these defects. According to Zou et *al.* [112] the corrosion resistance of AA2198 was found to decrease from the

solution-anneal to peak-ageing condition due to artificial ageing-induced microstructural transformations.

Investigation on the corrosion behaviour of Al-Cu-Li 2198 alloy is of major importance. Identifying the corrosion-induced degradation mechanisms is of crucial interest in the aircraft maintenance protocols. In the present chapter, the above mechanisms are identified for the AA2198 at T8 temper via accelerated corrosion tests on tensile as well as small rectangular metallographic coupons directly compared against the well-established AA2024 in order to report experimental evidence regarding the corrosion potential of this alloy.

2.3.4.1 Effect on corrosion mechanism

The electrochemical impedance spectroscopy (EIS) results for the innovative Al-Cu-Li alloy 2198-T8 as a function of exposure to 3.5 *wt.* % NaCl solution are presented in Figure 2-27 and Figure 2-28, in the form of Bode and Nyquist plots respectively. Two well-defined time constants are evident at low (10^{-2}-10^{-1}) and medium (10^{0}-10^{3}) frequencies regime for all exposure times, *e.g.,* Figure 2-27(a). Slight fluctuations are evident in the initial period of immersion (black curve) at low frequencies regime due to non-stationarities of the system at this period resulted from the metastable pitting formation. However, after 1 hour of immersion pits started to become stable. The respective time for stable pits formation in AA2024-T3 was after 6 hours of immersion. More intense differences between immersion times are noticed for this alloy, where an essential decrease of the capacitive behaviour was observed from the decrease in Theta phase degrees values between 3 and 6 hours as well as 6 and 12 hours of immersion. Furthermore, the relaxation process evident at higher frequencies up to 3 hours of immersion (green curve) indicates a response from the passive surface oxide film.

Impedance modulus is not notably decreased for the first hours of corrosion and up to 3 hours (represented by green curve in Figure 2-27(b)), at low frequencies regime (10^{-2}-10^{-1}). Nevertheless, an essential sudden drop of Z modulus is noticed after 6 hours of exposure followed by a gradual decreasing trend for higher exposure times. Essential decrease is noticed between 3 and 6 hours of exposure while further increase in immersion time seems not to decrease the impedance modulus significantly since by that time stable pits are formed, and the corrosion process is controlled by the diffusion limited cathodic oxygen reduction. This trend was noticed for both medium and low frequencies regime. Similar results were noticed for AA2024-T3; however, the impedance modulus in low frequencies regime remained almost unaffected by corrosion exposure up to 6 hours for AA2024-T3, while for AA2198-T8 a sudden drop was noticed after 3 hours. Nonetheless, the total impedance modulus was found to be higher for AA2198-T8 for the whole immersion time range indicating that this alloy is more corrosion resistant.

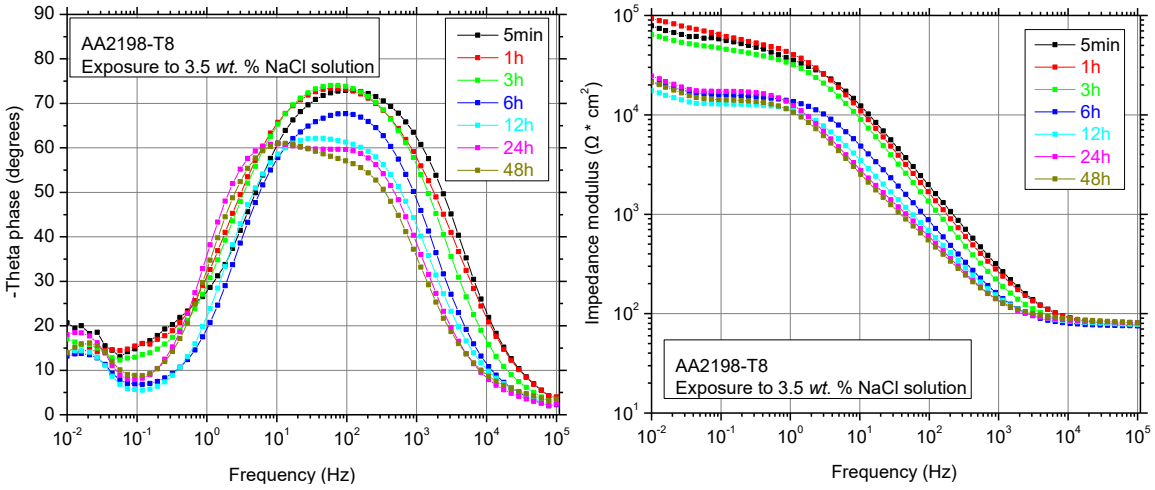

(a) (b)

Figure 2-27: Impedance spectra of AA2198-T8 measured in 3.5 wt. % NaCl solution.

Two clear capacitive loops in all immersion times are evident from the Nyquist plot in Figure 2-28. As was already mentioned in previous section (section 2.3.1.), the two capacitive loops in EIS correspond to the two parts of the alloy's surface; more precisely the high frequency (HF) capacitive loop (complete semi-circle) corresponds to the flat oxide passive film, while the capacitive loop that is present in low frequency values (LF) (one-fourth arc) is associated with the localized corrosion phenomena, such as pitting, intergranular and exfoliation corrosion. The same change trend with Bode plots was noticed regarding corrosion behaviour of AA2198-T8. Capacitive arc (semi-circle diameter) seems to remain unaffected up to 3 hours corrosion exposure time (represented by green curve), while an essential shrinkage is noticed after 6 hours. Fluctuations are noticed for higher exposure times. When compared against the Nyquist plot of AA2024-T3 (see Figure 2-2), more stable oxide film is noticed for AA2198-T8 from the higher diameter of the capacitive arc (or the late disappearance of semi-circle which corresponds to the oxide passive film) for the whole immersion time range.

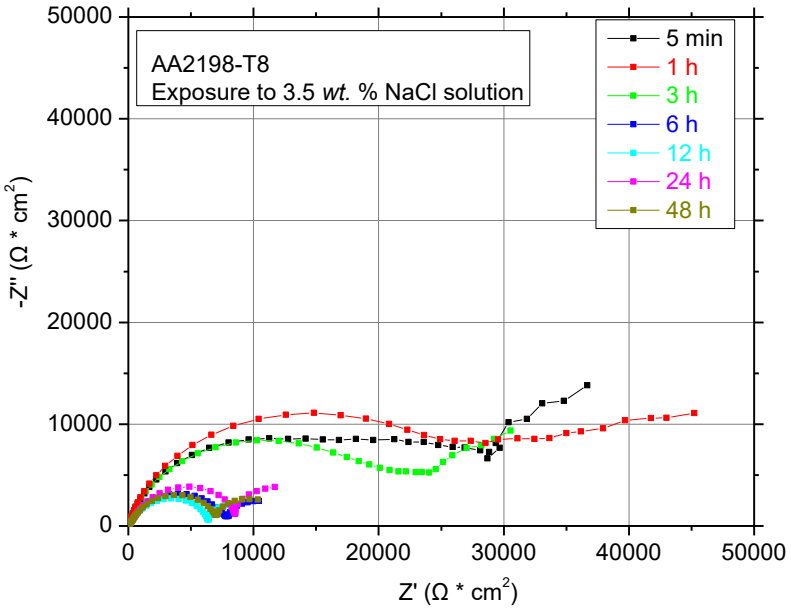

Figure 2-28: Nyquist plot of AA2198-T8 measured in 3.5 wt. % NaCl solution.

To gain a better insight into corrosion mechanisms, EIS response is modelled using equivalent electrical circuits, as shown in Figure 2-29. The same model used for AA2024-T3 was found to better simulate the corrosion mechanism of the innovative Al-Cu-Li alloy. From the equivalent electrical circuit model several useful parameters were calculated such as R_1 element which represents the solution resistance, the pair $R_2//Q_1$ which stands for the polarization resistance in parallel with capacitance of double layer as well as the W that stands for the Warburg element corresponds to diffusion phenomena. The more interesting parameter for further investigation is the charge transfer resistance R_2, which represents the material's resistance to oxidation.

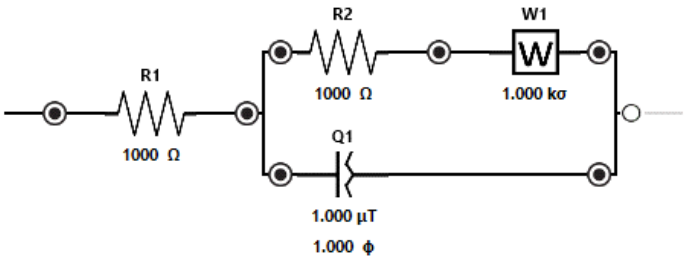

Figure 2-29: Equivalent circuit model of AA2198-T8 exposed to 3.5 wt. % NaCl solution.

The R_2 variation with increasing immersion time of AA2198-T8 directly compared against the one of AA2024-T3 is presented in Figure 2-30. An essential increase of the charge transfer resistance is noticed for the first hours of corrosion for AA2198-T8, followed by a linear decreasing trend up to 6 hours since by that time stable pits are formed. Slight fluctuations around 6000 Ω*cm^2 are noticed for higher exposure times of AA2198-T8. For the case of AA2024-T3, an increase in R_2 value is noticed after 3 hours of exposure but lower than the one observed for AA2198-T8, while fluctuations around 8000 Ω*cm^2 are evident for higher exposure times. Regarding short exposure times and up to

6 hours, the R_2 decreases with slightly higher rate for AA2198-T8 with increasing immersion time. Thus, the electron flow is enhanced by increasing immersion time at short exposure times of AA2198-T8 to 3.5 *wt.* % NaCl solution, while for the case of AA2024-T3 it is not essentially affected by corrosion evolution. However, the higher R_2 values noticed for AA2198-T8 at short exposure times revealed that corrosion attack is slower than in AA2024-T3. On the contrary, for long exposure times (≥ 12 hours) corrosion proceeds slightly faster for AA2198-T8. In general, these results indicate that AA2198-T8 is more sensitive to corrosion evolution but is more corrosion resistant than AA2024-T3 (as was shown by the higher charge transfer resistance values), meaning that is more difficult for corrosion to nucleate and propagate in this alloy at short exposure times.

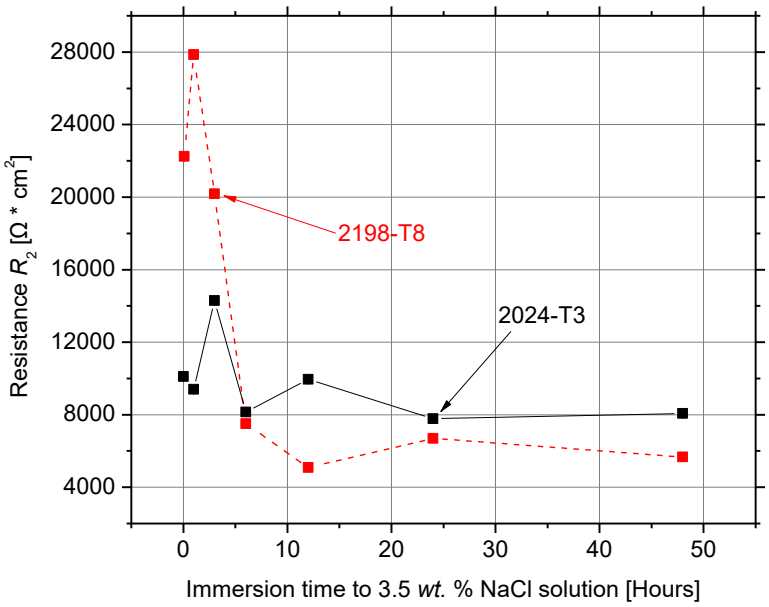

Figure 2-30: Variation of the charge transfer resistance R_2 as a function of immersion time to 3.5 wt. % NaCl solution for Al-Cu 2024-T3 alloy directly compared against the innovative Al-Cu-Li alloy 2198-T8.

2.3.4.2 Effect on tensile mechanical performance

2.3.4.2.1 Mechanical evaluation of pre-corroded specimens

The typical nominal tensile stress-strain curves for the investigated exposure times of AA2198-T8 to 3.5 *wt.* % NaCl solution can be seen in Figure 2-31. Regarding specimens exposed to 3.5 *wt.* % NaCl solution, the nominal axial stress seems to remain almost unaffected by corrosion exposure. On the contrary, the nominal axial strain decreased even from the short exposure times; however, no essential degradation is noticed up to 720 hours of exposure (≈1 month), while the property was reduced by more than half after 2184 hours (≈ 3 months) and almost reached the morphology of brittle fracture after 6 months exposure time.

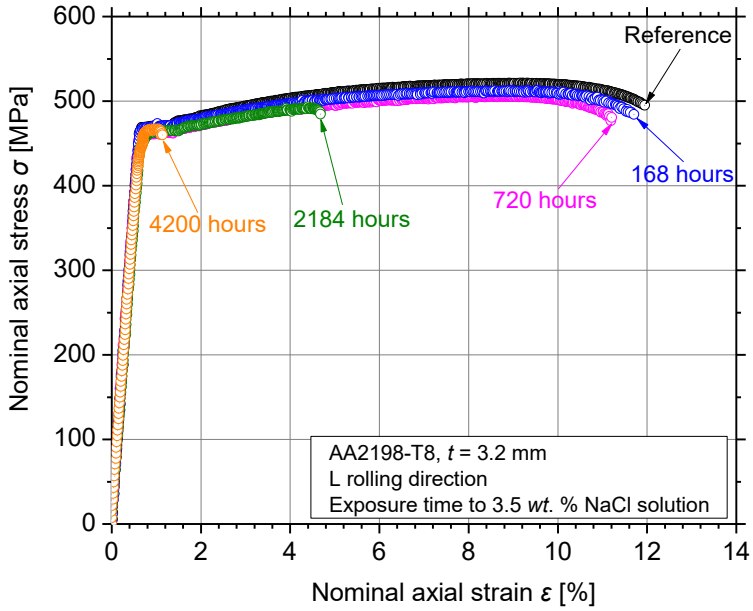

Figure 2-31: Typical tensile nominal stress-strain curves of AA2198-T8 after corrosion exposure to 3.5 wt. % NaCl solution for different exposure times.

2.3.4.2.2 Characterization of fractured pre-corroded specimens

The typical photographs of the fractured pre-corroded specimens of AA2198-T8 exposed to 3.5 *wt.* % NaCl solution, depicted in Figure 2-32, revealed that pitting corrosion is limited for short exposure times and up to 168 hours. The depicted area has dimensions of 12.5 mm * 55 mm, being the width and length of the exposed area (gauge length) of the tensile specimens. With increasing exposure time several pits are formed which are visible from the roughness of the specimens' surface. However, pitting formation seems to be uniformly distributed in the specimens' surfaces. Regarding fracture morphology, the formation of necking, as a consequence of high ductility, is visible up to 720 hours of exposure.

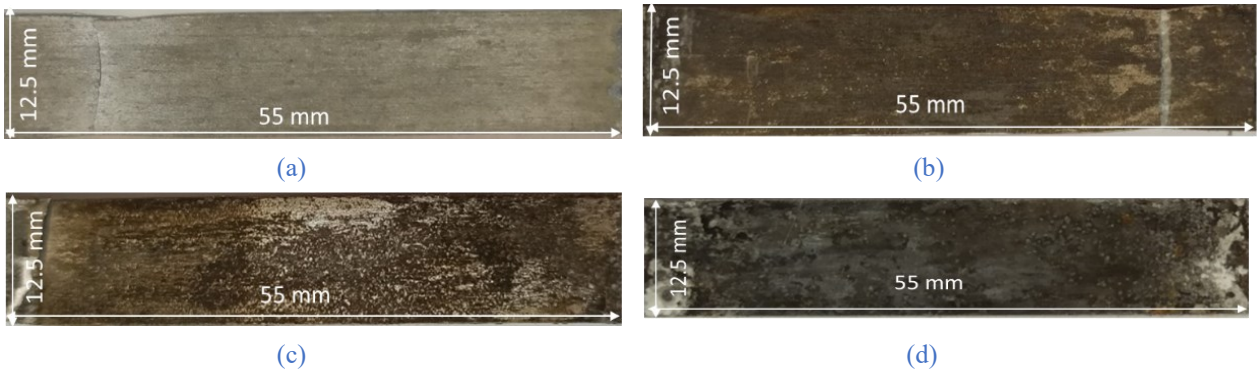

Figure 2-32: Typical photographs of fractured pre-corroded tensile specimens of AA2198-T8 exposed for (a) 168 h, (b) 720 h, (c) 2184 h and (d) 4200 h to 3.5 wt. % NaCl solution.

2.3.5 AA2198-T8: Effect of exposure to EXCO solution

2.3.5.1 Effect on tensile mechanical performance

2.3.5.1.1 Mechanical evaluation of pre-corroded specimens

The typical nominal tensile stress-strain curves for the investigated exposure times of AA2198-T8 to EXCO solution are presented in Figure 2-33. Specimens exposed to EXCO solution exhibited significant nominal axial stress drop as well as nominal axial strain decrease even from the short exposure times, *e.g.,* 6 hours (represented by blue curve). Nominal axial stress continued to essentially decrease up to 12 hours of exposure (represented by magenta curve) while further corrosion exposure did not reduce the property significantly probably due to maximum depth of cracks; this was not the case for nominal axial strain which was found to essentially decrease for the whole exposure time range. As was already mentioned for the case of AA2024-T3, the nominal axial stress decrease is attributed to the decrease of the "effective thickness" of the specimens [49] while the decrease in nominal axial strain probably includes hydrogen embrittlement phenomena.

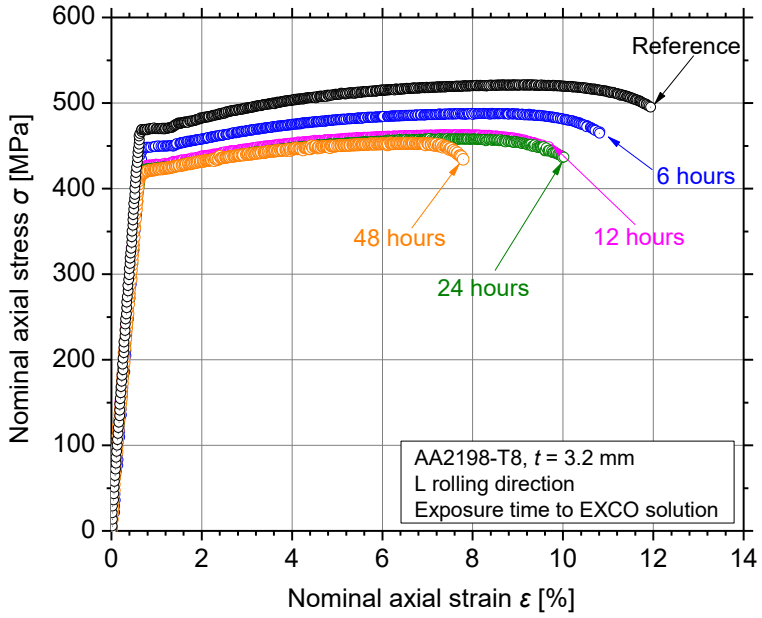

Figure 2-33: Typical tensile nominal stress-strain curves of AA2198-T8 after corrosion exposure to EXCO for different exposure times.

2.3.5.1.2 Characterization of fractured pre-corroded specimens

The typical photographs of the fractured pre-corroded specimens of AA2198-T8 exposed to EXCO solution, depicted in Figure 2-34, revealed that pitting corrosion in the form of localized attack is evident at short exposure times and up to 6 hours. With increasing exposure time, the pitting density tends to increase thus leading to exfoliation of the surface after 24 hours. Regarding fracture morphology, the formation of necking, as a consequence of ductile fracture, is slightly visible up to 24 hours of exposure while it was eliminated for higher exposure times, *e.g.*, 48 hours.

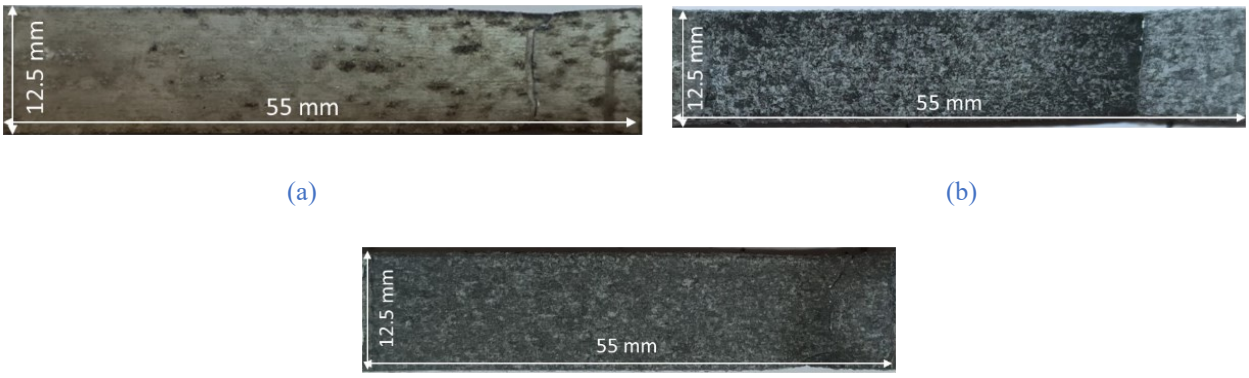

(a) (b)

(c)

Figure 2-34: Typical photographs of fractured pre-corroded tensile specimens of AA2198-T8 exposed for (a) 6 h, (b) 24 h and (c) 48 h to EXCO solution.

2.3.6 AA2198-T8: Effect of exposure to Harrison's diluted solution

2.3.6.1 Effect on corrosion mechanism

Two clear capacitive loops in all immersion times are evident from the Nyquist plot in Figure 2-35. Capacitive arc (semi-circle diameter) gradually decreases from the first hours of exposure, *e.g.,* 6 hours in the present case. Slight fluctuations of the curves at low frequencies regime and up to 6 hours of exposure can be caused by non-stationarities of the system at this period, resulted from the metastable pitting formation; stable pits started to form by that time in 3.5 *wt.* % NaCl solution. When compared to the Nyquist plot of AA2198-T8 exposed to 3.5 *wt.* % NaCl solution (see Figure 2-28), more stable oxide film is noticed in the case of Harrison's solution that was revealed from the higher diameter of capacitive arc (or the late disappearance of semi-circle), for the whole immersion time range. In general, Harrison's solution in diluted version was found to present the corrosion behaviour and mechanisms of AA2198-T8 more precisely since it is milder and do not accelerate corrosion kinetics.

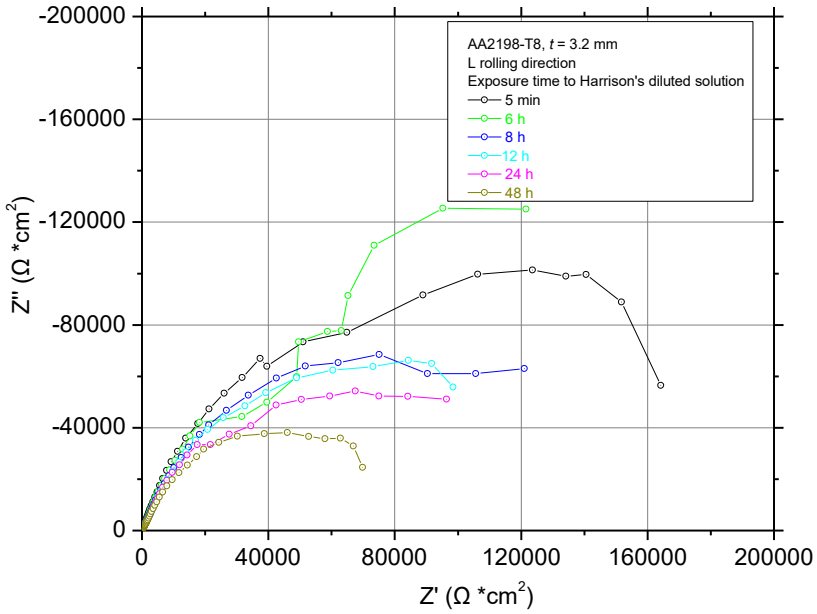

Figure 2-35: Nyquist plot of AA2198-T8 measured in Harrison's diluted solution.

2.3.6.2 Effect on tensile mechanical performance

2.3.6.2.1 Mechanical evaluation of pre-corroded specimens

The typical nominal tensile stress-strain curves for the investigated exposure times of AA2198-T8 exposed to Harrison's solution (diluted version) are presented in Figure 2-36(a). The nominal axial stress almost remained unaffected by exposure to this solution; this was not the case for nominal axial strain which was found to essentially decrease for the whole exposure time range. However, no notable strain decrease was noticed up to 168 hours of exposure. These results are similar to the respective in NaCl solution with the difference that nominal axial strain was essentially reduced for lower exposure times in Harrison's solution, *e.g.,* 720 hours.

All the above-mentioned results are summarized as average values of the properties' ($Rp_{0.2\%}$ and A_f) degradation in function with increasing exposure time to the several corrosive solutions in Figure 2-36(b) and Figure 2-36(c), respectively. It is obvious that specimens exposed to EXCO solution exhibited higher degradation of $Rp_{0.2\%}$ for the whole exposure time range. However, degradation rate was found to be higher up to 6 hours exposure to EXCO solution while the property reached a plateau for higher exposure times. This is probably evidence of maximum depth of attack (corrosion-induced micro-cracks). On the contrary, specimens exposed to 3.5 *wt.* % NaCl solution exhibited a continuous decrease of conventional yield stress up to the maximum exposure time. Regarding elongation at fracture A_f, higher degradation rate was noticed for the specimens exposed to Harrison's solution followed by EXCO at short exposure times (up to 6 hours), while essential ductility decrease revealed in the case of 3.5 *wt.* % NaCl solution after approximately 2000 hours of exposure (≈ 3 months). The ductility decrease can be attributed to hydrogen embrittlement phenomena that seems to be more intense in the case of Harrison and NaCl solutions, probably because of the transgranular attack which

enhances the diffusion of hydrogen to micro-voids in grains interior and not only on grain boundaries as was the case of EXCO.

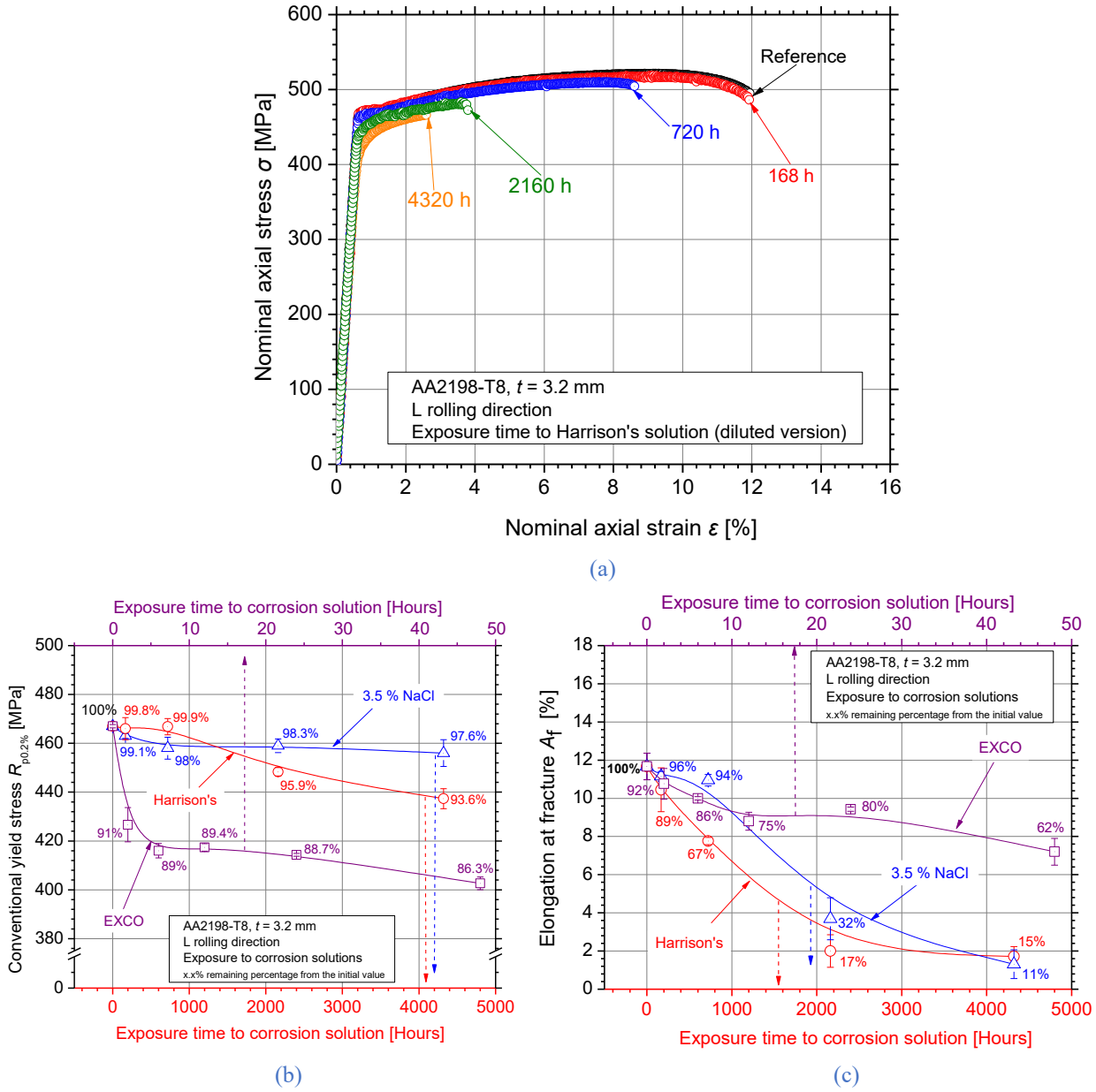

Figure 2-36: (a) Typical tensile nominal stress-strain curves of AA2198-T8 after corrosion exposure to Harrison's solution for different exposure times and (b) & (c) comparison of corrosion-induced degradation of mechanical properties between the three different investigated solutions (EXCO, NaCl, Harrison).

2.3.6.2.2 Characterization of fractured pre-corroded specimens

Figure 2-37 presents the typical photographs of fracture pre-corroded specimens of AA2198-T8 exposed to Harrison's solution for several hours. The depicted area has dimensions of 12.5 mm * 55 mm, being the width and length of the exposed area (gauge length) of the tensile specimens. No essential pitting formation is noticed up to 168 hours of exposure, however roughness of the specimen's surface is evident. Nevertheless, this solution was found to induce severe localized pitting corrosion and exfoliation with increasing exposure time. The fracture path follows a non-linear

pattern and definitely propagates from pit to pit. Regarding fracture morphology, the formation of necking, as a consequence of high ductility, is visible up to 720 hours of exposure as was also observed in NaCl solution.

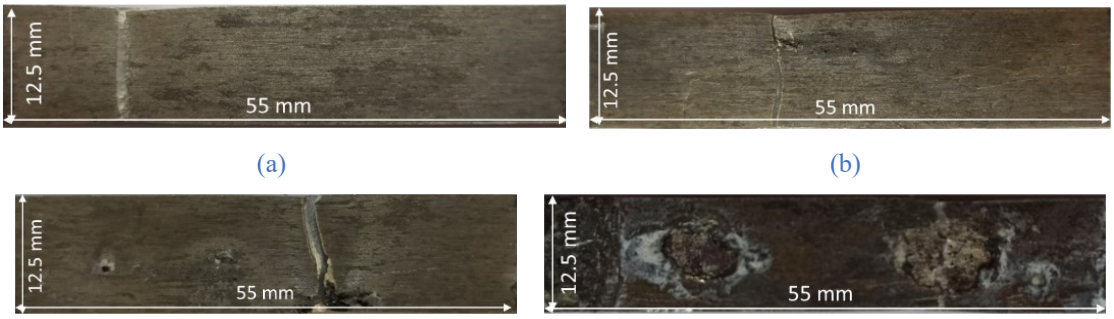

Figure 2-37: Typical photographs of fractured pre-corroded tensile specimens of AA2198-T8 exposed for (a) 168 h, (b) 720 h, (c) 2184 h and (d) 4200 h to Harrison's solution.

2.3.7 AA2198-T8: Correlation and comparison of corrosive environments

The experimental test results of the residual elongation at fracture A_f values for the exposure times to EXCO and to 3.5 *wt.* % NaCl solution are presented in Figure 2-38. The results are presented in the form of normalized values of A_f with double X-axis for comparison reasons. The black rectangles and solid line represent the experimental results and fitting line of exposure to EXCO solution and are linked to the bottom x-axis, while the orange triangles and dashed line corresponds to the fitting results of exposure to 3.5 *wt.* % NaCl solution and are linked to the upper x-axis of the figure. Corrosion exposure has a deteriorating effect on tensile elongation at fracture even from the short exposure times to both investigated corrosive solutions. The normalized decrease of elongation at fracture A_f is almost the same for both solutions at short exposure times where the pitting formation remains limited; approximately 95% remaining percentage of the initial mechanical property was observed after only 2 hours of exposure to EXCO solution while the same remaining value was noticed for the case of exposure to 3.5 *wt.* % NaCl solution after 168 hours. Almost the same was observed for 6 hours at EXCO and 720 hours at 3.5 *wt.* % NaCl with a normalized value of approximately 90%. Nevertheless, higher exposure times are needed for the 3.5 *wt.* % NaCl solution in order to result in the same degradation percentage with the respective specimens exposed to EXCO solution. It should also be taken into consideration that the hydrogen embrittlement phenomenon takes place in this case, especially at the short exposure times in EXCO solution. Regarding higher exposure times, elongation at fracture is essentially decreased (more than half) for specimens exposed to NaCl solution while for the specimens exposed to EXCO solution it remained in higher levels (less than 40% decrease).

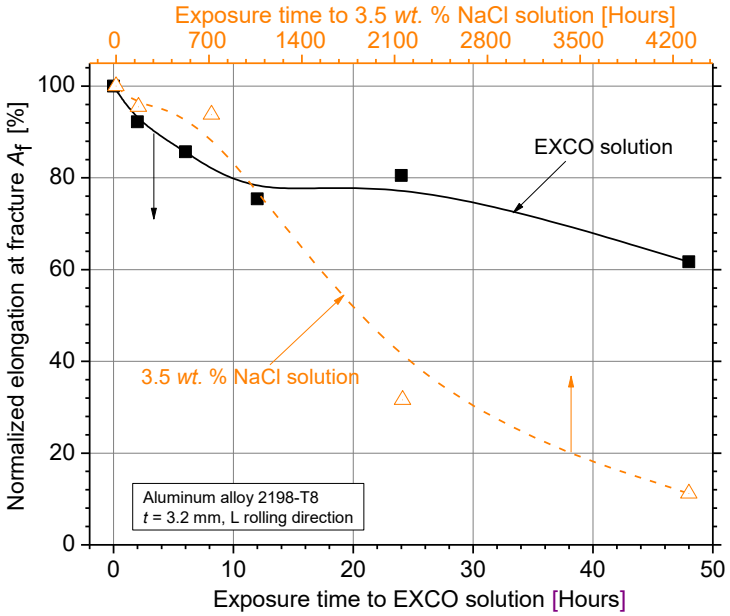

Figure 2-38: Normalized elongation at fracture (A_f) values of AA2198-T8 for the various exposure times to EXCO solution compared against 3.5 wt. % NaCl solution.

Figure 2-39 presents the correlation results of the effect of two corrosive environments, *e.g.,* EXCO and 3.5 *wt.* % NaCl solutions, with regard to the same corrosion-induced tensile elongation at fracture decrease. To this end, for the conversion of exposure times to EXCO solution to the respective times of exposure to NaCl solution, an empirical coefficient was devised (see section 2.3.2.4, Equation 2-4 (above)). The best calculation results were found by using the value $n = 107$ for the empirical coefficient and for the simulation of the tensile ductility decrease curve of the investigated specimens for short exposure times regime. The same rate decrease is evident between the two different corrosive solutions at the short exposure times where slight pitting formation is the dominant degradation mechanism. By using this coefficient value, is obvious that the results of exfoliation corrosion are very close to the experimental values of exposure to 3.5 *wt.* % NaCl up to 6 hours of exposure and 10% elongation at fracture. Thus, it can be concluded that 1 hour of exposure to EXCO solution is equivalent to 107 hours of exposure to 3.5 *wt.* % NaCl solution regarding the A_f degradation. For higher exposure times, there is no correlation between the corrosive environments regarding the ductility decrease since the corrosion-induced degradation mechanism is different.

It is worth to mention that correlation between EXCO and Harrison's solution could not be achieved since big differences on the normalized A_f values were noticed for the whole exposure time range of both corrosive environments and similar degradation percentage could not be observed. Thus, correlation only between the two most common corrosive environments, namely EXCO and 3.5 *wt.* % NaCl solution, was attempted in order to be directly compared against AA2024-T3.

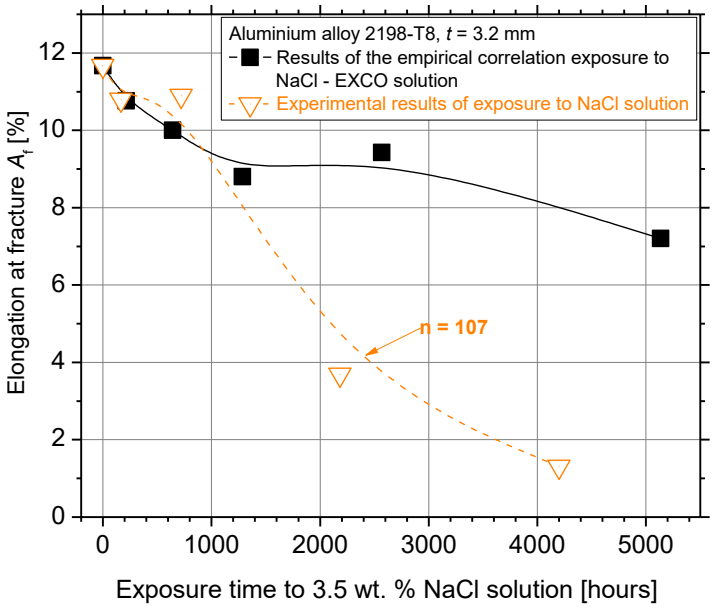

Figure 2-39: Correlation of the elongation at fracture A_f decrease due to exposure to EXCO solution as well as to 3.5 wt. % NaCl solution for AA2198-T8.

2.3.8 Comparison on the corrosion-induced mechanical properties degradation of AA2024-T3 and AA2198-T8

The effect of corrosion exposure to 3.5 *wt.* % NaCl solution on the mechanical properties' degradation of AA2024-T3 directly compared to AA2198-T8 is investigated in this chapter. The comparison was limited to 3.5 *wt.* % NaCl solution since the in-service obtained corrosion damage correlates well to the one caused by this solution [88]. Additionally, Harrison's solution is considered to better simulates the corrosion kinetics in Al-Cu-Li alloys.

Figure 2-40 shows the experimental results of AA2024-T3 and AA2198-T8 as average values and respective standard deviation derived from three specimens of each material. It should be mentioned that conventional yield stress $R_{p0.2\%}$ was calculated based on the nominal cross-section of the specimens and without taking into consideration the "effective thickness" of the specimens. The available experimental test results were simply interpolated with the aid of a B-Spline curve (eye-catch) to roughly assess the corrosion exposure effect on the mechanical properties of the two aluminium alloys tested. The corrosion exposure time range was divided into two distinct regimes, namely short exposure times (shown in grey background) and long exposure times (shown in yellow background), with different degradation rates and corrosion behaviour. AA2024-T3, represented by red squares, is not significantly affected by corrosion for short exposure times up to 720 hours where the remaining percentage of the conventional yield stress is approximately 99%. However, a significant decrease is noticed for long exposure times (> 1000 h) where the remaining percentage of the initial property value is almost 69% after the highest exposure time of 4320 hours in this case. Approximately the same degradation percentage noticed for AA2198-T8 for short exposure times

where pitting corrosion remains limited. Nevertheless, in contrary to AA2024-T3 further corrosion exposure of AA2198-T8 seems not to affect this mechanical property, since the remaining percentage remains constant even after heavily exposure specimens (black rectangles).

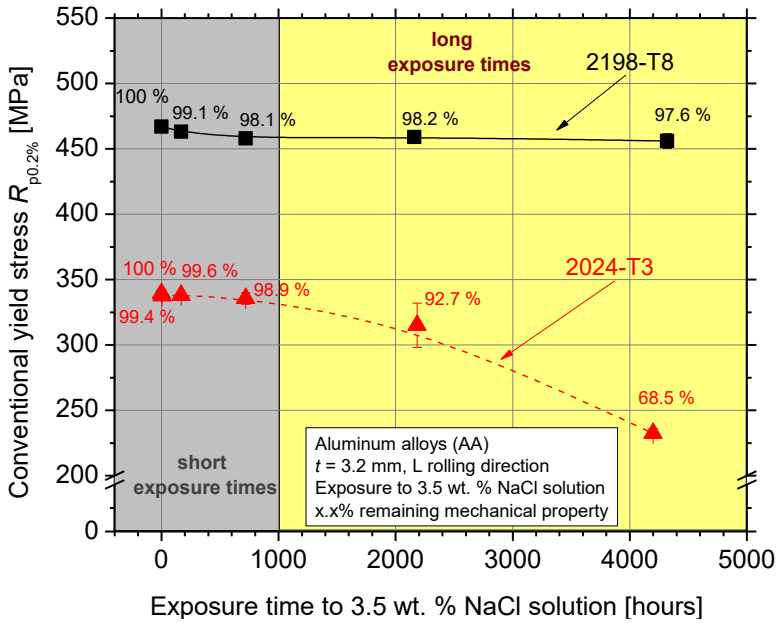

Figure 2-40: Conventional yield stress degradation of pre-corroded AA2024-T3 and AA2198-T8 specimens exposed for different times to 3.5 wt. % NaCl solution.

The values of the ultimate tensile strength R_m were again calculated by taking into account the nominal cross-sections of the specimens and the results are summarized in Figure 2-41. Comparative consideration of the plots for the two investigated aluminium alloys shows that AA2198-T8 degrades at slightly higher rates in comparison to AA2024-T3 regarding the short exposure times, *e.g.,* 96% remaining percentage of R_m was noticed after 720 hours of exposure while the respective value of AA2024-T3 was approximately 99%. On the contrary, long exposure times have a profound effect on AA2024-T3 where the remaining percentage of the initial property decreased to 86% while for AA2198-T8 the respective degradation was approximately 90% after the highest exposure time of 4200 hours.

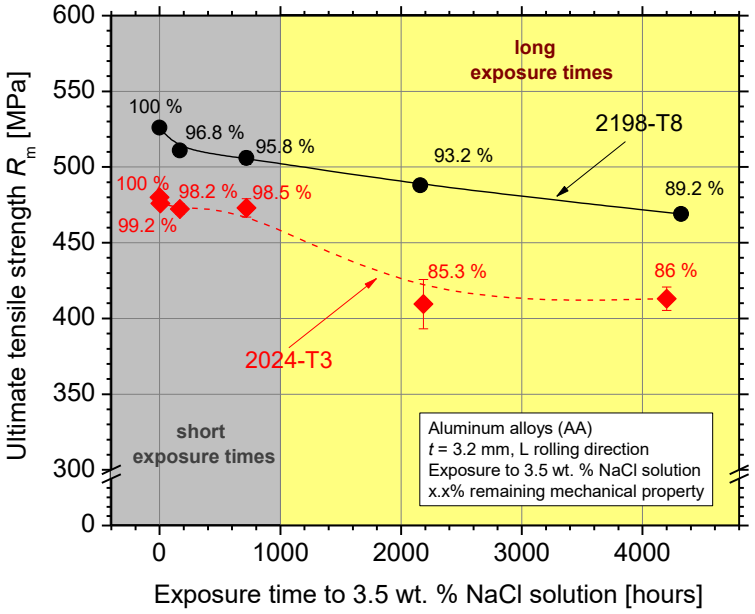

Figure 2-41: Ultimate tensile strength degradation of pre-corroded AA2024-T3 and AA2198-T8 specimens exposed for different times to 3.5 wt. % NaCl solution.

The values of elongation at fracture A_f of the pre-corroded tensile specimens can be seen in Figure 2-42 (the same notation and interpolation approach as in Figure 2-40 is followed), for both aluminium alloys studied in the present work. It can be seen from this figure that AA2198-T8 is more corrosion resistant than AA2024-T3 in terms of A_f degradation at the first stages of corrosion exposure and up to 720 hours (short exposure times regime) where pitting corrosion is limited and possibly the hydrogen embrittlement is the dominant degradation mechanism. It is worth mentioning that AA2198-T8 is superior to corrosion resistance even at the T8 condition (under-ageing) which leads to significant loss of ductility. However, almost the same degradation of elongation at fracture was noticed for the two investigated materials at long exposure times where pitting corrosion and cracking formation are the dominant degradation mechanisms. Hence, the AA2024-T3 specimens are losing their ductility potential at higher rates than AA2198-T8 giving evidence that Al-Cu-Li alloy is more corrosion resistant than its predecessor, in terms of highly maintaining its ductility characteristics when compared to the Al-Cu alloy for the same exposure time.

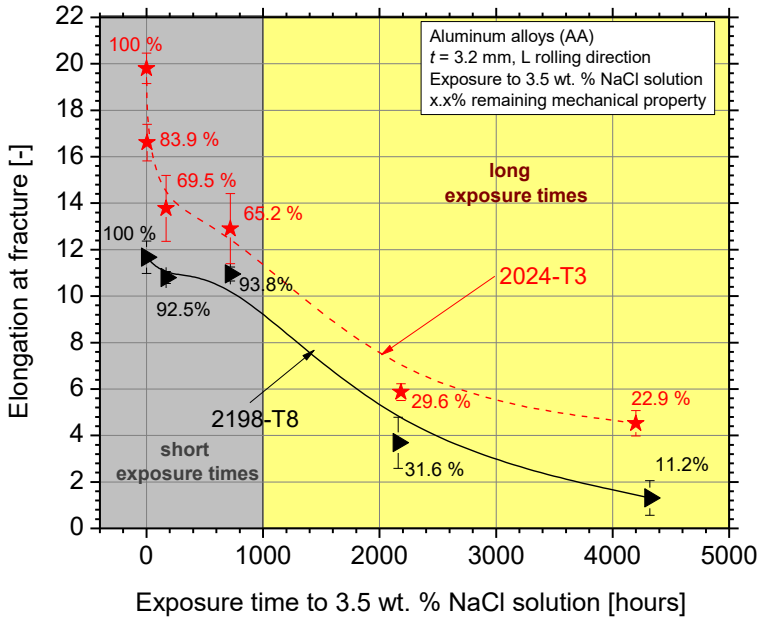

Figure 2-42: Elongation at fracture degradation of pre-corroded AA2024-T3 and AA2198-T8 specimens exposed for different times to 3.5 wt. % NaCl solution.

2.4 Conclusions

Summarizing the findings of the present experimental study, the following conclusions could be achieved:

1) Higher correlation of corrosion induced A_f decrease between EXCO and 3.5 *wt.* % NaCl solution was noticed for the short exposure times for both investigated aluminium alloys, where the slight pitting formation as well as hydrogen embrittlement (for the case of EXCO solution) are the dominant degradation mechanisms.
2) According to the empirical coefficient, 1 hour EXCO exposure of AA2024-T3 is equivalent to 92 hours of exposure to 3.5 *wt.* % NaCl solution, while 1 hour EXCO exposure of AA2198-T8 is equivalent to 107 hours of exposure to 3.5 *wt.* % NaCl solution, regarding tensile elongation at fracture decrease.
3) Different embrittlement mechanisms of AA2024-T3 are noticed for the different investigated corrosive environments. No grain-boundary embrittlement is noticed for NaCl-exposed specimens while severe embrittlement is evident for EXCO solution.
4) Approximately 50 μm intergranular cracking depth is revealed on AA2024-T3 specimens when exposed to EXCO solution for short times and prior to the formation of any substantial surface pitting.
5) Several secondary cracks up to a distance of approximately 4 mm ahead of the extended primary crack front are observed on the EXCO-exposed C(T) specimens of AA2024-T3. This observation correlates well with the calculated plastically affected zone of approximately 3.78 mm.

6) The depth of secondary cracks was found to be approximately 0.115 mm and correlates well with the thickness of the intergranular fracture surface, which was found to be approximately 0.12 mm. Thus, it gives evidence that the secondary cracks form due to some form of grain boundary embrittlement.
7) Approximately 11% decrease of the critical stress intensity factor K_{cr} is noticed for the AA2024-T3 specimens exposed for 2 hours to EXCO solution; the respective decrease for 24 hours exposure to 3.5 *wt.* % NaCl solution is approximately 13%. It is worth mentioning that 24 hours exposure to 3.5 *wt.* % NaCl solution corresponds to less than 1 hour exposure to EXCO regarding elongation at fracture decrease and according to the proposed correlation coefficient.
8) Signs of intergranular attack are also observed in the specimens exposed to 3.5 *wt.* % NaCl solution; however, IGC is not restricted to the grain boundary itself, but tends to develop transgranularly to the adjacent grains of the intergranularly attacked region. Transition from intergranular to transgranular corrosion attack leads to higher degradation of K_{cr} noticed in 3.5 *wt.* % NaCl solution.
9) Differences in corrosion degradation mechanism were also noticed for AA2198-T8 between the different corrosive environments. Harrison's solution was found to induce severe localized corrosion as well as exfoliation with increasing exposure time. However, no essential degradation of the "effective thickness" was noticed for both Harrison and NaCl solution, while the ductility was significantly decreased from the first stages of corrosion exposure.
10) Corrosion degrades all aspects of the tensile behaviour of AA2024-T3 at a higher level compared to the respective degradation of AA2198-T8 at long exposure times, where pitting corrosion mechanism takes place. Regarding elongation at fracture, AA2024-T3 was found to degrade at much higher rates even at short exposure times where hydrogen embrittlement is possibly the dominant degradation mechanism. Faster corrosion attack for AA2024-T3 was also revealed from the lower charge transfer resistance values at short exposure times. It was thus definitely concluded that Al-Cu-Li alloy is superior concerning corrosion resistance, since it maintains higher percentages of the initial (uncorroded) values of its tensile properties, against AA2024-T3.

Chapter 3

3 Effect of corrosion-induced micro-cracking on the structural integrity of 2xxx series aeronautical aluminium alloys

This chapter focuses on the micro-cracks' formation on AA2024 and AA2198, due to exposure to exfoliation corrosion solution, and their influence on mechanical properties degradation. Special concern is given on ductility which is described through elongation at fracture A_f. Measurements of the depth of cracks were performed, and a statistical analysis was made in order to reveal their increasing trend on different surfaces of the alloys with increasing exposure time. Additionally, different models for the calculation/simulation of the "effective thickness" decrease due to micro-cracks' propagation were developed. The chapter starts with an introduction regarding environmentally assisted cracking on 2xxx series aluminium alloys, continues with the description of the experimental protocol and finally the results are presented in order to be discussed. Comparison between the two investigated specimens is done in the whole chapter to highlight the potential of the advanced Al-Cu-Li alloy.

3.1 Introduction

Nowadays, rigorous improvements in energy consumption and mechanical performance on the aircraft industry sector have been pushed by market demand to face technically challenging requirements, especially due to CO_2 emissions regulations as well as demands for cost reduction in operation and maintenance. The need to reduce energy is driving the aeronautical manufacturers towards the development of lightweight metallic structures, through the incorporation of advanced lighter materials and new manufacturing techniques. As a consequence, there is an increasing demand to maintain or even increase structural integrity in these innovative aerospace applications. Hence, it is of imperative importance to easily assess the structural integrity of aircrafts and define their periodic inspection intervals. One of the major threats of aircraft's structural integrity is corrosion, where its co-existence with other forms of damage, such as fatigue, can lead to accelerated crack propagation [66] and eventually to premature material's failure. The most common used 2xxx series aeronautical aluminium alloys (*e.g.*, 2024 and 2198), which are commonly used in the aircraft industry due to their high strength to weight ratio, tend to be susceptible to corrosion according to [19]-[21] and [113]-[114]. For the case of aircraft structures from aluminium alloy 2024-T3, several types of damage have been reported over a large number of repairs [65], fatigue cracks was the most frequent damage observed, having a frequency of more than 57% out of the total repairs number. Second most frequent observed damage was corrosion, having approximately 30% of the total repairs.

Third generation Al-Cu-Li alloys were developed to replace the conventional Al-Cu alloys such as AA2024-T3, in aircraft structures where weight savings and damage tolerance are the critical design factors. Aluminium alloy 2198 was found to have excellent fatigue mechanical properties [115], as well as increased corrosion resistance [112], [116]-[117]. According to Moreto et *al*. [98], AA2198-T851 presented higher yield stress and ultimate tensile strength values than AA2524-T3 and better long-time corrosion resistance, despite of the higher corrosion potential due to the presence of Li. Significant differences in the corrosion attack mechanisms between Al-Cu-Li and conventional Al-Cu alloys were reported in [54] and [118]. Al-Cu-Li alloys were found to be susceptible to intragranular [118], transgranular as well as exfoliation corrosion attack with variations in the level of susceptibility between the different thermomechanical tempers [54], indicating the effect of micro-constituent particles on corrosion mechanism; the predominant corrosion mechanism of Al-Cu 2024-T3 alloy was found to be the intergranular corrosion (IGC). Despite of the increased corrosion susceptibility of Al-Cu-Li alloys, higher through thickness penetration of corrosion attack was noticed for AA2024-T3.

The improved mechanical properties of Al–Cu–Li alloys can be attributed to their microstructure and especially to the complex precipitation hardening system. Intermetallic phases including δ'

(Al_3Li), T_1 (Al_2CuLi), θ' (Al_2Cu) and S' (Al2CuMg) can be observed in the microstructure of such alloys [3] and [119]. T_1 precipitate is considered to be the major strengthening phase of Al-Cu-Li alloys [120]-[122] that preferably precipitates on dislocations, sub-grain and grain boundaries [22], [123]-[126]. Such strengthening intermetallic phases may influence the corrosion resistance of 2xxx aluminium alloys, as was noticed for AA2024, due to the different electrochemical behaviour of the matrix, *e.g.,* [19], [21] and the subsequent formation of a galvanic cell between the intermetallic particles (IMs) and the matrix or the adjacent particles [20], [24]. AA2024 is susceptible to intergranular corrosion attack due to precipitations formed on the grain boundaries. Al-Cu-Li alloys are highly susceptible to intergranular/intersubgranular corrosion attack due to high grain stored energy (dislocations density per grain) that promotes the nucleation of T_1 precipitates inside such grains [51]-[53], as well as to transgranular and exfoliation corrosion attack found by Araujo et *al.* in [54]. T_1 precipitates enhance localized corrosion due to the anodic behaviour with respect to the adjacent Cu depleted zones and the matrix, *e.g.,* [55]-[57] and [127], coming from the higher corrosion potential of Li [59]. Severe localized corrosion attack associated to micrometric precipitates [60] was evident in the interior of high energy grains. Pitting corrosion nucleated on the dispersed intermetallic (IMs) precipitates of AA2198-T3 exposed to neutral sulphate and chloride solutions according to Balbo et *al.* in [61].

Corrosion of aircraft structures initiates through the formation of pitting [22], [68]. Localized corrosion attack initiates at locations where the presence of intermetallic phases is evident, *e.g.*, [24], [29]-[30], [71]; localized corrosion initiates at the secondary phase particles of AA2024 [25]-[26]. The Cu-rich remnants within the clusters, as a result of *S*-type (Al_2CuMg) particles' dealloying [72], [128], switch the anode to the alloy matrix adjacent to these particles and eventually to grain boundaries [73]-[75], [129]; thus, leading to trenching around their periphery and subsequent formation of sub-surface micro-cracking [130]-[133]. Environmentally assisted cracking (EAC) is a deleterious process and includes mechanisms such as hydrogen induced cracking, hydrogen embrittlement, corrosion fatigue and stress corrosion cracking. Cracking generally starts at local defects that act as stress concentrators, which may be microstructural features inside the material, surface features or arise from an in-service damage process such as corrosion (*e.g.*, pitting) [76]-[77]. Crack growth rates as well as the crack path are strongly affected by corrosion exposure duration [134]-[135]. Hence, the effect of corrosion exposure duration is strongly influenced by the initial thickness of the specimen.

The ASTM G34 standard test method for exfoliation corrosion susceptibility in 2xxx and 7xxx series aluminium alloys [80] used for the execution of the experimental protocol, regarding the corrosion environment and exposure. The specification recommends the exposure of a single side of

the specimens to the corrosive solution. In a series of articles, the effect of corrosion exposure on 2xxx aluminium alloys was assessed, *e.g.,* by Kamoutsi in [78] as well as by Pantelakis et *al.* in [87] and [104], where exposure was performed on all surfaces (4 in number) of the typical tensile specimens. Posada et *al.* in [35] revealed that the side-surfaces of the specimens (thickness) are more prone to corrosion attack, and this was attributed to the long elongated grains and consequently to the higher density of grain boundaries due to the rolling process. Hence, it is of major importance to investigate the corrosion behaviour on the different surfaces and rolling directions of specimens as well as to quantify the effect of side-surfaces corrosion attack on the mechanical properties degradation.

Ageing aircrafts may have accumulated corrosion damage coming from the coexistence of several mechanisms, with the most detrimental to materials' structural integrity being the hydrogen embrittlement. Hydrogen is produced by surface corrosion reactions and afterwards diffuses into the material up to a certain distance and is trapped at preferential sites [37]. It has been shown, *e.g.*, [42] and [136] that lattice defects such as grain boundaries or intermetallic phases, provide hydrogen trapping sites. It is generally accepted that the presence of cracks assists the hydrogen embrittlement since hydrogen can be adsorbed at crack tips or diffuse ahead of cracks, and as a consequence the interatomic bonding languishes so that dislocation is facilitated [79]. These effects lead to intense plastic deformation and the embrittlement of the metal. Kamoutsi et *al*. [46] acknowledged that the hydrogen front increases with corrosion front and lead to the formation of a hydrogen-affected zone beneath the corroded layer.

Quite few articles were reported to characterize the effect of corrosion-induced micro-cracking on the structural integrity of aluminium alloy 2024-T3, and to correlate the metallographic features to the resulting degradation of its mechanical properties. It was shown, *e.g.*, [49] and [137], that the increasing exposure time to the corrosive environment leads to a deeper penetration of corrosion-induced micro-cracks. Hence, it was found that the cross-sectional area of specimens which was supposed to be unaffected by micro-cracks, referred as 'effective thickness', decreases exponentially with increasing exposure time to the EXCO solution due to the crack propagation mechanism. The reduction in cross-sectional area decreases the mechanical properties (*e.g.*, residual stress, modulus of elasticity) proportionally to the decrease in area. Alexopoulos et *al*. [85] also acknowledged that corrosion exposure has a negative effect on yield stress of AA2024-T3 mainly due to cross-section decrease at higher exposure times, as well as on ductility due to the combination of hydrogen embrittlement and cross-section degradation. Synergy of corrosion-induced surface micro-cracking and hydrogen embrittlement was found to decrease both, the fatigue life and the damage tolerance capability, *e.g.*, [67], [138]-[139].

The detrimental effects of corrosion damage on component's structural integrity are qualitatively acknowledged, to date there are few articles in the literature trying to quantify these properties for a material. The majority of the articles deals with the effect of corrosion on the microstructure of specimens and focus on the crack initiation mechanism, crack propagation and the shape of micro-cracks *i.e.*, Jones et *al.* [135]. It was observed that the critical crack in its early stages ($\Delta K < 5$ MPa·√m) interacts with adjacent corrosion pits and material microstructure and therefore low crack growth rates were observed. Likewise, it was found that the crack nucleation initiated at a point along the perimeter of a pit where stress concentration and microstructural discontinuities exist, or where the grain orientation is predisposed to grow along crystallographic slip planes, *e.g.,* [134] and [140]. A semi-elliptical surface crack grows up to a critical size leading to the rapid failure of the specimen. Pit depth was increased with increasing polarization time and therefore a linear relationship between critical pit depth and stress intensity factor was observed. Regarding Al-Cu-Li alloys, severe localized corrosion on AA2198-T851 after only 1 hour of corrosion exposure, as well as crystallographic propagation with increasing exposure time was revealed according to Donatus et *al*. in [62].

In the present work, the effect of corrosion-induced micro-cracking on the structural integrity of AA2024 and AA2198 is investigated. The mechanisms of micro-crack formation and propagation on the different surfaces of the specimens as well as the effect on mechanical properties degradation is investigated. Additionally, the quantification of micro-cracks contribution to tensile ductility decrease is attempted for the different surfaces of the specimens.

3.2 Materials and experimental procedure

Materials used were the wrought aluminium alloys 2024-T3 of 0.4- and 1.6 mm nominal thickness and 2198-T351 of 1.6 mm nominal thickness. The condition T351 includes the same treatments as for the T3 but with an additional stress-relieving stage by stretching. Tensile, fatigue and small rectangular flat specimens (10 x 20 mm^2) were machined from the sheets. The geometrical dimensions were 12.5 mm x 1.6 mm at the reduced cross section with total length of 190 mm for the tensile specimens, while the fatigue specimens had a continuous radius with 9.0 mm x 1.6 mm being the reduced cross-section and total length of 190 mm. Specimens were machined in both, longitudinal (L) and transverse (T) sheet rolling direction.

Figure 3-1 shows schematically the flow chart of the experimental procedure regarding the effect of corrosion-induced micro-cracking on ultra-thin (0.4 mm) specimens of AA2024-T3 and their synergy with hydrogen embrittlement. Prior to corrosive solution exposure, the surfaces of the small rectangular metallography specimens were cleaned with alcohol according to ASTM G1 specification [92]. Masking of a single out of two flat large surfaces was performed for several metallography

specimens, similar to the respective tensile specimens at their reduced cross-section region. Specimens with one side masked are called 'single-sided', while specimens without masking are called 'both-sided', as the two flat large sides were exposed to the accelerated corrosive solution. Specimens with and without masking were afterwards exposed to the laboratory exfoliation corrosion environment (hereafter called EXCO solution) according to ASTM G34 specification [80]. Different specimens were exposed to several times that were selected according to a relevant article of the authors [85]. Afterwards, more than three cross-sections of each specimen were mounted in epoxy matrix, surface ground up to 1200 grit, polished with 0.25 μm paste down and then examined in a Leica DM LM light optical microscope. Image Pro® software was used for the image analysis and the calculation of the pit depth or depth of corrosion attack. In total, more than 65 cross sections were investigated for the 21 different corrosion case studies in the present work. All depth of attack measurements per different corrosion case were inserted in the Origin® software for the statistical analysis of the results. Micro-crack results for the different case studies were correlated with the respective tensile test results [85] that were performed on standard specimens from the same thickness sheets with 50 mm gauge length and 3.3 x 10^{-4} s^{-1} strain rate.

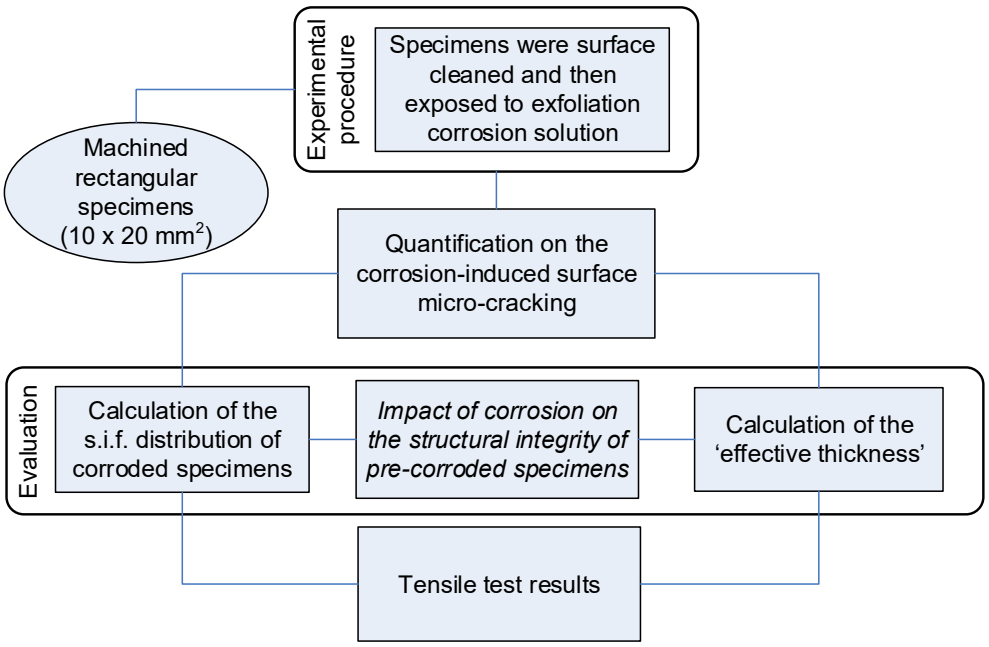

Figure 3-1: Flow chart of the experimental procedure for the effect of corrosion micro-cracking on ultra-thin (0.4 mm) AA2024-T3 specimens.

Figure 3-2 depicts the flow chart of the experimental procedure regarding the effect of corrosion-induced micro-cracking on mechanical properties' degradation as well as the quantification of the side-surfaces' cracks contribution to ductility decrease for AA2198-T351, directly compared against the respective of AA2024-T3 of 1.6 mm nominal thickness. Prior to the corrosive solution exposure, the side-surfaces of the tensile specimens were ground up according to ASTM E8 specification [90].

All surfaces to be corroded were cleaned with alcohol according to ASTM G1 specification [92]. The specimens were masked in the areas to be attached to the tensile test machine's grips with appropriate insulating PVC tape with excellent adherence, in order to avoid crevice corrosion beneath the masking tape. The exposed area was within the reduced cross-section to ensure fracture within the gauge length. Additionally, masking of the side-surfaces was performed for several tensile specimens as depicted in Picture 3-1(b), where the upper and bottom large surfaces to be corroded are indicated with grey colour, while for the fatigue specimens all (four) surfaces of the gauge length were exposed to the corrosive solution.

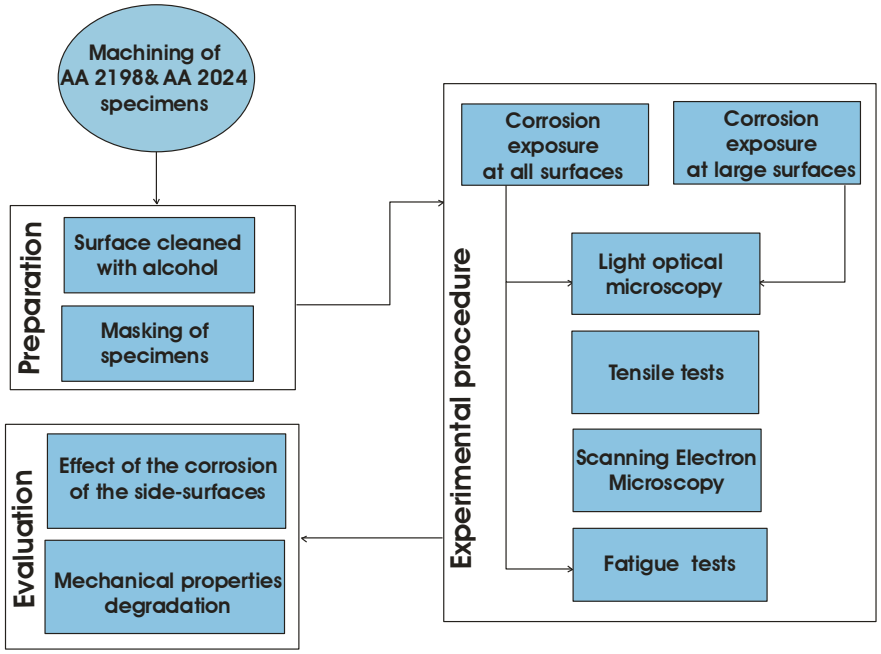

Figure 3-2: Flow chart of the experimental procedure for the effect of side-surfaces corrosion micro-cracking on AA2198-T351 specimens.

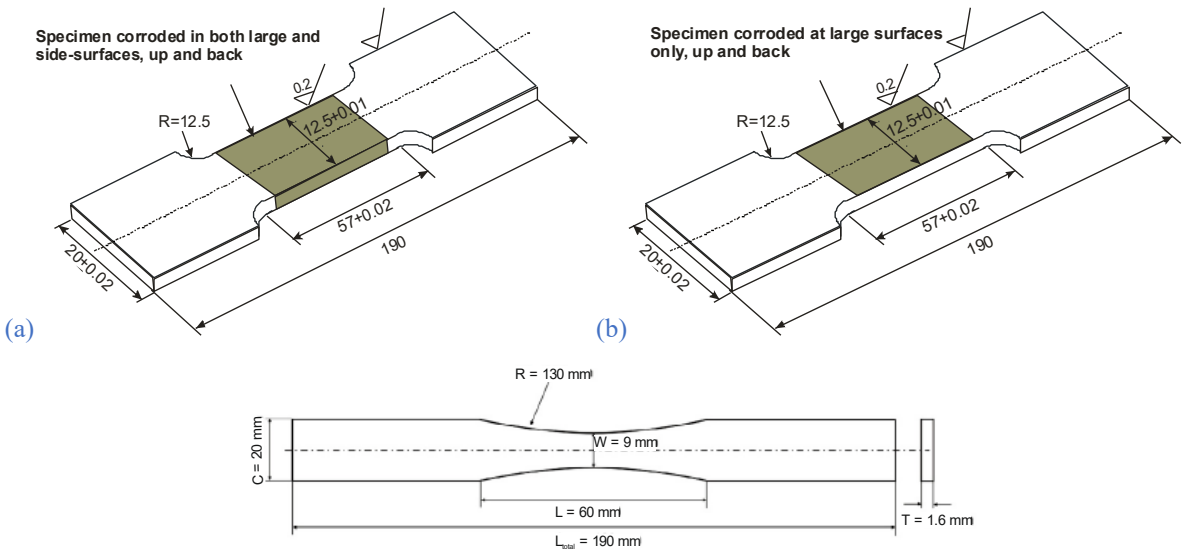

Picture 3-1: Schematic representation of specimens according to ASTM E8 and ASTM E 466 specifications; (a) specimens corroded at all surfaces, (b) specimens corroded at large surfaces only and (c) fatigue specimens.

Afterwards, the tensile specimens were exposed to the laboratory exfoliation corrosion environment (here after will be called as EXCO solution) for different times, according to ASTM G34 specification [80]. The specimens with masked side-surfaces are called "specimens corroded at large surfaces" while the specimens without masked side-surfaces are called "specimens corroded at all surfaces". After the corrosion exposure, the tensile specimens were immediately cleaned according to ASTM G34 specification and then subjected to mechanical testing (tension).

Electrochemical measurements were performed on polished small rectangular specimens (10 mm x 20 mm) with the use of a typical three electrodes cell system that was composed of a platinum electrode as counter electrode, a silver chloride electrode as reference electrode and the small rectangular specimens of the investigated aluminium alloys as working electrodes. A Gamry Interface 1000 potentiostat along with a cell with an exposed area of the working electrode of 0.5 cm^2 were used for the electrochemical measurements. Initially, the open circuit potential (OCP) was measured by recording values with 1 s interval for 30 min. Potentiodynamic polarization test started after the OCP measurement and from -0.2 V to the corrosion potential. The polarization potential range was from -0.2 V up to 0.6 V to the OCP, respectively and the potential scanning rate was 0.2 mV s^{-1}. For all samples, at least 2 polarization curves were plotted to ensure the reproducibility of the results.

Additionally, rectangular specimens were also exposed to EXCO solution for the same exposure times as for the tensile specimens and were examined in a Leica stereoscope in order to reveal the surface corrosion damage. Afterwards, more than three cross-sections of each rectangular were mounted in epoxy resin matrix, mechanically ground up to 1200 grit of SiC paper, polished with 3 μm diamond paste and examined in a Leica DFC 295 S6D light optical microscope in order to

investigate the corrosion attack in the interior material. The non-corroded specimens were additionally chemically etched with Kroll's reagent consisted of 100 ml distilled water, 6 ml HNO_3 and 2 ml hydrofluoric acid (HF) used for 20 s as well as with Dix–Keller's reagent consisted of 190 ml distilled water, 5 ml HNO_3, 3 ml hydrochloric acid (HCl) and 2 ml HF used for 40 s, for AA2024-T3 and AA2198-T351 specimens respectively, and then examined in the light optical microscope in order to reveal the microstructural characteristics of the investigated alloys.

Tensile tests were carried out in a servo hydraulic Instron 100 kN testing machine according to the ASTM E8 specification [90] and the crosshead displacement rate was kept constant and equal to 0.7 mm/min. An external Instron extensometer with 50 mm ± 10 mm maximum travel was attached at the reduced cross-section gauge length of the specimens. A data logger was used during all tensile tests and the values of load, displacement and axial strain were recorded and stored in a computer. More than three specimens were tested in each different case to get reliable average data. A total of more than 120 tensile stress-strain curves were analysed for the evaluation of the tensile mechanical behaviour of the pre-corroded specimens for both investigated alloys. Fractured surfaces of the tensile specimens were examined in a Leica stereoscope as well as with the aid of scanning electron microscopy (SEM) in order to investigate the fracture mechanism.

Fatigue tests were carried out for the AA2198-T351 specimens in the same testing machine; all tests were performed with load command and by using sine wave load. Load (or stress) ratio, the ratio of the minimum applied load (stress) to the maximum applied load (stress), $R = \sigma_{min}/\sigma_{max}$, was kept constant for fatigue tests and equal to $R = 0.1$, which is the typical waveform for testing aeronautical materials since it better simulates the true loadings in aerostructures. Fatigue load frequency was 10 Hz for all tests; the values of maximum and minimum load, displacement as well as cycles to fracture were recorded and stored in a computer.

3.3 Results and discussion

The corrosion-induced micro-cracking affects all mechanical properties of aluminium alloys. In this section the effect on the structural integrity as well as remaining ductility will be assessed.

3.3.1 Macro- and microstructure background

Surface macro- and stereoscopical examination of pre-corroded ultra-thin (0.4 mm) tensile specimens of AA2024-T3 showed that the surface pitting corrosion mechanism was slightly evident for short exposure times up to 1.33 hours. However, the microstructural examination revealed that corrosion exposure for the very short times resulted in the formation of surface cracks towards the centre of the specimen. Formation of small, scarce surface pits observed for higher exposure times,

e.g., 2 hours. For even higher exposure times and up to the investigated 4 hours, excessive surface pitting occurred. Cracks and corrosion products tend to grow in subsurface and in accordance with the specimen texture, resulting in crevice corrosion [85]. Figure 3-3 demonstrates several cross-sections of pre-corroded specimens investigated via an optical microscope. It is obvious that the depth of corrosion-induced cracks increases with increasing exposure time to the EXCO solution up to a specific depth, *e.g.*, 80 μm after only 4 hours of exposure; further exposure does not increase essentially their depth of attack.

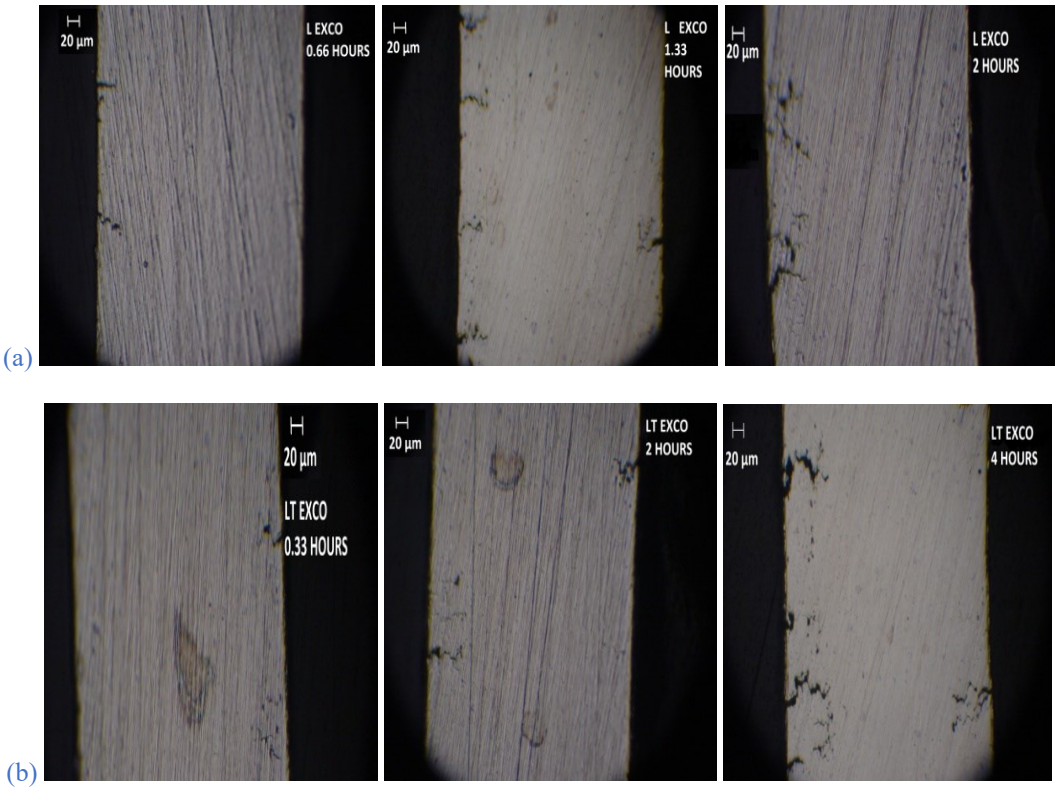

Figure 3-3: Typical photographs of the cross-section of pre-corroded AA2024 specimens for various exposure times to EXCO solution for (a) L and (b) T rolling directions.

Corrosion damage begins with the formation of surface pits, followed by the formation of sub-surface micro-cracks that finally lead to material fracture. At the early stages of corrosion, the pits nucleate and then propagate due to intergranular attack up to 80-100 μm in depth [85], [141]. Crack branching was noticed for the T-rolling direction only and for crack depth close to the above plateau value. With increasing exposure time, tilting of the cracks was observed to a plane in parallel with the rolling direction that lead to exfoliation of the surface layers of the specimen. Higher exposure time leads to excessive exfoliation of the specimen, Figure 3-4. The depth increase of corrosion-induced micro-cracks decreases the thickness of the material as well as the mechanical properties with increasing exposure time. Consequently, the propagation mechanism of micro-cracks has a deleterious effect on the structural integrity and durability of aluminium alloy 2024-T3.

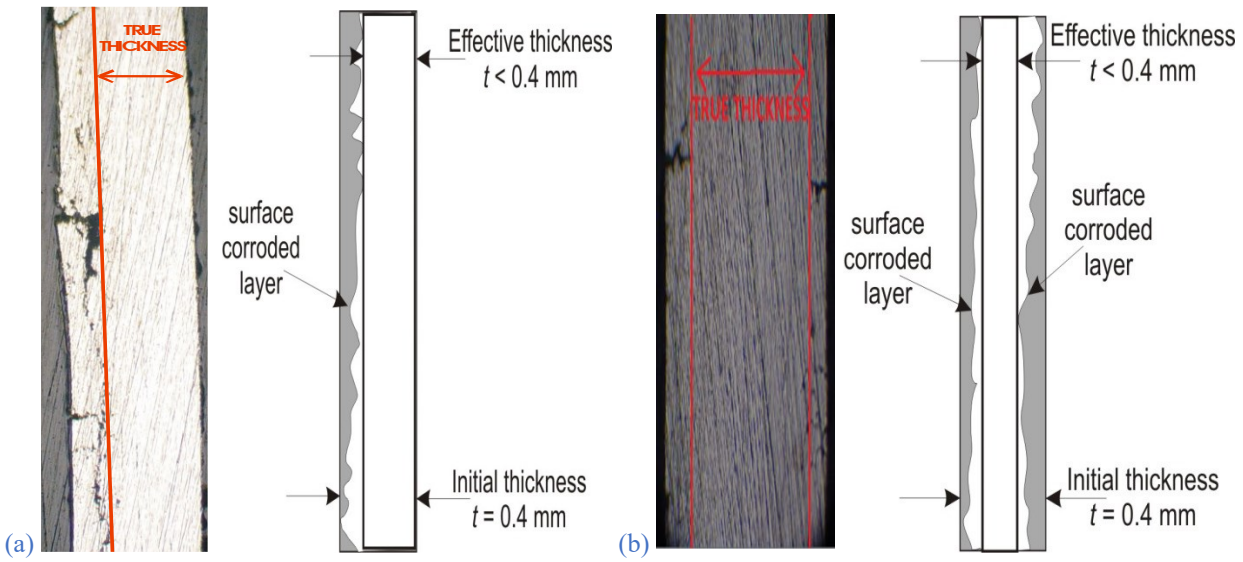

Figure 3-4: An example of the definition of the "effective thickness" of specimens after the formation of corrosion-induced surface cracks for (a) single-sided and (b) both-sided corroded specimens.

Quantitative results of the depth of attack can be seen in Figure 3-5, where the probability percentage of appearance among classes of depth of corrosion attack α can be seen for the different corrosion exposure times. The depth of attack of cracks tends to increase with increasing exposure time to the exfoliation corrosion solution. Hence, the depth of cracks tends to be higher at T than at L direction, confirming that the T-rolling direction is more susceptible to corrosion attack due to the ease of corrosion penetration between the grain boundaries. Additionally, it is observed that for the single-sided corroded specimens this depth is essentially higher than for both-sided, for the same exposure times. Figure 3-6 shows the average depth of corrosion attack values plotted against the exposure time to the EXCO solution. At the L-rolling direction, an essential difference of the maximum value of the average depth of attack values between the single- and both-sided corroded specimens (~ 100 μm) could not be observed. On the contrary, the average depth of attack of the single-sided corroded specimens is essentially higher than the respective both-sided at the T-rolling direction; this phenomenon is a matter of current investigation.

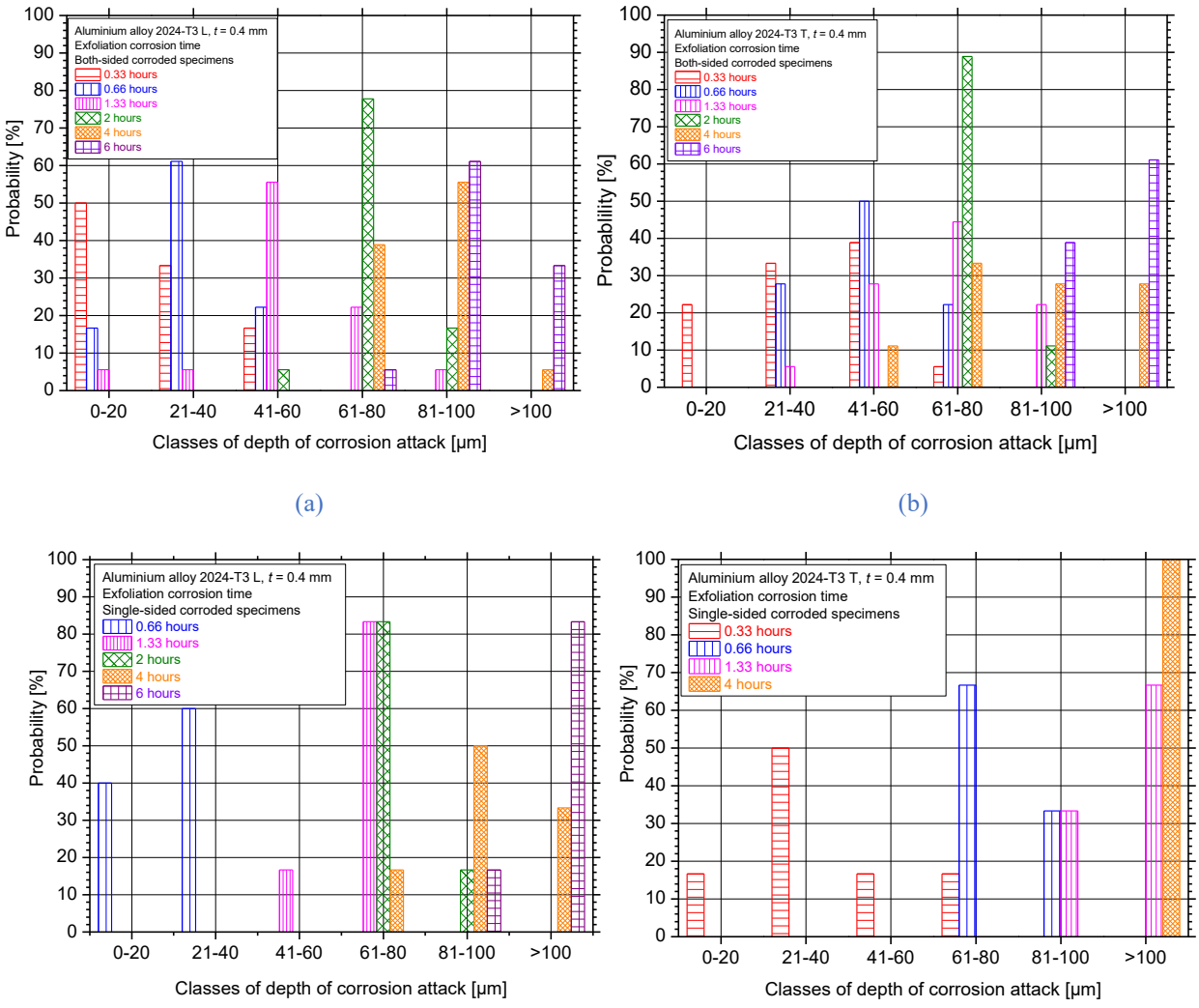

Figure 3-5: Probability percentage of appearance among classes of depth of corrosion attack for (a) and (b) both-sided as well as (c) and (d) single-sided corroded AA2024-T3 specimens for L and T rolling directions, respectively.

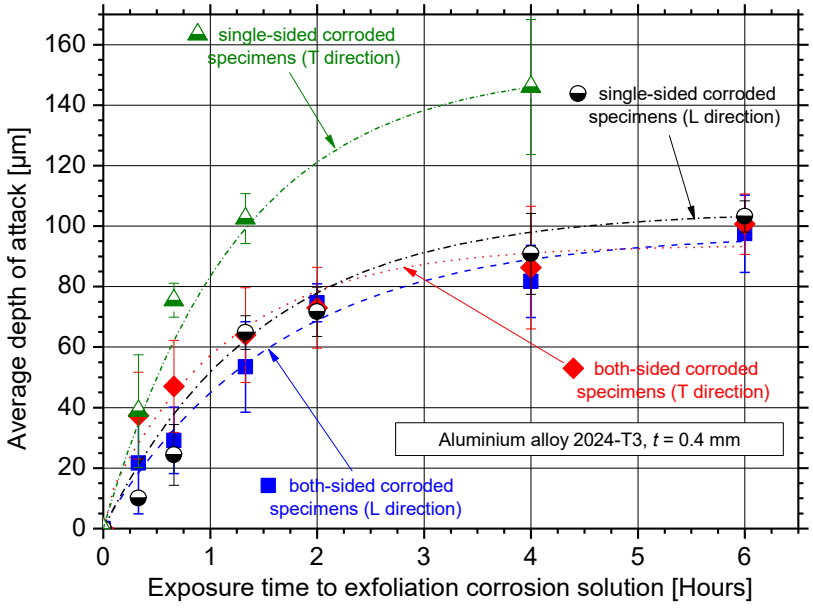

Figure 3-6: Average depth of attack of AA2024-T3 for various exposure times in EXCO solution.

3.3.2 Effect on stress intensity factor

The term stress intensity factor (s.i.f.) K is widely used in fracture mechanics to predict the stress state (or «stress intensity») near the tip of a crack or other discontinuities, caused by a remote mechanical load or residual stresses, more accurately. Near discontinuities, *e.g.*, corrosion-induced cracks in the present study, stresses take much higher values than in the far field, and the outcome is stress concentration in this region. Stress concentration is usually quantified by the stress intensity factor K, which is defined as the ratio of the maximum induced mechanical stress σ_{max} to the respective nominal stress σ_{nom} [142] as:

$$K = \frac{\sigma_{max}}{\sigma_{nom}}. \qquad (3\text{-}1)$$

For the case of presence of discontinuities, stress intensity factor can be calculated as a function of the stress state σ, the length of discontinuity α, *e.g.*, notches or depth of corrosion attack in this work, as well as a geometrical factor $Y\left(\frac{a}{W}\right)$ that takes into account the ratio of the length of discontinuity a to the available width w, *e.g.,* specimen thickness in the present work; this factor can be calculated [142] by the following equation below:

$$K = Y\left(\frac{\alpha}{w}\right)\sigma\sqrt{\pi\,\alpha} \qquad (3\text{-}2)$$

To take into account the geometrical problem, different analytical solutions are available in the literature [143]-[144] to solve the problem of the cracks in finite bodies. Equations (3-3) (below) and (3-4) (below) were used to calculate the geometrical factor when the surface discontinuity(ies) are in both sides or in a single side (thickness) of the specimen, respectively:

$$Y\left(\frac{a}{w}\right) = 1.99 + 0.76\left(\frac{a}{w}\right) - 8.48\left(\frac{a}{w}\right)^2 + 27.36\left(\frac{a}{w}\right)^3, \textit{ (both-sided)} \qquad (3\text{-}3)$$

$$Y\left(\frac{\alpha}{w}\right) = 1.99 - 0.41\left(\frac{\alpha}{w}\right) + 18.7\left(\frac{\alpha}{w}\right)^2 - 38.48\left(\frac{\alpha}{w}\right)^3 + 53.85\left(\frac{\alpha}{w}\right)^4, \textit{ (single-sided)} \qquad (3\text{-}4)$$

Nevertheless, in structural applications it is critical to calculate the maximum mechanical load or the critical length of discontinuities so as to prevent material fracture and generally to maintain the structural integrity [145]. When the discontinuity has a critical size and the local mechanical stress condition is adequate, then rapid crack growth takes place that leads to fracture of the specimen/structure. This critical condition that defines the onset of the unstable crack growth is the critical stress intensity factor or the threshold stress intensity factor K_{th} for corrosion cracking problems [146]. Therefore, the criterion for material failure/fracture can be met for specific length of discontinuities as well as stress condition that reaches the K threshold value as expressed by Equation (3-5) (below), while the criterion for the rapid growth of the cracks and subsequent fracture of the

material is when the value of the stress intensity factor exceeds the threshold value, Equation (3-6) (below), as:

$$K = K_{th} \text{ (critical value), and} \quad (3\text{-}5)$$

$$K > K_{th} \text{ (rapid fracture-cleavage)} \quad (3\text{-}6)$$

Corrosion pitting promotes the nucleation of sub-surface micro-cracks; as the specimen is exposed to the corrosive environment, it is expected that the surface corrosion-induced products (*e.g.*, pits, cracks) will increase their depth with increasing exposure time. In [24] it was observed that individual pits coalesce laterally and in depth in order to form sub-surface micro-cracks that lead to exfoliation of the alloy with increasing exposure time. Corrosion-induced micro-cracks initiate at the edges of the pit with the highest stress concentration. These cracks grow separately on both sides of the pit, with shapes approximately a quarter circle, up to the pit depth. Afterwards, these cracks grow further beyond the root of the pit with semi-elliptical shape [147]. Therefore, it is essential to characterize the corrosion-induced damage by means of microstructural features such as depth of attack, shape of pit, pitting density etc. as required by respective standards, *e.g.*, ASTM G34.

On the other hand, it is critical for the assessment of the structural integrity of a component to establish a correlation between the developing corrosion damage (*e.g.*, micro-cracks) and the ability of the structure to withstand the in-service mechanical loads. Hence, it is significant to know the critical values of the depth of attack of the corroded structures in order to sustain and prevent the material fracture.

Stress intensity factor was calculated by exploiting Equation (3-2) (above) for both- and single-sided corrosion exposure of the investigated specimens, while the geometrical factor was calculated from Equations (3-3) (above) and (3-4) (above), respectively. The depth of corrosion attack a (pit/crack) measurements were used as the length of discontinuity in Equation (3-2) (above), while a constant mechanical stress of σ = 100 MPa was used for all calculations since it is the normal design stress of the aircraft fuselage. The distribution of K values for the different cases of exposure time, sheet rolling direction as well as exposure surfaces can be seen in Figure 3-7. The calculated values were inserted in the Easyfit® software to calculate the best-fit of one-dimensional distribution according to *Kolmogorov-Smirnov* (KS) goodness-of-fit test [148]. The KS test has the advantage of making no assumption about the distribution of data and was preferably selected instead of the *Shapiro-Wilk* test or *Anderson-Darling* test [149]. Results of the KS test can be seen in Table 3-1 for the different investigated corrosion case studies, with the bold values to be the lowest values and therefore representing the best available fitting. Three typical distributions were selected (namely Normal, Lognormal and Weibull) to check their goodness-of-fit for the calculated K values. For the single-sided corroded specimens, the best fitted distribution was the Normal one as lowest fitting

values were calculated. For the case of both-sided corroded specimens, the results must be interpreted with the relative crack size. Two different groups can be identified; the short cracks (t < 1.33 hours) and the long cracks for higher exposure times (t >1.33 hours). It is evident that for the first case the lower values (marked in bold in Table 3-1) can be obtained for the Normal distribution. For the second case of longer cracks, the lognormal distribution was found to better fit the calculated results. The idea behind the goodness-of-fit tests is to measure the 'distance' between the experimental data and their distribution in order to compare this distance with a threshold value. If this distance (often called 'test statistic') is less than the threshold value (the 'critical value'), then the fit is considered good. Since the goodness-of-fit test statistics indicates the distance between the data and the fitted distributions, it is obvious that the distribution with the lowest statistic value is the best fitting model.

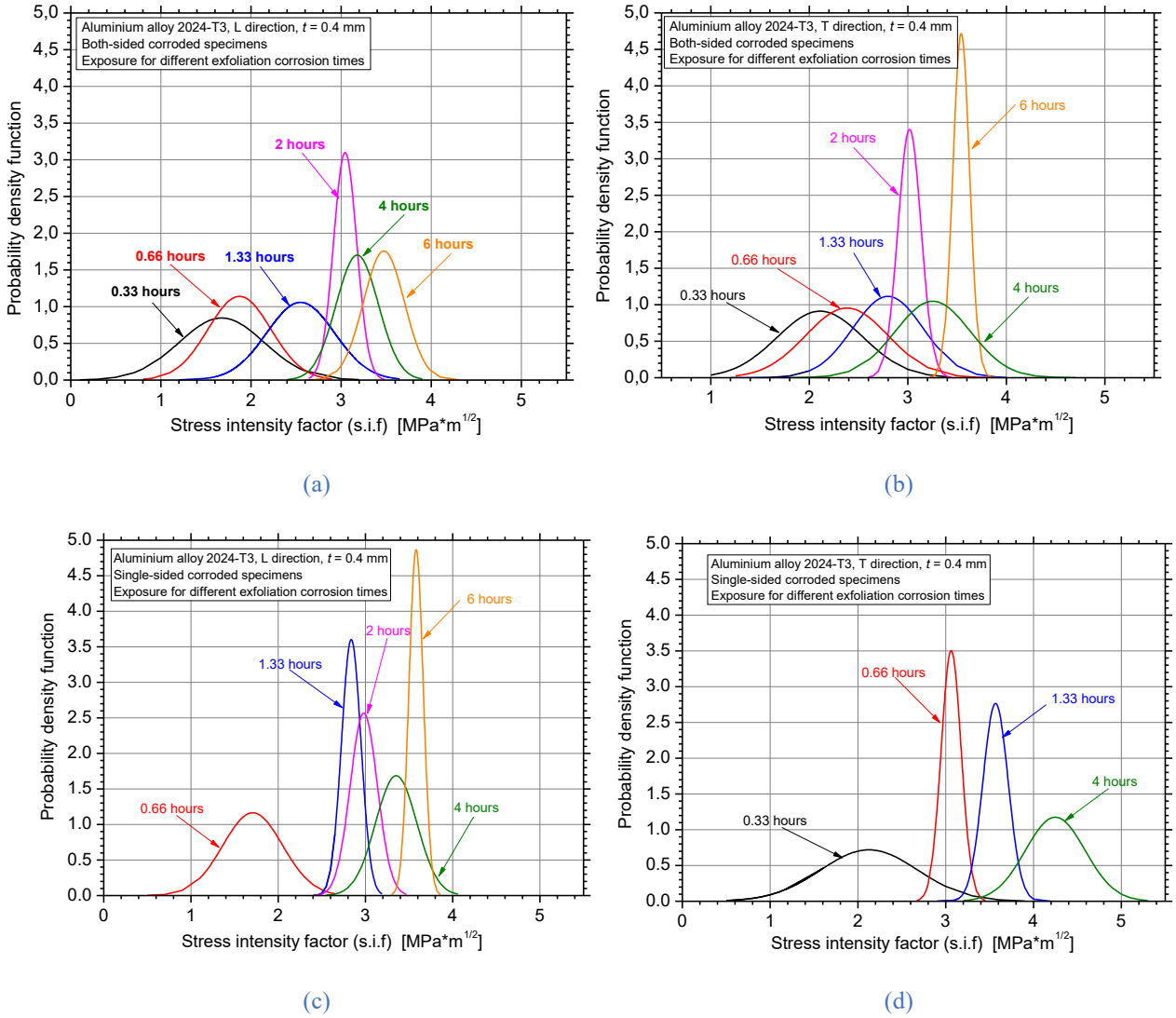

Figure 3-7: Distribution of stress intensity factor K for different times to exfoliation corrosion solution for (a) and (b) both-sided as well as (c) and (d) single-sided corroded specimens for L and T rolling directions, respectively.

Table 3-1: Goodness of fit for various statistical distributions according to Kolmogorov – Smirnov test for the investigated corrosion exposure cases of AA 2024.

Exposure time [h]	Both-sided corrosion exposure						Single-sided corrosion exposure					
	L direction			T direction			L direction			T direction		
	Normal	Lognormal	Weibull	Normal	Lognormal	Weibull	Normal	Lognormal	Weibull	Normal	Lognormal	Weibull
0.33	0.18166	0.17403	**0.14912**	**0.14977**	0.1648	0.15999	*	*	*	**0.18746**	0.23226	0.30226
0.66	**0.09477**	0.12239	0.12541	0.18047	0.20538	**0.16774**	**0.26021**	0.29589	0.27985	**0.21211**	0.22651	0.21754
1.33	**0.13631**	0.15924	0.18073	**0.14369**	0.16978	0.14458	**0.19061**	0.20315	0.19531	**0.11368**	0.13042	0.19873
2.0	0.12761	**0.12562**	0.15131	0.19991	**0.19447**	0.19669	**0.16546**	0.18712	0.23235	*	*	*
4.0	**0.12514**	0.13884	0.13072	0.10472	**0.09143**	0.11594	**0.26515**	0.27582	0.31163	**0.21253**	0.23046	0.26871
6.0	0.12684	**0.12527**	0.15058	0.14982	0.15243	**0.14649**	0.17481	**0.17098**	0.25598	*	*	*

As expected, the stress intensity factor distributions shifts to higher values with increasing exposure time for all investigated cases, since depth of attack *a* increases with exposure time. Lower *K* values were calculated for the longitudinal L-rolling direction when compared with the respective exposure times of the transverse T-rolling direction. The normal distribution was chosen in order to characterize the behaviour of *K* factor with increasing exposure time to the EXCO solution because it can be fully characterized by just two parameters, the mean and the standard deviation, and the probability of any value occurring can be obtained simply by knowing how many standard deviations separate the value from the mean. According to the literature [150], the threshold K_{th} value for aluminium alloy 2024-T3 was found to be equal to 3.2 MPa·√m. Hence, in order to calculate the possibility for a given corrosion exposure time to exceed this threshold value, we simply integrated the area below the distribution curves of Figure 3-7 with the criterion of $K > 3.2$ MPa·√m. Calculation results can be seen in Table 3-2 and are graphically represented in Figure 3-8. Higher possibility percentage for the *K* factor to exceed the threshold value was observed for the T than the L rolling direction for the case of single- and both-sided corroded specimens. For the low exposure times and up to 2 hours it is observed that both-sided corroded specimens exhibit higher possibility percentage to exceed the threshold stress intensity factor than single-sided at L-rolling direction. For higher exposure times, single-sided corroded specimens have higher fracture possibility.

Table 3-2: Probability calculations to exceed stress intensity factor threshold for the investigated corrosion exposure cases of AA 2024.

Exposure time [h]	Percentage probability for s.i.f. value > K_{th} = 3.2 MPa·√m			
	Both-sided corrosion exposure		Single-sided corrosion exposure	
	L direction	T direction	L direction	T direction
0.33	0.06	0.63	-	2.65
0.66	0.01	2.51	0.00	11.31
1.33	4.23	13.07	0.05	81.46
2.00	11.33	25.89	7.88	-
4.00	46.44	55.53	73.94	99.99
6.00	88.71	100	100	-

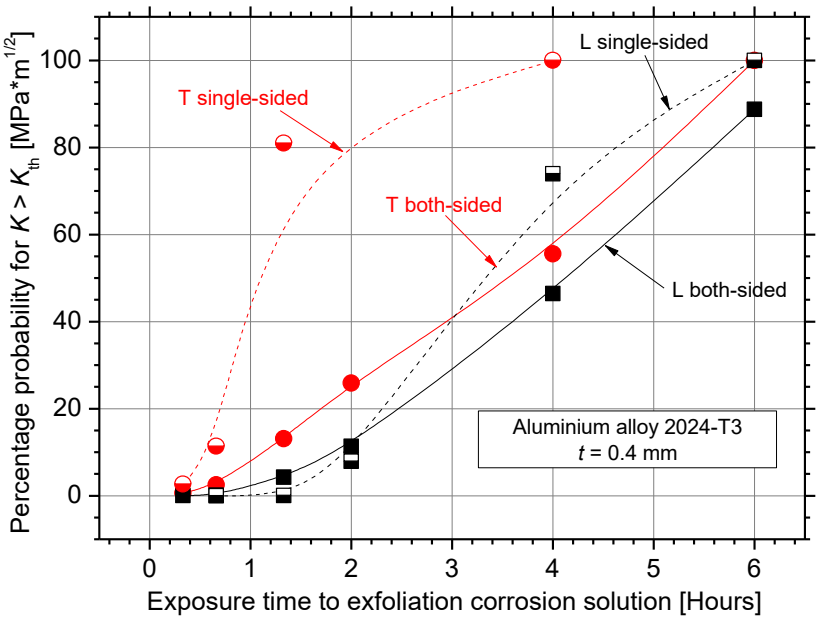

Figure 3-8: Possibility percentage to exceed the threshold stress intensity factor for the AA2024-T3.

3.3.3 Effect on the effective thickness

It was shown that with increasing exposure time to the EXCO solution, the depth of corrosion-induced micro-cracks tends to increase. Given from the literature that the outcome of corrosion is the surface micro-crack formation, it is eminent that the cross-section of the specimens that withstand the applied mechanical loading will be reduced. A typical example of a cross-section that shows the thickness of the material that the mechanical properties are considered to be unaffected by the presence of micro-cracks is shown in Figure 3-4 and it is called "effective thickness". In the previous section, the depth of attack of cracks *a* was measured and hence, the average values of "effective thickness" were calculated. Three mechanical models have been devised to calculate the decrease of the effective thickness of the specimens when subjected to different corrosion exposure times.

3.3.3.1 The iso-modulus of elasticity concept

This model utilizes the decrease of the tensile modulus of elasticity of the pre-corroded specimens to address the effective thickness calculation problem. By making the hypothesis that there is no degradation of the material due to hydrogen embrittlement, then the difference in the slope of the nominal stress–strain tensile curves in the elastic region is attributed to the reduction of the effective thickness of the specimen. It is thought that the true value of modulus of elasticity *E* of the specimen effective thickness is independent of the exposure time to the EXCO solution as it is supposed to be unaffected by the corrosion exposure. There is also the possibility that the loss of surface-elongated grains with increased work-hardening capability and higher mechanical strength might lead to a small decrease in modulus of elasticity. The authors agreed to neglect this probable small variance and for the assumptions of the proposed model the modulus of elasticity depends solely on the effective

thickness of specimens. The specimen thickness B_j after j hours exposure to the EXCO solution can be calculated by means of the respective values of nominal modulus of elasticity E_j calculated in [85] and the specimen initial thickness B_0 and initial modulus of elasticity (uncorroded) E_0, as proposed by Alexopoulos and Papanikos [49]:

$$B_j = \frac{B_0 \cdot E_j}{E_0} \qquad (3\text{-}7)$$

3.3.3.2 The iso-yield stress concept

This mechanical model was devised based on the concept that the unaffected by corrosion exposure material presents the same yield stress. This model utilizes the mechanical load F that corresponds to the yield stress R_p of the specimens. Nevertheless, the effective thickness of the specimens decreases with increasing exposure time. The thickness B_j of the specimen after j hours exposure to the EXCO solution, can be calculated by means of the respective values of axial force F_j that corresponds to yield stress point, the specimen initial thickness B_0:

$$B_j = \frac{B_0 \cdot F_j}{F_0} \qquad (3\text{-}8)$$

where F_0 is the axial mechanical load value that corresponds to the yield stress point of the reference (uncorroded) specimens. Same for the previous model, there is the possibility that the loss of surface-elongated grains with increased work-hardening capability and higher mechanical strength to negatively influence the global yield stress of the specimen. The assumptions of the proposed model lies on the concept that the yield stress remains unaffected despite: (a) the loss of the 'work-hardened' surface layers and (b) hydrogen embrittlement of the core material. Taking into account the above considerations, the difference in the yield stress R_p of the force-displacement tensile curves is attributed to the reduction of the effective thickness solely. It is a logical consideration that the true value of axial force F, corresponds to the yield stress, of the effective thickness of the specimens is independent of the exposure time to the EXCO solution as the effective thickness supposed to be unaffected by the corrosion exposure. Hence, the true value of load F depends only on the effective thickness of specimens.

3.3.3.3 The stress reduction concept

This model utilizes the values of stress at given 1% axial strain for different exposure times to the EXCO solution and the stress of reference uncorroded specimen at the same elongation. The value of 1% axial nominal elongation was individually selected to have identical measuring instructions for calculation in all specimens and corresponds to a given stress just when the yield stress point was just exceeded. This model has specific limitations and utilizes the cumulative assumptions of the

previously presented models, since this 1% axial strain involves both elastic (modulus of elasticity involved) and plastic (yield stress involved) strain. Figure 3-9 demonstrates the typical stress reduction $\Delta\sigma = \sigma_0 - \sigma_j$ for tensile specimens, pre-corroded at different exposure times to the EXCO solution. The ratio of remaining stress σ_j to baseline stress σ_0 was assumed to be equivalent to the ratio of remaining, undamaged cross-sectional area A_j to the original section area A_0 [137]. Additionally, with the consideration that the width of specimens w is unaffected by the corrosion exposure time and taking into account that $A = w * B$, it leads to the conclusion that the effective thickness B_j is dependent on the stress reduction, *e.g.*, at 1% elongation, as:

$$\frac{\sigma_j}{\sigma_0} = \frac{A_j}{A_0} \xrightarrow{yields} B_j = B_0\left(1 - \frac{\Delta\sigma}{\sigma_0}\right) \qquad (3\text{-}9)$$

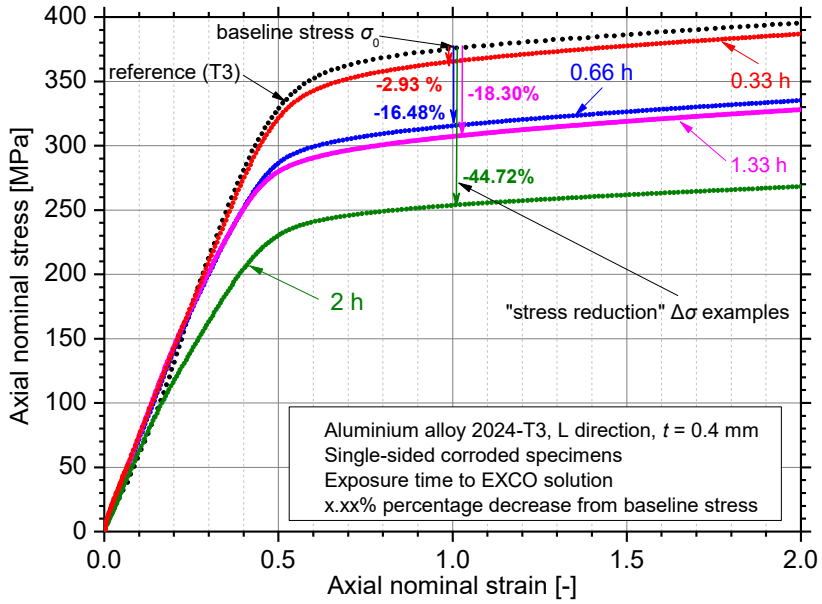

Figure 3-9: Calculation example of the axial stress reduction at 1% axial strain for different exposure times to EXCO solution.

Figure 3-10 shows the comparison results of the three concepts with the experimentally derived values that calculate the reduction of the effective thickness coming from the occurrence of corrosion-induced micro-cracking. Effective thickness linearly decreases with increasing exposure time to exfoliation corrosion solution for small exposure times (*e.g.*, 1.33 hours) until it reaches a specific plateau that is rolling direction sensitive. The linear decrease regime can be correlated with the crack nucleation and propagation mechanism. Crack tilting to the transverse direction and subsequent exfoliation of the surface grains are the dominant mechanisms for all cases of the presented plateau regime of Figure 3-10. It is obvious that for the both-sided corroded specimens at L direction, the results of the iso-modulus of elasticity concept are very close to the experimental values; minor deviation is observed for higher than 1.33 hours exposure.

This phenomenon was also observed for the both-sided corroded specimens at T direction. For the case of single-sided corroded specimens at L direction and up to 1.33 hours exposure, both the stress reduction and the iso-modulus of elasticity concepts gives close values with the experimental results and hence can better describe the effective thickness decrease due to corrosion-induced crack nucleation and subsequent propagation. For even higher exposure times, the experimental values were very well simulated by employing the stress reduction concept. For the case of T direction, both the stress reduction and iso-yield stress concepts give close values to the experimental ones. At this point we have to underline that almost all concepts (especially yield stress) might underestimate the experimental measurements in high exposure times (> 1.33 hours), mainly because they cannot take into account the synergetic degradation due to hydrogen embrittlement and possible loss of the different (elongated) grain structure due to the rolling process.

Likewise, the T direction suffered higher effective thickness decrease than the L direction as well as the both-sided corroded specimens exhibited higher degradation than the single-sided. The higher degradation of the effective thickness for the T direction can be attributed to the crack propagation mechanism, since micro-cracks propagate up to 80-100 μm depth (for single- and both-sided specimens, respectively) and afterwards continue to grow parallel to L direction [85]. In specific, the effective thickness of the specimens is reduced significantly up to 2 hours exposure time. A reduction of approximately 21% was noticed, using the stress reduction concept, for the both-sided corroded specimens at L direction after 1.33 hours exposure time while a reduction of approximately 16% was noticed for the single-sided corroded specimens at the same rolling direction and the same time period. On the other hand, a reduction of almost 20% was observed for the single-sided corroded specimens at T direction for the same exposure time. Further exposure to the EXCO solution beyond 2 hours decreases insignificantly the effective thickness of the specimens.

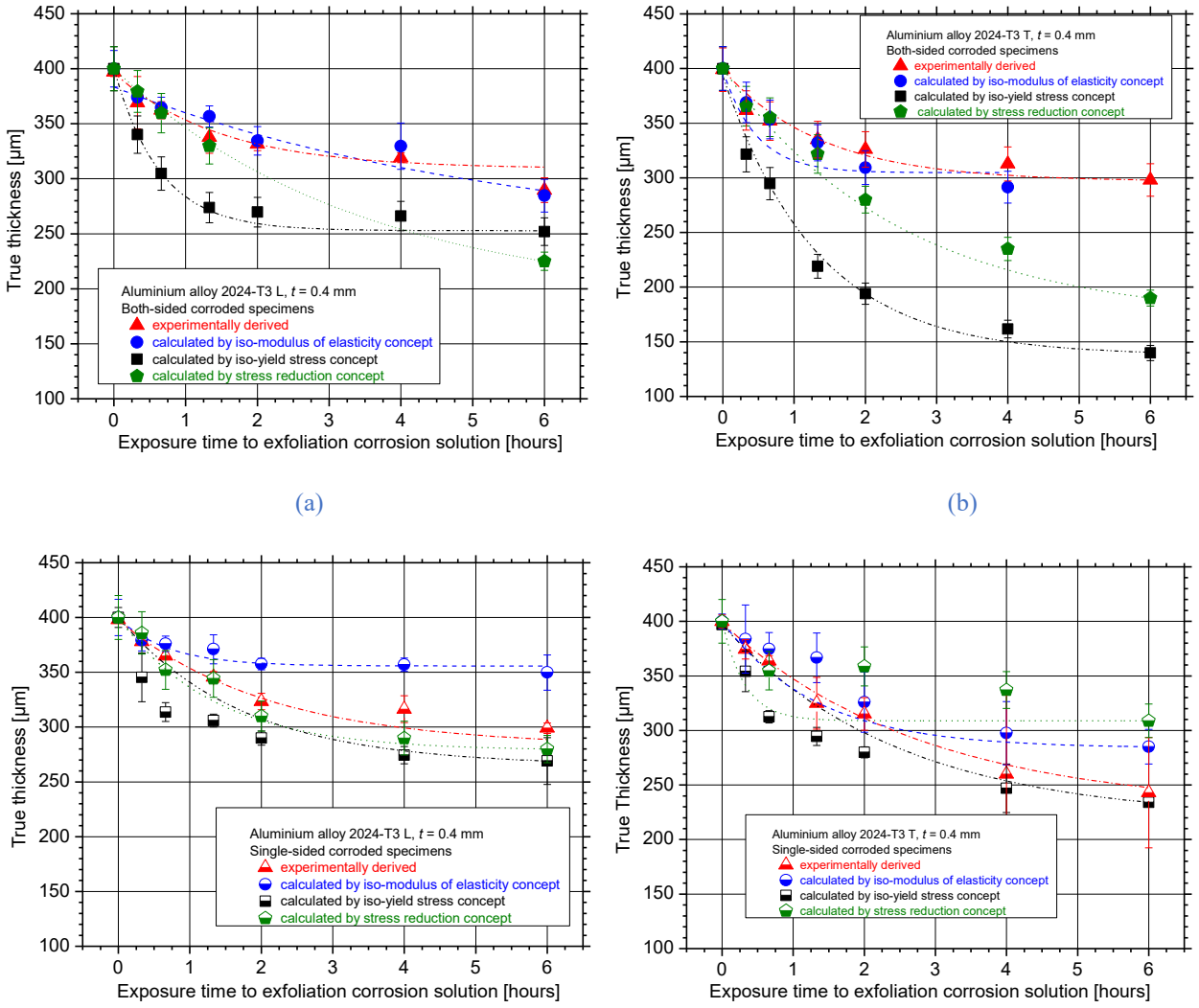

Figure 3-10: Reduction of the effective thickness of AA 2024-T3 specimens for different exposure times to EXCO solution for (a) and (b) both-sided as well as (c) and (d) single-sided corroded specimens for L and T rolling directions, respectively.

3.3.4 Effect on remaining ductility

It is evident that two synergetic mechanisms are responsible for the tensile ductility decrease: (a) corrosion-induced micro-cracking and (b) hydrogen embrittlement. To eliminate one of the above mechanisms, elongation at fracture was correlated with the experimental values of depth of attack (DOA) after various exposure times to EXCO solution, Figure 3-11. Please note that square root of discontinuity was preferred since stress intensity factor is analogous to the square root of the length of the crack. Similar results were obtained for the respective plot of the experimentally derived A_f versus DOA values for the same specimens. The proposed linear equation gives the best fit of the experimentally derived values since with all cases the linear regression had $R^2 > 0.96$; the present experimental protocol describes the synergetic effect of surface notches and subsequent hydrogen embrittlement. To cope with this phenomenon, the problem of notches was interpreted with the

classical fracture mechanics approach so as to eliminate this parameter and to calculate the effect of the hydrogen embrittlement parameter. The proposed approach has some limitations, for example when proposing linearity between A_f and DOA. This implies that corrosion damage by hydrogen embrittlement is proportional to DOA. To a specific extend this assumption seems logical, as the cracks create new pathways for corrosion damage, hydrogen diffusion and subsequent embrittlement; nevertheless, their correlation cannot be easily found in the literature. Extrapolation of these lines to very small discontinuity values, the notch problem is eliminated and, hence, the remaining degradation is mainly due to the hydrogen embrittlement problem. This simplistic approach assumes that extrapolation of the results is valid for the very small discontinuity levels. This concept shows that for the extremely low discontinuity levels a ductility decrease is noticed that is directly attributed to hydrogen embrittlement. For the L rolling direction, the hydrogen embrittlement decreases the elongation at fracture A_f from the approximate value of 15% to 14.5%, that corresponds to approximately 11% decrease. For the case of both-sided corrosion, more than double (~ 27%) decrease is noticed and hence, almost one quartile of the ductility decrease is attributed to the hydrogen embrittlement and the rest 73% to the classical micro-cracks' mechanism. Respective results were calculated for the T rolling direction in Figure 3-11. It was evident from Figure 3-6 that corrosion attack is more severe in this rolling direction. Calculation results prove this harsh attack and deleterious exfoliation between the grains for actually no formed surface deterioration. Hydrogen embrittlement is responsible for almost 22% of the total ductility decrease in single-sided corroded specimens while half (~ 49%) of the damage is governed by the hydrogen embrittlement in both-sided corroded specimens. To our knowledge, this is the first attempt to quantify the effect of each degradation parameter in such corrosion problems.

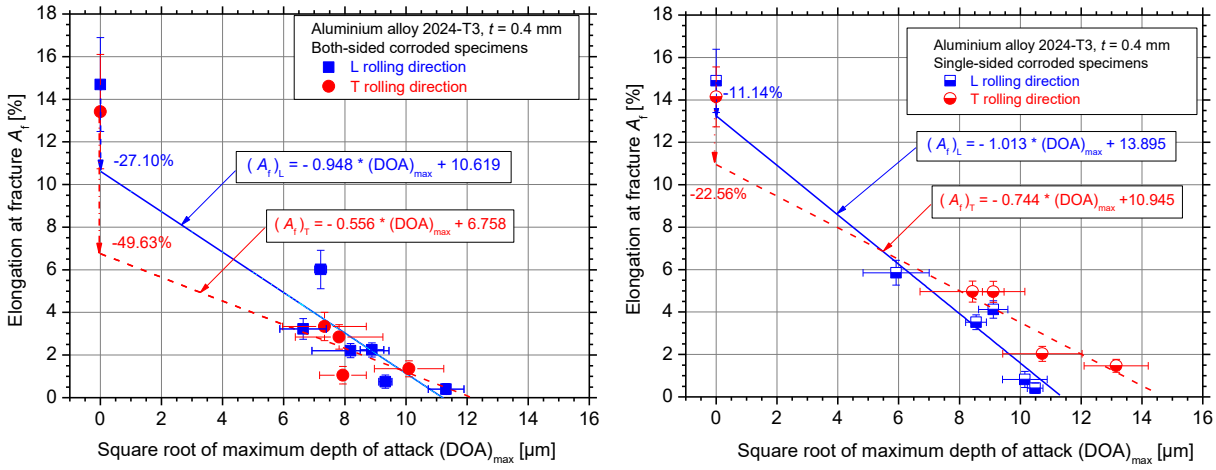

(a) (b)

Figure 3-11: The elongation at fracture decrease for the different calculated maximum depth of attack values of AA2024-T3 for different exposure times to exfoliation corrosion solution: (a) both-sided and (b) single-sided corroded specimens.

3.3.5 Effect on side-surfaces attack

3.3.5.1 Microstructural examination and corrosion behaviour of pre-corroded specimens

Figure 3-12 shows the optical micrographs of the grain structure for the large- and the side-surfaces of non–corroded AA2024-T3 (left) and AA2198-T351 (right) for comparison purposes. A typical recrystallised, equiaxed pancake-like morphology of the grains is evident for both AA2024-T3 and AA2198-T351 specimens in the large surfaces (L/LT direction), *e.g.*, Figure 3-12(a) and Figure 3-12(b), respectively. Similar grain structures were reported in similar studies, *e.g.*, [4], [151]-[152]. The dispersed dark spots uniformly distributed throughout the microstructure of AA2024-T3 are signs of the presence of Al_2CuMg precipitates, *e.g.*, [153]. Precipitates located both in grain boundaries and inside grains are also evident for AA2198-T351. The microstructure of AA2198-T351 consisted of flattened grains in the L/LT direction and elongated grains parallel to the rolling direction as well as clustering of grains at the side-surfaces area (L/ST), with average diameter of approximately 130 ± 25 μm and average thickness of approximately 30 ± 4 μm, calculated by using the linear intercept method according to ASTM E112 [154]. Similar grain morphologies were reported in similar studies for Al-Cu-Li alloys, *e.g.*, [155]-[159]. Larger sized grains were noticed for AA2198-T351 than AA2024-T3 due to the cold stretching process that is included in the T351 condition as was also shown in [62] and [160]. The microstructural examination revealed higher grain density for the AA2024-T3 specimens that provide preferable sites for corrosion initiation as also referred by Posada et *al*. in [35]. The above-mentioned sentence implies that the alloy microstructure with smaller grains (side-surfaces) have higher tendency for corrosion attack (breakdown), that is in accordance with the less noble breakdown potential (E_{corr}) of the polarization curves, nevertheless they support a lower corrosion rate that is obvious from the lower current density values when compared to large surfaces.

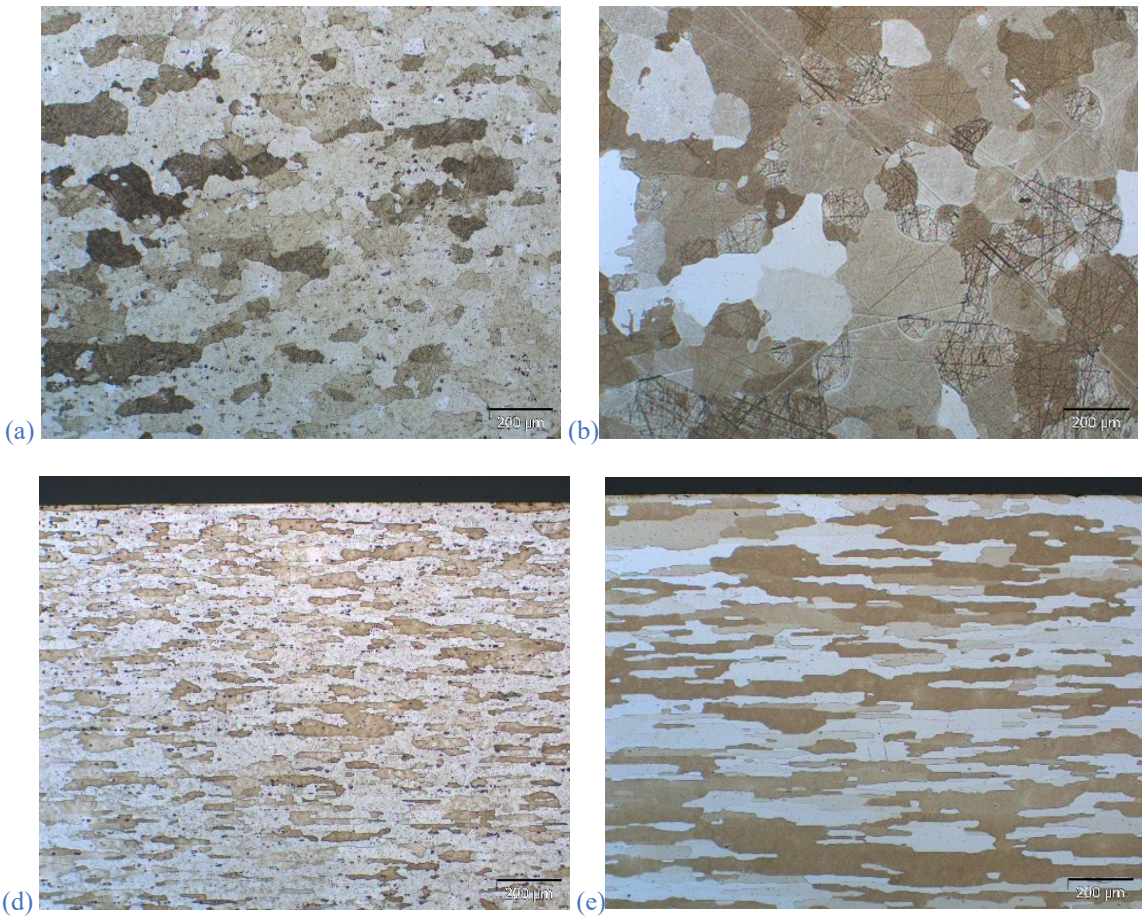

Figure 3-12: Light optical microscopy of AA2024-T3 (left) and AA2198-T351 (right) showing the microstructural differences of two alloys in both (a)-(b) large and (c)-(d) side- surfaces.

Figure 3-13 shows the OCP curves for the large – and the side–surfaces of AA2024-T3 directly compared to the respective curves of AA2198-T351. The duration of OCP measurements was 30 min for both aluminium alloys. An essential decrease (shift to less noble values) of the OCP was noticed for the side–surfaces in both aluminium alloys. Higher corrosion potential decrease for the corrosion exposure of the side–surfaces was evident for AA2198-T351, *e.g.*, Figure 3-13(b). Different behaviour of the OCPs was noticed for the two investigated alloys; OCP of the large surfaces of AA2024-T3 almost stabilized after only 200 s of corrosion exposure time while for the side–surfaces it started to stabilize after 500 s. Regarding AA2198-T351 a continuous decrease in the OCP was noticed for both exposed surfaces along with slight fluctuations in the curve of the large surfaces that can be correlated to transient currents due to pitting process.

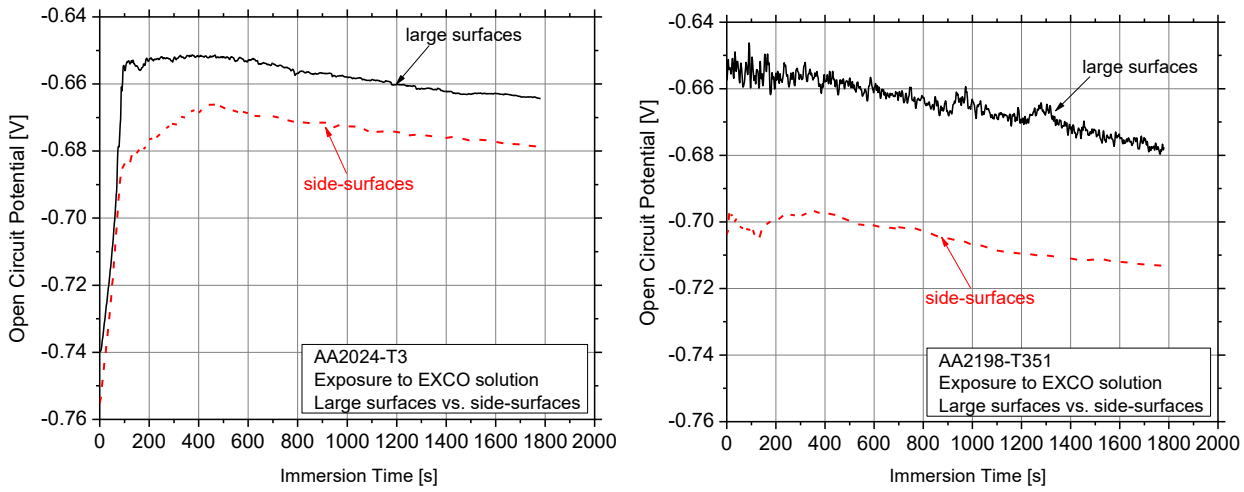

(a) (b)

Figure 3-13: Comparison of the open circuit potential curves of the specimens corroded at large surfaces only and specimens corroded at side-surfaces for (a) AA2024-T3 and (b) AA2198-T351 during 30 min of immersion in the EXCO solution.

Potentiodynamic polarization measurements for the large- and side- surfaces of AA2024-T3 and AA2198-T351 exposed to EXCO solution are shown in Figure 3-14(a) and Figure 3-14(b), respectively. It is generally accepted that the electrochemical behaviour of the AA2024 with a complex precipitation system depends on several parameters, such as the clustering, the morphology and distribution of precipitates and intermetallics, the relative areas of exposed phases, the electrode kinetics of each phase as well as the development of galvanic cells among them, *e.g.*, [22]-[24] and [29]. The two branches (cathodic and anodic) of the potentiodynamic polarization curves are nearly asymmetrical. Absence of passivation plateau in the anodic branch was noticed for all curves of both aluminium alloys throughout the scanned potential range. The sharp increase of the anodic current density right after the corrosion potential E_{corr} indicates an immediate pitting attack, confirming that the alloys are already in their breakdown potential at E_{corr} in such an aggressive electrolyte, exhibiting localized corrosion. Similar observations have been reported in the literature, *e.g.*, [161]-[163]. The cathodic branch of the polarization curves corresponds to the diffusion-controlled reduction of protons accompanied by hydrogen evolution in acidic EXCO solution. However, the measured cathodic current densities on AA2024-T3 are significantly higher than that on AA2198-T351. Moreover, the cathodic Tafel slope is significantly higher in the former case. The lower cathodic activity of the side-surfaces of AA2024-T3 indicates a lower cathodic activity (lower corrosion rate) in the side-surfaces, when compared to the large surfaces. Regarding AA2198-T351, the cathodic activity was also essentially decreased for the side-surfaces. However, an essential decrease (shift to less noble values) of the breakdown potential was noticed for the side-surfaces, when compared to the large surfaces of the same alloy that clearly highlights that the side-surfaces have higher tendency for a breakdown, nevertheless they support a lower cathodic activity.

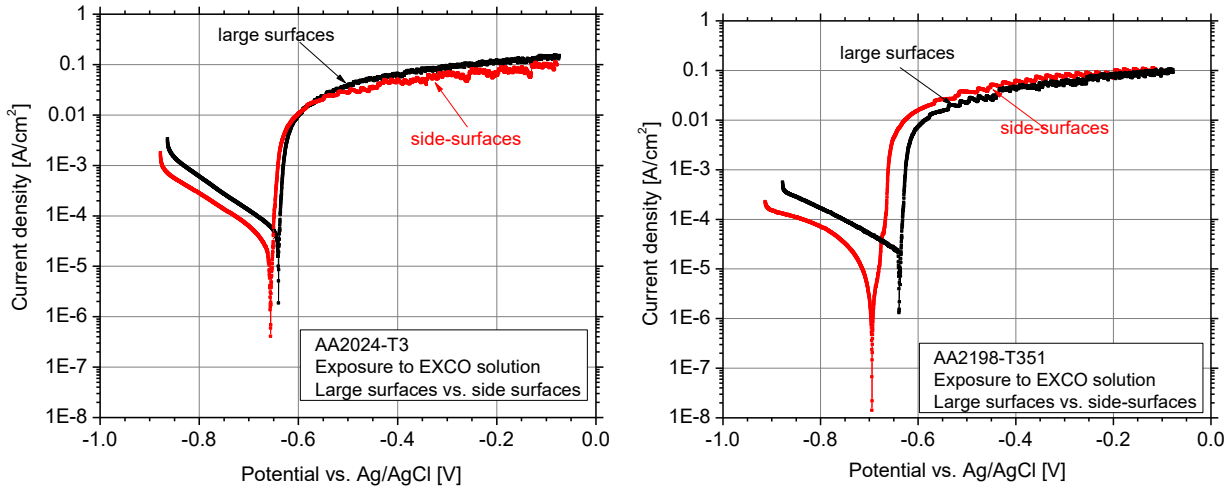

(a) (b)

Figure 3-14: Polarization curves of (a) AA2024-T3 and (b) AA2198-T351 specimens for large surfaces and side – surfaces exposed to EXCO solution.

The exposure of AA2198-T351 specimens to the corrosive environment (*e.g.*, EXCO solution in the present case) results in the deterioration of the surface of the specimens due to the nucleation of corrosion induced surface pits, Figure 3-15. For short exposure times and up to 2 hours, pitting formation on the corroded surfaces remains limited, *e.g.*, Figure 3-15(a). However, with increasing exposure time the pitting density and size tend to increase on both, large and small side-surfaces, *e.g.*, Figure 3-15(b) and Figure 3-15(c) for 6 and 12 hours of exposure, respectively. For even higher exposure times (≥ 24 hours), two cases of corrosion damage can be noticed: a) the formation of corrosion induced surface cracks on the small side-surfaces along with exfoliation on the large surfaces and b) the accumulated corrosion products on the large surfaces, *e.g.*, Figure 3-15(d) to Figure 3-15(f). Extensive pitting nucleation and subsequent crack formation on the small side-surfaces of the specimens confirms their high susceptibility to pitting corrosion attack, as was experimentally observed in Kamoutsi [78] and Pantelakis et *al.* [104]. Figure 3-16 shows several cross-sections of the pre-corroded specimens of AA2198-T351 for different exposure times. For the short exposure times, *e.g.,* up to 6 hours in Figure 3-16(a), the intergranular attack as well as the nucleation of cracks at the grain boundaries is evident for both large- and small side- surfaces of the specimens. For higher exposure times exfoliation corrosion mechanism is evident; delamination of the grain layers takes place for 24 hours of exposure (Figure 3-16(b)) due to the higher intergranular attack on the side-surfaces of the specimens and the subsequent formation of micro-cracks beneath the large surfaces. Likewise, for 72 hours exposure time it can be noticed that the nucleated micro-cracks on the small side-surfaces of the specimens lead to exfoliation corrosion of the large surfaces. Additionally, the higher depth of attack with increasing exposure time, especially from the side-surfaces, leads to the decrease of the effective thickness and width of the material (Figure 3-16(c)).

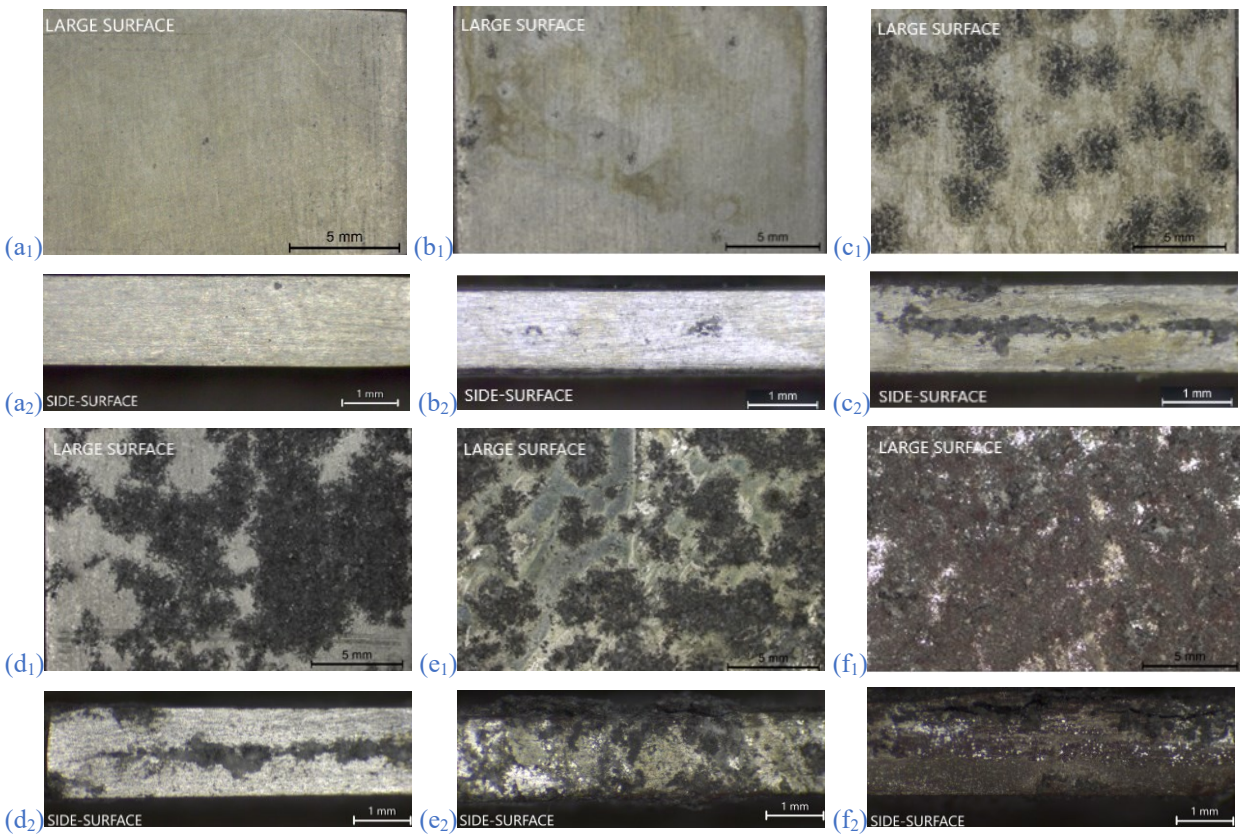

Figure 3-15: Typical photographs of the (1) large surfaces and (2) side surfaces of AA2198-T351 pre-corroded specimens for (a) 2 h, (b) 6 h, (c) 12 h, (d) 24 h, (e) 72 h and (f) 96 h exposure to EXCO solution.

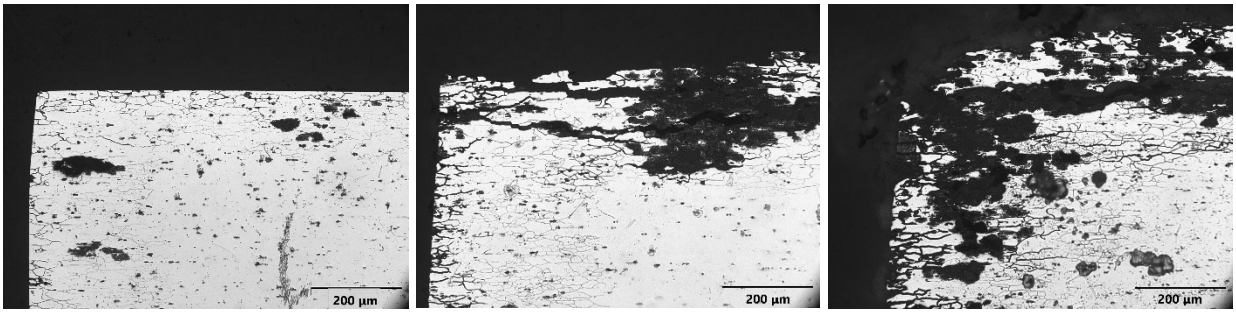

(a) (b) (c)

Figure 3-16: Typical microscopic photographs of pre-corroded specimens of AA2198-T351 for (a) 6 h, (b) 24 h and (c) 72 h of exposure to EXCO solution.

3.3.5.2 Mechanical evaluation of pre-corroded specimens

Typical tensile curves of the pre-corroded specimens of AA2024-T3 and AA2198-T351 for the different corrosion exposure times are presented in Figure 3-17. It is obvious that the corrosion exposure has a negative effect on both, axial nominal stress and axial nominal strain values of the specimens, with the highest decrease to be noticed for the axial nominal strain values with increasing exposure time to EXCO solution. Even for short exposure times, where the pitting corrosion mechanism is limited, *e.g.,* for 2 hours, a significant ductility decrease was observed for both investigated aluminium alloys. No significant decrease of the axial nominal stress values is evident

up to 6 hours corrosion exposure time for AA2198-T351; this was not the case for AA2024-T3 where a considerable decrease of the respective property can be noticed for the same exposure times. According to Alexopoulos et *al.* [49], any decrease in the maximum axial nominal stress of AA2024-T3 is related to the decrease of the effective thickness of the specimens, while in [48] several mechanical models were proposed to calculate the effective thickness of pre-corroded specimens. For even higher exposure times, especially after 24 hours where a transition from pitting to exfoliation corrosion damage on the large surfaces takes place, *e.g.,* Figure 3-15, an essential decrease on both, axial nominal strain and axial nominal stress values was observed and therefore the exposure times were arbitrarily marked as 'short exposure times' up till 24 hours and 'long exposure times' for times exceeded 24 hours corrosion exposure time.

The evaluation procedure of several mechanical properties derived from the tensile flow curves is marked in Figure 3-17. Nominal yield stress R_p can be identified in aluminium alloys where the transition from the elastic to the plastic regime is discrete in the flow curve, *e.g.,* see marked point in Figure 3-17(a). When nominal yield stress cannot be easily identified from the engineering stress-engineering strain curve, conventional yield stress $R_{p0.2\%}$ is often used for standardization purposes, where $R_{p0.2\%}$ refers to a specific stress value of the tensile flow curve that corresponds to 0.2% axial strain value, *e.g.*. see marked point in Figure 3-17(b). Additionally, elongation at fracture A_f is marked in Figure 3-17(a) evaluated from the fracture point and by removing the elastic deformation of the specimen. Hence, it represents the ability of the specimen/material for irreversible plastic deformation.

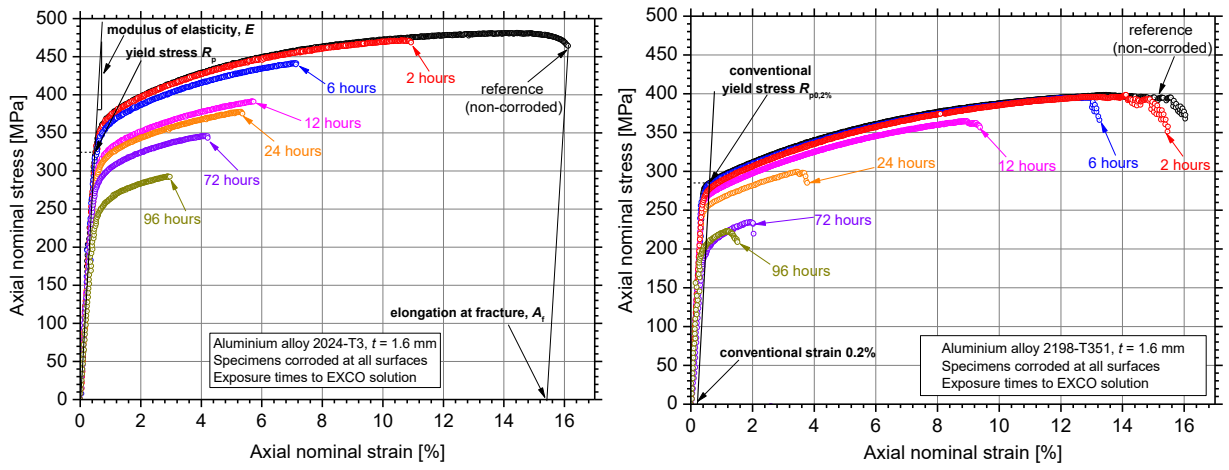

(a) (b)

Figure 3-17: Typical tensile curves of (a) AA2024-T3 and (b) AA2198-T351 specimens pre-corroded to all surfaces at the gauge length and for different exposure times to EXCO solution.

Figure 3-18(a) presents the experimental tests results of the nominal yield stress R_p as average values for the pre-corroded specimens of AA2198-T351. The experimental results were directly compared against the respective of AA2024-T351 reported in Pantelakis et *al.* in [87], for a sound

comparison between the two materials of the same temper (-T351). Available specimens of AA2024 in T3 temper were used in the present work for an extensive characterization of the corrosion mechanisms and mechanical properties degradation. The difference between T351 and T3 temper is based on the fact that T351 includes stress relief by cold work stretching. The strength properties of AA2024 are almost the same for the two different tempers with the elongation at fracture A_f to be higher for T351, *e.g.,* 20% instead of 18% for the T3 condition. Identical corrosion mechanisms were observed for the two tempers since the chemical composition is not affected by cold work strecthing.

The nominal yield stress R_p was selected to compare the already published data. Nevertheless, for the sound comparison of the experimental results of the present research work between sheets of the same thickness (AA2024-T3 against AA2198-T351), we have used the conventional yield stress $R_{p0.2\%}$ values, as according to the authors opinion, it turns to be more standarized and eliminates the factor of human error during the evaluation procedure.

Nominal yield stress R_p, seems to decrease exponentially with increasing exposure time to EXCO solution. It is obvious that for the short exposure times, the difference on the remaining percentage of R_p between the two investigated alloys is not considerable; however, AA2198-T351 presented higher corrosion resistance than AA2024-T351 by means of lower mechanical property decrease. Even after 12 hours corrosion exposure time, AA2198-T351 maintains more than 95% of the initial property; hence R_p remains almost unaffected by the corrosion exposure. On the contrary, an essential yield stress decrease of AA2198-T351 was noticed for long corrosion exposure times. At the longest exposure time, *e.g.*, 96 hours, the remaining percentage of R_p for AA2198-T351 was approximately 66%, while the respective value for AA2024-T351 was approximately 85%. Therefore, AA2198-T351 is considered to be superior than AA2024-T351 regarding yield stress decrease for short corrosion exposure times, where the pitting corrosion mechanism is evident, despite of the fact that AA2024-T351 has higher R_p values; similar behaviour was noticed in Alexopoulos et *al.* in [116] for the AA2198-T3 with 3.2 mm nominal sheet thickness. Further analysis of the corrosion behaviour for the short exposure times is of imperative importance since the slight observed pitting formation does not essentially affect the effective thickness of the specimens.

Experimental results of ultimate tensile strength R_m can be seen in Figure 3-18(b) as average values for the pre-corroded specimens of AA2198-T351; respective results for AA2024-T351 were retrieved from Pantelakis et *al.* [87]. Corrosion resistance of AA2198-T351 is superior to AA2024-T351 for short exposure times up to 24 hours, as slightly lower decrease of the ultimate tensile strength of the novel aluminium alloy was noticed. For instance, after 24 hours corrosion exposure time AA2198-T351 maintained approximately 82% of its initial value, while the residual percentage of R_m for AA2024-T351 was almost 77%. Nevertheless, AA2024-T351 presented higher corrosion

resistance for the long investigated exposure times, where exfoliation corrosion was the dominant degradation mechanism as was revealed by the microscopic examination in Figure 3-16; the residual R_m value is approximately 65% even after the highest exposure time (*e.g.*, 96 hours) whereas the respective value of AA2198-T351 was almost 50%. Furthermore, it was noticed that the residual R_m values reached at a plateau after 48 hours exposure time for both aluminium alloys, meaning that further corrosion exposure will not reduce the R_m essentially; this is evidence of maximum depth of attack of the surface corrosion-induced cracks [85].

Figure 3-19 shows the experimental results of elongation at fracture A_f of the investigated alloy against the respective conventional alloy from Pantelakis et *al*. in [87]. It is evident that A_f decreases exponentially with increasing exposure time to EXCO solution for both investigated aluminium alloys. AA2024-T351 presents higher tensile ductility ($A_f \approx 18.5\%$) than AA2198-T351 ($A_f \approx 15.5\%$) when non-corroded. However, AA2198-T351 presents higher corrosion resistance regarding the A_f decrease when compared to AA2024-T351 as well as to AA2024-T3 for the short corrosion exposure times. For instance, after only 2 hours of exposure, the remaining percentage of A_f value for AA2024-T351 is approximately 32%, while the respective percentage for AA2198-T351 is approximately 96%, almost remaining unaffected. As can be seen in Figure 3-20, the decrease rate of elongation at fracture is lower for the case of AA2198-T351 for short corrosion exposure times, where the property values were found to be ranging from 50 to 100% higher than the respective of AA2024-T351, confirming the superiority of the investigated Al-Cu-Li alloy. The A_f decrease for the selected exposure times can be atrributed to the well-established hydrogen embrittlement phenomenon for AA2024, *e.g.,* [78] and [104], since the pitting corrosion mechanism rather remains limited [87]; however, this phenomenon is a matter of current investigation for the case of AA2198. On the other hand, for the long corrosion exposure times, where excessive micro-cracks formation as well as exfoliation occured, a high ductility decrease was noticed for AA2198-T351 that almost reached the AA2024-T351 respective ductility values while higher decrease than AA2024-T3 is evident that is attributed to the stretch forming of T351 temper. For the highest exposure time of 96 hours, the residual percentage of A_f for AA2198-T351 was approximately 8%, on the contrary of only 3% remaining A_f for AA2024-T351. Furthermore, it was observed that after 48 hours exposure time, the elongation at fracture of AA2198-T351 reached at a plateau and further corrosion exposure did not decrease the tensile ductility considerably.

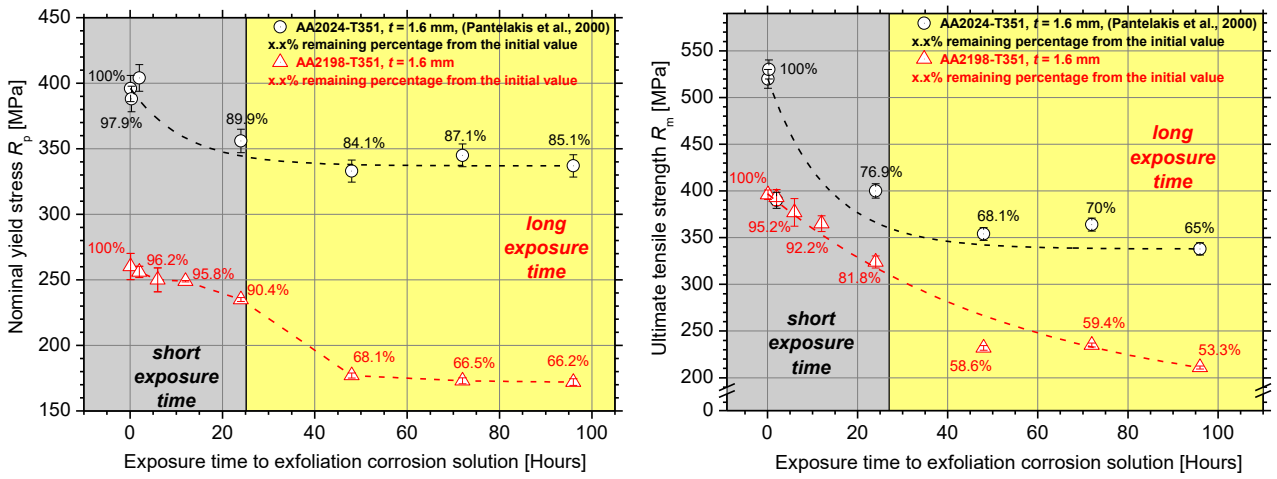

(a) (b)

Figure 3-18: Experimental results of (a) nominal yield stress Rp and (b) ultimate tensile strength Rm of AA2198-T351 specimens compared with the respective of AA2024-T351 for different corrosion exposure times.

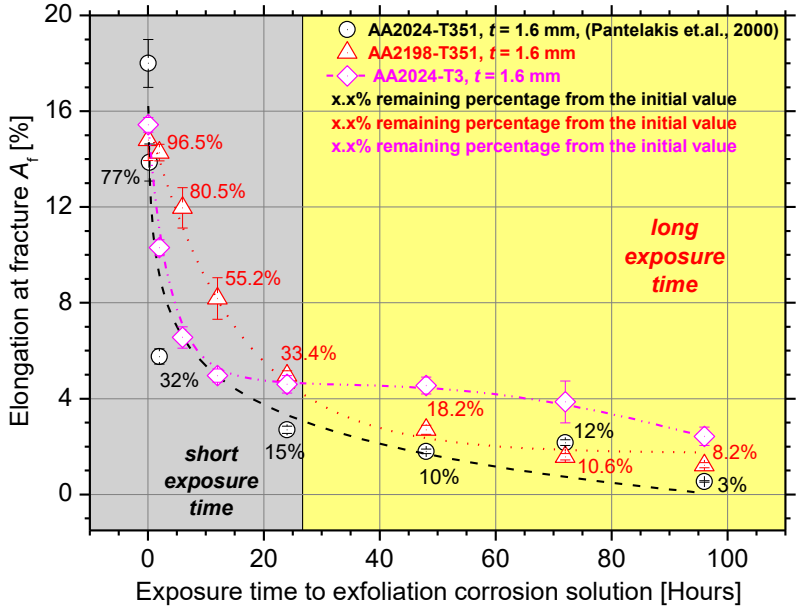

Figure 3-19: Experimental elongation at fracture A_f results of AA2198-T351 specimens compared with the respective of AA2024-T351 and AA2024-T3 for two different tempers and for different corrosion exposure times.

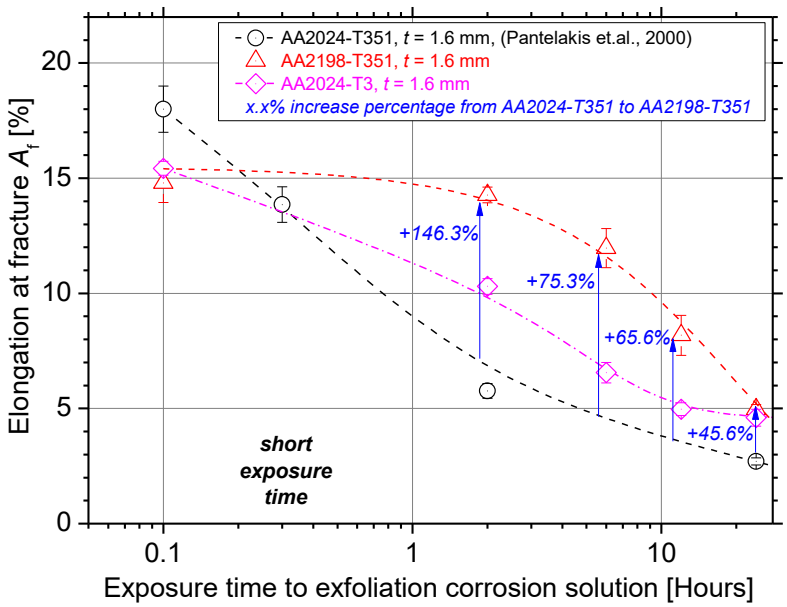

Figure 3-20: Experimental elongation at fracture A_f results of AA2198-T351 specimens compared with the respective of AA2024 for two different tempers (-T3 and -T351) and for short corrosion exposure times.

Fatigue tests results of pre-corroded AA2198-T351 specimens are presented in Figure 3-21 in the form of applied stress (*S*)-fatigue cycles (*N*). In the same figure, *S*-*N* curves for similar materials available from Alexopoulos et *al.* in [115] were also added. Kermanidis et *al*. [67] conducted fatigue tests of AA2024-T351 of 1.6 mm nominal thickness and stress ratio $R = 0.1$. It can be seen that the *S*-*N* curves present qualitatively similar behaviour with the investigated aluminium alloy; AA2198 is superior to AA2024 in fatigue behaviour in high cycle fatigue regime as approximately 70% to 100% higher number of cycles to fracture were noticed for the same applied stress. For the case of fatigue endurance limit, this enhacement is approximately 40% higher, since more than 65 MPa difference was noticed. Fatigue cycles to fracture were decreased by approximately 85% when the specimens of AA2198-T351 were pre-exposed to the EXCO solution for 6 hours. Additionally, the fatigue endurance limit was decreased by approximately 50% due to the same corrosion exposure. This corrosion-induced fatigue life degradation can be attributed to the elimination of the fatigue crack initiation phase due to the presence of corrosion pits higher than 400 μm in depth as well as to the hydrogen embrittlement phenomenon; similar behaviour was observed in Kermanidis et *al.* in [67] and Guerin et *al.* in [82].

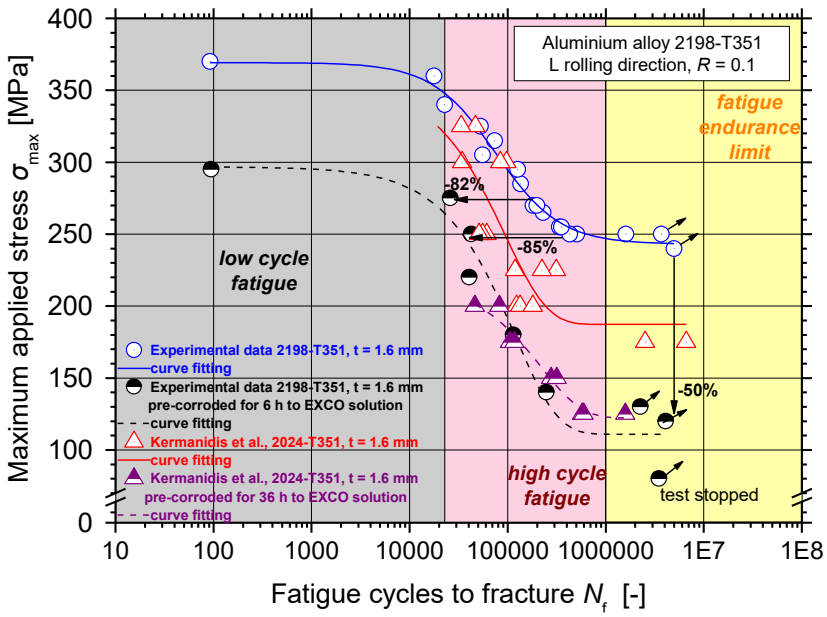

Figure 3-21: Fatigue S-N curves of non- and pre- corroded specimens of AA2198-T351 and comparison against AA2024-T351.

3.3.5.3 Evaluation of fractured specimens

Stereoscopical examination on the fractured, pre-corroded specimens of AA2198-T351 revealed that the pitting corrosion mechanism is limited for the very short corrosion exposure times up to 2 hours, Figure 3-22. A ductile fracture mechanism is evident from the 45˚ slope of the fracture surface and respective shear lips, *e.g.,* Figure 3-22(a). After 6 hours exposure time, a slight increase in pitting density was observed on both large and small side-surfaces with no essential difference between the two surfaces, *e.g.,* Figure 3-22(b). A mixed-mode fracture was presented, showing signs that the fracture mechanism has altered; moderate shear fracture, possibly originating from small side-surfaces corrosion products and essential shear lips on the back surface of the specimen were formed. From the side-surface view, fracture resembling cup and cone geometry can be noticed. Severe surface pitting is evident for higher exposure times, as can be seen in Figure 3-22(c) and Figure 3-22(d) for 24 and 48 hours exposure time, respectively; thus, with increasing corrosion exposure time significant increase of pitting density and size was detected, revealing the heavily corroded areas that cracks nucleate, coalesce and are transformed into cracked areas. Additionally, it was noticed that fracture cracks seem to be initiated from the edge pits and are propagated along the way of the nearest pit. However, higher pitting density and subsequent crack formation was detected at the side-surfaces, confirming their higher susceptibility to corrosion attack, *e.g.,* Figure 3-22(c) and Figure 3-22(d). Fracture mechanism seems to be consistent along with surface pits formation; fracture begins from corrosion-damaged areas, preferably on the edges at the side-surfaces of the specimens. Then fracture crack path follows the easiest way to propagate, *i.e.*, through other corrosion-cracked areas, thus minimizing the capability of the specimens to plastic deformation.

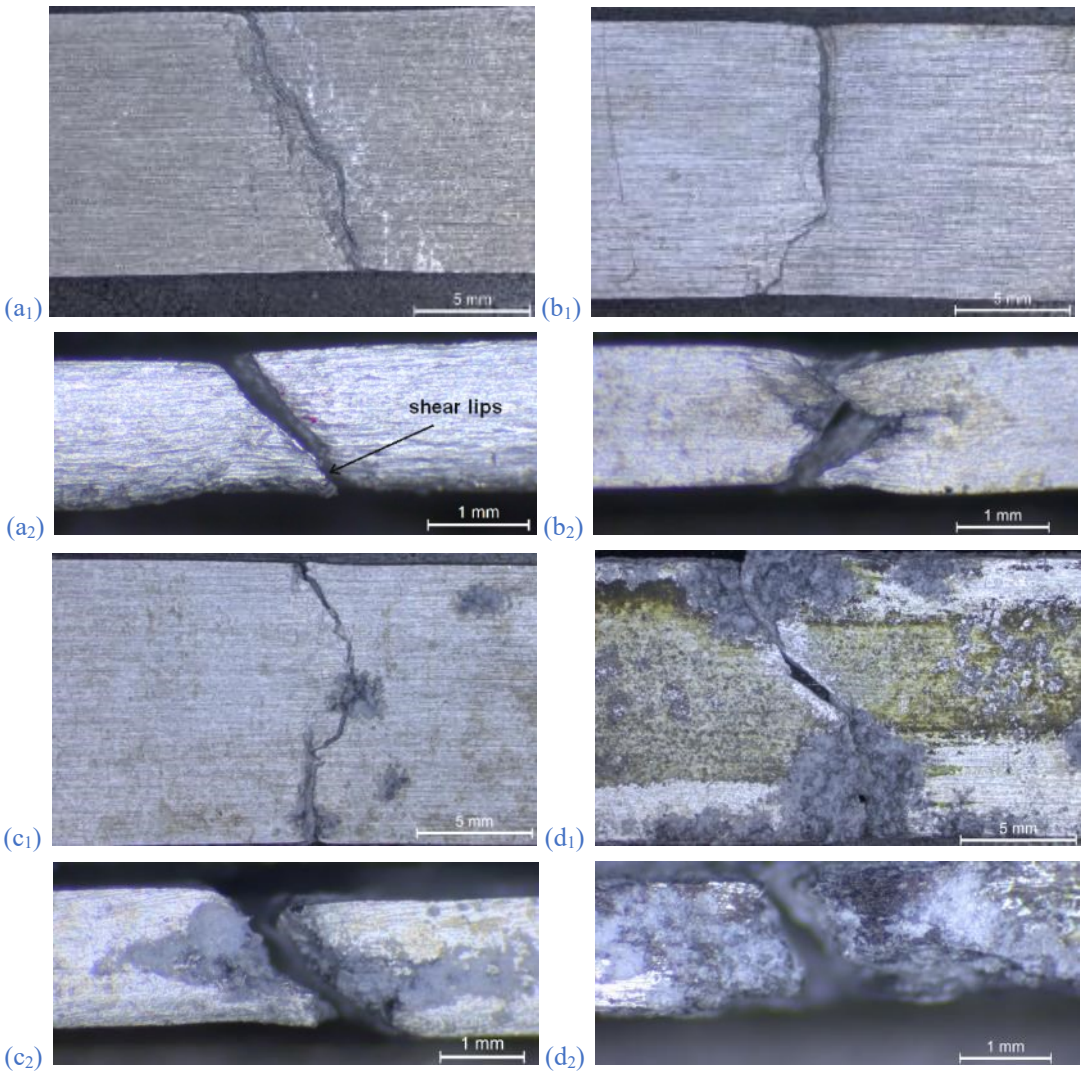

Figure 3-22: Typical stereoscopical photographs of fractured AA2198-T351 specimens, pre-corroded at all surfaces for (a) 2 h (b) 6 h (c) 24 h and (d) 48 h and (1), (2) corresponds to large and side - surfaces of the tensile specimen.

The tensile test results revealed that the materials suffered significant corrosion-induced ductility degradation. In relevant publications by Alexopoulos et *al.* in [48] and [49], it was found that this degradation in AA2024-T3 can be attributed to the formation of corrosion-induced surface micro-cracks and the subsequent decrease of the effective thickness as well as to hydrogen diffusion and subsequent embrittlement. Figure 3-23 shows SEM images of pre-corroded, fractured tensile specimens of AA2024-T3 with nominal thickness of 3.2 mm from a previous article of the authors [63] in order to compare the corrosion morphology of the fracture surfaces between the two materials. Figure 3-23(a) present a general view of the fracture surface of the specimen pre-corroded for 2 hours, where a ductile-based fracture mechanism is evident from the 45° inclination. Figure 3-23(b) shows the large corroded surface with a few corrosion pits as well as edge notches due to accumulative straining. Additionally, signs of de-alloying of some intermetallic particles (white spots) are evident. Pitting corrosion is more pronounced on the small side-surfaces as can be seen from Figure 3-23(c) and Figure 3-23(d) for the large and small side-surfaces, respectively. It is worth mentioning that the

pits were all concentrated on the mid thickness of the specimen. Detail of a corroded area on the large surface, *e.g.,* Figure 3-23(e), reveals the formation of micro-cracks at the edges of the pits as well as signs of plastic deformation. Excessive surface pitting, higher pitting density as well as micro- cracks resulting from the pits coalescence due to axial straining are evident on the small side-surface, Figure 3-23(f). Corrosion onset was noticed within grain boundaries for small exposure time (*e.g.,* 2 hours) and for higher exposure time, linking of the corrosion sites along with cracking between grain layers and multilayers was noticed. Corrosion products in between the grain layers tend to expand with increasing corrosion exposure and therefore they act as wedges that result in leafing and the complete loss of sheet thickness integrity. Similar results were noticed by Posada et *al.* in [35] for AA2024 of approximate the same thickness 1.81 mm sheet alloy.

Pre-corroded specimens of AA2198-T351 were examined with the aid of scanning electron microscopy (SEM) in order to investigate the tensile ductility degradation mechanism. SEM images presented in Figure 3-24 show the fracture surfaces of pre-corroded tensile specimens when corroded for 2- and 6 hours exposure time and without covering of the side-surfaces. Figure 3-24(a) present a general view of the fracture surface of the specimen corroded for 2 hours; a ductile-based fracture mechanism is evident from the 45˚ slope of the fracture surface. Several corrosion pits can be noticed on the large surfaces of the specimen, while only a few are evident at the edges of the small side-surfaces, *e.g.,* Figure 3-24(b). The specimen suffered heavily from plastic deformation that the strain gradients are also evident in the surface. A magnification of a pit on the large surface revealed plastic deformation as well as micro-cracks nucleation at the edges of the pit due to straining, *e.g.*, Figure 3-24(c). Figure 3-24(d) gives a general view of the fracture surface of the specimen corroded for 6 hours, where a ductile fracture mechanism is still evident from the 45˚ slope of the fracture surface. Fewer surface pits are evident on the specimen large surface while severe pitting corrosion as well as crack formation can be noticed on the side-surfaces, revealing their high corrosion susceptibility. Several corrosion pits with varying depths of attack as well as corrosion-induced cracks can be noticed in Figure 3-24(e). Plastic deformation at the edges of the side-surface pits was observed, proving that additionally to corrosion-induced cracks, cracking due to the plastic deformation occurred. It is obvious that the small side-surfaces exhibited sights of higher plastic deformation than the large surfaces of the specimens. A corrosion pit higher than 400 μm in depth can be noticed on the specimen side-surface as well as rugged surfaces below it Figure 3-24(f), corresponding to quasi-cleavage fracture mechanism probably due to the hydrogen embrittlement as was also mentioned in Kamoutsi et *al.* in [136] for the AA2024. Furthermore, the nucleation of several micro-cracks at the end of the pit and their subsequent coalescence due to the heavily straining is evident. Several dimples

can be noticed beyond these smooth surfaces and towards to the centre of the specimen that reveals a ductile fracture mechanism, Figure 3-24(g).

Performed microstructural analysis for higher exposure times did not result in higher depth of attack of the corrosion-induced cracks from the side-surfaces. Hence, it can be resulted that the concept of possible propagation of exfoliation in the side surfaces because of the hard products of corrosion that create wedging stresses is rather limited in this alloy. One possible explanation is the high damage tolerance capability of Al-Cu-Li alloy that in microscopic level is possibly transferred by high intergranular fracture energy that results in low crack propagation in the parallel boundaries along the rolling direction.

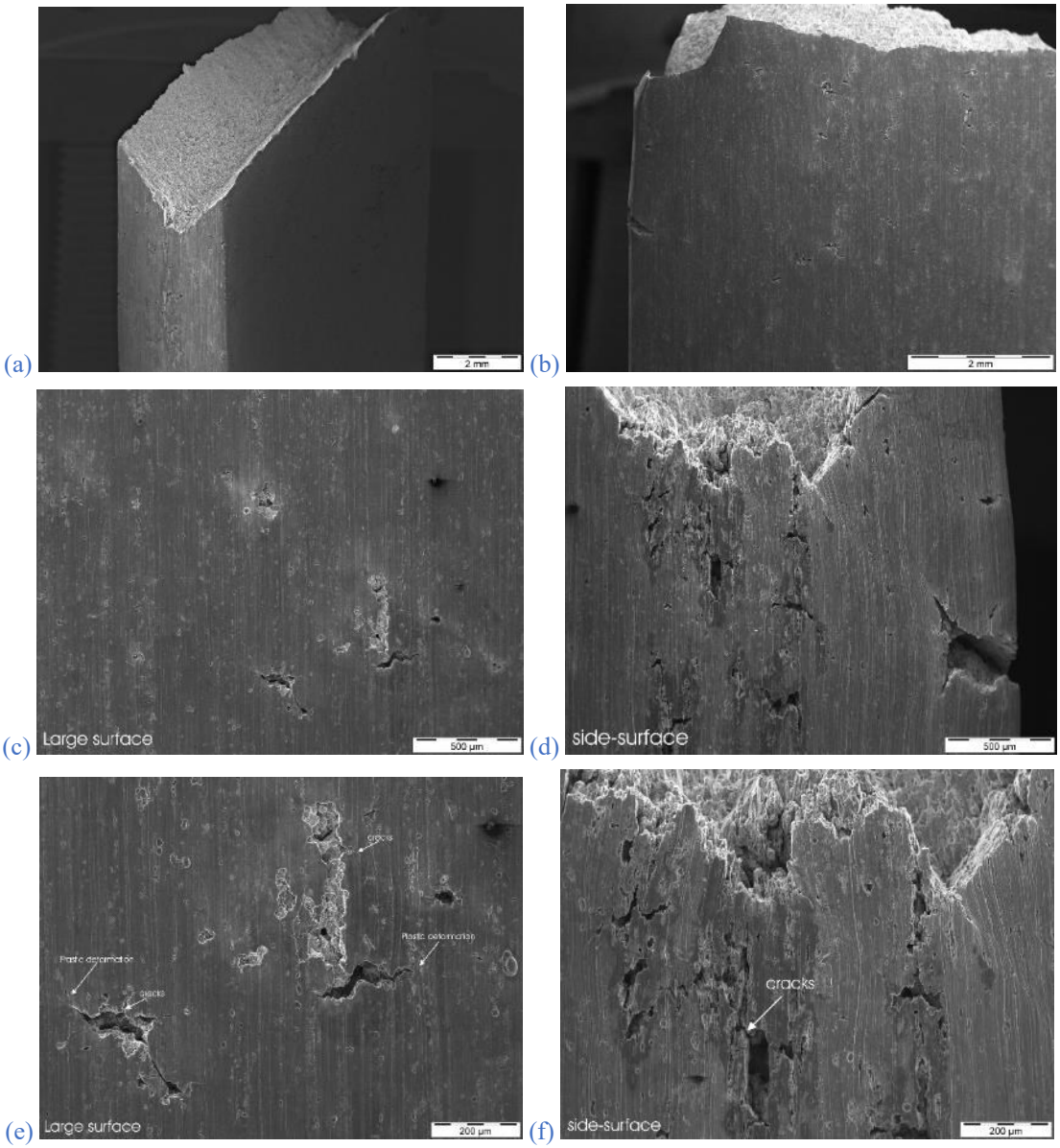

Figure 3-23:SEM images of AA2024-T3 specimens corroded at all surfaces for 2 h exposure time [63].

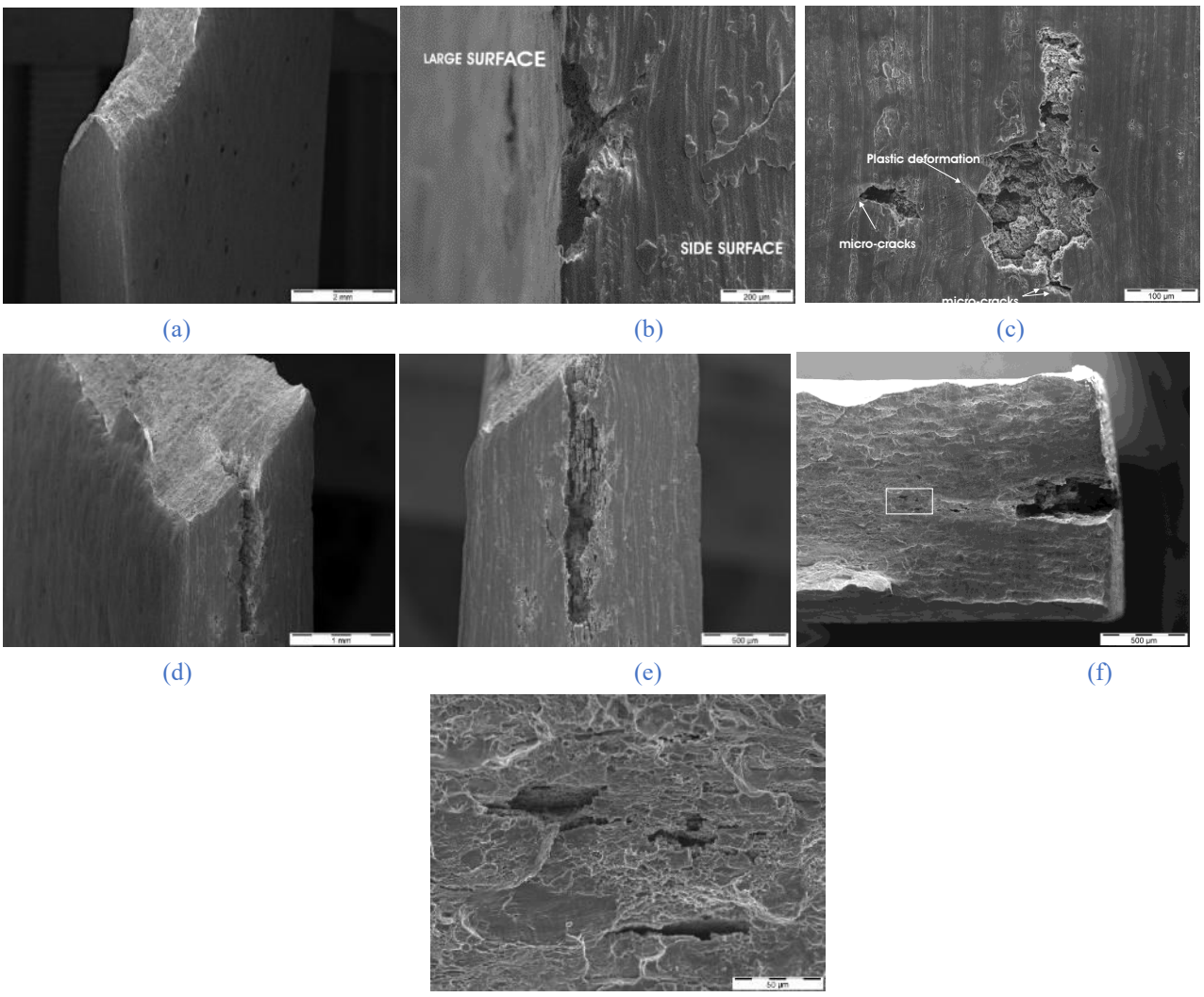

(a) (b) (c)

(d) (e) (f)

(g)

Figure 3-24: SEM images of AA2198-T351 specimens corroded at all surfaces for (a) to (c) 2h and (d) to (f) 6 h exposure time and (g) higher magnification of the captured area in (f).

3.3.5.4 Contribution of the side-surfaces cracks to corrosion resistance

In this section, the experimental tensile tests results for the AA2024-T3 and AA2198-T351 specimens corroded at large surfaces only, are described. A comparison against the results of the specimens corroded at all surfaces was performed, in order to estimate the contribution of the side-surfaces to corrosion-induced mechanical properties degradation as according to previous works, corrosion effect was found to be more aggressive on the side-surfaces of the specimens, *e.g.,* [35], [78], [87], [104]. Figure 3-25 shows typical tensile curves of AA2024-T3 and AA2198-T351 specimens corroded at large surfaces only. These tensile specimens exhibit less corrosion-induced decrease of axial nominal stress and strain values than specimens corroded at all surfaces for the same corrosion exposure time. A considerable decrease in strain was noticed for both investigated aluminium alloys even for the short exposure times, *e.g.,* 2 hours, where no significant surface attack is evident that will be discussed in the following. However, no essential stress decrease was evident up to 12 hours corrosion exposure time for AA2198-T351, while the respective decrease was

observed after only 2 hours of exposure for the specimens corroded at all surfaces. For the case of AA2024-T3 an essential stress drop was observed after the 2 hours corrosion exposure time that was attributed to the reduction of the effective thickness, according to Alexopoulos et *al.* in [63].

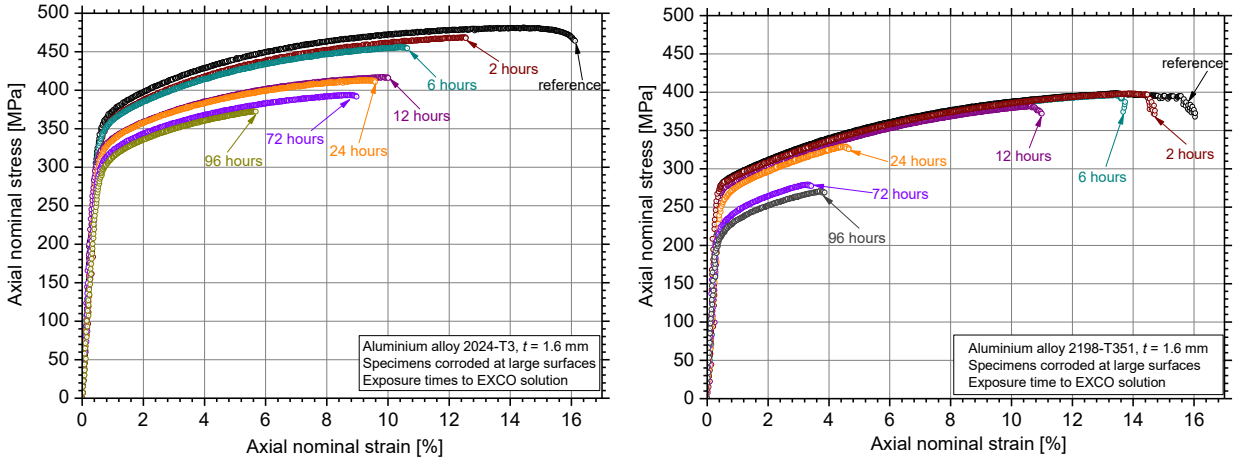

(a) (b)

Figure 3-25: Typical tensile curves of AA2024-T3 (left) and AA2198-T351 (right) specimens corroded at large surfaces only and for different exposure times to EXCO solution.

Figure 3-26 presents some typical photographs of the fractured specimens, corroded at large surfaces for different corrosion exposure times. Similar to the specimens corroded at all surfaces, the surface pitting formation is limited for the very short exposure times, *e.g.*, Figure 3-26(a). The typical ductile fracture is evident from the 45˚ slope of the fracture surface even after 6 hours exposure time, *e.g.*, Figure 3-26(b). It is obvious that specimens suffered heavily plastic deformation. When comparing Figure 3-22 with Figure 3-26, it can be noticed that the specimens corroded at large surfaces have higher deformation capability than the specimens without covering. Cracking and corrosion products are absent from the mid-thickness due to masking. In the cases of heavily corroded specimens (*e.g.,* 24 and 48 hours) in Figure 3-26, starting fracture point was located at the corroded sites at the edges of the specimen. The fracture path follows the nearest pits, minimizing fracture energy as also noticed for the specimens without covering of the side-surfaces.

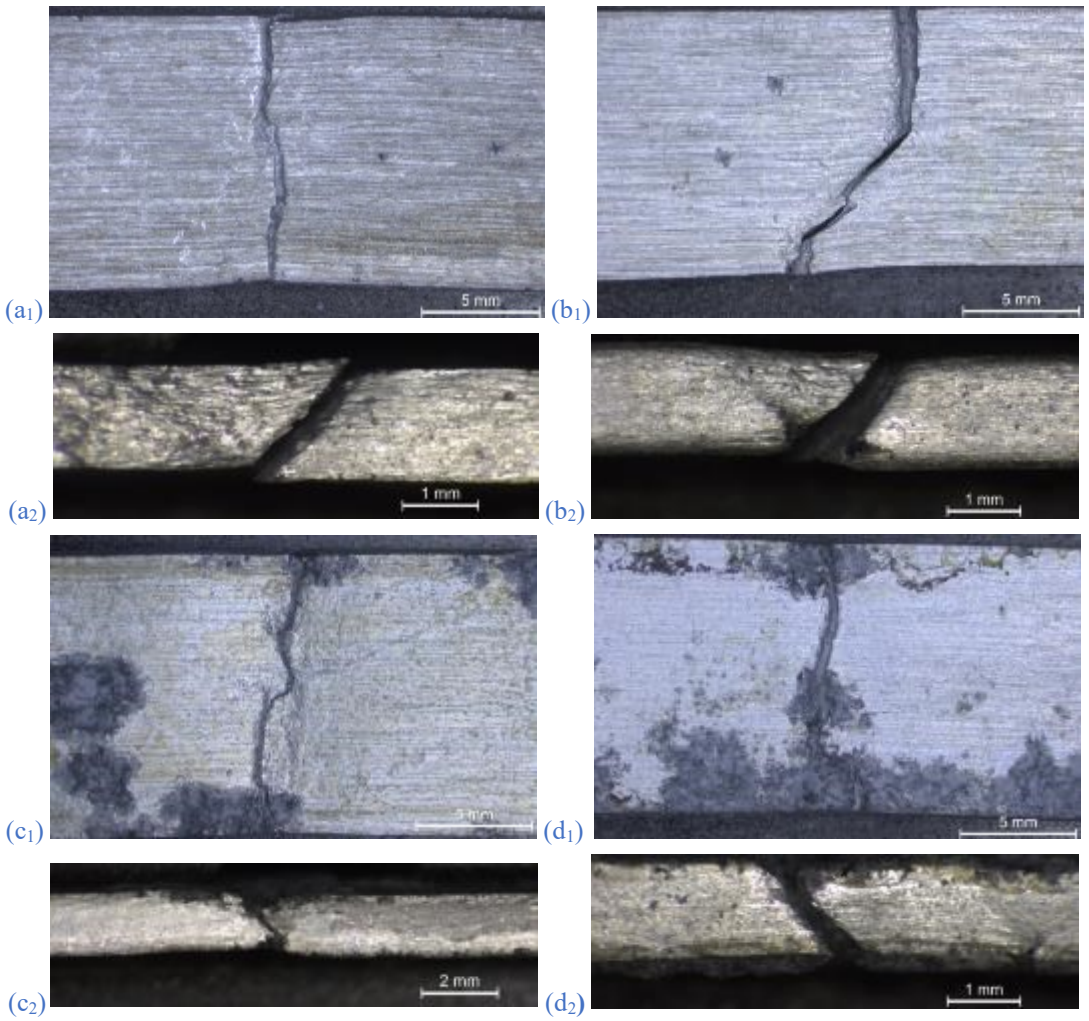

Figure 3-26:Typical stereoscopical photographs of AA2198-T351 specimens corroded at large surfaces after the tensile tests for (a) 2 h (b) 6 h (c)24 h and (d) 48 h of exposure for (1) large surfaces and (2) side-surfaces of the specimens.

Figure 3-27 shows the corrosion-induced degradation of the conventional yield stress $R_{p0.2\%}$ for the specimens corroded at large surfaces only and were directly compared against specimens corroded at all surfaces of AA2024-T3 (left) and AA2198-T351(right), respectively. For the short exposure times and up to 24 hours, there is not an essential difference in the residual conventional yield stress $R_{p0.2\%}$ between the two types of corroded specimens for both aluminium alloys. However, specimens corroded at large surfaces exhibited higher corrosion resistance for the same exposure times, in terms of less corrosion-induced decrease of the mechanical property. It can be noticed that $R_{p0.2\%}$ of AA2024-T3 decreases at higher rates than the respective of AA2198-T351 with increasing corrosion exposure time. An improvement of the remaining percentage of $R_{p0.2\%}$ by approximately 2% was noticed for both aluminium alloys at the short exposure times regime by simply covering of the specimens side-surfaces. On the contrary, for the long exposure times where excessive micro-cracks nucleation on the side-surfaces as well as exfoliation on the large surfaces take place, a considerable difference in the residual $R_{p0.2\%}$ values due to the covering of the side-surfaces was noticed. For instance, at the highest exposure time of 96 hours, the effect of covering of the side-surfaces resulted

in an approximate 14% increase in the residual $R_{p0.2\%}$ values for the AA2198-T351 and 18% for AA2024-T3, respectively. It is worth to mention that, after 48 hours of corrosion exposure the $R_{p0.2\%}$ of AA2198-T351 reach a plateau for both types of corroded specimens and further exposure to the EXCO solution does not decrease this mechanical property considerably; this is evidence of maximum depth of attack of the surface corrosion-induced cracks [85]. For the case of AA2024-T3, remaining $R_{p0.2\%}$ values of specimens corroded at all surfaces continuously decreases; hence, with increasing exposure time the difference in the residual $R_{p0.2\%}$ values between the two types of corroded specimens tend to increase. Therefore, it can be concluded that the side-surfaces are more susceptible to pitting corrosion attack as they effectively contribute to the mechanical properties degradation; a qualitative observation, without providing any quantitative measurements, were noticed for AA2024 in Kamoutsi in [78] and Pantelakis et *al.* in [104]. The susceptibility of the side-surfaces to corrosion attack can be attributed to the long elongated grains in longitudinal (L) rolling direction as well as to the higher density of grain boundaries due to the rolling process; consequently, it is easier for the corrosive solution to penetrate between the grain boundaries [35]. Likewise, Li et *al.* in [119] attributed the corrosion susceptibility of Al-Cu-Li alloys to the precipitation of T_1 phase on the grain boundaries, thus forming galvanic cells and subsequent pitting corrosion.

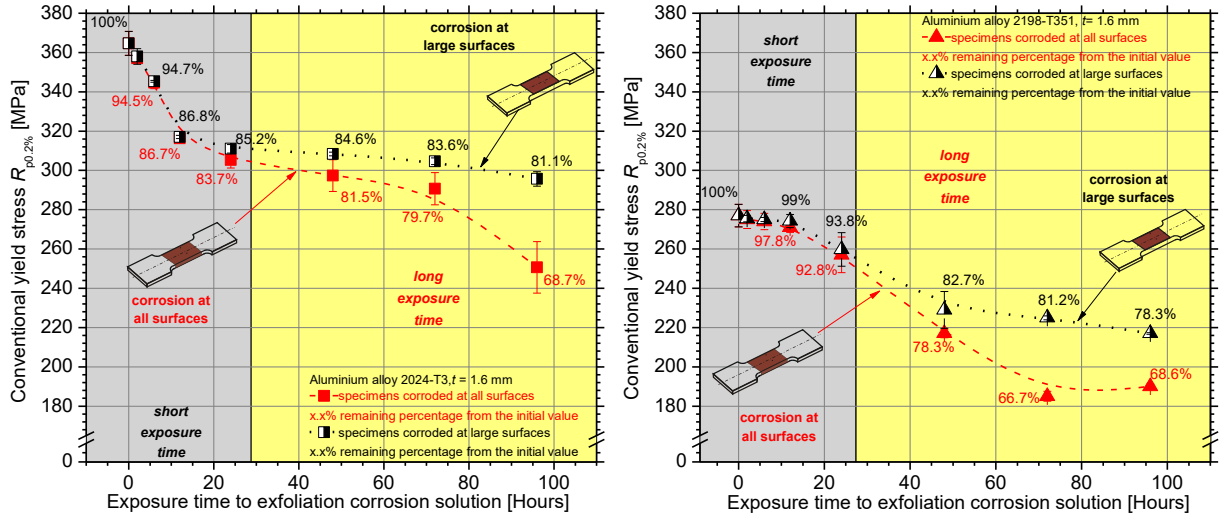

Figure 3-27: Comparison of conventional yield stress $Rp_{0.2\%}$ of specimens corroded at all surfaces and specimens corroded at large surfaces for AA2024-T3 (left) and AA2198-T351 (right).

Figure 3-28 shows the comparison of ultimate tensile stress R_m decrease between the pre-corroded specimens of AA2024-T3 and AA2198-T351 with and without covering of the side-surfaces. For the short exposure times (< 24 hours), where the micro-cracks formation is limited, the specimens corroded at large surfaces exhibited slightly higher corrosion resistance as approximately 3% increase in the residual R_m value was noticed. On the contrary, the effect of covering of the side-surfaces on the residual R_m was essential for the long exposure times where severe micro-cracking and exfoliation

corrosion are evident; approximately 28% increase on the residual R_m value after 96 hours of exposure was attributed to the covering of the side-surfaces. Covering the side-surfaces of the AA2024-T3 specimens contributed to an essential increase on the residual ultimate tensile stress values even for the short corrosion exposure times, *e.g.,* approximately 8% after 24 hours of exposure. With increasing exposure time, the difference on the residual R_m values between specimens corroded at large- and at all surfaces tend to increase and reach the respective value of AA2198-T351 for the highest exposure time, *e.g.,* 28%. Thus, it can be easily concluded that the side-surfaces are preferable for the nucleation of pitting corrosion.

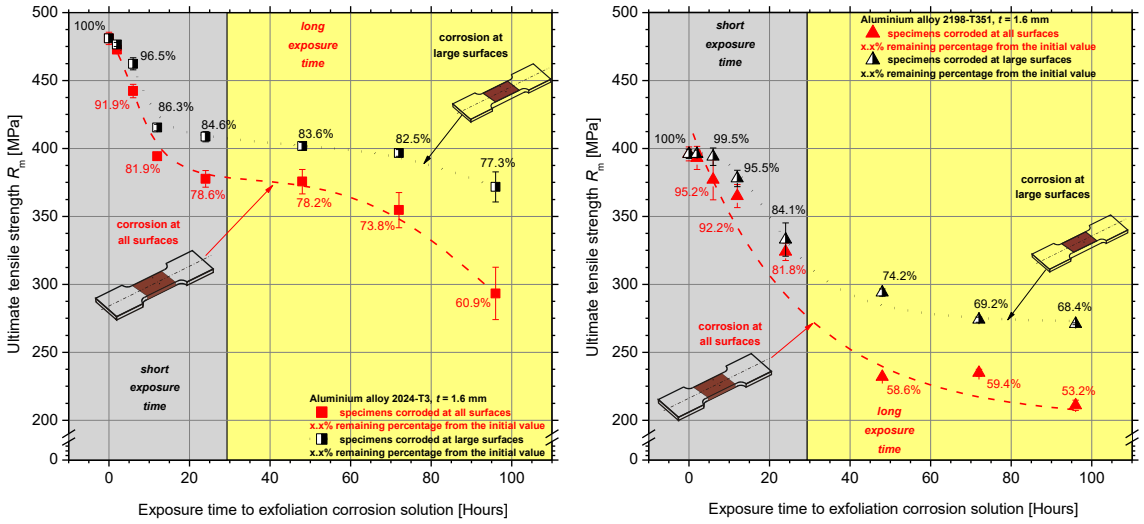

Figure 3-28: Comparison of ultimate tensile strength R_m of specimens corroded at all surfaces and specimens corroded at large surfaces for AA2024-T3 (left) and AA2198-T351 (right).

The effect of covering of the side-surfaces on the residual elongation at fracture A_f for the two investigated aluminium alloys can be seen in Figure 3-29. Elongation at fracture decreases exponentially with increasing exposure time to the EXCO solution for both types of specimens. Specimens corroded at large surfaces presented higher corrosion resistance in terms of lower A_f decrease than specimens corroded at all surfaces. Covering of the specimens side-surfaces contributed to an increase on the residual A_f values either for AA2024-T3 or AA2198-T351; however, for the case of AA2198-T351, corrosion damage on the side-surfaces does not essentially affect the elongation at fracture for the short exposure times (< 24 hours). Even though that cracking nucleation from corrosion pits takes place on the side-surfaces, they do not influence the capability of specimens for plastic deformation.

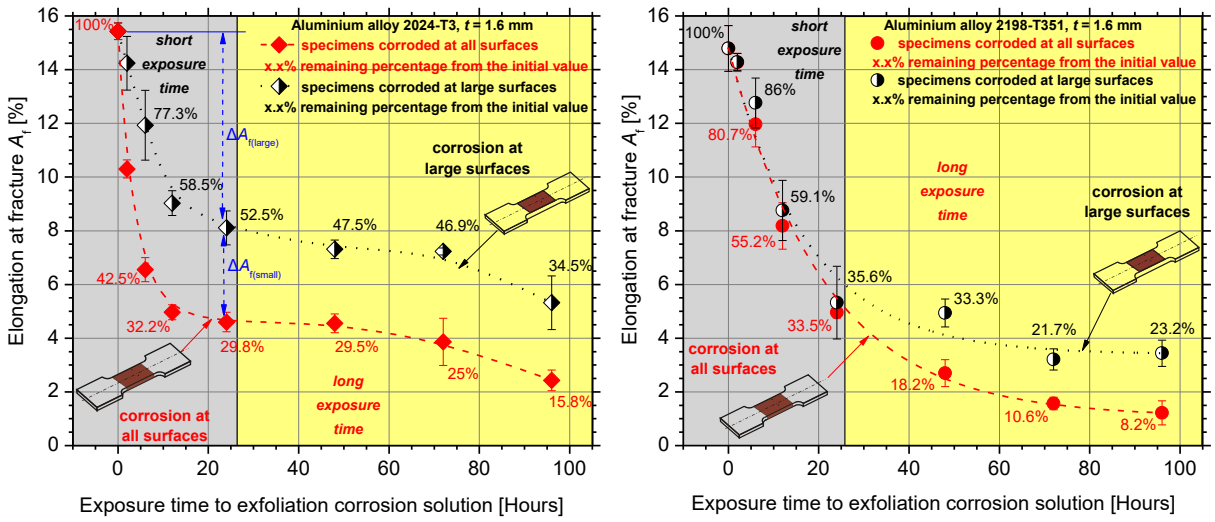

Figure 3-29: Comparison of elongation at fracture A_f of specimens corroded at all surfaces and specimens corroded at large surfaces for AA2024-T3 (left) and AA2198-T351 (right).

The mechanism to address this phenomenon is related to the corrosion potential and susceptibility to corrosion degradation of the Al-Cu-Li alloy itself. Corrosion products are preferentially formed at the side surfaces for short exposure times due to possibly high density of grain boundaries as well as of precipitates parallel to rolling direction. The corrosion products tend to expand with increasing corrosion exposure time and act as wedges to introduce a stress field that accelerate in-plane intergranular cracks. Measurements of the depth of corrosion-induced cracks performed on the pre-corroded specimens cross-sections were performed with the aid of light optical microscopy, as can be seen in Figure 3-30 and Figure 3-31 for AA2024-T3 and AA2198-T351, respectively. The above described mechanism is the prevailing degradation mechanism for short exposure times up to 6 hours, where an essential depth of attack on the side-surfaces higher than the respective on large surfaces was measured, Figure 3-32. For higher exposure times, a plateau in corrosion-induced degradation due to side-surfaces attack is noticed for AA2198-T351 and therefore this might be attributed to either the absence of copper-rich precipitates in the in-plane parallel boundaries, due to unstable Cu-rich clusters and the subsequent liberation of Cu as was revealed for Al-Cu-Li alloys in Bucheit et *al.* in [164] as well as in Li et *al.* in [165], or from the mechanics point of view to the high capability for damage tolerance that deals with crack arrest or crack retardation due to the complex grain structure. This is also evident in Figure 3-32, where the depth of side-surfaces cracks after 6 hours of exposure is lower than the respective of the large surfaces and a plateau in the crack depth is noticed. In general, it is noticed that the depth of corrosion-induced cracks is higher for AA2024-T3 than AA2198-T351 for both the specimens corroded at large surfaces and specimens corroded at all surfaces. Depth of corrosion-induced cracks increases linearly up till 12 hours corrosion exposure time for both types of corroded specimens of AA2024-T3 while for the case of AA2198-T351 depth of cracks on the large surfaces increases linearly in contrary to side-surfaces where the depth is almost stabilized up till 12

hours of exposure, giving evidence that side-surfaces attack does not affect the specimens mechanical properties significantly.

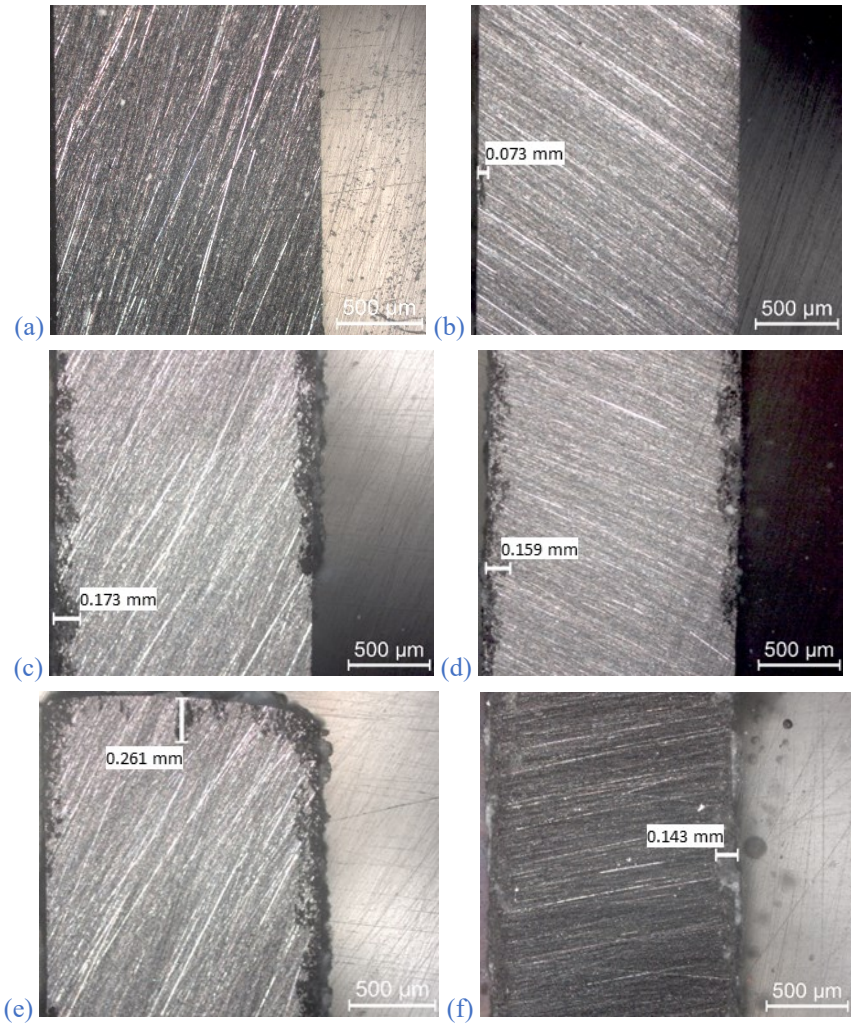

Figure 3-30: Cross - sections of AA2024-T3 specimens corroded at all surfaces (left column) and large surfaces (right column) for (a) – (b) 2 h, (c) – (d) 12 h and (e) – (f) 24 h of corrosion exposure.

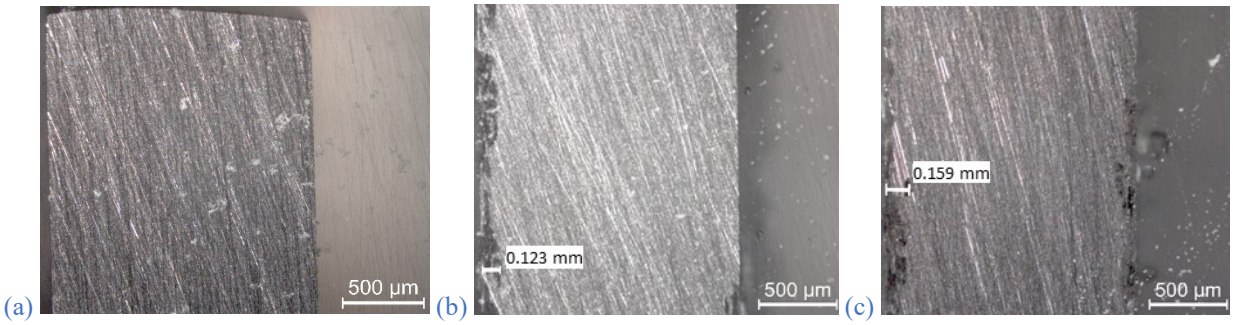

Figure 3-31: Cross-sections of AA2198-T351 specimens corroded at all surfaces for (a) 2 h, (b) 12 h and (c) 24 h of corrosion exposure.

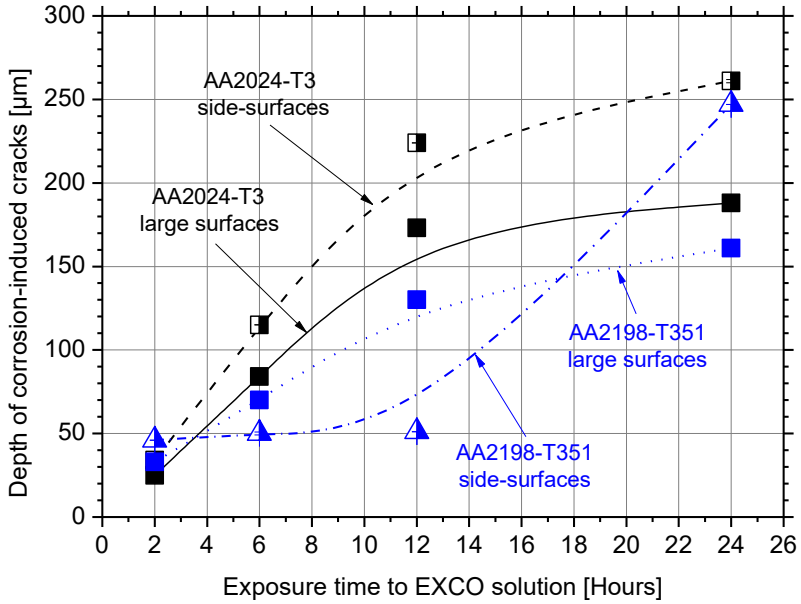

Figure 3-32: Depth of attack on large surfaces and side - surfaces for different exposure times to EXCO solution.

As shown in Figure 3-29, the side-surfaces corrosion exposure on AA2024-T3 plays a significant role on the tensile elongation at fracture even for the short corrosion exposure times; the A_f of specimens corroded at large surfaces only decreases in essentially lower rate than the respective of specimens corroded at all surfaces. The severity of the corrosion exposure of the two different surfaces (large- and side-) on the elongation at fracture decrease ΔA_f was quantified by assuming that the total elongation at fracture decrease $\Delta A_{f(all)}$ is attributed to the ductility decrease by the corrosion-induced degradation on the large surfaces $\Delta A_{f(large)}$ as well as to the ductility decrease by the corrosion-induced degradation on the small surfaces $\Delta A_{f(small)}$. This consideration can be expressed by the following equation as:

$$\Delta A_{f(all)} = \Delta A_{f(large)} + \Delta A_{f(small)}, \qquad (3\text{-}10)$$

while the concept of this consideration can be graphically seen with marked arrows in Figure 3-29. This consideration is logical, since each surface (large- or small-) that is exposed to corrosion, imposes a specific degradation to the elongation at fracture of the specimen. Hence, the ductility decrease caused by the corrosion of the small surfaces $\Delta A_{f(small)}$ can be simply calculated by the available experimental measurements, *i.e.,* $\Delta A_{f(large)}$ and $\Delta A_{f(all)}$ by the corrosion exposure on the large- and all surfaces, respectively. The values for $\Delta A_{f(large)}$ and $\Delta A_{f(small)}$, for both investigated alloys, were normalized to the total elongation at fracture decrease $\Delta A_{f(all)}$ and the calculation results are graphically presented in Figure 3-33, where it is clear that the side-surfaces cracking plays a role on the corrosion-induced decrease of ductility for short exposure times. Almost 15% (one-sixth) decrease in A_f is attributed to corrosion products in the small side-surfaces for AA2198-T351. The side-surfaces contribution to remaining A_f decrease exceeds 50% for short corrosion exposure times

of AA2024-T3, confirming that corrosion attack is more aggressive on the side-surfaces due to the ease of corrosive solution (and possibly hydrogen) penetration between the grain boundaries. This is in agreement with the results in Figure 3-32, where higher depth of cracks on the side-surfaces was noticed. For the long corrosion exposure times where micro-cracks formation and exfoliation corrosion on the large surfaces are the dominant mechanical properties degradation mechanisms, the contribution of side-surfaces to the residual A_f values was decreased and approximately 75% of the total decrease in elongation at fracture is attributed to the large surfaces corrosion exposure.

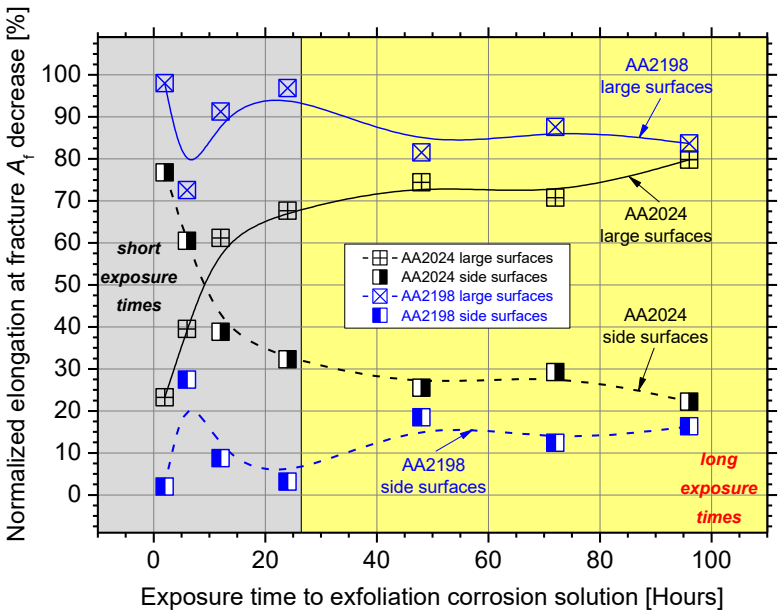

Figure 3-33: Contribution of the tensile specimen surfaces to be corroded of the two investigated aluminum alloys to elongation at fracture Af decrease.

Summing up the effect of side-surfaces corrosion on the tensile ductility decrease, it is evident that the two alloys respond with different behaviour to corrosion exposure. AA2024-T3 shows extreme sensitivity to side-surfaces corrosion attack, that can be noticed for the short exposure times (< 24 hours). For higher exposure times, the side-surfaces contribute to almost one-fourth of the total ductility decrease. A complete different mechanism can be noticed for AA2198-T351; corrosion attack and subsequent cracking formation on the side-surfaces seems to not contribute to the tensile ductility decrease, especially for short corrosion exposure times. Therefore the corrosion susceptibility and degradation mechanisms seems to be completely different for the two investigated materials.

3.3.6 Effect of artificial surface notches on ductility degradation

To better simulate the notch effect on ductility degradation of AA2024-T3, machining of artificial notches was decided to be performed on the large surfaces of the tensile specimens from a sheet of

AA2024-T3 with 3.2 mm nominal thickness, namely vertical to the loading axis. A drawing of the specimen with manufactured two surface notches can be seen in Picture 3-2. The two artificial notches facing one the other (on the same vertical level) can be well seen in the Figure as well as the maximum depth of 0.5 mm per notch. This notch depth per surface was the maximum depth of attack of corrosion products (pits and cracks) generated after approximating 72 hours exposure time in exfoliation corrosion solution. In different specimens, notches with smaller depths were manufactured (ranging from 0.1 till 0.5 mm) to incrementally simulate the corrosion surface damage on AA2024-T3 as well as the specimen's residual tensile strength and tensile ductility after the corrosion exposure.

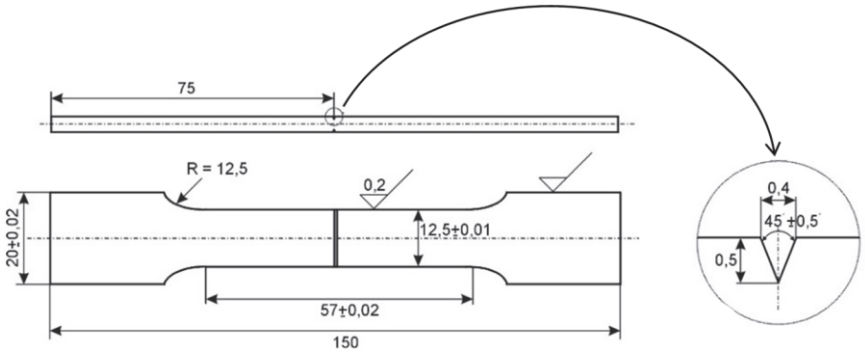

Picture 3-2: Sketch of the tensile specimen with machined two (upper and lower) surface notches on the large surfaces.

Typical nominal tensile curves for the specimens of AA2024-T3 with machined surface notches can be seen in Figure 3-34; the surface notch depth is a varying parameter. In the same figure, a reference tensile curve without any notches (black circles) was added for comparison purposes. As can be seen, the surface notches act as stress concentrators and tend to decrease the tensile mechanical properties of the alloy and especially elongation at fracture that decreases in higher rates than the yield stress. An essential decrease of the axial nominal strain was noticed even for the low-depth notches, but this was not the case for the strength properties that seem to be almost unaffected even for the notch depth of 0.30 mm. For instance, the tensile curves of 0.10 mm and 0.15 mm notch depths showed quite the same behavior with the reference one with the exception of the significant loss in ductility. By increasing the notch depth, up to 0.50 mm in this work, a continuous elongation at fracture decrease was noticed (magenta circles) exhibiting extremely low tensile elongation at fracture values.

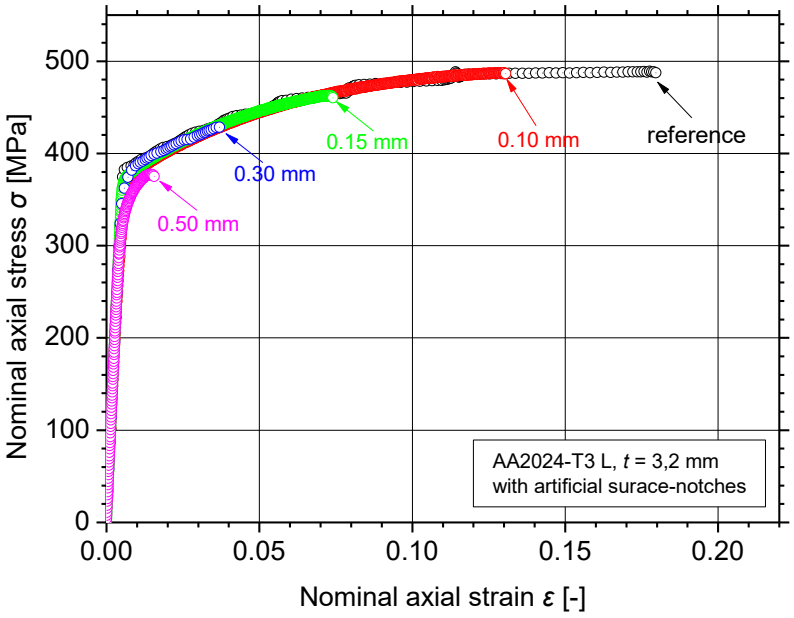

Figure 3-34: Typical tensile nominal stress - strain curves of AA2024-T3 after manufacturing of artificial surface notches.

Comparison of the results of residual elongation at fracture A_f values between corrosion exposure to EXCO solution and artificial surface notches are presented in Figure 3-35. The results are presented in the form of normalized values of A_f with double X-axis for comparison reasons. The black circles and dotted line represent the values as well as the fitting curve of the specimens exposed to EXCO solution and are linked to bottom X-axis, while the blue open squares and the dashed line represent the experimental values and fitting curve of the specimens with artificial surface notches and are linked to the upper X-axis. It is evident that the normalized A_f decrease is not linear proportional to the notch depth nor to the exposure time increase in the reduced cross-section. An essential A_f decrease was observed even for the low-depth notches, *e.g.*, approximately 30% normalized decrease for 0.10 mm, as well as for the short exposure times, such as 25% decrease after 1 hour of exposure. After 12 hours of exposure to exfoliation corrosion solution, the A_f decrease seems to reach a plateau value and further corrosion exposure did not reduce the tensile ductility considerably while for the increasing notch depth it decreases continuously to extremely low values, such as 6% remaining percentage for the 0.50 mm notch depth; this is evidence of maximum depth of attack of the surface corrosion-induced cracks [85]. It is well accepted that the ductility decrease from the short corrosion exposure times can be attributed to the hydrogen embrittlement phenomenon.

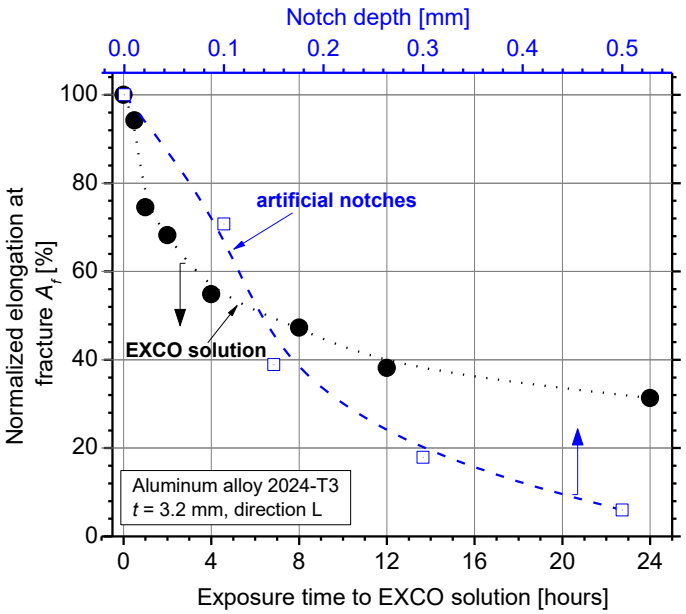

Figure 3-35: Normalized decrease of elongation at fracture A_f values for the various exposure times to EXCO solution of AA2024-T3 compared with notch depth.

As shown in the previous figures, the increase of surface notch depth decreases the tensile elongation at fracture (ductility) of AA2024-T3 and to a lesser extent the conventional yield stress. From the experimental tensile test results of pre-corroded 2024-T3 specimens, an essential decrease in tensile ductility was noticed even for the short corrosion exposure times to EXCO solution as well as for small artificial notch depth values. Hence, it is obvious that the empirical correlation between the problem of corrosion-induced degradation and the equivalent problem with artificial surface notches should be assessed through the residual tensile ductility property.

The experimental results of the residual elongation at fracture A_f of the pre-corroded in EXCO solution tensile specimens of AA2024-T3 can be seen in Figure 3-36. In the same figure, the exponential decrease curve fitting was plotted as well. For the conversion of the total depth of the surface notches in equivalent exposure time to corrosion solution, an empirical coefficient was devised. The value of this coefficient was selected such as to 'tailor' the equivalent ductility decrease curve of the surface notches in order to take approximate values with the experimental ductility decrease curve of the pre-corroded specimens. The empirical correlation factor m was calculated based on the following equation to correlate the available elongation at fracture test results as:

$$equivalent\ notch\ depth\ (mm) = \frac{\boldsymbol{exposure\ time\ (h)}}{\boldsymbol{m}} \qquad (3\text{-}11)$$

Figure 3-36 shows the correlation of the elongation at fracture decrease induced by the exposure to EXCO solution as well as by the presence of the surface notches. The best calculation results were found by using the value m = 20 for the empirical coefficient and the simulation of the ductility decrease curve of the investigated AA2024-T3 specimens for the short exposure times, where the

synergy of pitting formation and hydrogen embrittlement is the dominant degradation mechanism. By using this coefficient value, it is obvious that the results of the artificial notch depths are very close to the experimental values for the short corrosion exposure times and up to 2 hours exposure to EXCO solution. It seems that the total notch depth of 0.10 mm corresponds to 2 hours of exfoliation corrosion regarding the elongation at fracture decrease. On the other hand, the empirical coefficient that better simulates the tensile ductility decrease for the long exposure times, where the exfoliation of the corroded surfaces along with hydrogen embrittlement are the responsible mechanisms for the elongation at fracture decrease, was found to be approximate m = 100. For instance, a total depth of 150 μm surface notch results in the same A_f decrease as for 15 hours of exposure to exfoliation corrosion solution. Summarizing the available test results, the factor m takes values as:

$$m_{\text{EXCO to notch}} = \begin{cases} 20, & 0 < t < 4\ \text{h}, \\ 100, & 16 < t < 48\ h, \end{cases} \quad \begin{matrix} \text{pitting and hydrogen emrittlement} \\ \text{exfoliation} \end{matrix} \qquad (3\text{-}12)$$

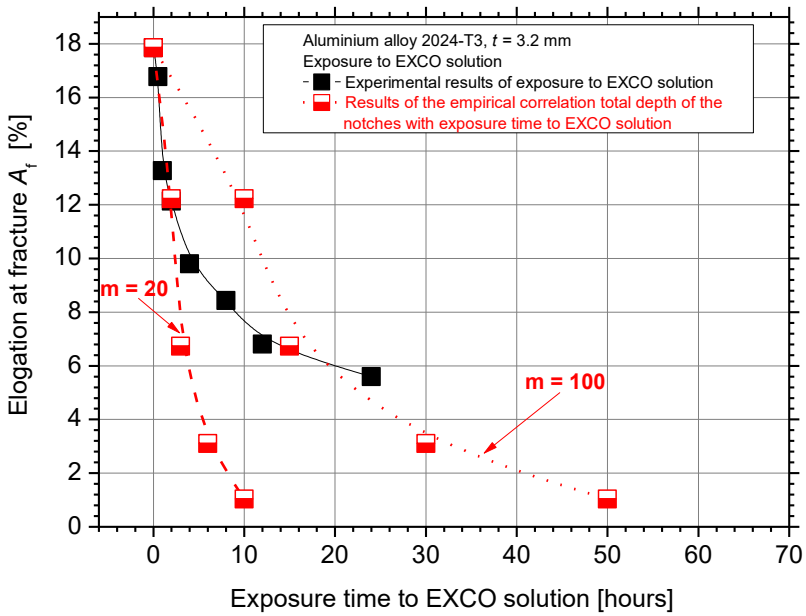

Figure 3-36: Correlation of the elongation at fracture Af decrease due to exposure to EXCO solution as well as presence of surface notches.

3.4 Conclusions

The findings of the present work can be summarized briefly:

1) Depth of corrosion attack (micro-cracks) increases with increasing exposure time. For the single-sided corroded specimens of AA2024-T3 this depth is essentially higher than for the respective half-corrosion exposure time for the both-sided corroded specimens.
2) Stress intensity factor K for ultra-thin specimens of AA2024-T3 was found to follow the normal distribution for the low exposure times to EXCO solution where pitting is the main degradation

mechanism, while for even higher exposure times (where micro-cracking and exfoliation is evident) K was found to follow the lognormal distribution.

3) Probability to exceed the threshold value K_{th} = 3.2 MPa·√m exceeded 50% after only 4 hours exposure time.
4) Three mechanical models were devised to calculate the effective thickness of corroded specimens:

   (a) iso-modulus of elasticity showed the best results in most of the investigated cases,

   (b) iso-yield stress worked well in low exposure times and for small depth of attack values, and

   (c) stress reduction concept gave satisfactory results on both-sided corroded specimens only.
5) Plots of remaining tensile ductility of corroded specimens over depth of attack showed the synergetic effect of the presence of micro-cracks and hydrogen embrittlement.
6) Extrapolated linearities for zero depth of attack (uncorroded material) showed a ductility decrease that was attributed to the hydrogen embrittlement effect. It was found that hydrogen embrittlement contributes to approximate 11% and 22% of ductility decrease for the single-sided corroded specimens of ultra-thin AA2024-T3 in L and T-sheet rolling directions, respectively.
7) For both-sided corroded specimens at the L-rolling direction, hydrogen embrittlement contributed to 27% of the ductility decrease while micro-crack formations to the rest 73%. The results for the T-rolling direction showed an equal contribution of the two mechanisms that proves its high susceptibility to corrosion attack and especially to hydrogen embrittlement.
8) AA2024-T3 has higher density of grains on both flat large surfaces and small side-surfaces when compared to AA2198-T351, which contains enlarged grains due to stretching. The higher density of grains is associated with the higher pitting density noticed in the former alloy. This is also evident from the mechanical properties response, where higher corrosion-induced degradation of the mechanical properties were noticed for AA2024-T3 with the phenomenon being more intense at short exposure times (≤ 24 hours).
9) Different corrosion mechanisms were noticed between the short and the long corrosion exposure times in both aluminium alloys. Pitting corrosion on both surfaces of AA2198-T351 was noticed for the short corrosion exposure times with essential pitting density to be noticed after 6 hours of exposure, while two cases of corrosion damage were noticed after 24 hours of exposure: a) the formation of corrosion-induced surface cracks on the small side-surfaces along with transition to exfoliation on the large surfaces due to grain boundaries delamination and b) the accumulated corrosion products on the large surfaces. Regarding AA2024-T3, pitting corrosion within grain boundaries was evident for short exposure times, while connection of corrosion-attacked sites

along with cracking between the grains, was the dominant corrosion degradation mechanism for long exposure times.

10) The differences in the corrosion-induced degradation mechanism between the two studied aluminium alloys is more obvious in the elongation at fracture property. Lower corrosion-induced decrease rate of A_f was noticed for AA2198-T351 than for AA2024-T351 and AA2024-T3; approximately more than 100% higher value was evident for the short corrosion exposure times of AA2198-T351 when compared to AA2024-T351, while more than 50% higher value was noticed against AA2024-T3.

11) The side-surfaces attack essentially affects the total A_f decrease of AA2024-T3 at short exposure times, having a contribution percentage to the total ductility decrease of more than 60%. For higher exposure times, this percentage tends to eliminate and the accumulated damage on the large surfaces governs the elongation at fracture decrease. This can be attributed to the slightly lower corrosion evolution rate of the small-side surfaces, as revealed from the electrochemical tests.

12) Accumulated corrosion damage on the side-surfaces does not essentially affect elongation at fracture for AA2198-T351, unlike the conventional AA2024-T3. Corrosion damage on the large surfaces is critical for tensile ductility decrease for all investigated exposure times. This is confirmed by the comparison of the electrochemical behaviour between the two exposed surfaces, where despite of the lower corrosion potential (less noble) of the side-surfaces, they exhibited lower cathodic activity and as a consequence lower corrosion rate. The difference in the corrosion rate between the two surfaces is more pronounced in the case of AA2198-T351.

13) According to the correlation between exposure to EXCO solution and artificial surface notches, a total notch depth of 0.10 mm corresponds to 2 hours of exfoliation corrosion for AA2024-T3 of 3.2 mm nominal thickness with regard to the same tensile ductility degradation.

Chapter 4

4 Effect of artificial ageing kinetics on corrosion behaviour

In this chapter a comparison on the effect of ageing on corrosion susceptibility and evolution in AA2024 and AA2198 is presented and analyzed. The effect of ageing-induced microstructural transformations on the corrosion behaviour as well as on corrosion propagation mechanism is studied through electrochemical techniques and mechanical testing. Specimens exposed for different times to artificial ageing and then subjected to exfoliation corrosion solution for several times before tensile testing. Similar to the previous chapters, it includes an introduction regarding the technological problem, a description of the experimental protocol and the presentation and discussion of the results. Finally, the main concluding remarks are given.

4.1 Introduction

Aluminium alloy 2024 is one of the most utilized aeronautical aluminium alloys of the 2xxx (Al-Cu-Mg) series due to its great combinations of physical and mechanical properties. Among the advantages of AA2024 are the high specific mechanical properties, enhanced damage tolerance capabilities, and increased corrosion resistance which are attributed to its complex precipitation hardening system and microstructure evolution during ageing. The microstructure of AA2024 consists of the aluminium matrix as well as of several intermetallic particles (IMs) and dispersoids. *S*- (Al_2CuMg) and θ phase (Al_2Cu) are the most common intermetallic particles found in the microstructure of AA2024 [74], [166]. Additionally, dispersoid particles such as Al_6(Cu, Fe, Mn), Al_7Cu_2Fe and $(Al, Cu)_6Mn$ are formed by the addition of other alloying elements. It is generally accepted [5] that the precipitation hardening system follows the sequence of supersaturated solid solution (SSS), formation of GPB zones, precipitation of the coherent with the matrix *S*" phase and finally the transition to the equilibrium incoherent *S* phase with the following sequence:

SSS → GPB zone → *S*" → *S*' → *S*.

The *S*″ phase is a coherent ordering of Cu and Mg solutes, while *S* phase is an incoherent, lath-shaped equilibrium phase – usually larger than 0.5 μm – which is formed at the over-aged (OA) condition. The GPB zones and *S* phase precursors (*e.g.*, *S*" and *S*′) are considered as the dominant hardening phases at the strengthening regime of the ageing curve, while the *S* phase particles are evident in the over-ageing regime, *e.g.*, Ringer et *al.* [167]-[168]. Shearing of the precipitates by dislocations is not possible in the over-ageing condition where coarsening and growth of the precipitates takes place; looping of the precipitates is the main bypassing mechanism of dislocations. Additionally, the precipitates lose their coherency with the aluminium matrix in this temper, and consequently, the mechanical strength of the alloy is decreased. The size, shape and volume fraction of precipitates is evolving with appropriate heat-treatment and this kinetics affect the mechanical behaviour of the alloy [169].

Regarding Al-Cu-Li alloys, which are supposed to replace the conventional Al-Cu alloys in aircraft structures, the main strengthening intermetallic phases observed in these alloys are the T_1 (Al_2CuLi), those of the θ sequence (with its metastable precursors) (Al_2Cu), *S* (Al_2CuMg) and δ' (Al_3Li). Other slow diffusing elements are added to these alloys to form fine, coherent and non-shearable dispersoid particles such as β (Al_3Zr) and $Al_{20}Cu_2Mn_3$, which control the grain refinement due to retardation of recrystallization and grain growth [3] and [108]. Initially, the δ'' phase is formed that is coherent with the matrix (T3 condition). By applying appropriate heat-treatment conditions, the θ', S' and T_1 metastable phases can be detected that contribute to the mechanical behaviour of the

alloy [170]-[171]. T_1 precipitate is considered to be the major strengthening phase of Al-Cu-Li alloys because it acts as non-shearable obstacles that have to be bypassed by dislocations during deformation [120], [122], [172] and preferentially nucleate on dislocations, sub-grain and grain boundaries [123]-[124]. The competition between these different phases is closely linked to the Cu/Li ratio, minor solute element content [173]-[174] and the thermomechanical history of the alloy. Copper and magnesium addition promotes the formation of T_1 phase [175], at the expense of δ which is absent for Li levels lower than 1.3% *wt*. [174], [176]-[177].

For the simulation of natural ageing of aluminium alloys several approaches have been used in laboratory scale − including artificial ageing heat treatments − to accelerate microstructural transformations [4], [6]-[8] and assess their effect on mechanical properties [9]-[11] and [13]-[15]. In the research work of Alexopoulos et *al*. [9], a drastic effect of artificial ageing holding time and isothermal temperature on the yield stress and elongation at fracture of AA2024-T3 was noticed; the first one was essentially increased up to the peak-ageing condition while elongation at fracture was decreased due to precipitation of *S*-type particles, respectively. Additionally, a significant hardness improvement with increasing ageing time is referred by Astika in [10]. Ringer et *al.* [178] showed that the hardness values for different investigated ageing time and tempers are controlled by the type, size, and distribution of precipitates. Wang et *al.* [11] found that both strength and ductility properties are influenced by the precipitation of S'' and S phases and the subsequent decrease in dislocation density, but not by the grain and texture characteristics. In recent years, many researchers have studied the strengthening mechanisms of Al alloys during solution and ageing treatments. Artificial ageing was found to lead to a significant reduction of the residual stresses in AA2024, according to Araghchi et *al.* [179]. In [12] a gradually increase of the mechanical properties of AA2024 − with a 1070 coating − with increasing solution temperature up to 510°C was noticed, while a further increase in temperature resulted in elongation at fracture decrease. Zhang et *al.* [170] showed that the composition and morphology of precipitates in AA2198 differentiate among different artificial ageing tempers and temperatures, while a change in fracture mechanism from dimple fracture to mixed-mode dimple-intergranular fracture was noticed with increasing ageing temperature. Precipitation evolution in Al-Cu-Li alloys was found to follows the sequence: SSS→ δ', θ', T_1→ θ', T_1, [180] while increasing ageing time and temperature to the over-ageing temper leads to significant reduction of the mechanical properties due to formation of incoherent θ phase and coarsening of the precipitates [157].

Several studies [18], [32], [181] have showed that ageing may influence the corrosion behaviour of aluminium alloys due to the occurrence of galvanic corrosion phenomena between the intermetallic phases precipitated on grain boundaries – *e.g.*, θ- and *S*-type in the case of AA2024 – and the matrix

or the adjacent Cu-depleted particles. According to [18] the precipitated phases continuously distributed along grain boundaries lead to intergranular corrosion (IGC) which is easily evolved into exfoliation corrosion (EXCO). Susceptibility of AA2024 in IGC after artificial ageing heat-treatments (*i.e.*, solution treating and re-ageing) was examined by Wang et *al*. in [182]; the *S*-phase precipitation on the dislocation cell walls accelerated anodic dissolution of the cell interiors and led to aggregated pitting corrosion in over-re-aged samples. Higher Cu content in the matrix of the altered surface layer (ASL) of AA2024 resulted in less pitting corrosion susceptibility of the ASL when compared to the underlying substrate [183]. The role of microstructure (*e.g.*, *S*-type particles in the aluminium matrix) on the tensile ductility decrease of pre-corroded specimens of AA2024 was investigated in Alexopoulos et *al*. [63]; corrosion-induced tensile ductility decrease was correlated with the precipitation of *S*-phase particles, showing that the specimens at peak-ageing (*S″* and *S'* precipitates) and over-ageing (*S* precipitates) conditions exhibited the lowest corrosion-induced decrease (~ 11% and ~ 22%, respectively) (referred to Figure 4-1) while the highest ductility decrease (~ 26%) was noticed for the T3 condition where limited GPB zones were present on the grain boundaries. Zhang and Frankel [184] also studied the pitting and intergranular corrosion behaviour of various tempers of AA2024. Artificial ageing was found to have a strong effect on polarization curves and localized corrosion morphology of AA2024. Susceptibility of Al-Cu-Li AA2099 to corrosion was found to be highly correlated to thermomechanical treatments and microstructural transformations [185]; the T8 temper showed higher tendency for localized corrosion attack. The presence of δ′ (Al_3Li) and T_1 (Al_2CuLi) phases within grains during artificial ageing heat-treatment was noticed for Al-Cu-Li AA1460, while T_1 phase was also evident in the vicinity of grain boundaries [186]; the evolution of inter- and intra-granular precipitates influenced both the local and global electrochemical characteristics. Even though several studies dealing with the effect of artificial ageing on corrosion susceptibility of conventional 2xxx aluminium alloys started many years ago [16], [184], [187]-[188], the crucial mechanisms of corrosion evolution and propagation in different ageing tempers remain still unclear.

In the present chapter, the effect of different artificial ageing tempers on corrosion nucleation and propagation of AA2024 regarding tensile mechanical properties degradation will be investigated. Additionally, a comparison with the innovative Al-Cu-Li 2198 alloy is also attempted in order to report experimental evidence regarding the corrosion potential of this alloy. Rectangular (for microstructural analysis) and tensile specimens, artificially aged to different tempers corresponding to Under-Aged (UA), Peak-Aged (PA) and Over-Aged (OA), selected from a relevant article of the authors [63], and subsequently exposed to exfoliation corrosion environment for different exposure

times in order to investigate the rate of corrosion–induced ductility degradation in different ageing tempers.

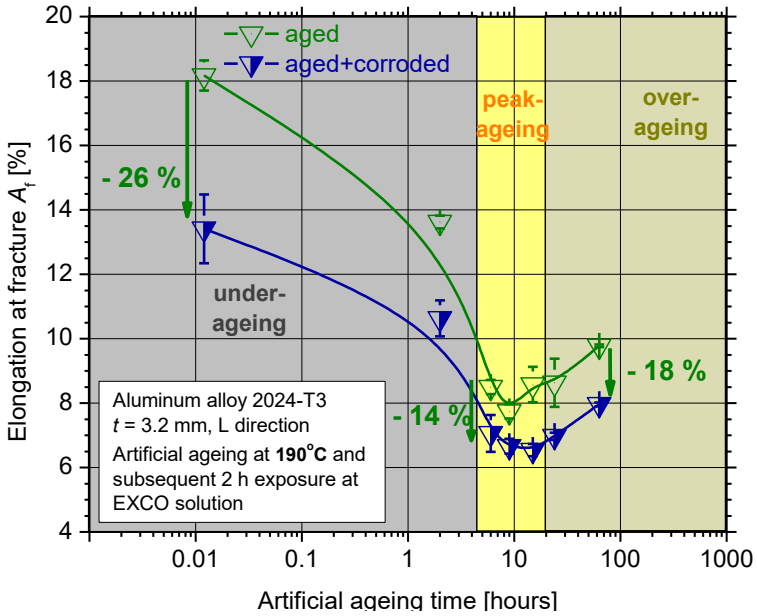

Figure 4-1: Ductility comparison between artificially aged against artificially aged and subsequent corroded for 2 h specimens at 190°C artificial ageing temperature [63].

4.2 Materials and experimental procedure

4.2.1 Materials preparation

The materials used in the current research work were the aeronautical aluminium alloy 2024-T3 and 2198 in T3 and T8 condition, which were received in 3.2 mm nominal thickness. Tensile as well as rectangular metallographic specimens were machined from the longitudinal (L) rolling direction of the sheet in accordance with ASTM E8 specification [90]. The geometrical dimensions of the tensile specimens were 12.5 mm x 3.2 mm at the reduced cross section, with a total length of 190 mm, while the respective dimensions for the rectangular specimens were 10 mm x 20 mm x 3.2 mm.

The exfoliation corrosion (EXCO) solution was used for the exposure of tensile specimens, in accordance with ASTM G34 standard [80]. Masking of the side-surfaces (thickness) was performed in order to eliminate the effect of micro-cracking in the decrease of ductility (elongation at fracture), where according to Charalampidou et *al*. [105] the side-surfaces attack has a contribution percentage to the total ductility decrease of more than 60%, at short exposure times to EXCO solution. For the investigation of the respective corrosion rates of different tempers, 3.5% *wt*. NaCl solution was used for electrochemical measurements according to ASTM G44 standard [93].

Prior to corrosive solution exposure, the side-surfaces of the tensile specimens as well as the upper surfaces of the small rectangular specimens (surfaces to be exposed) were polished up according to

ASTM E8 specification [90]. Further preparation of the tensile specimens included shielding of the specimens' surfaces so that only specific areas of interest were exposed, as can be seen in Figure 4-2. Afterwards, the specimens' surfaces (both tensile and rectangular) were cleaned with alcohol according to ASTM G1 specification [92].

To investigate the effect of artificial ageing condition of aluminium alloy 2024 on the corrosion susceptibility and evolution mechanisms of the materials, prior artificial ageing heat-treatment at 190 °C was performed. The temperature of 190 °C was selected as an intermediate heat-treatment temperature for artificial ageing (range varies from 170 °C to 210 °C) according to the study of Alexopoulos et *al*. [9], where it is shown that essentially no long ageing times, *i.e.*, below 10 hours, are required to achieve the peak-aged (PA) condition. Yield stress continuously increased with ageing time up to 8 hours. This increase in yield stress is characterized as under-aged (UA) region. A plateau in the yield stress was noticed from 6 hours up to 12 hours ageing time, which is a characteristic for the PA condition. Finally, by further increasing the artificial ageing time to 63 hours at 190 °C an essential decrease in yield stress was observed due to the coarsening of the precipitates, so that this heat-treatment condition is considered to belong to the over-aged (OA) region. To this end, three different ageing times were selected for the present study, namely 2 hours, 8 hours, and 63 hours to correspond to UA, PA, and OA conditions, respectively. Regarding AA2198, prior artificial ageing heat-treatment at 170 °C was performed. Lower temperature was selected for the investigation of artificial ageing kinetics in the innovative aluminium alloy since it is well-known that lower ageing temperature enables higher peak strength to be achieved due to the well-balanced formation of coherent and subsequent, semi-coherent S'' and S' (Al_2CuMg) precipitates, respectively [190]. Hence, because of the fact that the thermomechanical kinetics are not well defined and fully understood for this alloy, the formation of well-balanced precipitates was preferable. To this end, three different ageing times were selected for the present study, namely 3 hours, 48 hours, and 400 hours to correspond to UA, PA, and OA conditions, respectively. The specimens were prior isothermally artificially aged in an electric oven Elvem T101 (2600 W) with ± 0.1 °C temperature control and subsequently exposed to corrosion exposure, to investigate the corrosion mechanism in different artificial ageing conditions. After corrosion exposure, the specimens were removed from the containers and cleaned with acetone before performing the tensile tests.

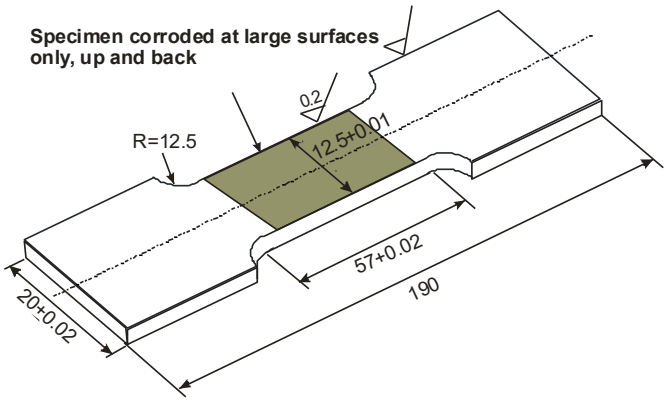

Figure 4-2: Schematic representation of tensile specimens according to ASTM E8, corroded at large surfaces.

4.2.2 Electrochemical tests

The corrosion behaviour of aluminium alloys in different tempers was assessed by electrochemical impedance spectroscopy (EIS) tests, which were carried out using a PalmSens® potentiostat at 25 ± 1 °C. The experiments were carried out in naturally aerated 3.5 *wt*. % NaCl solution at room temperature (25 ± 2) °C. A typical three electrodes cell system that was composed of a platinum electrode as counter electrode, a silver chloride electrode Ag/AgCl as reference electrode and the small rectangular specimens of the investigated aluminium alloys as working electrodes was used. A surface area of 0.5 cm^2 of the working electrode was exposed to the electrolyte. The voltage perturbation range used in the EIS measurements was 10 mV (rms), and the acquisition rate was 10 points per decade in a frequency range from 10^5 Hz down to 0.01 Hz. The measurements were repeated at fixed intervals of 0 (after 5 min immersion), 1, 3, 6, 12, 24, and 48 hours of immersion time. Additionally, in the case of AA2198 specimens potentiodynamic polarization tests were performed to investigate the corrosion tendency and rates of the different tempers of the alloy. The Harrison's solution (diluted version) was used for these experiments, according to ASTM D5894 specification [94], since it better simulates the conditions of atmospheric corrosion and allows the overall corrosion mechanism evolution to occur and be easily recognized (*e.g.*, presence of passivation). A Gamry Interface 1000 potentiostat along with a cell with an exposed area of the working electrode of 0.5 cm^2 were used for the electrochemical measurements. Initially, the open circuit potential (OCP) was measured by recording values with 1 s interval for 30 min. Potentiodynamic polarization test started after the OCP measurement and from -0.2 V to the corrosion potential. The polarization potential range was from -0.2 V up to 0.6 V to the OCP, respectively and the potential scanning rate was 0.2 mV s^{-1}. Each test was performed at least three times to evaluate the reproducibility of the results. The obtained data was fitted employing a PStrace5® analysis software.

4.2.3 Tensile tests

The tensile properties of the specimens were evaluated after testing in an INSTRON 8801 Testing Machine. The software was programmed to apply a tensile strain to the specimen–under crosshead displacement control–at a rate of 0.7 mm/min. An extensometer of 50 mm initial gauge length was installed onto specimens and zeroed before applying a 1 kN preload to the specimen. The raw data from each test was then analyzed using a specially programmed Excel spreadsheet and edited with the aid of Microcal Origin© software. For the reproducibility of the results, at least three tensile tests have been carried out per each test series. Evaluated properties were the conventional yield stress $R_{p0.2\%}$ (0.2% proof stress), ultimate tensile strength R_m and elongation at fracture A_f.

4.3 Results and discussion

4.3.1 AA2024: Macroscopic evaluation of pre-corroded specimens

Exposure of AA2024 specimens to the corrosive environment (EXCO solution in the current research work) results in deterioration of the specimens' surface due to breakdown of the oxide layer [32] and [181] and the subsequent nucleation of corrosion-induced surface pits (refer to Figure 4-3 to Figure 4-6 for the different artificial ageing conditions). The depicted corroded area has dimensions of 12.5 mm x 55 mm being the width and length of the exposed area of the specimens, respectively. For the case of T3 condition (refer to Figure 4-3), pitting formation on the corroded surfaces remains rather limited for short exposure times up to 2 hours. With increasing exposure time to EXCO solution, an increase in pitting density is evident. Localized corrosion with the form of randomly dispersed pits (black signs) is evident for 4- (refer to Figure 4-3(c) and 24 hours (refers to Figure 4-3(d)), respectively.

The effect of corrosion evolution seems to be more intense in under-aged (UA) condition regarding surface deterioration. Notable differences in the surfaces of pre-corroded specimens are noticed with increasing exposure time; for short exposure times pitting corrosion remains rather limited, *e.g.*, Figure 4-4(a), while slight increase in pitting density is evident from the surface roughness after 2 hours corrosion exposure time, *e.g.*, Figure 4-4(b). Additionally, severe localized corrosion is noticed for the under-aged specimens after only 4 hours of corrosion exposure, which evolves to exfoliation corrosion after 24 hours corrosion exposure time (refer to Figure 4-4(d)).

Regarding peak-aged (refer to Figure 4-5) and over-aged (refer to Figure 4-6) conditions, no significant surface deterioration is noticed with increasing exposure time to EXCO solution. Pitting corrosion remains limited for the very short exposure times (*i.e.*, 0.5 hours) as was the case for T3 and UA conditions. However, increased pitting density is noticed for higher exposure times, *e.g.*,

Figure 4-5(b) and Figure 4-6(b). Further corrosion exposure (up to 24 hours) does not affect the surface of pre-corroded specimens significantly. The corrosion morphology-characterized by uniformly dispersed pits in the whole exposed surface (no signs of localized corrosion) is almost the same for the specimens exposed to EXCO solution for 2- (Figure 4-5(b), Figure 4-6(b)), 4- (Figure 4-5(c), Figure 4-6(c)) and 24 hours (Figure 4-5(d), Figure 4-6(d)) for both ageing conditions respectively. This can be attributed to the higher density of precipitates which are more uniformly distributed to the whole specimen's surfaces.

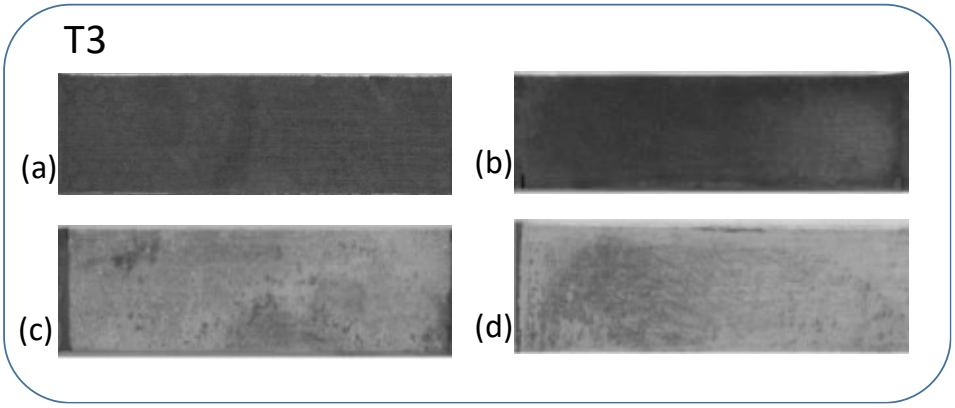

Figure 4-3: Images of corroded surfaces (12.5 x 55 mm) of AA2024 in T3 condition after exposure for different times to exfoliation solution, namely (a) 0.5 h, (b) 2 h, (c) 4 h and (d) 24 h, respectively.

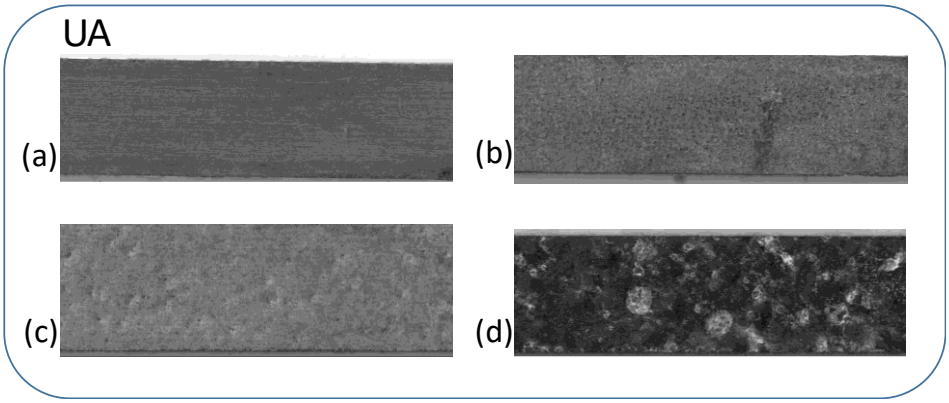

Figure 4-4: Images of corroded surfaces (12.5 x 55 mm) of AA2024 in UA condition (2 h at 190 °C) after exposure for different times to exfoliation solution, namely (a) 0.5 h, (b) 2 h, (c) 4 h and (d) 24 h, respectively.

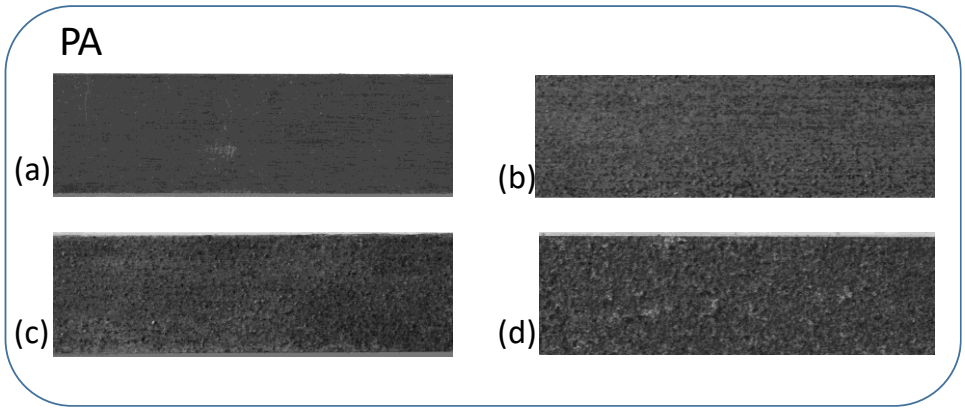

*Figure 4-5: Images of the corroded surfaces (12.5 * 55 mm) of AA2024 in PA condition (8 h at 190 °C) after exposure for different times to exfoliation solution, namely (a) 0.5 h, (b) 2 h, (c) 4 h and (d) 24 h, respectively.*

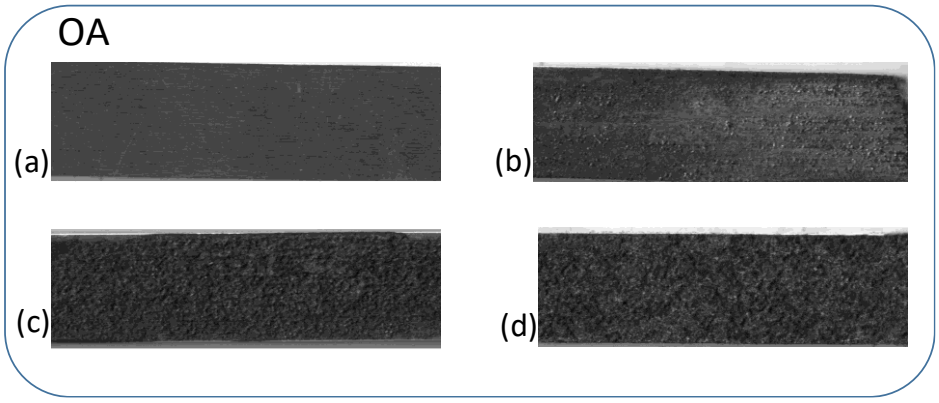

*Figure 4-6: Images of the corroded surfaces (12.5 * 55 mm) of AA2024 in OA condition (63 h at 190 °C) after exposure for different times to exfoliation solution, namely (a) 0.5 h, (b) 2 h, (c) 4 h and (d) 24 h, respectively.*

4.3.2 AA2024: Effect on corrosion mechanism

Electrochemical impedance spectroscopy (EIS) results for the different artificial ageing tempers of AA2024, as a function of immersion time in 3.5 *wt*. % NaCl solution, are shown in the form of Bode diagrams in Figure 4-7(a) to Figure 4-7(d), respectively. Figure 4-7(a) presents the results for T3 temper where two-time constants are evident at low (10^{-2}-10^{-1}) and medium (10^{0}-10^{3}) frequencies regime after above one hour of immersion. In contrast, at the initial period of immersion the relaxation process at higher frequencies being responsible for the response from the passive film can also be evidenced. Time constants in medium frequencies are related to charge transfer processes coupled to the double layer capacitance, while the time constant at low frequencies is likely to be associated to a diffusion-control. Slight fluctuations of the curves in 1 hour and 3 hours at low frequencies regime can be caused by non-stationarities of the system at this period resulted from the metastable pitting formation. After 6 hours of exposure the pits seem to become more stable leading to much less scattering of the low-frequency impedance values. The same behaviour was noticed for specimens in UA temper; however, stable pits formed slightly faster than in T3 temper as can be seen in Figure

4-7(b). Regarding PA and OA tempers, it can be concluded that formation of stable pits becomes faster with increasing artificial ageing time. Furthermore, the response from the surface oxide passive film is still evident after 1 hour of immersion (red curve) while specimens in PA condition presented slightly higher capacitive behaviour than the other three tempers, as was shown form the higher Theta phase degrees at the initial period of immersion (back curve).

Impedance modulus of specimens in T3 condition slightly increase for short exposure times and up to 3 hours at low frequencies regime (10^{-2}-10^{-1}) followed by a gradual decreasing trend for higher exposure times, *e.g.*, Figure 4-7(a). Essential decrease is noticed between 6 and 12 hours of exposure while further corrosion exposure seems not to reduce impedance modulus essentially since by that time stable pits are formed, and the corrosion process is controlled by the diffusion limited cathodic oxygen reduction. Formation of voluminous corrosion products after long exposure times seal the pits and impede transport to/from the active areas. As for the specimens in UA temper, a similar behaviour can be observed. The main difference is that the stabilization of the pits occurs after shorter time. The measurement performed after 3 hours demonstrates a clear drop of low frequency impedance value and absence of data scattering related to the metastable pits. Regarding specimens in PA temper, the impedance modulus at low frequencies almost remains unaffected by corrosion for short exposure times and up to 3 hours. It is also important that the disappearance of the time constant related with the oxide film takes significantly longer in this case. Additionally, the impedance modulus at low frequencies is higher in this temper even after the highest exposure time (*e.g.*, 48 hours) in comparison to the other systems. In over-aged temper fluctuations were noticed, and only slight decrease was observed for the time range between 6 to 48 hours of exposure.

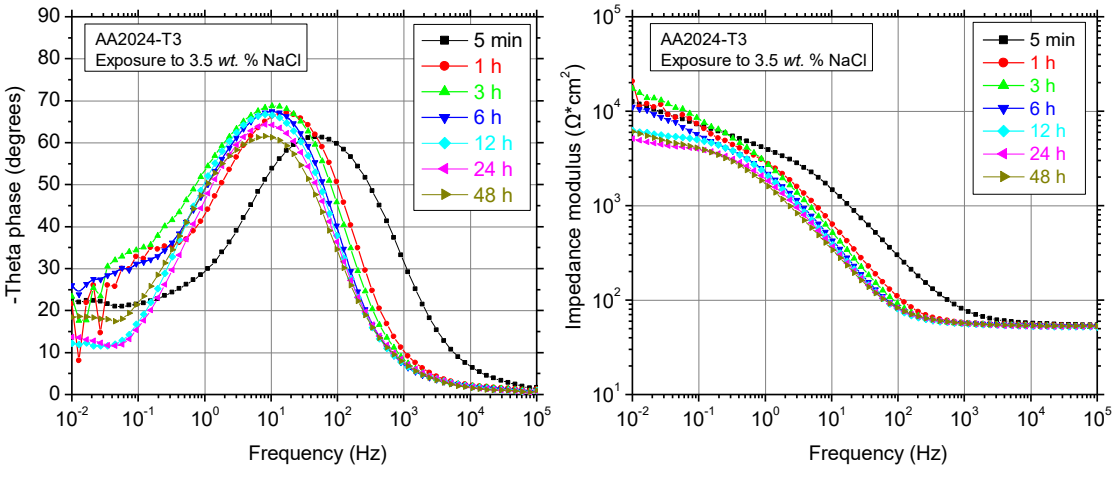

(a)

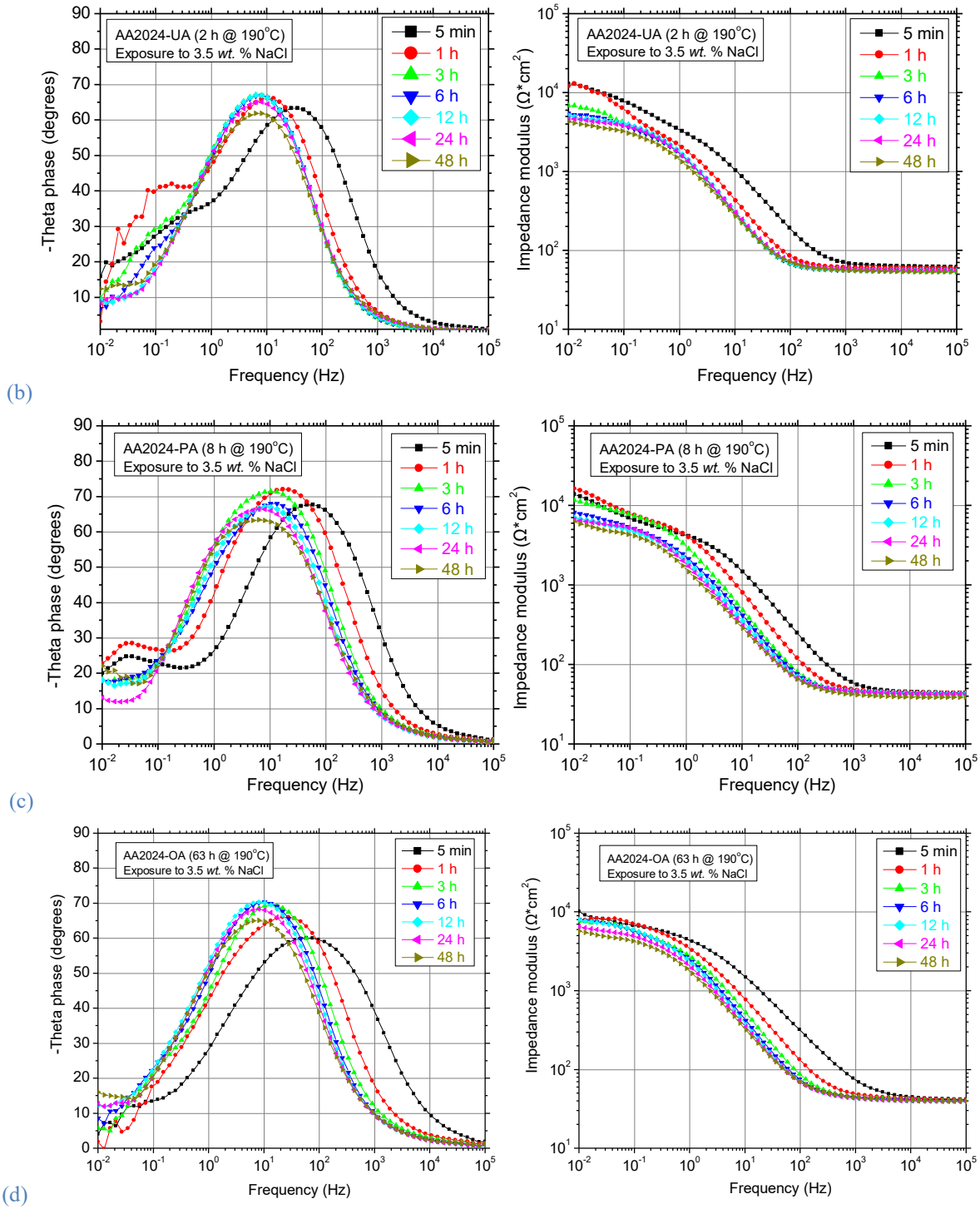

Figure 4-7: Impedance spectra of AA2024 (a) in T3, (b) under–aged (UA), (c) peak–aged (PA) and (d) over–aged (OA) tempers measured in 3.5 wt. % NaCl solution.

To gain a better insight into corrosion mechanisms, EIS response is modelled using equivalent electrical circuits, as shown in Figure 4-8. The R_1 element in circuit model represents the resistance of electrolyte. The pair $R_2//Q_1$ stands for the polarization resistance, *i.e.*, the resistance of electron flow through double layer, in parallel with capacitance of double layer. A constant phase element (*CPE*) - that is denoted with Q in the present work - was used instead of an ideal capacitor to take into consideration the heterogeneity of the surface, as already mentioned in literature, *e.g.*, [20] and

[100]. *W* element refers to Warburg impedance which is ascribed to the response at low frequencies being controlled by diffusion processes. It is worth mentioning that for short exposure times in PA condition another equivalent circuit model showed good fitting. The model included an extra constant phase element (*R*//*Q*) that corresponds to oxide film resistance in parallel with conductive pathways associated with defective sites created by intermetallic particles (IMCs). Nevertheless, the simple circuit model that better simulates most of the investigated cases used in this research work to simulate corrosion mechanism in AA2024 specimens.

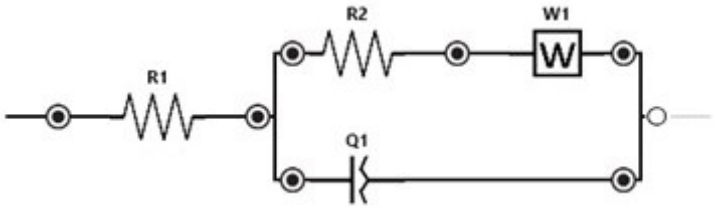

Figure 4-8: Equivalent circuit model for all ageing tempers.

The evolution of resistance values of the circuit components (R_2 in this case) is depicted in Figure 4-9. Resistance was found to decrease even from the early stages of corrosion for under-aged specimens (shown in green curve) while this was not the case for the other three investigated tempers. The lower values of resistance in UA temper indicate fast charge transfer on aluminium surface. Fast corrosion attack was also observed in T3 temper while for PA and OA conditions it was essentially slower.

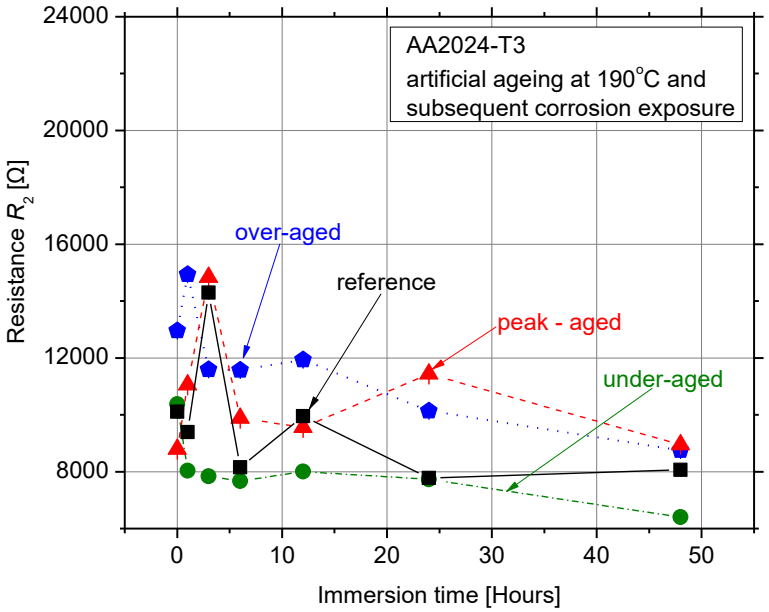

Figure 4-9: Variation of charge transfer resistance R_2 element as a function of immersion time to 3.5 wt. % NaCl solution for AA2024-T3 exposed to different artificial ageing tempers.

4.3.3 AA2024: Mechanical evaluation of pre-corroded specimens

Typical tensile curves of the pre-corroded specimens of AA2024 in different tempers – exposed to an EXCO solution – are presented in Figure 4-10. The nominal stress calculation was based on the nominal cross-section of the tensile specimens; namely, (width x thickness) = (12.5 mm x 3.2 mm), respectively. Prior exposure of AA2024 to the EXCO solution resulted in significant modifications to the overall tensile mechanical properties of the alloy. However, the corrosion–induced modifications are different for each artificial ageing condition of the alloy. The effect of corrosion is more severe in T3 and under-aged (UA) conditions, refer to Figure 4-10(a) and Figure 4-10(b), respectively. A significant decrease of the axial nominal strain is noticed after only 0.5 hours of corrosion exposure in T3 condition, shown in Figure 4-10(a). With increasing corrosion exposure time, the axial nominal strain is further decreased; almost half value of the initial property value is noticed after 24 hours corrosion exposure time. On the contrary, the axial nominal stress is not essentially decreased even after the highest exposure time, *i.e.*, 24 hours, in T3 condition.

Essential corrosion-induced modifications of the overall tensile mechanical properties are noticed in under-aged (UA) condition (Figure 4-10(b)); however, these modifications are different from the T3 condition. Axial nominal strain is not notably decreased for the very short exposure times, *i.e.,* 0.5 hours where hydrogen embrittlement is the dominant degradation mechanism [48], [78], [85] and [104], while after 2 hours of corrosion exposure a sudden drop of both the axial nominal strain and the axial nominal stress is noticed. The significant stress drop noticed in this alloy is attributed to the decrease in the effective thickness due to micro-cracking propagation, as was referred in the work of Alexopoulos and Papanikos [49]. Further increase of corrosion exposure time tends to decrease the tensile mechanical properties of AA2024 significantly.

Regarding peak-aged (PA) and over-aged (OA) conditions - refer to Figure 4-10(c) and Figure 4-10(d), respectively - no significant alterations on the overall tensile mechanical properties are evident with increasing corrosion exposure time. Nevertheless, both the axial nominal strain and the axial nominal stress tend to decrease with corrosion evolution but in lower rate when compared to T3 and UA conditions. The slight decrease of stress even after the highest exposure time (*i.e.*, 24 hours) revealed that micro-cracks propagate in lower rates in these tempers probably, since they are blocked by the precipitations formed after ageing.

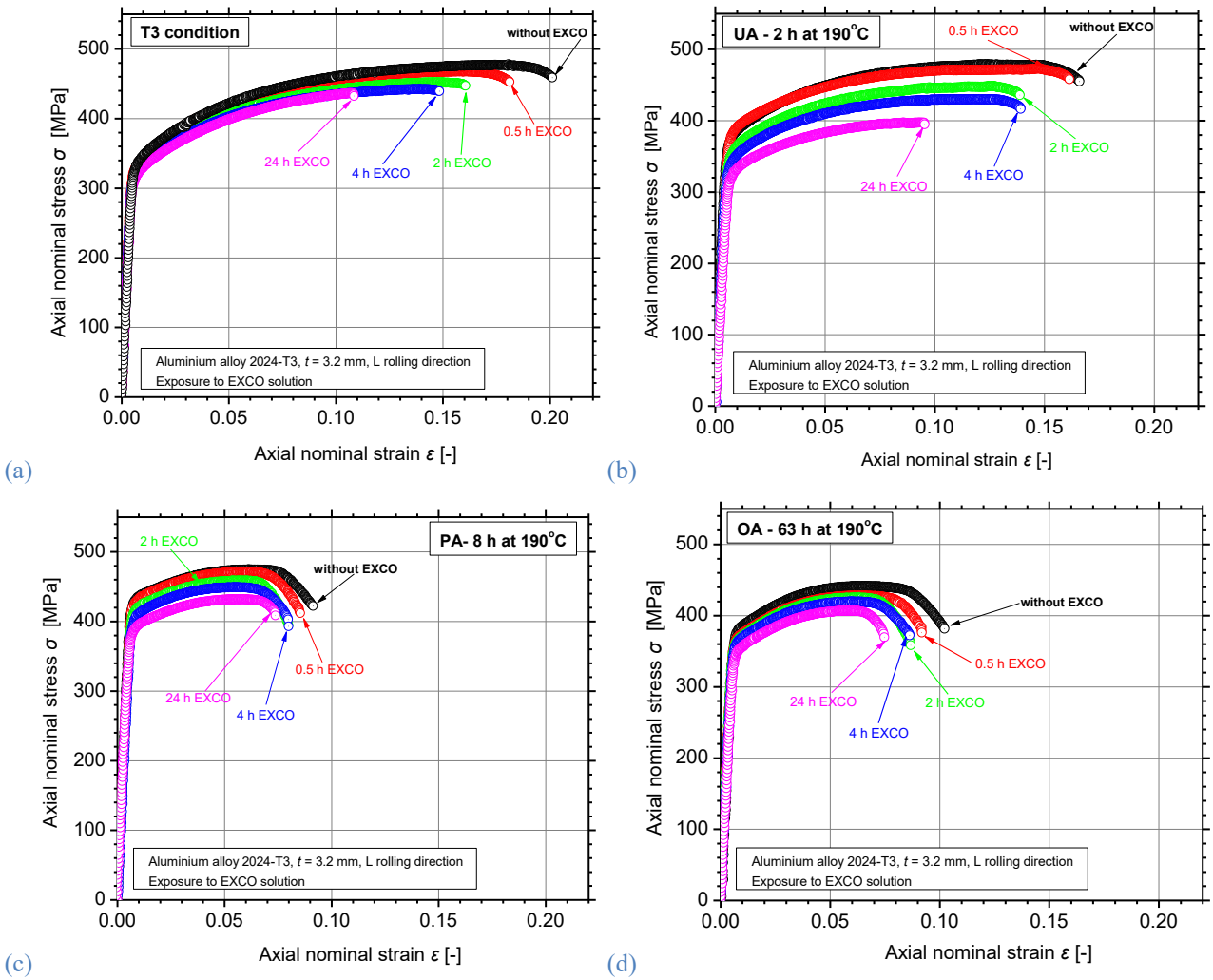

Figure 4-10: Typical experimental tensile flow curves of pre-corroded for different exposure times to EXCO solution AA2024 specimens at (a) T3, (b) under-aged (UA), (c) peak-aged (PA)and (d) over-aged (OA) conditions.

4.3.4 AA2024: Effect on corrosion evolution

Figure 4-11(a) summarizes the conventional yield stress $R_{p0.2\%}$ (based on the nominal cross-section of the specimens) results for the pre-corroded - for different exposure times to EXCO solution - specimens in different tempers. Marked in diagram are the regions of under-, peak- and over-aged conditions as a function of ageing time with different colours. Each curve in the diagram represents the evolution of $R_{p0.2\%}$ with increasing ageing time for the different pre-exposed specimens. It is obvious that with increasing artificial ageing time, $R_{p0.2\%}$ tends to increase up to its maximum value in the peak-aged condition; further increase of ageing time (OA condition) leads to $R_{p0.2\%}$ decrease due to the growth and coarsening of the precipitates [7], [191]. Regarding the effect of artificial ageing time on corrosion–induced degradation of $R_{p0.2\%}$, it is evident that the highest decrease of the conventional yield stress due to corrosion exposure is taking place in under-aged condition; approximately 23% degradation is evident after 24 hours of exposure. The corrosion-induced

degradation of $R_{p0.2\%}$ is more severe in under-aged condition, where the biggest difference between the property values of the different corrosion exposure times is noticed.

On the contrary, the less corrosion–induced decrease of conventional yield stress between the different corrosion exposure times is noticed in T3 as well as in over-aged conditions. Nevertheless, significant degradation of $R_{p0.2\%}$ is noticed due to corrosion exposure but the respective degradation tends to be eliminated with increasing exposure time. For instance, the non–artificially aged (T3 condition) and non–corroded material (shown in black curve) exhibited approximately 14.7% decrease of the conventional yield stress after only 0.5 hours corrosion exposure time (from 387 MPa to 330 MPa) [63]. Further increase of corrosion exposure time does not decrease the $R_{p0.2\%}$ significantly, since after the highest exposure time (*e.g.*, 24 hours) the conventional yield stress is approximately 320 MPa (decreased by 17.5% from the initial value and only 3% from the first corrosion exposure time). As the logarithmic scale was used to express the artificial ageing time in hours, it is mathematically impossible to illustrate the reference condition T3 without any artificial ageing time (zero hours); to cope with this problem a very small value of 0.015 hours was used in all figures to address the reference specimens without any kind of artificial ageing heat treatment.

The respective results for elongation at fracture A_f are presented in Figure 4-11(b). As expected, the essential yield stress increase in peak-aged condition is followed by a ductility decrease where elongation at fracture A_f reach to a minimum. A different corrosion-induced degradation mechanism is noticed for the elongation at fracture in different artificial ageing tempers when compared to the conventional yield stress. As for the case of $R_{p0.2\%,}$ the specimens in under-ageing condition exhibited the highest A_f degradation due to corrosion exposure, *e.g.*, -50.9% after 24 hours of exposure. Additionally, significant A_f decrease is evident for the T3 condition where higher degradation between the different corrosion–exposure times is noticed for the short corrosion exposure times and up to 4 hours. In this case the less effect of corrosion exposure is evident in peak-aged condition followed by over-aged, with the highest decrease of A_f to be -21.1% and -25.8% after 24 hours of exposure, respectively.

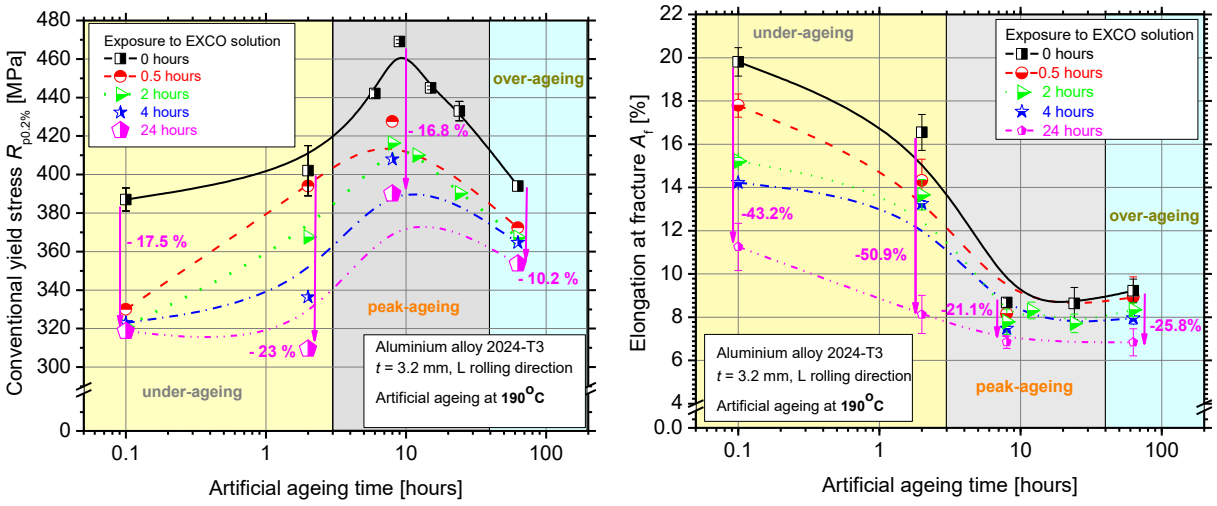

Figure 4-11: Evaluated mechanical properties (a) conventional yield stress $R_{p0.2\%}$ and (b) elongation at fracture A_f of pre-corroded AA2024 specimens for different corrosion exposure times and in different artificial ageing times.

4.3.5 AA2024: Evaluation of fractured specimens

The tensile test results revealed that corrosion-induced mechanical properties decrease (*i.e.*, $R_{p0.2\%}$ and A_f) is artificial-ageing sensitive; hence, the corrosion-induced degradation mechanism depends on artificial-ageing condition of the alloy. In order to investigate the possible phenomena related to the behaviour noticed in tensile tests, pre-corroded fractured specimens from under-, peak- and over-aged conditions were examined with the aid of stereoscope (refer to Figure 4-12 up to Figure 4-15) and scanning electron microscope (SEM) (refer to Figure 4-16 up to Figure 4-18).

Stereoscopical analysis revealed an increasing surface deterioration, by means of pitting density and size, with increasing EXCO time in T3 as well as in under–aged tempers, shown in Figure 4-12 and Figure 4-13, respectively. Furthermore, a decrease in ductility with increasing exposure time is evident in these tempers from the small side–surfaces, where the presence of necking is eliminated. On the contrary, regarding specimens in peak–aged (Figure 4-14) and over–aged (Figure 4-15) conditions no essential difference in the surface corrosion morphology is observed with increasing corrosion exposure time, while these specimens seem to maintain their ductility even after long exposure times where the necking phenomenon is still evident.

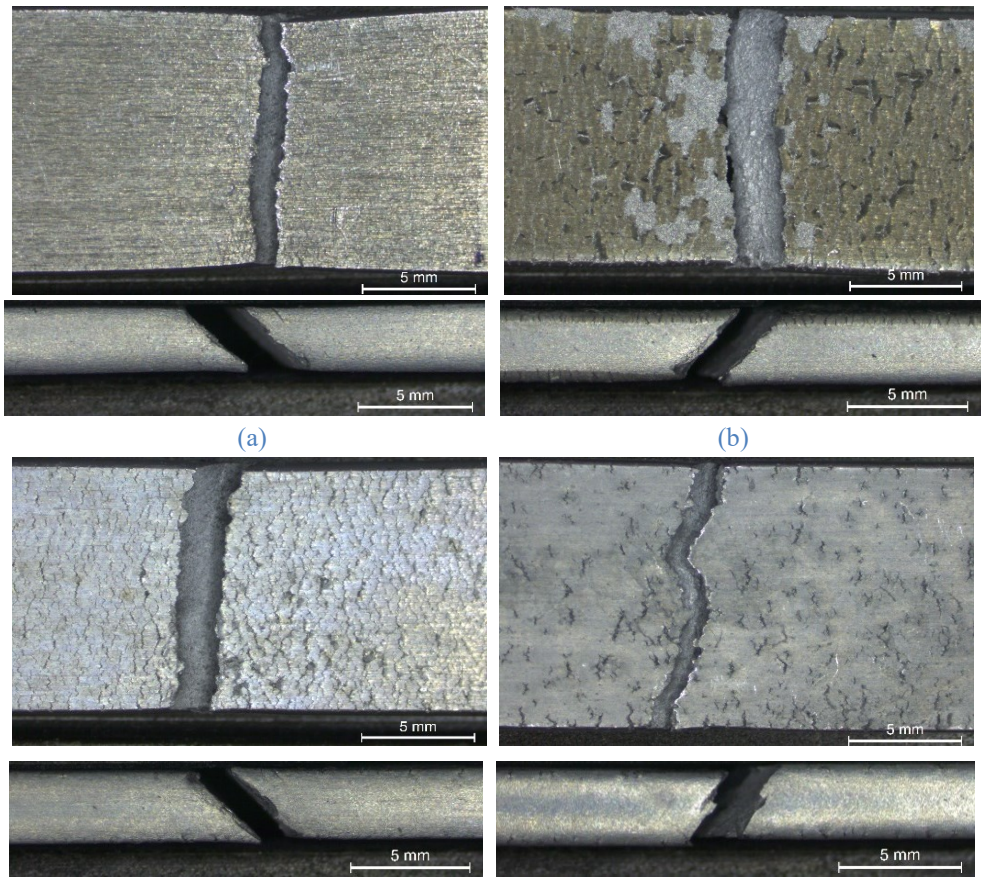

Figure 4-12: Images of fractured pre-corroded surfaces of AA2024 in T3 condition after exposure for different times to exfoliation corrosion solution, namely (a) 0.5 h, (b) 2 h, (c) 4 h and (d) 24 h, respectively.

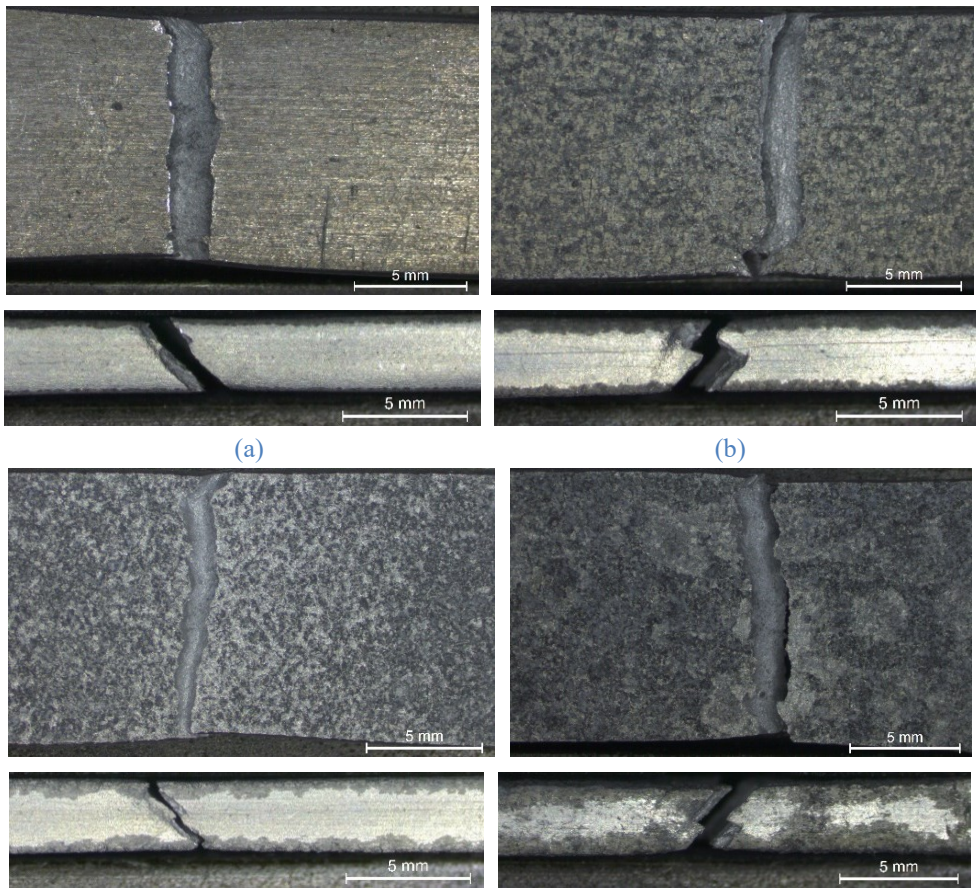

Figure 4-13: Images of fractured pre-corroded surfaces of AA2024 in under–aged (2 h at 190 °C) condition after exposure for different times to exfoliation corrosion solution, namely (a) 0.5 h, (b) 2 h, (c) 4 h and (d) 24 h, respectively.

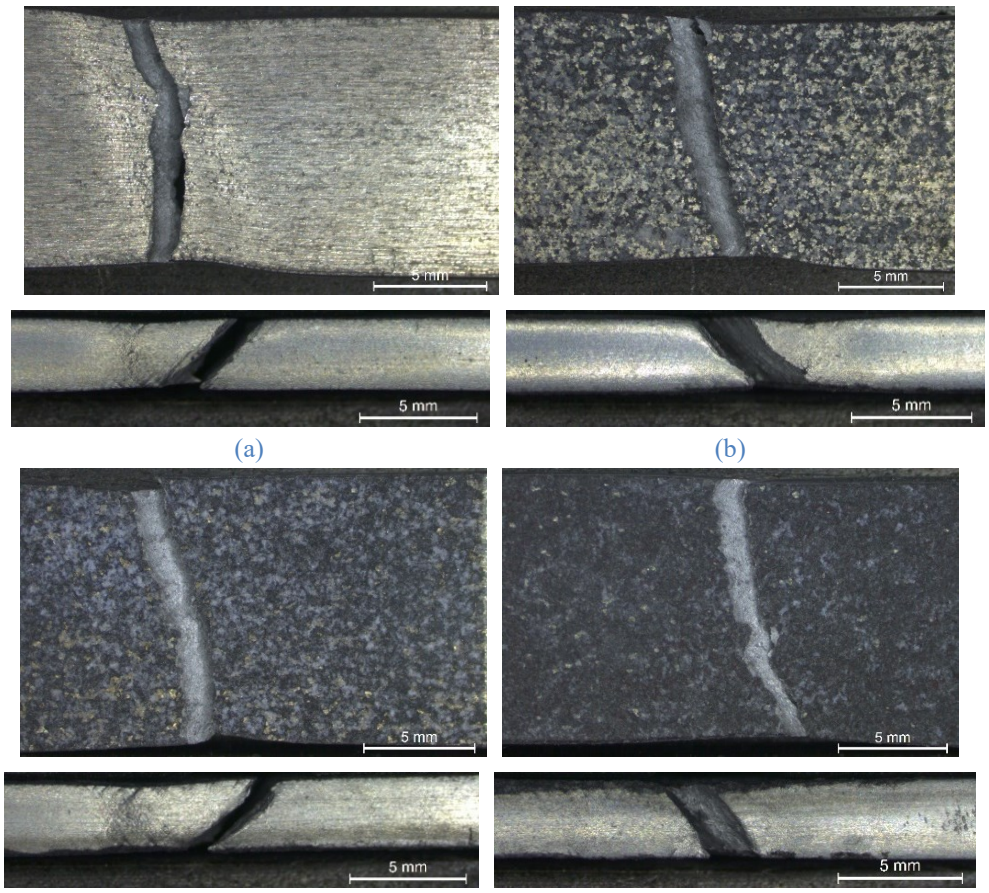

Figure 4-14: Images of fractured pre-corroded surfaces of AA2024 in peak–aged (8 h at 190 °C) condition after exposure for different times to exfoliation corrosion solution, namely (a) 0.5 h, (b) 2 h, (c) 4 h and (d) 24 h, respectively.

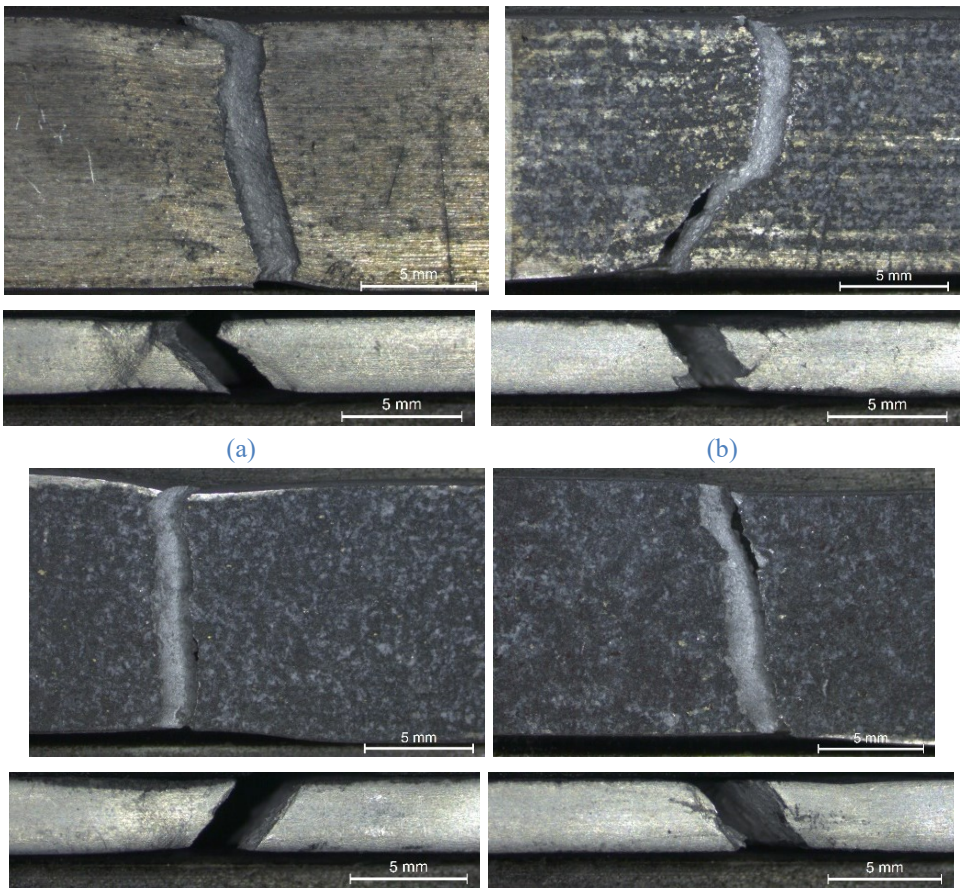

Figure 4-15: Images of fractured pre-corroded surfaces of AA2024 in over–aged (63 h at 190 °C) condition after exposure for different times to exfoliation corrosion solution, namely (a) 0.5 h, (b) 2 h, (c) 4 h and (d) 24 h, respectively.

Figure 4-16 shows SEM pictures from the pre-corroded specimens in under-aged condition after tensile testing. The right column of the figure provides a general view of the fractured specimens for 0.5, 4, 24 hours (in different rows) of corrosion exposure where a ductility-based fracture mechanism is evident from the 45° inclination of the fracture surface. It can be noticed that pitting density in the large, exposed surfaces of the specimens increase with increasing exposure time, leading to exfoliation after 24 hours. Regarding fracture surface shown in the left column of the figure, it is evident that the specimen exposed to corrosion for 0.5 hours is characterized by several dimples in the whole surface interrupted by some smooth surfaces in the edge of the specimen's surface. With increasing exposure time, the smooth surfaces are expanded to the specimen's thickness along with formation of micro-cracks up to a maximum depth shown for 4 and 24 hours. Additionally, fracture resembling cup and cone geometry can be noticed after 24 hours of corrosion.

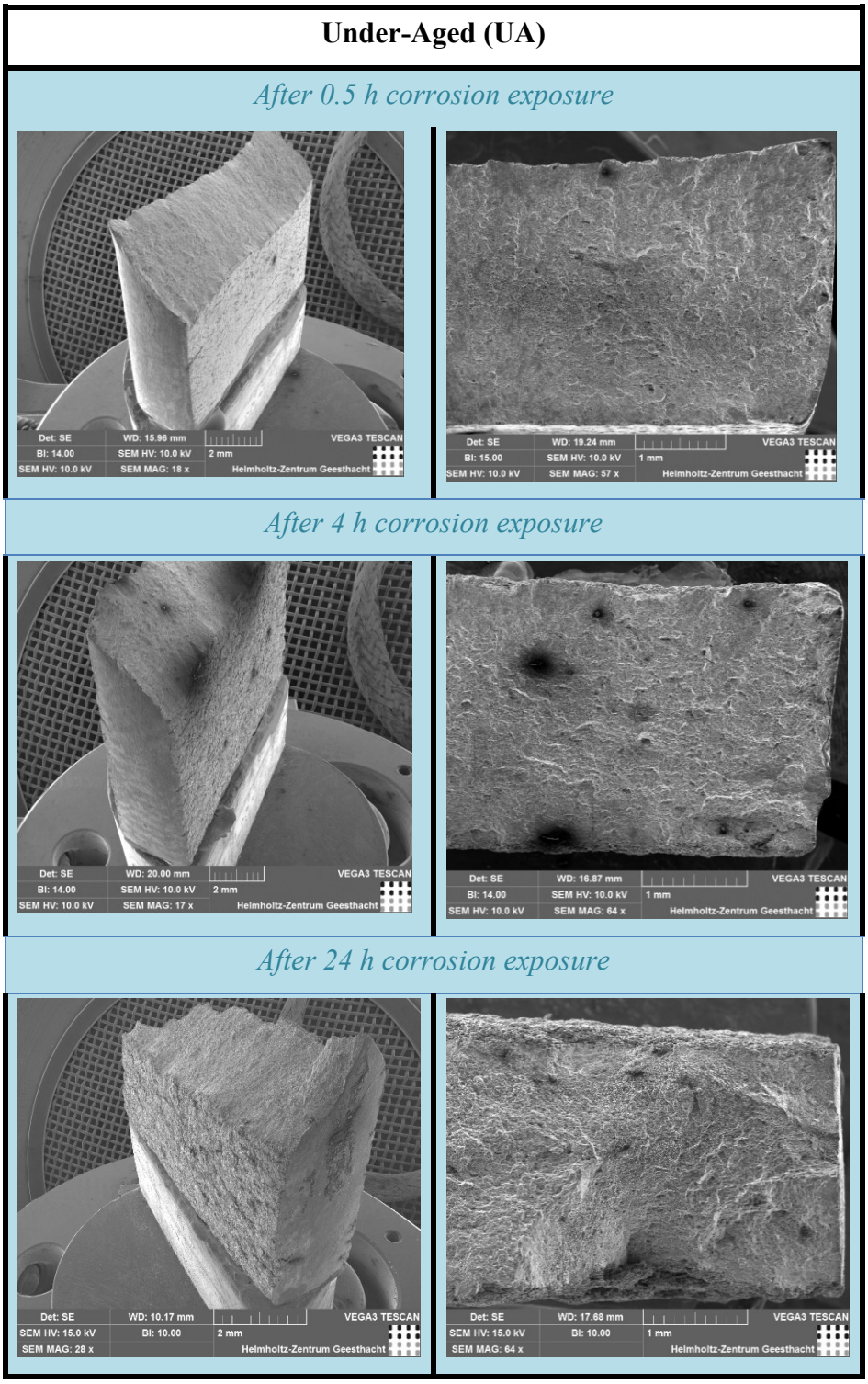

Figure 4-16: SEM images of artificially aged specimens of AA2024 in UA condition for (a) 0.5 h, (b) 4 h and (c) 24 h of exposure to EXCO solution.

Figure 4-17 presents the SEM images of the fractured specimens exposed to peak-aged temper and afterwards to exfoliation corrosion solution. Right column provides the general view of the fractured specimens corroded for 0.5, 4, 24 hours (in different rows) where a ductility-based fracture mechanism is still evident from the 45° inclination of the fracture surface up to the highest exposure time. An increase in pitting density on the large, exposed surfaces is evident with increasing exposure time. The fractured surfaces of the PA specimens are characterized by dimples for all the investigated

exposure times. Additionally, the existence of some smooth areas next to the exposed surface is evident; however, these areas expand to a less extend into the specimen's thickness than in the case of UA condition. Furthermore, there is no notable crack propagation along the thickness of the specimens - as was the case for UA temper - that could reduce the specimens' effective thickness significantly. This observation is in accordance with the tensile test results, where the yield stress is not essentially reduced by corrosion evolution for the peak-aged specimens. Regarding over-aged specimens shown in Figure 4-18, the fractured surfaces are characterized by large smooth surfaces with the dimples to be concentrated to the middle thickness. There are no notable differences between the different exposure times, meaning that fracture mechanism is not essentially changed by corrosion evolution. Cracking formation is obvious, but the cracks do not propagate deep into material.

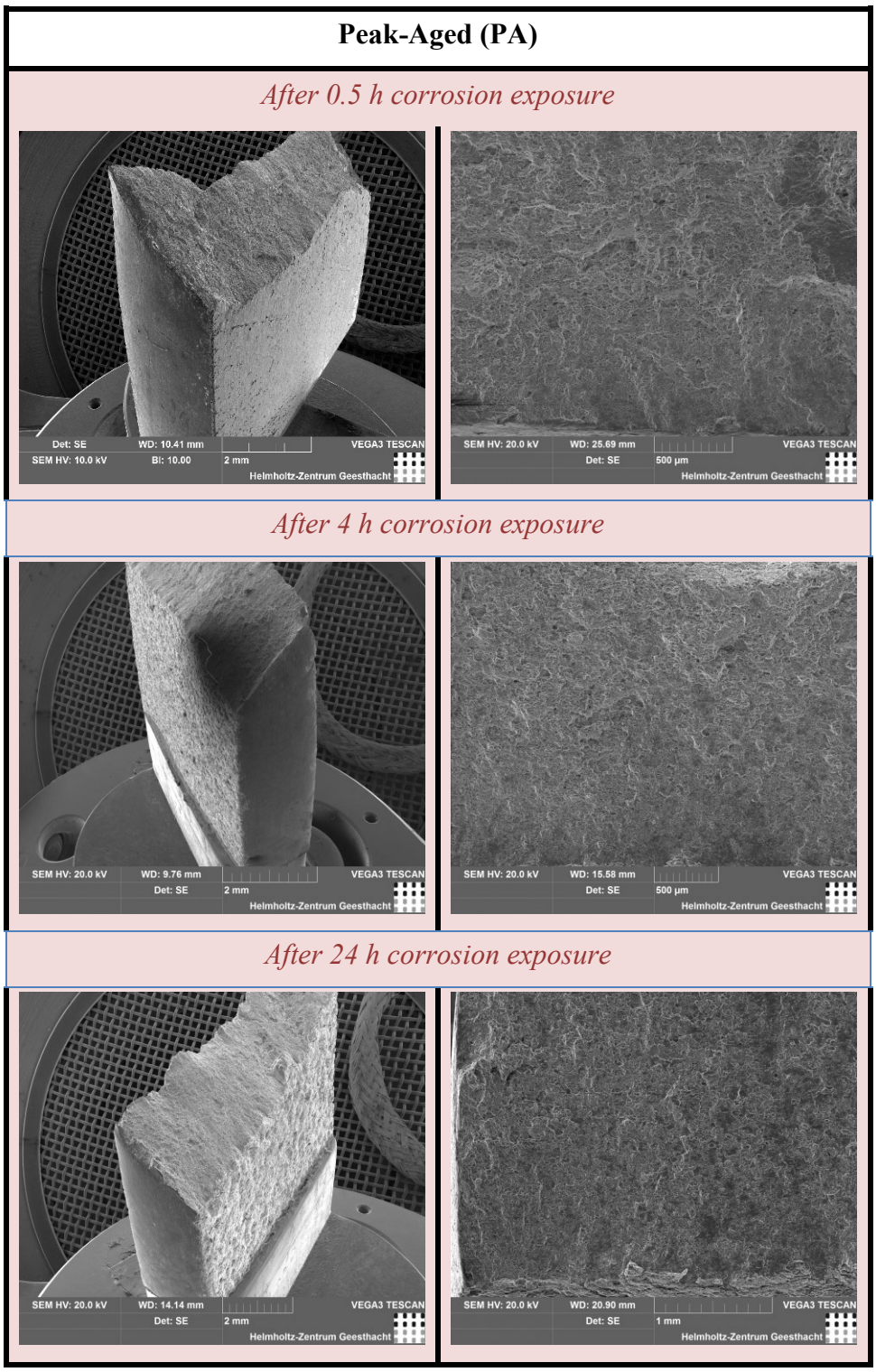

Figure 4-17: SEM images of artificially aged specimens of AA2024 in PA condition for (a) 0.5 h, (b) 4 h and (c) 24 h of exposure to EXCO solution.

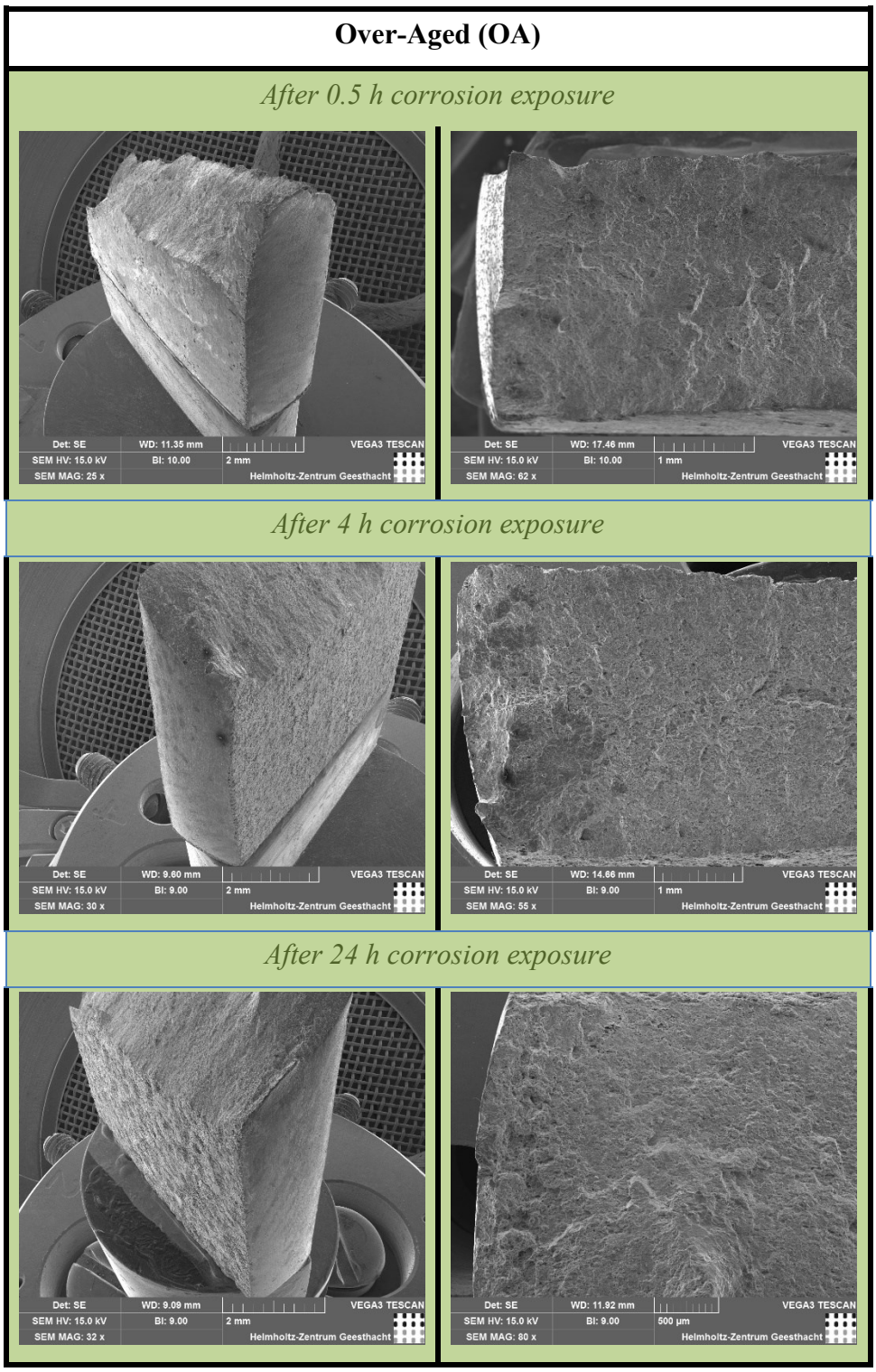

Figure 4-18: SEM images of artificially aged specimens of AA2024 in PA condition for (a) 0.5 h, (b) 4 h and (c) 24 h of exposure to EXCO solution.

4.3.6 AA2198: Microscopic evaluation of artificial aged specimens: Analysis of the precipitates

Precipitation morphology and growth characteristics with respect to artificial ageing times are depicted in Figure 4-19 and Figure 4-20. A selected-area diffraction (SAD) pattern, which is corresponding to the <110> matrix zone axis is inserted to each corresponding figure. In Figure 4-19,

where the low magnification TEM bright field (BF) images of AA2198 are depicted, grain boundaries precipitates are well defined for all investigated artificial ageing tempers. The level of such precipitates was found to be lower for the case of T3 and UA tempers, *e.g.*, Figure 4-19(a) and Figure 4-19(b), respectively. With increasing ageing time significant higher population of elongated and thin T1 precipitates in the form of laths is evident both on grain boundaries and inside grains, *e.g.*, Figure 4-19(c). Regarding OA temper, shown in Figure 4-19(d), the density of T1 precipitates was further increased but their size was not essentially changed. Regarding T3 temper, few dot-shaped δ' (Al_3Li) phases were noticed in the <110> Al matrix, as it is shown in Figure 4-20(a). The δ' phase is one of the main secondary phases present in T3 temper [170], and the diffraction pattern fails to show the superlattice reflection characteristic of these precipitates due to the low quantity. The presence of T1 precipitates is evident for higher artificial ageing times, *e.g.*, Figure 4-20(b). The T1 has a hexagonal crystal structure, which forms with thin hexagonal platelets on the <111> Al matrix. Both the density and size of T1 precipitates tend to increase with artificial ageing time evolution as was also mentioned in [170] for AA2198. In higher ageing times that correspond to PA and OA conditions interactions between T1/T1 precipitates were also noticed. Figure 4-20(c) presents the cutting of vertical T1 phase from the horizontal while the latter is increasing. This observation is in accordance with [192] where T1 phase was found to increase in length instead of width after peak-ageing temper. The enhanced strength in PA condition can be also attributed to the intersection of T1/T1 precipitates due to the high strain fields formed around these areas that can impede the dislocations movements [192]. The interactions between these precipitates were also discussed for Al-Cu-Li alloys in [124].

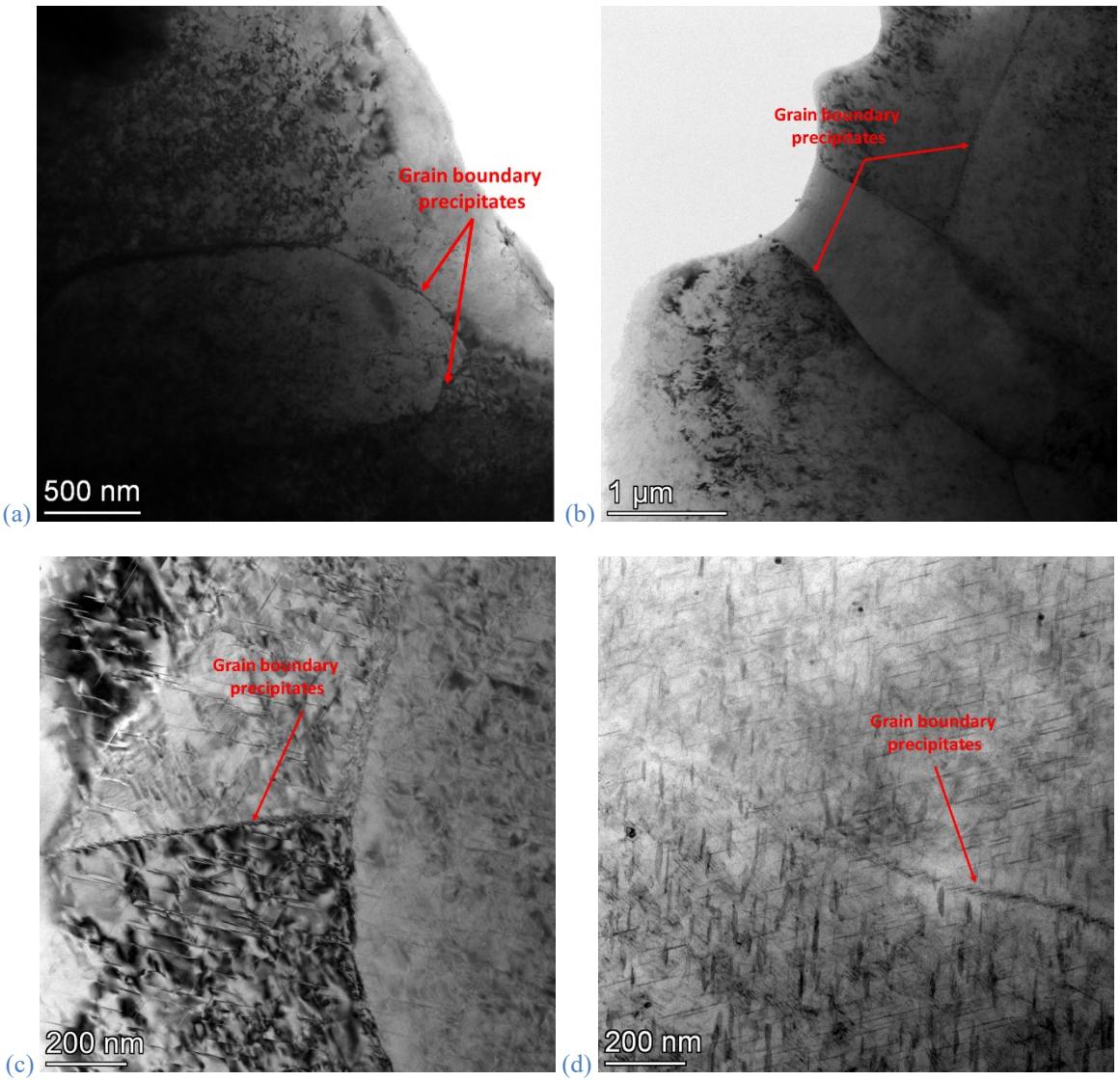

Figure 4-19: Bright field images of AA2198 grain boundary precipitates for (a) T3 temper, (b) under-aged (3 h @ 170°C), (c) peak-aged (48 h @ 170°C) and (d) over-aged (400 h @ 170°C).

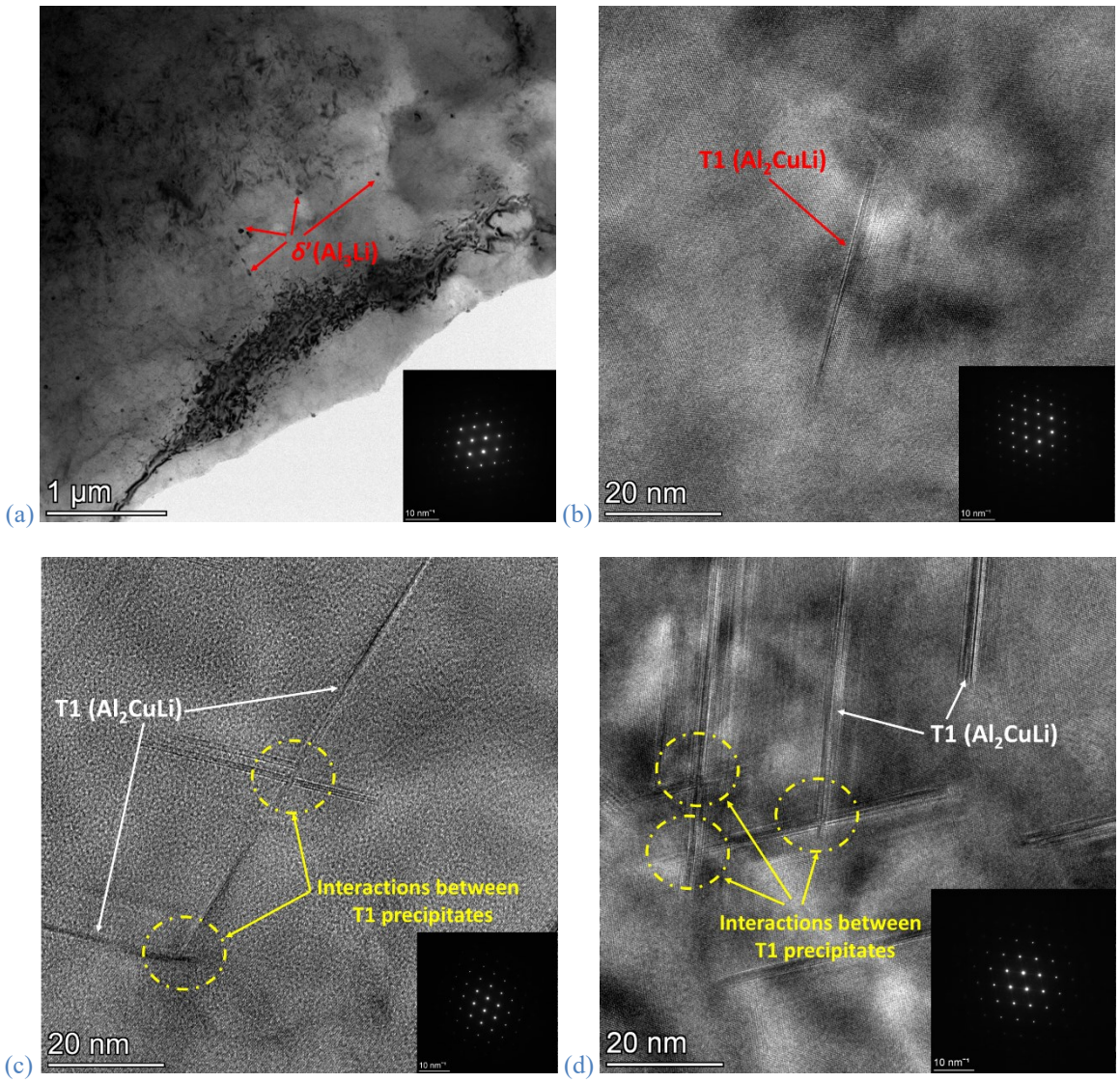

Figure 4-20: TEM bright field images of AA2198-T3 along <110> zone axis for (a) T3 temper, (b) under-aged, (c) peak-aged and (d) over-aged specimens with the corresponding selected-area diffraction pattern.

4.3.7 AA2198: Effect on corrosion mechanism

Figure 4-21 presents the impedance spectra of AA2198 for the different artificial ageing times in the form of Bode plots. Two time constants, located at low (10^{-2}-10^{-1}) and medium (10^{0}-10^{3}) frequencies regime, are evident from the initial period of immersion for all investigated artificial ageing tempers. Slight fluctuations of the curves at low frequencies regime − in the figure where Theta phase vs. frequency are presented − can be caused by non-stationarities of the system at this period resulted from the metastable pitting formation. These fluctuations are evident up to 1 hour of exposure (red curve) in T3 temper, up to 6 hours (blue curve) in UA temper and at the initial period of immersion (black curve) in T8 temper while by increasing artificial ageing time the formation of stable pits becomes faster (no fluctuations noticed in PA and OA conditions). For the case of UA, PA and OA conditions, at the initial period of immersion (black curve) the relaxation process at higher frequencies being responsible for the response from the passive film can also be evidenced while this

was not the case for T3 and T8 tempers. Impedance modulus of specimens in T3 temper was notably decreased from the first stages of corrosion, *e.g.*, 1 hour (red curve), followed by a gradual decreasing trend for higher exposure times. Similar behaviour is observed for UA specimens; essential degradation was noticed from the first stages of exposure and up to 6 hours (green curve) while further immersion did not reduce the impedance modulus significantly since by that time stable pits are formed, and the corrosion process is controlled by the diffusion limited cathodic oxygen reduction. The same trend was observed for T8 temper; the main difference is that the stabilization of the pits occurs after shorter time than in T3 and UA tempers and impedance modulus almost remains unaffected for short exposure times up to 3 hours. The measurement performed after 12 hours demonstrates a clear drop of low frequency impedance value and absence of data scattering related to the metastable pits. Regarding specimens in PA temper, the impedance modulus at low frequencies almost remains unaffected by corrosion for short exposure times and up to 6 hours. Furthermore, increasing of immersion time did not result to significant changes in impedance modulus. In over-aged temper fluctuations were noticed, with a notable decrease to be observed for the time range between 0 to 6 hours 12 to 24 hours of exposure.

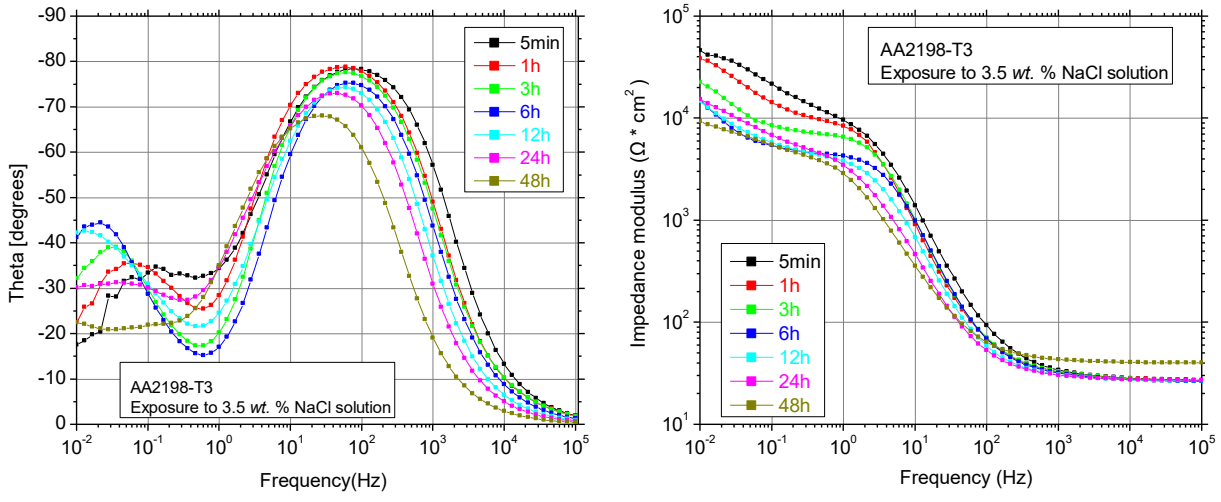

(a)

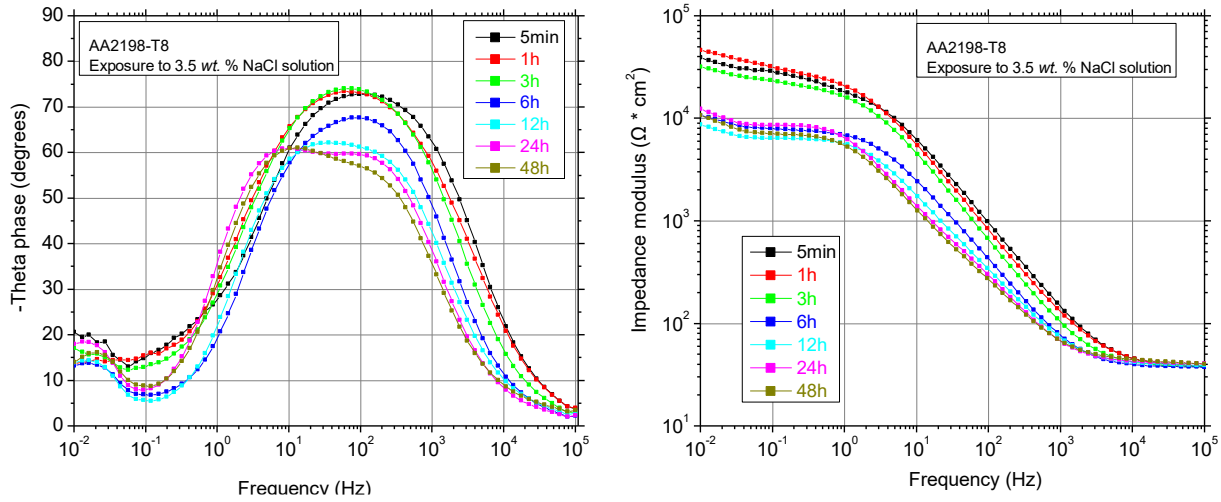

(b)

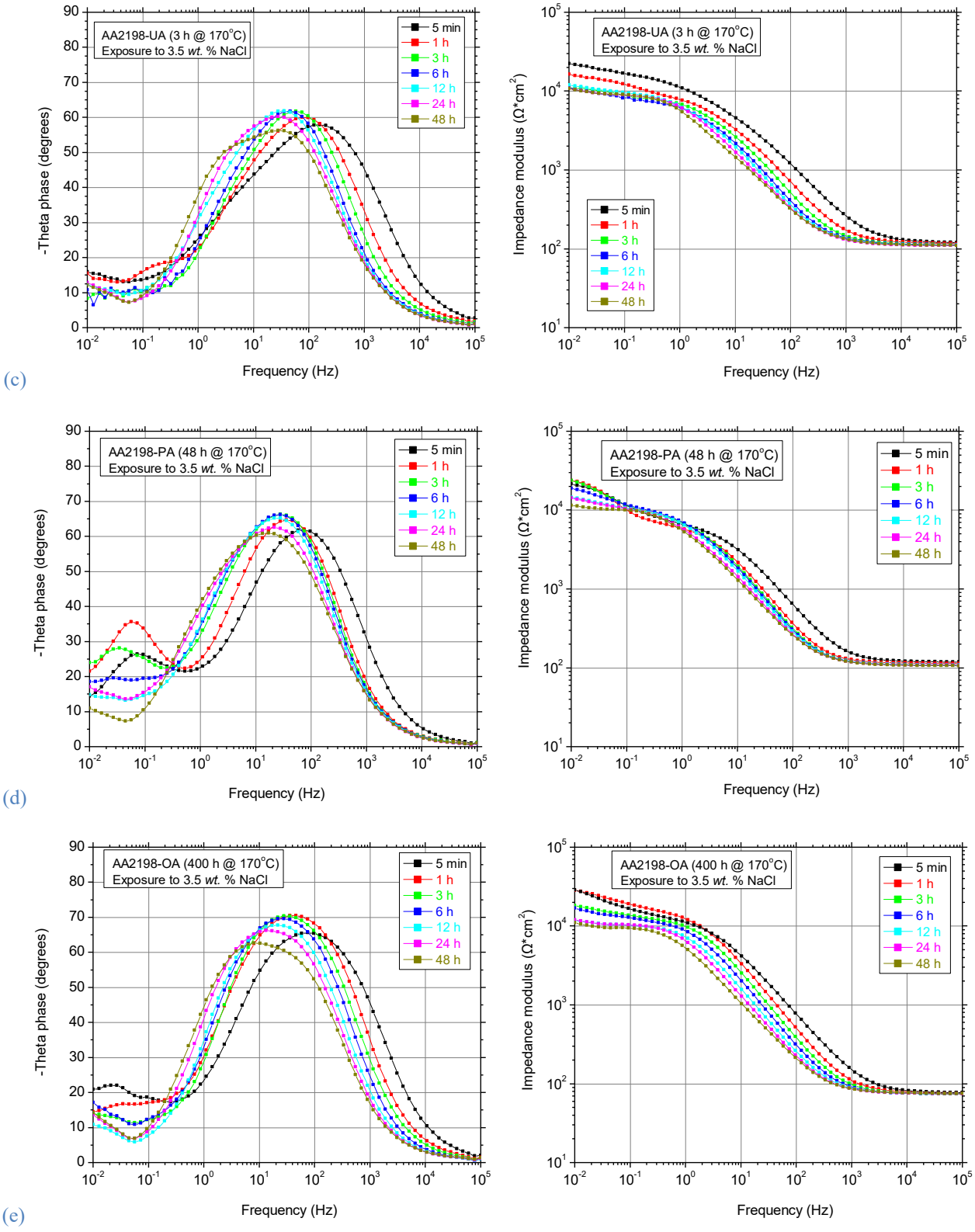

Figure 4-21: Impedance spectra of AA2198 in (a) T3, (b) T8, (c) UA, (d) PA and (e) OA temper measured in 3.5 wt. % NaCl solution.

The simple Randless circuit model was found to better simulate the EIS response of AA2198 for all exposure times and artificial ageing tempers, Figure 4-22. It is worth mentioning, that the same equivalent model was used for AA2024 (see section 4.3.2). At short exposure times in PA condition another equivalent circuit model with an extra constant phase element ($R//Q$) that corresponds to

oxide film resistance in parallel with conductive pathways associated with defective sites created by intermetallic particles (IMCs) showed good fitting. Nevertheless, the simple circuit model that better simulates most of the investigated cases used in this research work to simulate corrosion mechanism in AA2198 specimens.

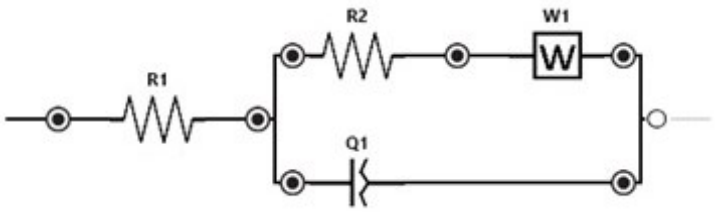

Figure 4-22: Equivalent circuit model for all ageing tempers of AA2198.

Figure 4-23 presents the evolution of charge transfer resistance values of the circuit components (R_2 in this case). Charge transfer resistance represents the resistance of electron flow on aluminium surface. Resistance was found to essentially decrease even from the early stages of corrosion for the T3 specimens and with high rate up to 12 hours; for instance, a decrease from approximately 55000 $\Omega*cm^2$ at the initial immersion period to 8000 $\Omega*cm^2$ after 12 hours of immersion was noticed. However, for higher exposure times (> 12 hours) R_2 was stabilized at values that almost reached the respective values of artificially aged specimens since by that time stable pits have formed. A similar trend is evident for the T8 temper where R_2 quickly decreases up to 6 hours immersion time. Nevertheless, for the early stages of exposure of T8 specimens and up to 1 hour a slight increase in charge transfer resistance is evident suggesting a difficulty in electron flow. Almost the same trend is presented for UA condition with the difference that R_2 slightly decreases from the first stages of corrosion and up to 3 hours while a higher decrease is noticed after 6 hours. Further increase in immersion time did not affect the resistance essentially. Regarding PA and OA tempers, no essential changes in charge transfer resistance were noticed with increasing corrosion exposure time revealing that the specimens in these tempers are not significantly affected by corrosion evolution. A slight increase in charge transfer resistance at the early exposure times, indicating some kind of blocking effects on electron flow on the surface, is also evident in these tempers with the increasing trend to be evident up to 3 hours for PA and up to 1 hour for OA. The higher values of R_2 noticed at short exposure times of T3 specimens point out a slower charge transfer on specimens' surface when compared to artificially aged specimens. Additionally, it can be noticed that the corrosion-induced degradation rate of R_2 tends to decrease with increasing artificial ageing time indicating a slower corrosion propagation.

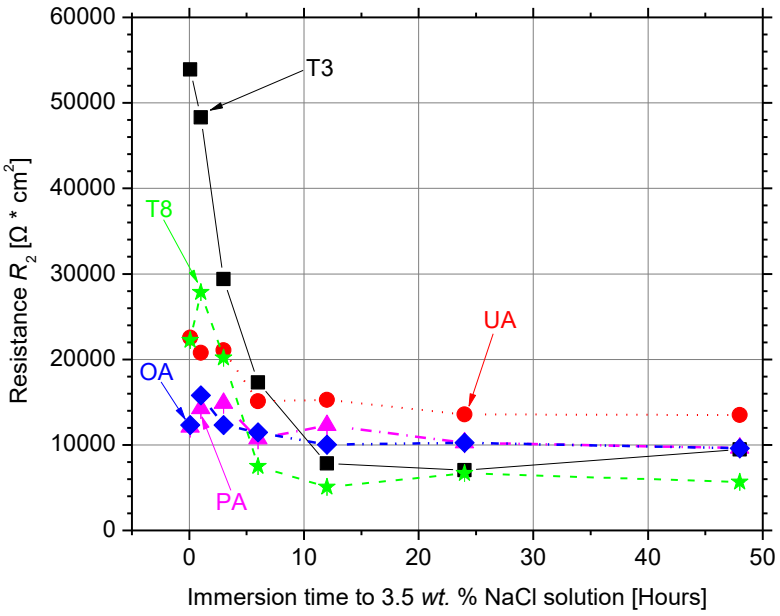

Figure 4-23: Variation of charge transfer resistance R_2 element as a function of immersion time to 3.5% wt. NaCl solution for AA2198 in different artificial ageing tempers.

Figure 4-24 presents the OCP curves of AA2198 specimens in different ageing tempers measured in Harrison's diluted solution. The duration of OCP measurements was 30 min for all specimens. An essential decrease (shift to less noble) values was noticed with increasing artificial exposure time. However, more noble OCP value was observed for T8 temper when compared to the other tempers, including T3. Different behaviour of the OCPs was noticed for the different tempers. The OCP seems to stabilize earlier with increasing artificial ageing time; while slight fluctuations noticed in PA condition can be correlated to transient currents due to the pitting process.

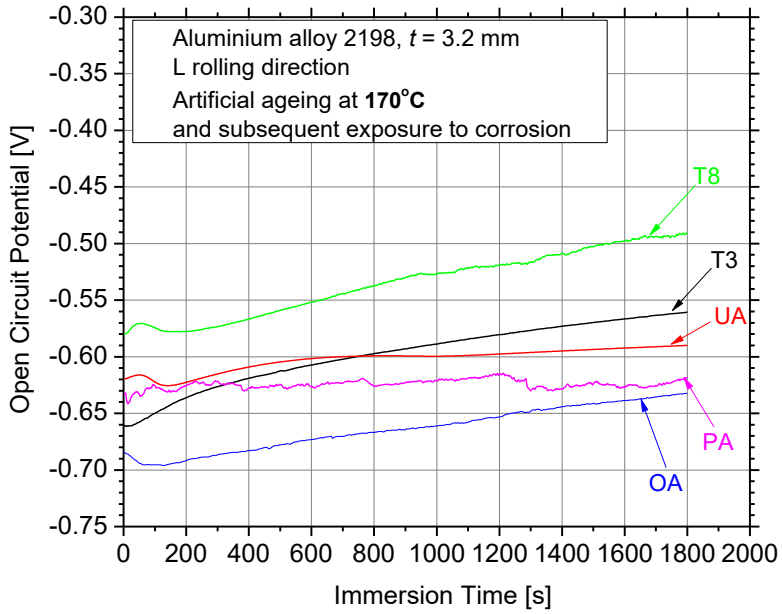

Figure 4-24: Comparison of the open circuit potential curves of AA2198 specimens in different artificial ageing tempers.

Potentiodynamic polarization measurements for the different artificial ageing tempers of AA2198 are presented in Figure 4-25. The current-potential curves have almost the same shape for all investigated tempers with the two branches (cathodic and anodic) of the potentiodynamic polarization curves to be nearly asymmetrical. The cathodic branch of the polarization curve includes information regarding the kinetics of the reduction reactions taking place on the specimen's surface. In this case the cathodic branch corresponds to the diffusion-controlled reduction of dissolved oxygen (O_2). In general, in the cathodic branch the potential applied by the potentiostat is more negative than the corrosion potential (E_{corr}) of the specimen; thus, actually the specimen is protected from attack by the corrosion medium, which was the cathodic protection effect. In the anodic branch of the curve, the applied potential is more positive than the E_{corr} of the working electrode; thus, the specimen loose the electrons and release the metal ions that react with the hydroxyl ions distributed in the solution to combine and generate corrosion products of hydroxides. Additionally, presence of passivation plateau is evident in all different tempers, in the region where current density is independent of potential, as well as the breakdown points of the passive film where the current density starts to increase again with increasing potential. It can be noticed from Figure 4-25 that the current density at which breakdown of passive film takes place is slightly decreases with increasing artificial ageing time. The corrosion potential shifts to more negative values with increasing artificial ageing time, meaning that the specimens become more susceptible to corrosion attack. This can be attributed to the precipitation of second-phase particles that are cathodic with respect to the matrix and trigger corrosion nucleation at their periphery. However, the artificially aged specimens exhibited lower cathodic activity than T3 specimens indicating lower corrosion rate.

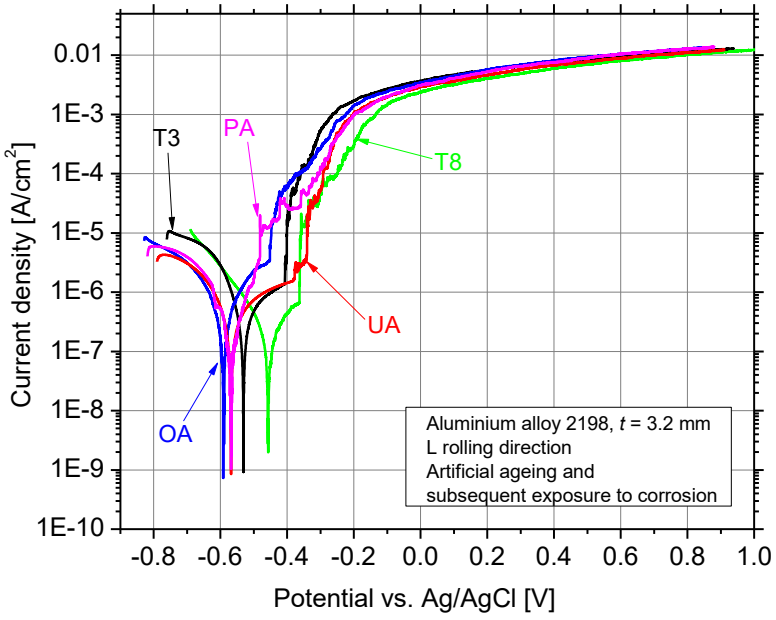

Figure 4-25: Polarization curves of AA2198 in different artificial ageing tempers.

4.3.8 AA2198: Mechanical evaluation of pre-corroded specimens

Prior to the characterization and evaluation of the corrosion-induced mechanical properties degradation of artificially aged specimens of AA2198, it is necessary to examine the effect of artificial ageing in the aluminium alloy in order to have reference data. According to Figure 4-26, the total tensile behaviour of AA2198 changes under different artificial ageing times at 170°C. These changes are related to transformations in microstructure during ageing and the precipitation of intermetallic phases [7], [191]-[192]. For instance, the specimens' axial nominal stress increases with increasing ageing time when it reaches its maximum value after 48 hours. On the other hand, the axial nominal strain continuously decreases with increasing ageing time up to the same exposure hours. Thus, the 48 hours artificial ageing time is considered to belong to the peak-ageing region for AA2198 at 170°C. Further increase in ageing time above 48 hours resulted in degradation of axial nominal stress while a slight recovery of the axial nominal strain was noticed.

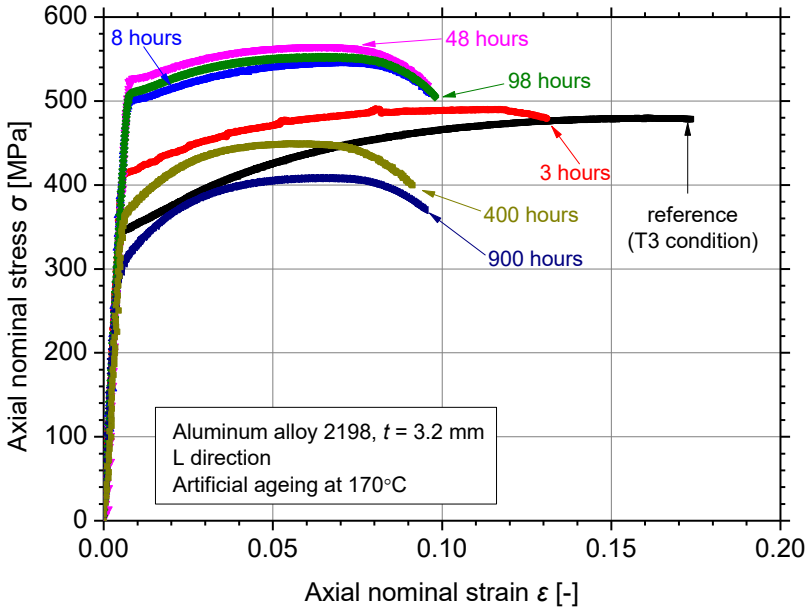

Figure 4-26: Typical tensile stress-strain curves of AA2198 for different artificial ageing times.

Figure 4-27 summarizes the experimental results of conventional yield stress $R_{p0.2\%}$, ultimate tensile strength R_m and elongation at fracture A_f of the artificially aged AA2198 specimens as average values. Marked in the diagram are the regimes of under- (UA), peak- (PA) and over-ageing (OA) conditions as a function of ageing time with different colours of background. According to Figure 4-27(a) a rapid increase in both $R_{p0.2\%}$ and R_m values is noticed in the under-ageing regime and up to 8 hours of exposure to 170°C. After 8 hours these properties are still increasing but with lower rate up to 48 hours where the maximum percentage of increase is noticed, *e.g.*, +17% for the ultimate tensile strength (red open circles and fitting curve) and +51% for the conventional yield stress (black open squares and fitting curve). For higher ageing times (> 48 hours) a rapid decrease is evident for

both properties that represents the over-ageing regime. This decrease is caused by the coarsening and growth of the precipitates as was also mentioned in [119], [157], [180]. Regarding the response of elongation at fracture with increasing artificial ageing time, *e.g.*, Figure 4-27(b), it is shown that the A_f is continuously decreases up to 48 hours with the higher percentage of decrease to be approximately 46%. However, higher degradation percentage is noticed in the first hours of ageing and up to 8 hours; thus, this time range is believed to be the under-ageing regime. Further increase of ageing time above 48 hours led to fluctuations of A_f with a slight recovery to be noticed so as to characterize this region as over-ageing.

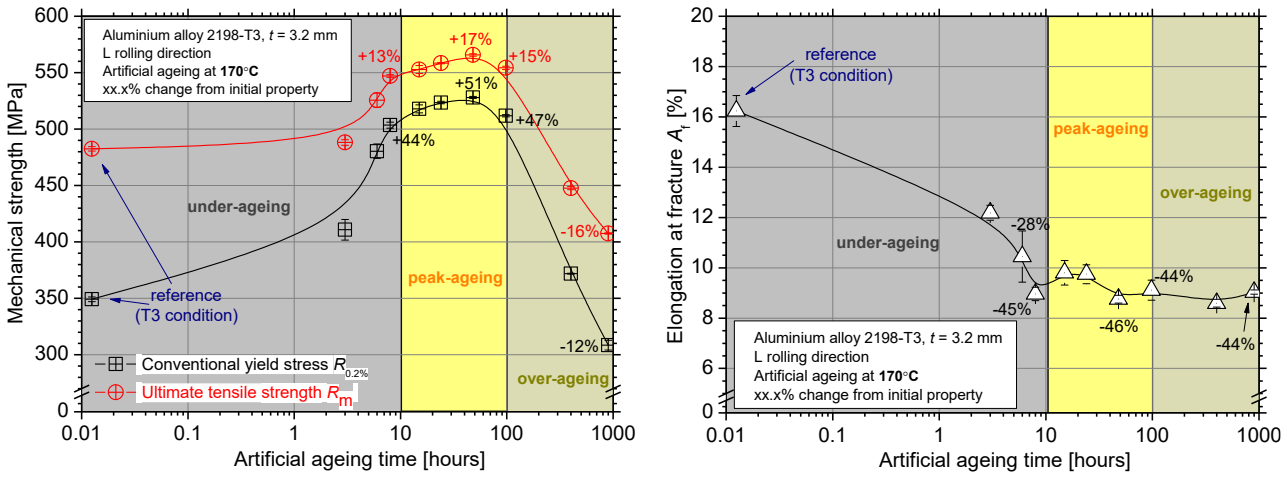

(a) (b)

Figure 4-27: Evaluated mechanical properties (a) conventional yield stress $R_{p0.2\%}$ & ultimate tensile strength R_m and (b) elongation at fracture A_f of AA2198 specimens in different artificial ageing times.

In order to assess the response of different artificial ageing tempers of AA2198 on corrosion and estimate the synergetic phenomena that can lead to material's failure, exposure of specimens to exfoliation corrosion (EXCO) solution was performed. The EXCO solution was selected in this investigation for both time saving reasons, since according to Alexopoulos et *al.* [86] 1 hour exposure to EXCO solution is equivalent to 92 hours exposure to 3.5 *wt.* % NaCl solution regarding elongation at fracture decrease, and for comparison with AA2024 [63]; the effect of artificial ageing on the corrosion behaviour of AA2024 was investigated by exposing the artificially-aged specimens for 2 hours to EXCO solution [63]. It is worth mentioning, that the 2 hours EXCO exposure were selected because according to the findings of Alexopoulos et *al.* [63] and [110] a noteworthy corrosion-induced degradation of elongation at fracture was noticed for this exposure time despite of the fact that no essential pitting corrosion attack was evident. Furthermore, a significant corrosion-induced degradation of charge transfer resistance of AA2198 at short exposure times was revealed by the electrochemical tests performed in this chapter (see section 4.3.7).

As can be seen in Figure 4-28 to Figure 4-30 the degradation of both strength properties and ductility due to exposure to EXCO solution for 2 hours is approximately the same for all the investigated artificial ageing times. Figure 4-29 demonstrates that the corrosion-induced degradation of the conventional yield stress $R_{p0.2\%}$ and elongation at fracture A_f of AA2198 does not presents significant differences among the different artificial ageing time. However, slightly higher corrosion-induced degradation is evident in the under-ageing regime for both properties but in general the degradation can be characterized as stable in the whole artificial ageing time range.

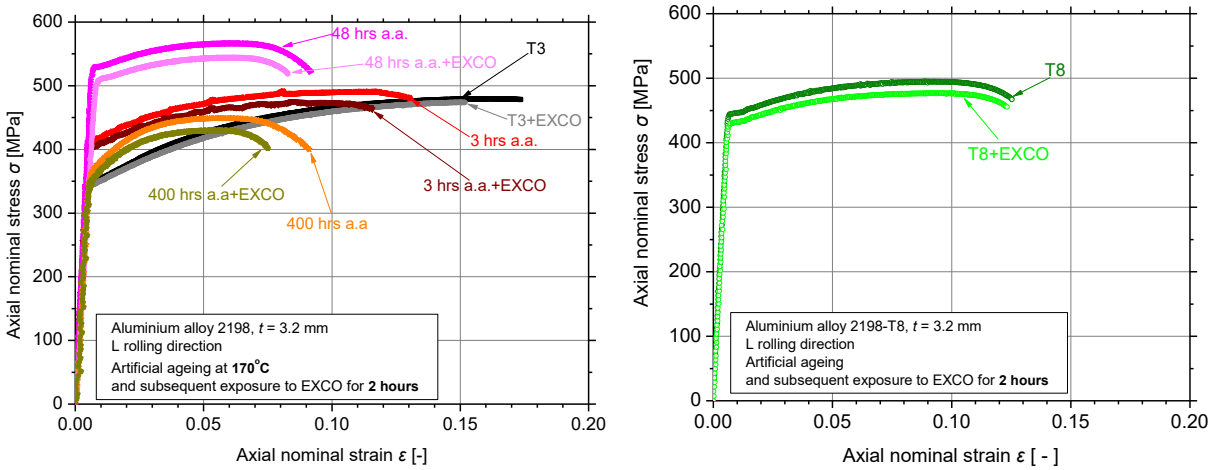

(a) (b)

Figure 4-28: Typical tensile stress-strain curves of AA2198 for (a) different artificial ageing times at 170°C and (b) T8 temper directly compared to artificially aged and subsequent corroded specimens for 2 h to EXCO solution.

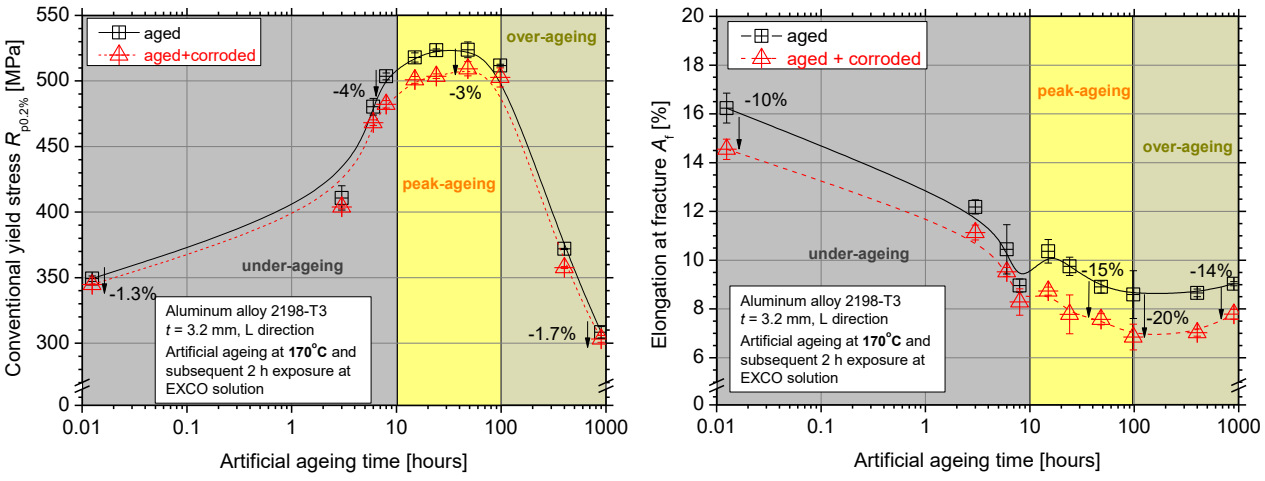

(a) (b)

Figure 4-29: Comparison of evaluated mechanical properties (a) conventional yield stress $R_{p0.2\%}$ and (b) elongation at fracture A_f between artificially aged at 170°C AA2198 specimens and artificially aged with subsequent corrosion for 2 h to EXCO solution.

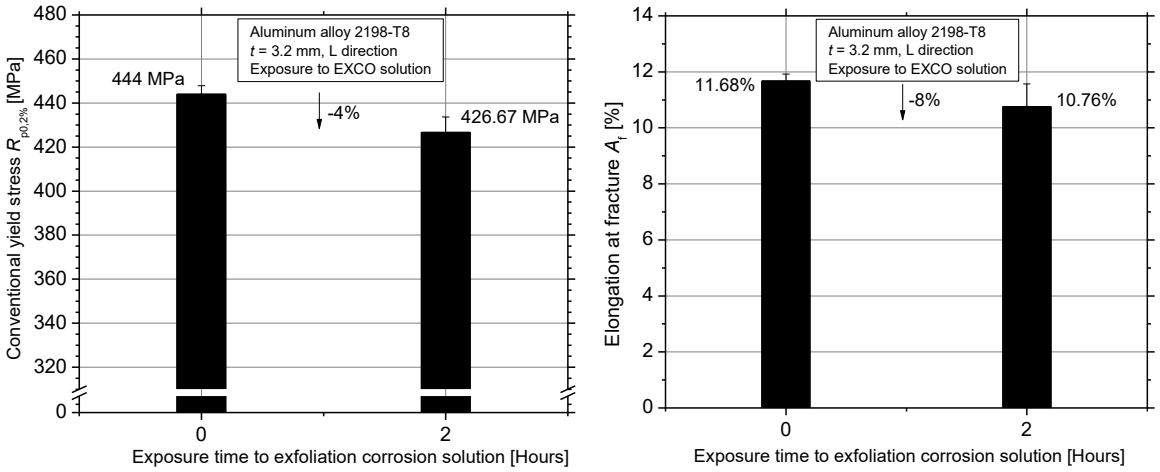

(a) (b)

Figure 4-30: Effect of 2 h exposure to EXCO solution on the evaluated mechanical properties (a) conventional yield stress $R_{p0.2\%}$ and (b) elongation at fracture A_f of AA2198 in T8 temper.

4.3.9 AA2198: Effect on corrosion evolution

In the previous section of this chapter (section 4.3.8) the effect of corrosion exposure on the mechanical performance of AA2198 specimens exposed to different artificial ageing times was investigated. However, only one hour of corrosion exposure, *e.g.*, 2 hours, was used for that study in order to eliminate the multiple corrosion mechanisms involved in higher exposure times. However, the electrochemical analysis presented earlier in this chapter (section 4.3.7) revealed differences in the corrosion kinetics for the different corrosion exposure times. These differences were more intense in the case of T3 and T8 temper that are the most common used commercial tempers of AA2198. Hence, these two tempers were selected for further investigation of the corrosion-induced degradation mechanism of their mechanical properties. The following analysis will be focused on the comparison of the corrosion-induced degradation only. According to Figure 4-31 an essential decrease of axial nominal strain is evident on both tempers after only 2 hours of exposure (*e.g.*, red curve); however further increase of corrosion exposure time above 2 hours does not decreases the axial nominal strain of AA2198 in T8 temper notably while for the case of T3 temper a continuous decreasing trend is observed. In contrast, the axial nominal stress seems not be essentially affected by corrosion exposure in T3 temper and for the whole exposure time range while for T8 temper a noteworthy reduction of axial nominal stress is observed after 6 hours of exposure. Nevertheless, this decrease is eliminated for higher exposure times.

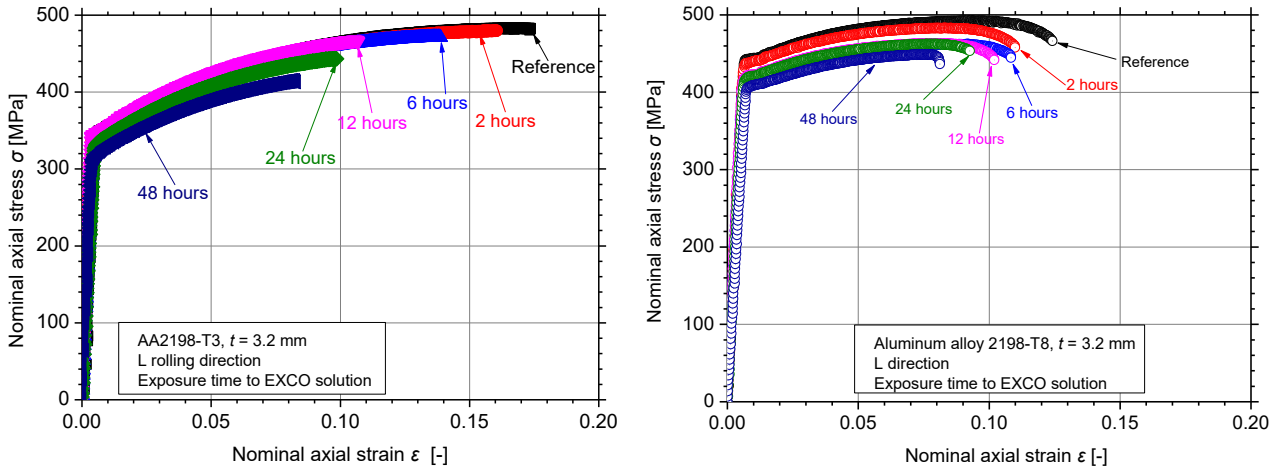

(a) (b)

Figure 4-31: Typical experimental tensile flow curves of pre-corroded for different exposure times to EXCO solution AA2198 specimens in (a) T3 and (b) T8 temper.

4.3.10 Comparison of AA2024 and AA2198

To justify the observations from the fractographic analysis of AA2024, a model is exploited to calculate the "effective thickness" of the specimens exposed for different times to EXCO solution. The "effective thickness" concept was introduced in a previous publication of the authors [48] and refers to the cross-section (and hence to the thickness of the specimen) that remains unaffected from the corrosion exposure, as the surface pits and micro-cracks essentially decrease the loading capability of the cross-section. The model was introduced in the previous chapter (chapter 3, section 3.3.3.1) and is referred as iso-modulus of elasticity based on the concept that the modulus of elasticity of the unaffected "non-corroded" material remains the same with the reference material. To this end, it utilizes the decrease of the tensile modulus of elasticity E of pre-corroded specimens to address the effective thickness calculation problem. It is well known that corrosion–induced degradation of AA2024 is attributed to synergy of cracking and hydrogen embrittlement. In case that hydrogen embrittlement phenomenon is not taken into consideration, because it is difficult to quantify, then the change in the slope of the nominal stress−strain tensile curves in the elastic region is attributed to cracking phenomena. Micro–cracking leads to reduction of the effective thickness of the specimen, according to Alexopoulos et *al.* [48]. It is thought that the true value of E of the specimen's effective thickness is independent of corrosion exposure time as it is supposed to be unaffected by corrosion. However, for the assumptions of the proposed model the modulus of elasticity depends solely on the effective thickness of specimens and not to other phenomena which may influence the material's property, such as loss of surface-elongated grains with increased work-hardening capability. Thus, the decrease in effective thickness calculated by the following equation (below):

$$B_j = \frac{B_0 \times E_j}{E_0} \qquad (4\text{-}1)$$

The results derived from the above-mentioned mechanical model are shown in Figure 4-32, where it is obvious that the specimens in under-aged temper (green curve) exhibited the higher decrease of the effective thickness while lower degradation was noticed for specimens in T3 and peak–aged conditions. There is no significant difference of the effective thickness of specimens in under-aged and over-aged tempers up to 0.5 hours corrosion exposure time, while after 2 hours of exposure specimens in over-aged temper exhibited slightly higher decrease of the effective thickness probably due to easier bypassing of precipitates from the dislocations coming from micro-cracks. Nevertheless, for long exposure times and after 4 hours corrosion exposure time the effective thickness of over-aged specimens tends to reach a plateau while for the case of under-aged specimens' effective thickness is continuously reduced.

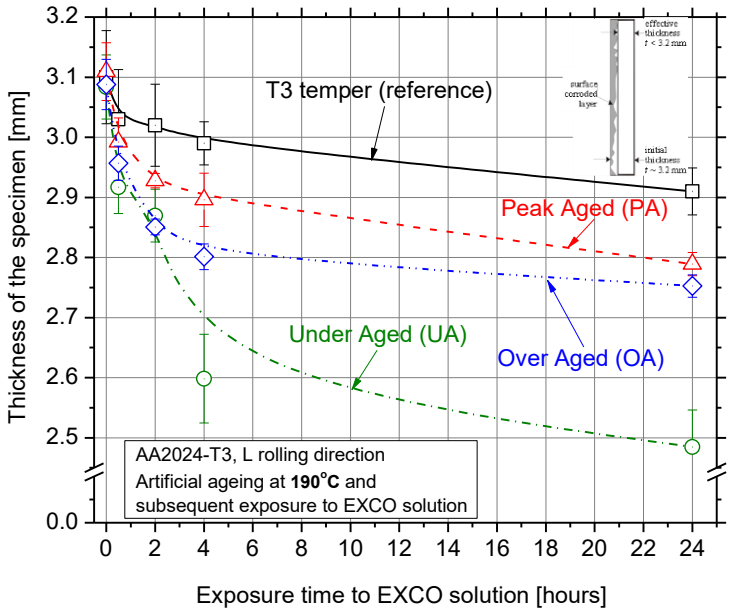

Figure 4-32: Decrease of the effective thickness for various investigated tempers and for different exposure time to corrosion solution.

Figure 4-33 summarizes the same results of the conventional yield stress and elongation at fracture as in Figure 4-11 shown in a different way, *e.g.*, as a function of corrosion exposure time instead of artificial ageing time, in order to highlight the corrosion-induced degradation evolution in different ageing tempers of AA2024. Marked in diagram are the regions of short exposure times (grey colour background) and long exposure times (yellow colour background) as were arbitrarily selected from the authors in the regions where the slope of the degradation curve is changed. It is evident from Figure 4-33(a) that the specimens in UA temper exhibited the highest corrosion-induced degradation of $R_{p0.2\%}$. The conventional yield stress of under-aged specimens is significantly decreased even from the early stages of corrosion exposure time (*e.g.*, 0.5 hours) and continued up to 24 hours reaching to

lower values than the respective in T3 condition. For the case of T3 condition the respective degradation is lower for short exposure times. However, for long corrosion exposure times (> 4 hours) the conventional yield stress seems to be stabilized probably because micro-cracks reached their maximum depth as was noticed in Alexopoulos *et al*. [85] and Charalampidou *et al*. [105] for the pre-corroded specimens of AA2024 with 0.4 mm and 1.6 mm nominal thickness respectively. Regarding PA and OA tempers, a notable decrease of $R_{p0.2\%}$ due to corrosion exposure is evident for up to 4 hours. Nevertheless, the respective degradation percentage of $R_{p0.2\%}$ with increasing corrosion exposure time is significantly lower when compared against under-aged and T3 conditions. Additionally, as was the case for T3 temper, the $R_{p0.2\%}$ tend to be stabilized in long corrosion exposure times. The lower corrosion-induced degradation of $R_{p0.2\%}$ in PA and OA tempers can be attributed to the blocking of the corrosion-induced cracks by the second-phase precipitates.

As for the case of elongation at fracture A_f the highest corrosion-induced degradation is noticed in UA temper followed by T3 (refer to Figure 4-33(b)). Significant degradation of the property is evident even from the short exposure times (*e.g.*, 0.5 hours) − where no essential surface pitting is evident (refer to Figure 4-3 to Figure 4-6) − that is attributed to hydrogen embrittlement phenomenon [78] and [104]. Elongation at fracture is continuously decreases up to the highest corrosion exposure time (*e.g.*, 24 hours) for under-aged and T3 tempers while for peak- and over-aged conditions the A_f seems not to be notably affected by corrosion for the whole exposure time range. Less but not least it should be referred that the curve fitting used in Figure 4-33(a) and Figure 4-33(b) − that better simulates the corrosion-induced degradation of the properties − is the exponential linear fitting and its mathematical type is included in the figures.

The same analysis was made for AA2198 in T3 and T8 tempers in Figure 4-34. Slightly higher degradation percentage of $R_{p0.2\%}$ was observed for T8 temper at short exposure times and up to 6 hours. For instance, the remaining percentage of $R_{p0.2\%}$ for the specimens in T8 temper was found to be approximately 93% while the respective percentage for T3 temper was approximately 98%. However, for higher exposure times (> 6 hours) the $R_{p0.2\%}$ was stabilized at around 410 MPa and further corrosion exposure of AA2198-T8 did not influence the property notably. On the contrary, regarding T3 temper the $R_{p0.2\%}$ almost remained unaffected by corrosion exposure up to 24 hours but a sudden drop noticed at the maximum exposure time of 48 hours where the remaining percentage of the property (≈ 92%) reached the respective in T8 temper.

A remarkable corrosion-induced degradation was noticed even from the short exposure times for the T3 specimens with respect to A_f. Approximately 20% degradation of the property was observed after 6 hours of corrosion exposure for the T3 temper while the respective decrease in T8 temper was noticed after 12 hours (≈ 23% decrease). Higher remaining percentage of A_f is evident for the T8

temper even after 24 hours while after 48 hours the property reduced to almost half from the initial value for both tempers.

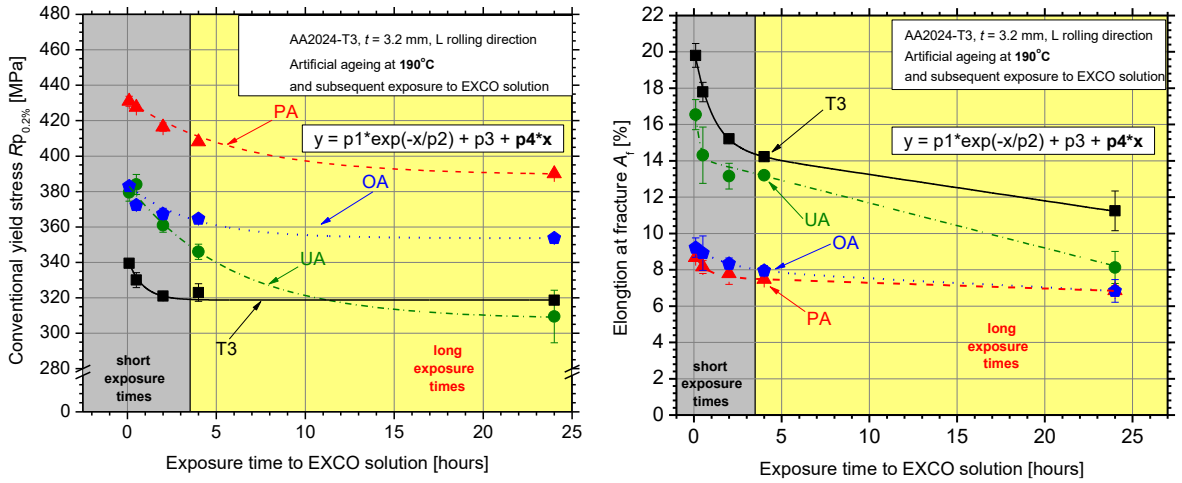

Figure 4-33: Degradation of the mechanical properties (a) conventional yield stress $R_{p0.2\%}$ and (b) elongation at fracture A_f of artificially aged AA2024 specimens due to EXCO-exposure for different exposure times.

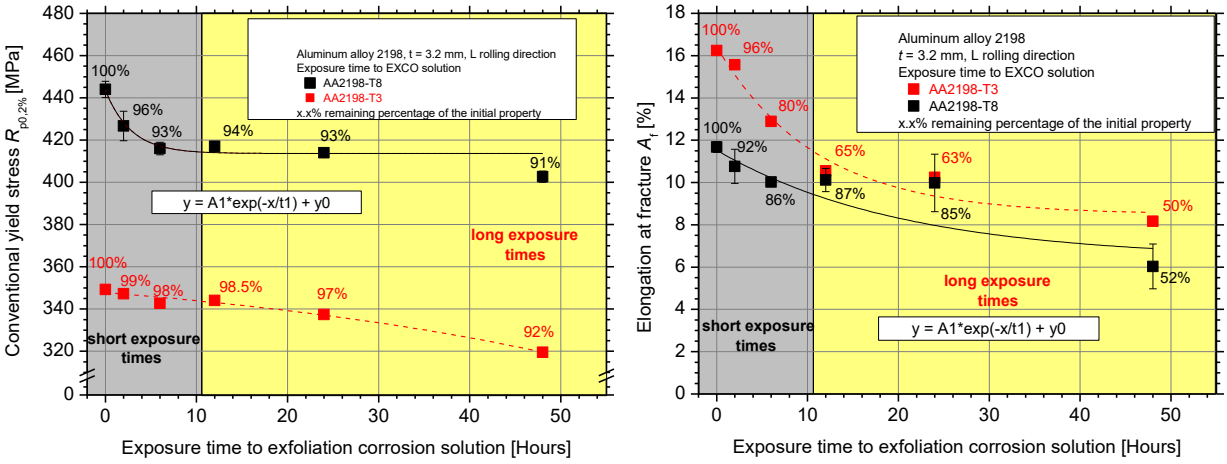

Figure 4-34: Degradation of the mechanical properties (a) conventional yield stress $R_{p0.2\%}$ and (b) elongation at fracture A_f of AA2198 specimens in T3 and T8 temper due to EXCO-exposure for different exposure times.

However, for the convenience of the readers logarithmic diagrams were also used to present the corrosion-induced degradation rate factor of the mechanical properties. It was calculated by the slope of degradation curves as shown in Figure 4-35 and Figure 4-36 for AA2024 and AA2198, respectively. It is obvious from Figure 4-35 that the slope of degradation curves of AA2024 is higher in UA condition for both, investigated mechanical properties ($R_{p0.2\%}$ and A_f) followed by T3 temper. More intense difference in the slopes of degradation curves for the different ageing tempers is noticed

for A_f. Concerning AA2198 no remarkable difference in the slope of the degradation curves of T3 and T8 temper is observed for both mechanical properties. Last but not least, the degradation curves of A_f are not simulated by linear decrease, as was the case for $R_{p0.2\%}$ in 2198 and for both properties in AA2024, since the proposed 2nd degree polynomial equation was found to give the best fit of the experimentally derived values, with all cases to have $R^2 \geq 0.9$.

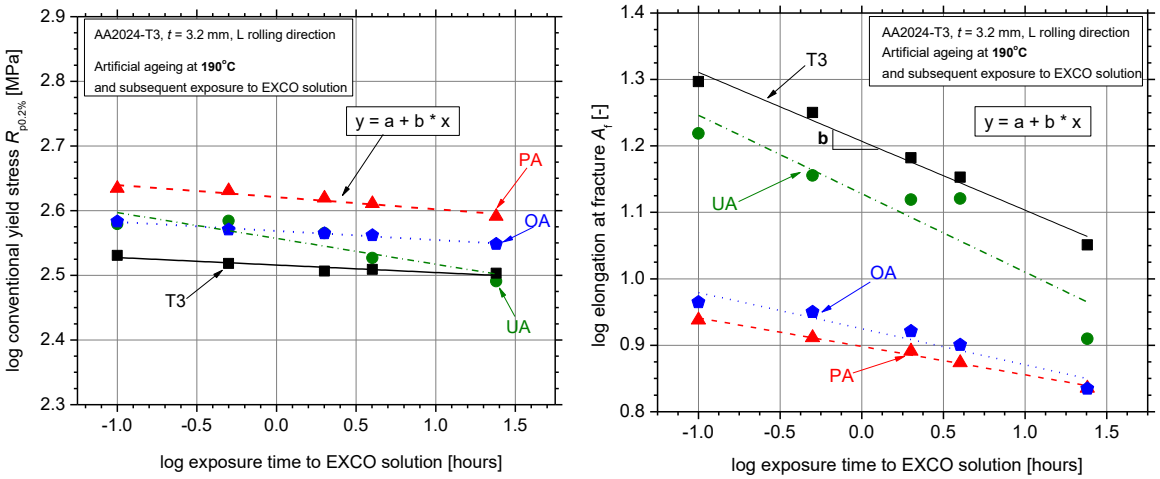

(a) (b)

Figure 4-35: Degradation rate factor of (a) conventional yield stress and (b) elongation at fracture Af of pre-corroded AA2024 specimens for different exposure times to EXCO solution in different artificial ageing tempers.

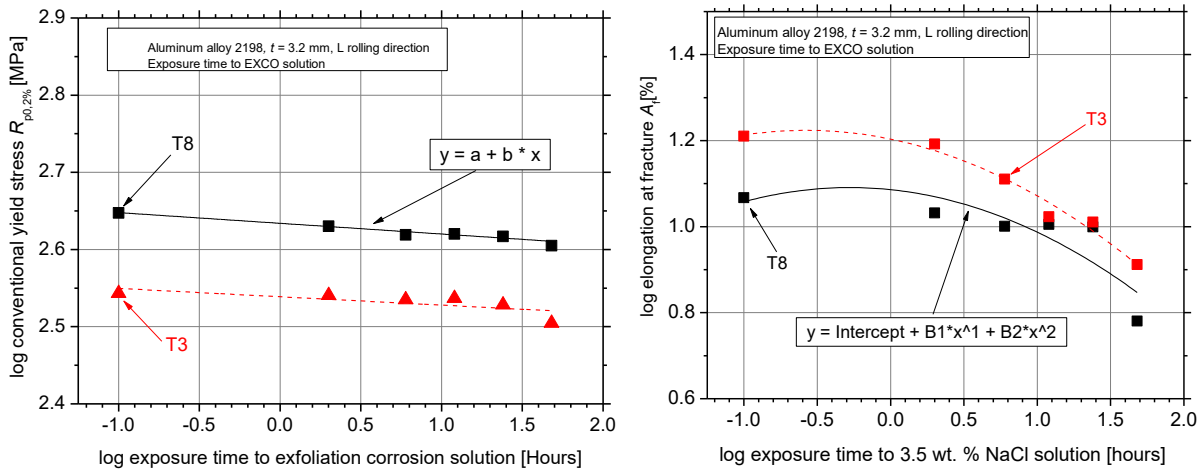

(a) (b)

Figure 4-36: Degradation rate factor of (a) conventional yield stress and (b) elongation at fracture Af of pre-corroded AA2198 specimens for different exposure times to EXCO solution T3 (red curve) and T8 (black curve) tempers.

The calculated slope values for AA2024 are summarized in Table 4-1 and Table 4-2, for the elongation at fracture and conventional yield stress respectively. According to Table 4-1 it is noticed that the UA temper exhibits the highest A_f degradation rate factor (*i.e.*, -0.11804), while the specimens in PA temper exhibited the lowest A_f degradation rate factor of approximately -0.04281. Thus, it seems that precipitates formed in PA condition impede corrosion evolution and therefore decrease

the degradation rate of the mechanical properties of the alloy. The same trend was noticed for the case of conventional yield stress in Table 4-2 but the lower degradation rate factor was noticed for T3 specimens. Hence, it seems that the UA temper exhibits the higher corrosion-induced degradation probably because of the nucleation of metastable phases that make the specimen unstable. As for the AA2198, the degradation rate factor of conventional yield stress shown in Table 4-3 was found to be slightly higher for T8 temper, however the difference can be considered as negligible. Concerning the degradation rate factor of elongation at fracture, it could not be directly calculated as in the case of linear regression. In order to gain information regarding the degradation rate in the 2nd degree polynomial regression both the average change of rate as well as the instantaneous rate of change were calculated and an average from the calculated values of each exposure time was extracted. The above analysis showed no significant difference in the degradation rate factor of A_f between the two investigated tempers of AA2198; nonetheless, T8 temper exhibited lower degradation rate. The slightly better results noticed in T8 temper can be attributed to the more finely dispersed precipitates and to its medium size that contribute to more effective blocking of the dislocations, since T8 was found to be in the region just before peak-ageing temper.

Table 4-1: Degradation rate factor values of elongation at fracture of pre-corroded AA2024 specimens for different artificial ageing tempers.

A_f [-]	Artificial ageing temper			
y = a + b*x	T3	UA	PA	OA
Degradation rate factor (Slope b)	-0.10377	**-0.11804**	-0.04281	-0.05438

Table 4-2: Degradation rate factor values of conventional yield stress of pre-corroded AA2024 specimens for different artificial ageing tempers.

$R_{p0.2\%}$ [MPa]	Artificial ageing temper			
y = a + b*x	T3	UA	PA	OA
Degradation rate factor (Slope b)	-0.01159	**-0.03996**	-0.01869	-0.01394

Table 4-3: Degradation rate factor values of conventional yield stress of pre-corroded AA2198 specimens T3 and T8 tempers.

$R_{p0.2\%}$ [MPa]	Artificial ageing temper	
y = a + b*x	**T3**	**T8**
Degradation rate factor (Slope b)	-0.01079	**-0.01386**

Table 4-4: Degradation rate factor values of elongation at fracture of pre-corroded AA2198 specimens T3 and T8 tempers: Calculation of average rate of change.

Af [%]	Artificial ageing temper	
y = Intercept + B1*x + B2 * x^2	**T3**	**T8**
Exposure time [Hours]	Average rate of change from the initial value	
2	-0.01	-0.03
6	-0.06	-0.04
12	-0.09	-0.03
24	-0.08	-0.03
48	-0.11	-0.11
Average	-0.07	-0.05

Table 4-5: Degradation rate factor values of elongation at fracture of pre-corroded AA2198 specimens T3 and T8 tempers: Calculation of instantaneous rate of change.

***Af* [%]**	**Artificial ageing temper**	
y = Intercept + B1*x + B2 * x^2	**T3**	**T8**
Exposure time [Hours]	Instantaneous rate of change / Slope	
2	-0.11	-0.07
6	-0.17	-0.13
12	-0.20	-0.17
24	-0.24	-0.21
48	-0.28	-0.25
Average	-0.20	-0.17

4.4 Conclusions

1) The macroscopic evaluation of pre-corroded specimens − for different exposure times to EXCO solution − revealed that specimens in T3 and under-ageing (UA) conditions exhibited localized corrosion attack which evolved to exfoliation with increasing exposure time. On the contrary, more uniform corrosion attack to the whole exposed surface of the specimens - due to precipitation distribution - is noticed in PA and OA tempers, while no significant differences on the surface deterioration is observed with increasing exposure time.
2) EIS analysis revealed that specimens in PA and OA tempers exhibited higher stability of the surface oxide film when compared against UA and T3 conditions. Corrosion was found to start faster in UA and T3 tempers, while the evaluation of charge transfer resistance R_2 showed that corrosion propagates in lower rates for peak-aged specimens.
3) Specimens in UA temper exhibited the highest corrosion-induced degradation of $R_{p0.2\%}$ (≈ 23% after 24 h of exposure). Additionally, the increasing corrosion exposure time seems to affect under

– aged specimens significantly since high differences between the $R_{p0.2\%}$ values were noticed for the different exposure times. However, corrosion evolution seems not to affect specimens in PA and OA tempers significantly, regarding decrease of $R_{p0.2\%.}$ This can be attributed to the decrease of the effective thickness - due to propagation of micro-cracks - that is more intense in UA condition as was revealed from the SEM images of the fractured surfaces.

4) Fractographic analysis showed that specimens surfaces are characterized by several dimples interrupted by some smooth surfaces in the edges of specimen's surface. With increasing exposure time, the smooth surfaces are expanded to the specimen's thickness along with formation of micro-cracks up to a maximum depth. Expansion of smooth surfaces and micro-cracks to higher depth was noticed for UA temper. This is in accordance with the results of the iso – modulus of elasticity model - used to calculate the decrease of effective thickness – where higher thickness degradation was noticed for under – aged specimens.
5) Regarding elongation at fracture, the less effect of corrosion exposure is evident in PA condition followed by OA, with the highest decrease of A_f to be -21.1% and -25.8% after 24 hours of exposure, respectively. On the contrary, the respective decrease for specimens in T3 and UA conditions is -43.2% and -50.9%.
6) Corrosion evolution seems not to affect the specimens in PA temper essentially, where the lowest degradation rate factor is noticed (≈ -0.04281). It may be attributed to the precipitation hardening mechanism and the electrochemical behavior of the second phase precipitations.

Chapter 5

5 General Conclusions

In the present Thesis the corrosion mechanisms and their effect on the mechanical performance of AA2024 and AA2198 was investigated through accelerated laboratory techniques. The main results of this investigation can be summarized in the following points:

- The corrosion initiation and propagation mechanism is extremely sensitive in the corrosive environment's aggressiveness; significant differences on the embrittlement mechanism were noticed for both aluminium alloys when exposed to different solutions with the EXCO to show severe grain boundary embrittlement while a mixed-mode of intergranular and transgranular was evident at 3.5 *wt.* % NaCl solution.
- Formation of intergranular secondary cracks in a depth range from 50-100 μm were noticed on Al-Cu 2024-T3 alloy prior to the formation of any substantial surface pitting. This micro-cracking formation was correlated to hydrogen embrittlement phenomena.
- Corrosion degrades all aspects of the tensile behaviour of Al-Cu 2024-T3 at a higher level and rate compared to the respective degradation of Al-Cu-Li 2198-T8 at long exposure times, where pitting corrosion mechanism takes place. Higher differences were noticed with respect to elongation at fracture; A_f of AA2024-T3 was found to degrade at much higher rates even at short exposure times where hydrogen embrittlement is possibly the dominant degradation mechanism. Faster corrosion attack for AA2024-T3 was also revealed from the lower charge transfer resistance values at short exposure times. It was thus definitely concluded that Al-Cu-Li alloy is superior concerning corrosion resistance, since it maintains higher percentages of the initial (uncorroded) values of its tensile properties, against AA2024-T3.
- Different corrosion attack mechanisms between the different exposure times and exposed surfaces of the specimens were observed for both investigated aluminium alloys. Pitting corrosion on both surfaces of Al-Cu-Li 2198-T351 alloy was noticed for the short exposure times while two cases of corrosion damage were noticed for long exposure time (≥ 24 hours): a) the formation of corrosion-induced surface cracks on the small side-surfaces along with transition to exfoliation on the large surfaces due to grain boundaries delamination and b) the accumulated corrosion products on the large surfaces. Regarding Al-Cu 2024-T3 alloy, pitting corrosion within grain boundaries was evident for short exposure times, while connection of corrosion-attacked sites along with cracking between the grains, was the dominant corrosion degradation mechanism for long exposure times. AA2024 seems to be more sensitive to side-

surfaces attack by means of higher elongation at fracture A_f decrease at short exposure times, with the side-surfaces to have a contribution percentage to the total ductility decrease of more than 60%. In contrast, corrosion damage on the large surfaces was found to be critical for tensile ductility decrease of AA2198 for all investigated exposure times.

- AA2024 is more vulnerable to ageing-induced microstructural transformations regarding its corrosion propagation mechanism. Essential differences in the corrosion initiation and propagation rates were noticed for the different ageing tempers of AA2024, with the peak-ageing (PA) to remain almost unaffected by increasing corrosion exposure time. Regarding 2198 no essential differences in the corrosion propagation rate were noticed between the different ageing tempers.
- In general, the potential of the innovative Al-Cu-Li 2198 alloy is met in corrosion degradation rates. This alloy is not so vulnerable to corrosion evolution even if it is significantly aged. It maintains high levels of its mechanical properties, and especially with respect to elongation at fracture, even after long corrosion exposure times and ageing. Furthermore, it is worth mentioning that this superiority is more intense in short exposure times that can lead to higher damage tolerance of this alloy.

Proposal for future research

As the present work has shown, Al-Cu-Li alloys are superior to Al-Cu alloys regarding corrosion resistance especially at short exposure times. Although several aspects of the subject were covered and some preliminary results regarding the corrosion-induced degradation mechanism of the advanced Al-Cu-Li alloys were extracted, the present Thesis is concluded with some suggestions for future work:

- Investigation of the corrosion mechanisms of 2198 Al-Cu-Li alloy at micro-level and assessment of their effect on mechanical performance and corrosion resistance.
- Experimental investigation of environmentally assisted cracking phenomena on this alloy such as hydrogen embrittlement and/or hydrogen trapping. Measurements for trapped hydrogen should be performed in order to check for hydrogen embrittlement and justify the significant degradation at short exposure times where pitting corrosion is limited.
- Assessment of the governing corrosion degradation mechanisms and to deploy any synergetic effects that accelerate fracture.
- Application of an optimal anodized coating layer, tailored to new Al-Cu-Li alloys for efficient corrosion protection and assess its drawbacks on the mechanical properties. Since these alloys are used in the aircrafts with incorporated anodized coatings for corrosion protection, it is of major importance to search for the appropriate anodization system which will provide the best anti-corrosion protection and will have the less impact on mechanical performance.
- Investigation of crevice corrosion on riveted Al-Cu-Li alloy in order to simulate joint configurations and assess the susceptibility of these areas to corrosion attack. Since there are still many parts of the aircraft structure which are joint with rivets and these areas are highly susceptible to corrosion attack due to stress concentration phenomena, it is of imperative importance to study the corrosion kinetics in these areas and try to eliminate the accelerated corrosion behaviour.

6 References

[1] S. G. Epstein, J. G. Kaufman, P. Pollak, Aluminum and its alloys, Aluminum Association, Inc, Washington, D.C., 1994.

[2] G. N. Haidemenopoulos, Physical Metallurgy: Principles and Design, CRC Press, Taylor & Francis, 2018.

[3] N. E. Prasad, A. A. Gokhale, R. J. H. Wanhill, Aluminum-Lithium Alloys Processing, Properties and Applications, first ed., Butterworth-Heinemann, USA, 2013.

[4] C. K. S. Moy, M. Weiss, J. Xia, G. Sha, Influence of heat treatment on the microstructure, texture and formability of 2024 aluminium alloy, Mater. Sci. Eng. A 552 (2012) 48-60.

[5] Y. A. Bagaryatsky, Structural changes on aging Al-Cu-Mg alloys, Dokl. Akad. nauk SSSR 87(3) (1952) 397-401.

[6] J. R. Davis, Aluminum and Aluminum Alloys, in: ASM Specialty Handbook, ASM International, Metals Park, Ohaio, USA, 1993.

[7] J. W. Martin, Precipitation Hardening, 2nd ed., Butterworth-Heinemann, Oxford, United Kingdom, 1998.

[8] N. Radutoiu, J. Alexis, L. Lacroix, M. Abrudeanu, J.-A. Petit, Study of the Influence of the Artificial Ageing Temperature on the AA2024 Alloy Microstructure, Key Eng. Mater. 550 (2013) 115-125.

[9] N. D. Alexopoulos, Z. Velonaki, C. Stergiou, S. K. Kourkoulis, Effect of ageing on precipitation kinetics, tensile and work hardening behavior of Al-Cu-Mg (2024) alloy, Mater. Sci. Eng. A 700 (2017) 457-467.

[10] I. M. Astika, Hardness improvement of aluminum alloy 2024 T3 after artificial aging treatment, IOP Conf. Series: Mater. Sci. Eng. 539 (2019) 012004.

[11] Z. Wang, M. Chen, H. Jiang, H. Li, S. Li, Effect of artificial ageing on strength and ductility of an Al-Cu-Mg-Mn alloy subjected to solutionizing and room-temperature rolling, Mater. Charact. 165 (2020) 110383.

[12] M. C. Liang, L. Chen, G. Q. Zhao, Y. Y. Guo, Effects of solution treatment on the microstructure and mechanical properties of naturally aged EN AW 2024 Al alloy sheet, J. Alloys Compd. 824 (2020) 153943.

[13] R. Yang, Z. Liu, P. Ying, J. Li, L. Lin, S. Zeng, Multistage-aging process effect on formation of GP zones and mechanical properties in Al−Zn−Mg−Cu alloy, Trans. Nonferrous Met. Soc. China 26 (2016) 1183-1190.

[14] X. Xu, Y. Deng, S. Chi, X. Guo, Effect of interrupted ageing treatment on the mechanical properties and intergranular corrosion behavior of Al-Mg-Si alloys, J. Mater. Res. Technol. 9 (2020) 230-241.

[15] K. Pakravan, A. H. Monazzah, S. Farahmand, Ageing condition of tensile specimens: fracture behavior of notched Al2024 sheet under tensile loading, Mater. Res. Express. 7 (2020) 056522.

[16] S. Y. Sun, P. Liu, J. Y. Hu, C. Hong, X. Qiao, S. Y. Liu, R. Zhang, C. Wu, Effect of solid solution plus double aging on microstructural characterization of 7075 Al alloys fabricated by selective laser melting (SLM), Opt. Laser Technol. 114 (2019) 158-163.

[17] L. Sun, Y. Guo, L. Chen, G.Zhao, Effects of solution and aging treatments on the microstructure and mechanical properties of cold rolled 2024 Al alloy sheet, J. Mater. Res. Technol. 12 (2021) 1126-1142.

[18] S. Sun, Y. Fang, L. Zhang, C. Li, S. Hu, Effects of aging treatment and peripheral coarse grain on the exfoliation corrosion behaviour of 2024 aluminium alloy using SR-CT, J. Mater. Res. Technol. (2020) 3219-3229.

[19] A. Boag, A. E. Hughes, A. M. Glenn, T. H. Muster, D. McCulloch, Corrosion of AA2024-T3 part I: localised corrosion of isolated IM particles, Corros. Sci. 53 (2011) 17-26.

[20] C. Blanc, B. Lavelle, G. Mankowski, The role of precipitates enriched with copper on the susceptibility to pitting corrosion of the 2024 aluminum alloy, Corros. Sci. 39 (1997) 495-510.

[21] V. Guillaumin, G. Mankowski, Localized corrosion of 2024-T351 aluminum alloy in chloride media, Corros. Sci. 41 (1999) 421-438.

[22] J. R. Davis, Corrosion of Aluminum and Aluminum Alloys, ASM International, Materials Park, United States, 1999.

[23] G. S. Chen, M. Gao, R. P. Wei, Microconstituent-induced pitting corrosion in aluminum alloy 2024-T3, Corrosion 52 (1996) 8-5.

[24] A. Boag, R. J. Taylor, T. H. Muster, N. Goodman, D. McCulloch, C. Ryan, B. Rout, D. Jamieson, A. E. Hughes, Stable pit formation on AA2024-T3 in a NaCl environment, Corros. Sci. 52 (2010) 90-103.

[25] M. K. Cavanaugh, J. C. Li, N. Birbilis, R. G. Buchheit, Electrochemical characterization of intermetallic phases common to aluminum alloys as a function of solution temperature, J. Electrochem. Soc. 161 (12) (2014) C535-C543.

[26] W. Qafsaoui, M.W. Kendig, H. Perrot, H. Takenouti, Effect of 1-pyrrolidinedithiocarbamate on the galvanic coupling resistance of intermetallics−aluminum matrix during corrosion of AA 2024-T3 in a dilute NaCl, Corros. Sci. 92 (2015) 245-255.

[27] D. W. Hoeppner, C. A. Arriscorreta, Exfoliation Corrosion and Pitting Corrosion and Their Role in Fatigue Predictive Modeling: State-of-the-Art Review, J. Aerosp. Eng. (2012).

[28] E. H. Hollingsworth, H. Y. Hunsicker, Corrosion of Aluminum and Aluminum Alloys, in: Corrosion, ASM International, 1987.

[29] J. O. Park, C. H. Paik, Y. H. Huang, R. C. Alkire, Influence of Fe-Rich Intermetallic Inclusions on Pit Initiation on Aluminum Alloys in Aerated NaCl, J. Electrochem. Soc. 146 (1999) 517-523.

[30] G. O. Ilevbare, O. Schneider, R. G. Kelly, J. R. Scully, In-Situ Confocal Laser Scanning Microscopy of AA2024-T3 Corrosion Metrology: I. Localized Corrosion of Particles, J. Electrochem. Soc. 151 (2004) B453-B464.

[31] O. Schneider, G. O. Ilevbare, J. R. Scully, R. G. Kelly, In-Situ Confocal Laser Scanning Microscopy of AA2024-T3 Corrosion Metrology: II. Trench Formation Around Particles, J. Electrochem. Soc. 151 (2004) B 465-B472.

[32] L. Lacroix, L. Ressier, C. Blanc, G. Manikowski, Statistical study of the corrosion behavior of Al2CuMg intermetallics in AA2024-T351, J. Electrochem. Soc. 155 (2008) C8-C15.

[33] L. Lacroix, L. Ressier, C. Blanc, G. Manikowski, Combination of AFM, SKPFM, and SIMS to study the corrosion behavior of S-phase particles in AA2024-T351, J. Electrochem. Soc. 155 (2008) C131-C137.

[34] A. Hughes, T.H. Muster, A. Boag, A.M. Glenn, C. Luo, X. Zhou, G.E. Thompson, D. McCulloch, Co-operative corrosion phenomena, Corros. Sci. 52 (2010) 665-668.

[35] M. Posada, L. E. Murr, C.-S. Niou, B. Roberson, D. Little, R. Arrowood, D. George, Exfoliation and related microstructures in 2024 aluminum body skins on aging aircraft, Mater. Charact. 38 (1997) 259-272.

[36] M. J. Robinson, N. C. Jackson, The influence of grain structure and intergranular corrosion rate on exfoliation and stress corrosion cracking of high strength Al–Cu–Mg alloys, Corros. Sci. 41 (1999) 1013-1028.

[37] D. E. Azofeifa, N. Clark, A. Amador, A. Sáenz, Determination of hydrogen absorption in Pd coated Al thin films, Thin Solid Films 300 (1997) 295-298.

[38] S. P. Knight, M. Salagaras, A. M. Wythe, F. De Carlo, A. R. Trueman, In situ X-ray tomography of intergranular corrosion of 2024 and 7050 aluminium alloys, Corros. Sci. 52 (2010) 3855-3860.

[39] S. P. Knight, M. Salagaras, A. R. Trueman, The study of intergranular corrosion in aircraft aluminium alloys using X-ray tomography, Corros. Sci. 53 (2011) 727-734.

[40] C. Larignon, J. Alexis, E. Andrieu, L. Lacroix, G. Odemer, C. Blanc, Combined Kelvin probe force microscopy and secondary ion mass spectrometry for hydrogen detection in corroded 2024 aluminium alloy, Electrochim. Acta 110 (2013) 484-490.

[41] G. Scamans, C. Tuck, Sensitive Fracture of Engineering Materials, in: Z. Foroulis, The Metallurgical Society of the AIME (1979) 464-483.

[42] H. Saitoh, Y. Iijima, K. Hirano, Behaviour of hydrogen in pure aluminium, Al-4 mass% Cu and Al-1 mass% Mg2 Si alloys studied by tritium electron microautoradiography, J. Mater. Sci. 29 (1994) 5739-5744.

[43] G. M. Bond, I. M. Robertson, H. K. Birnbaum, The influence of hydrogen on deformation and fracture processes in high-strength aluminum alloys, Acta Metall. 359 (1987) 2289-2296.

[44] A. R. Troiano, The Role of Hydrogen and Other Interstitials in the Mechanical Behavior of Metals, Trans. Am. Soc. Met. 52 (1960) 54-80.

[45] P. V. Petroyiannis, A. T. Kermanidis, P. Papanikos, Sp. G. Pantelakis, Corrosion-induced hydrogen embrittlement of 2024 and 6013 aluminum alloys, Theor. Appl. Fract. Mech. 41 (2004) 173.

[46] H. Kamoutsi, G.N. Haidemenopoulos, V. Bontozoglou, Sp. G. Pantelakis, Corrosion-induced hydrogen embrittlement in aluminium alloy 2024, Corros. Sci.48 (2006) 1209.

[47] N. D. Alexopoulos, On the corrosion-induced mechanical degradation for different artificial aging conditions of 2024 aluminum alloy, Mater. Sci. Eng. A 520 (2009) 40-48.

[48] N. D. Alexopoulos, C. Charalampidou, P. Skarvelis, S. K. Kourkoulis, Synergy of corrosion-induced micro-cracking and hydrogen embrittlement on the structural integrity of aluminium alloy (Al-Cu-Mg) 2024, Corros. Sci. 121 (2017) 32-42.

[49] N. D. Alexopoulos, P. Papanikos, Experimental and theoretical studies of corrosion induced mechanical properties degradation of aircraft 2024 aluminum alloy, Mater. Sci. Eng. A 498 (2008) 248-257.

[50] C.-M. Charalampidou, C. C. E. Pretorius, R. J. Mostert, N. D. Alexopoulos, Effect of Solution Aggressiveness on the Crack Growth Resistance and Cracking Mechanism of AA2024-T3, Corrosion 77 (2021) 1029-1040.

[51] Y. Ma, X. Zhou, Y. Liao, Y. Yi, H. Wu, Z. Wang, W. Huang, Localised corrosion in AA2099-T83 aluminium-lithium alloy: the role of grain orientation, Corros. Sci. 107 (2015) 41-48.

[52] Y. Ma, X. Zhou, W. Huang, Y. Liao, X. Chen, X. Zhang, G.E. Thompson, Crystallographic defects induced localised corrosion in AA2099-T8 aluminium alloy, Corros. Eng. Sci. Technol. 50 (2015) 420-424.

[53] X. Zhang, X. Zhou, T. Hashimoto, J. Lindsay, O. Ciuca, C. Luo, Z. Sun, X. Zhang, Z. Tang, The influence of grain structure on the corrosion behaviour of 2A97-T3 Al- Cu-Li alloy, Corros. Sci. 116 (2017) 14-21.

[54] J. V. de S. Araujo, M. X. Milagre, R. O. Ferreira, C. de S. C. Machado, A. de F. S. Bugarin, I. F. Machado, I. Costa, Exfoliation and intergranular corrosion resistance of the 2198 Al–Cu–Li alloy with different thermomechanical treatments, Mater. Corros. (2020) 1-14.

[55] R. G. Buchheit, J. P. Moran, G.E. Stoner, Electrochemical behavior of the T1 (Al2CuLi) intermetallic compound and its role in localized corrosion of Al-2% Li- 3% Cu alloys, Corrosion 50 (1994) 120-130.

[56] V. Proton, J. Alexis, E. Andrieu, J. Delfosse, A. Deschamps, F. De Geuser, M. C. Lafont, C. Blanc, The influence of artificial ageing on the corrosion behaviour of a 2050 aluminium–copper–lithium alloy, Corros. Sci. 80 (2014) 494-502.

[57] J. E. Kertz, P. I. Gouma, R. G. Buchheit, Localized corrosion susceptibility of Al-Li- Cu-Mg-Zn alloy AF/C458 due to interrupted quenching from solutionizing temperatures, Metall. Mater. Trans. A 32 (2001) 2561-2573.

[58] J. F. Li, C. X. Li, Z. W. Peng, W. J. Chena, Z.Q. Zheng, Corrosion mechanism associated with T1 and T2 precipitates of Al–Cu–Li alloys in NaCl solution, J. Alloys. Compd. 460 (2008) 688-693.

[59] J. V. de S. Araujo, R. M. P. da Silva, U. Donatus, C. de S. C. Machado, I. Costa, Microstructural, Electrochemical and Localized Corrosion Characterization of the AA2198-T851 Alloy, Mater. Res. 23 (2020) e20200161.

[60] C. de S. C. Machado, R. M. P. da Silva, J. V. de S. Araujo, M. X. Milagre, U. Donatus, B. V. G. de Viveiros, R. E. Klumpp, I. Costa, Influence of chloride ions concentration on the development of severe localised corrosion and its effects on the electrochemical response of the 2198-T8 alloy, Corros. Eng. Sci. Technol. 56 (2020) 341-350.

[61] A. Balbo, A. Frignani, V. Grassi, F. Zucchi, Electrochemical behaviour of AA2198 and AA2139 in neutral solutions, Mater. Corros. 66 (2015) 796-802.

[62] U. Donatus, M. Terada, C. R. Ospina, F. M. Queiroz, A.F.S. Bugarin, I. Costa, On the AA2198-T851 alloy microstructure and its correlation with localized corrosion behaviour, Corros. Sci. 131 (2018) 300-309.

[63] N. D. Alexopoulos, Z. Velonaki, C. I. Stergiou, S. K. Kourkoulis, The effect of artificial ageing heat treatments on the corrosion-induced hydrogen embrittlement of 2024 (Al–Cu) aluminium alloy, Corros. Sci. 102 (2016) 413-424.

[64] B. Abdessamad, F. Jamel, B. Benattou, Exfoliation Corrosion Impact on Microstructure, Mechanical Properties, and Fatigue Crack Growth of Aeronautical Aluminum Alloy, J. Fail. Anal. Prev. 20 (2020) 197-207.

[65] L. B. Vogelesang, A. Vlot, Development of fibre metal laminates for advanced aerospace structures, J. Mater. Process. Technol. 103 (2000) 1-5.

[66] F. Menan, G. Henaff, Influence of frequency and exposure to a saline solution on the corrosion fatigue crack growth behavior of the aluminum alloy 2024, Int. J. Fatigue 31 (2009) 1684-1695.

[67] Al. Th. Kermanidis, P. V. Petroyiannis, Sp. G. Pantelakis, Fatigue and damage tolerance behaviour of corroded 2024 T351 aircraft aluminum alloy, Theor. Appl. Fract. Mech. 43 (2005) 121-132.

[68] Z. Szklarska - Smialowska, Pitting corrosion of aluminum, Corros. Sci. 41(1999) 1743-1767.

[69] L. L. Shreir, R. A. Jarman, C. T. Burstein, Corrosion., Vol. 1 metal/environmental reactions, Butterworth & Heinemann Ltd, Oxford, 1994.

[70] H. H. Strehblow, Mechanisms of pitting corrosion, in: Corrosion mechanisms in theory and practice, Marcel Dekker Inc., New York, 1995, pp. 201-238.

[71] N. Birbilis, M. K. Cavanaugh, R. G. Buchheit, Electrochemical behavior and localized corrosion associated with Al7Cu2Fe particles in aluminum alloy 7075-T651, Corros. Sci. 48 (2006) 4202-4215.

[72] H. Shi, Z. Tian, T. Hu, F. Liu, E. H. Han, M. Taryba, S. V. Lamaka, Simulating corrosion of Al2CuMg phase by measuring ionic currents, chloride concentration and pH, Corros. Sci. 88 (2014) 178-186.

[73] A. E. Hughes, A. Boag, A. M. Glenn, D. McCulloch, T. H. Muster, C. Ryan, C. Luo, X. Zhou, G. E. Thompson, Corrosion of AA2024-T3 part II: co-operative corrosion, Corros. Sci. 53 (2011) 27-39.

[74] R. G. Buchheit, R. P. Grant, P. F. Hlava, B. Mckenzie, G. L. Zender, Local dissolution phenomena associated with S phase (Al2CuMg) particles in aluminum alloy 2024-T3, J. Electrochem. Soc. 144 (1997) 2621-2628.

[75] T. Hashimoto, X. Zhang, X. Zhou, P. Skeldon, S. J. Haigh, G. E. Thompson, Investigation of dealloying of S phase (Al2CuMg) in AA 2024-T3 aluminium alloy using high resolution 2D and 3D electron imaging, Corros. Sci. 103 (2016) 157-164.

[76] K. N. Lyon, T. J. Marrow, S. B. Lyon, Influence of milling on the development of stress corrosion cracks in austenitic stainless steel, J. Mater. Process. Technol. 218 (2015) 32-37.

[77] S. Ishihara, S. Saka, Z. Y. Nan, T. Goshima, S. Sunada, Prediction of corrosion fatigue lives of aluminium alloy on the basis of corrosion pit growth law, Fatigue Fract. Eng. Mater. Struct. 29 (2005) 472-480.

[78] H. Kamoutsi, Corrosion-induced hydrogen embrittlement in high-strength aluminum alloys, Department of Mechanical and Industrial Engineering, Doctoral dissertation, University of Thessaly, Volos, 2004.

[79] S. P. Lynch, Mechanisms and kinetics of environmentally assisted cracking: current status, issues, and suggestions for further work, Metall. Mater. Trans. A 44 (2013) 1209-1229.

[80] ASTM G34, Standard Test Method for Exfoliation Corrosion Susceptibility in 2XXX and 7XXX Series Aluminum Alloys (EXCO Test), ASTM International, West Conshohocken, PA, 2001.

[81] D. O. Sprowls, J. D. Walsh, M. B. Shumaker, Simplified exfoliation testing of aluminum alloys, ASTM STP 516 (1972).

[82] M. Guérin, J. Alexis, E. Andrieu, C. Blanc, G. Odemer, Corrosion-fatigue lifetime of Aluminium–Copper–Lithium alloy 2050 in chloride solution, Mater. Des. 87 (2015) 681-692.

[83] Y. Chen, C. Liu, J. Zhou, X. Wang, Multiaxial fatigue behaviors of 2024-T4 aluminum alloy under different corrosion conditions, Int. J. Fatigue 98 (2017) 269-278.

[84] K. Jones, D. W. Hoeppner, Prior corrosion and fatigue of 2024-T3 aluminum alloy, Corros. Sci. 48 (2006) 3109-3122.

[85] N. D. Alexopoulos, C. J. Dalakouras, P. Skarvelis, S. K. Kourkoulis, Accelerated corrosion exposure in ultra thin sheets of 2024 aircraft aluminium alloy for GLARE applications, Corros. Sci. 55 (2012) 289-300.

[86] N. D. Alexopoulos, N. Siskou, C.-M. Charalampidou, S. K. Kourkoulis, Simulation of the corrosion-induced damage on aluminum alloy 2024 specimens with equivalent surface notches, Frat. ed Integrità Strutt. 50 (2019) 342-353.

[87] Sp. G. Pantelakis, P. G. Daglaras, Ch. Alk. Apostolopoulos, Tensile and energy density properties of 2024, 6013, 8090 and 2091 aircraft aluminum alloy after corrosion exposure, Theor. Appl. Fract. Mech. 33 (2000) 117-134.

[88] M. Guérin, E. Andrieu, G. Odemer, J. Alexis, C. Blanc, Effect of varying conditions of exposure to an aggressive medium on the corrosion behavior of the 2050 Al–Cu–Li alloy, Corros. Sci. 85 (2014) 455-470.

[89] M. Vasco, A. N. Chamos, S. G. Pantelakis, Effect of environment's aggressiveness on the corrosion damage evolution and mechanical behavior of AA 2024-T3, Fatigue Fract. Eng. Mater. Struct. 40 (2017) 1551-1561.

[90] ASTM E8M, Standard Test Methods for Tension Testing of Metallic Materials, ASTM International, West Conshohocken, PA, 2009.

[91] ASTM E561, Standard Practice for R-Curve Determination, ASTM International, West Conshohocken, PA, 1998.

[92] ASTM G1, Standard Practice for Preparing, Cleaning, and Evaluating Corrosion Test Specimens, ASTM International, West Conshohocken, PA, 1999.

[93] ASTM G44, Standard Practice for Exposure of Metals and Alloys by Alternate Immersion in Neutral 3.5% Sodium Chloride Solution, ASTM International, West Conshohocken, PA, 2005.

[94] ASTM D5894, Standard Practice for Cyclic Salt Fog/UV Exposure of Painted Metal, (Alternating Exposures in a Fog/Dry Cabinet and a UV/Condensation Cabinet), ASTM International West Conshohocken, PA, 2021.

[95] ASTM E1681, Standard Test Method for Determining Threshold Stress Intensity Factor for Environment-Assisted Cracking of Metallic Materials, ASTM International, West Conshohocken, PA, 1999.

[96] ASTM E1820, Standard Practice for Measurement of Fracture Toughness, ASTM International, West Conshohocken, PA, 2001.

[97] X. H. Wang, J. H. Wang, X. Yue, Y. Gao, Effect of aging treatment on the exfoliation corrosion and stress corrosion cracking behaviors of 2195 Al–Li alloy, Mater. Des. 67 (2015) 596-605.

[98] J. A. Moreto, C. E. B. Marino, W. W. B. Filho, L. A. Rocha, J. C. S. Fernandes, SVET, SKP and EIS study of the corrosion behaviour of high strength Al and Al–Li alloys used in aircraft fabrication, Corros. Sci. 84 (2014) 30-41.

[99] P. Campestrini, E. P. M. VanWesting, J. H. W. DeWit, Influence of surface preparation on performance of chromate conversion coatings on Alclad 2024 aluminium alloy–Part II: EIS investigation, Electrochim. Acta 46 (2001) 2631-2647.

[100] P. Schmutz, G. S. Frankel, Characterization of AA2024-T3 by Scanning Kelvin Probe Force Microscopy, J. Electrochem. Soc. 145 (2006) 2285-2295.

[101] C. Vargel, Initiation and Propagation of Corrosion Pits, in: Corrosion of Aluminium, s.l (2004) 115-116.

[102] K. H. Gayer, L. C. Thompson, O. T. Zajicek, The solubility of aluminum hydroxide in acidic and basic media at 25 °C, Can. J. Chem. 36 (1958) 1268-1271.

[103] X. Zhang, Y. Jiao, Y. Yu, B. Liu, T. Hashimoto, H. Liu, Z. Dong, Intergranular corrosion in AA2024-T3 aluminium alloy: The influence of stored energy and prediction, Corros. Sci. 155 (2019) 1-12.

[104] Sp. G. Pantelakis, D. Setsika, A. Chamos, A. D. Zervaki, Corrosion damage evolution of the aircraft aluminum alloy 2024 T3, Int. J. Struct. Integr. 7 (2016) 25-46.

[105] C. Charalampidou, W. Dietzel, M. Zheludkevich, S.K. Kourkoulis, N. D. Alexopoulos, Corrosion-induced mechanical properties degradation of Al-Cu-Li (2198-T351) aluminium alloy and the role of side-surface cracks, Corros. Sci. 183 (2021) 109330.

[106] C. Luo, X. Zhou, G. E. Thompson, A. E. Hughes, Observations of intergranular corrosion in AA2024-T351: The influence of grain stored energy, Corros. Sci. 61 (2012) 35-44.

[107] T. Dursun, C. Soutis, Recent developments in advanced aircraft aluminium alloys, Mater. Des. 56 (2014) 862-871.

[108] R. J. Rioja, J. Liu, The evolution of Al-Li base products for aerospace and space applications, Metall. Mater. Trans. A 43 (2012) 3325-3337.

[109] N. E. Prasad, A. A. Gokhale, P. R. Rao, Mechanical behaviour of aluminium-lithium alloy, Sadhana 28 (2003) 209-246.

[110] J. A. Moreto, O. C. Gamboni, C. E. B. Marino, W. B. Filho, J. C. S. Fernandes, L. A. Rocha, Corrosion behaviour of Al and Al-Li alloys used as aircraft materials, Corros. Prot. 31 (2012) 60-64.

[111] P. W. Kai, Local chemistry and growth of single corrosion pits in aluminum, J. Electrochem. Soc. 137 (1990) 3010-3015.

[112] Y. Zou, X. Chen., B. Chen, Corrosion behavior of 2198 Al–Cu–Li alloy in different aging stages in 3.5 wt% NaCl aqueous solution, J. Mater. Res. 33 (2018) 1011-1022.

[113] J. A. DeRose, J. Suter, T. Bałkowiec, A. Michalski, K. J. Kurzydlowski, P. Schmutz, Localised corrosion initiation and microstructural characterisation of an Al 2024 alloy with a higher Cu to Mg ratio, Corros. Sci. 55 (2012) 313-325.

[114] P. Campestrini, E. P. M. van Westing, H. W. van Rooijen, J. H. W. de Wit, Relation between microstructural aspects of AA2024 and its corrosion behaviour investigated using AFM scanning potential technique, Corros. Sci. 42 (2000) 1853-1861.

[115] N. D. Alexopoulos, E. Migklis, A. Stylianos, D. P. Myriounis, Fatigue behavior of the aeronautical Al–Li (2198) aluminum alloy under constant amplitude loading, Int. J. Fatigue 56 (2013) 95–105.

[116] N. D. Alexopoulos, A. Proiou, W. Dietzel, C. Blawert, V. Heitmann, M. Zheludkevich, S. K. Kourkoulis, Mechanical properties degradation of (Al-Cu-Li) 2198 alloy due to corrosion exposure, Procedia Struct. Integr. 2 (2016) 597-603.

[117] J. A. Moreto, O. Gamboni, C. O. F. T. Ruchert, F. Romagnoli, M. F. Moreira, F. Beneduce, W. W. Bose Filho, Corrosion and fatigue behavior of new Al alloys, Procedia Eng. 10 (2011) 1521-1526.

[118] M. X. Milagre, U. Donatus, C. S. C. Machado, J. V. S. Araujo, R. M. P. da Silva, B. V. G. de Viveiros, A. Astarita, I. Costa, Comparison of the corrosion resistance of an Al–Cu alloy and an Al–Cu–Li alloy, Corros. Eng. Sci. Technol. 54 (2019) 402-412.

[119] H. Li, Y. Tanga, Z. Zeng, Z. Zheng, F. Zheng, Effect of ageing time on strength and microstructures of an Al–Cu–Li–Zn–Mg–Mn–Zr alloy, Mater. Sci. Eng. A 498 (2008) 314-320.

[120] C. P. Blankenship, E. A. Starke, Improved toughness in Al–Li–Cu–Mg–Ag–Zr alloy X2095, Scr. Metall. Mater. 26 (1992) 1719-1722.

[121] C. P. Blankenship, E. A. Starke, Mechanical behavior of double-aged AA8090, Metall. Mater. Trans. A 24 (1993) 833-841.

[122] J. F. Nie, B. C. Muddle, I. J. Polmear, The effect of precipitate shape and orientation on dispersion strengthening in high strength aluminium alloys, Mater. Sci. Forum. (1996) 1257-1262.

[123] G. Itoh, Q. Cui, M. Kanno, Effects of a small addition of magnesium and silver on the precipitation of T1 phase in an A1-4%Cu-l.l%Li-0.2% Zr alloy, Mater. Sci. Eng. A 211 (1996) 128-137.

[124] V. Araullo-Peters, B. Gault, F. Geuser, A. Deschamps, J.M. Cairney, Microstructural evolution during ageing of Al–Cu–Li–x alloys, Acta Mater. 66 (2014) 199-208.

[125] J. M. Howe, J. Lee, A. K. Vasudévan, Structure and deformation behavior of T1 precipitate plates in an Al- 2Li- 1 Cu alloy, Metall. Trans. A 19 (1988) 2911-2920.

[126] J. F. Nie, B. C. Muddle, On the form of the age-hardening response in high strength aluminium alloys, Materials Science and Engineering A319–321 (2001) 448-451.

[127] J. F. Li, C. X. Li, Z. W. Peng, W. J. Chena, Z. Q. Zheng, Corrosion mechanism associated with T1 and T2 precipitates of Al–Cu–Li alloys in NaCl solution, J. Alloys Compd. 460 (2008) 688-693.

[128] J. Li, N. Birbilis, R. G. Buchheit, Electrochemical assessment of interfacial characteristics of intermetallic phases present in aluminium alloy 2024-T3, Corros. Sci. 101 (2015) 155-164.

[129] X. Zhou, C. Luo, T. Hashimoto, A. E. Hughes, G. E. Thompson, Study of localized corrosion in AA2024 aluminium alloy using electron tomography, Corros. Sci. 58 (2012) 299-306.

[130] T. C. Lindley, P. Mcintyre, P. J. Trant, Fatigue-crack initiation at corrosion pits, Metal. Technol. 9 (1982) 135-42.

[131] Y. Kondo, Prediction of Fatigue Crack Initiation Life Based on Pit Growth, Corrosion 45 (1989) 7-11.

[132] K. van der Walde, J. R. Brockenbrough, B. A. Craig, B. M. Hillberry, Multiple fatigue crack growth in pre-corroded 2024-T3 aluminum, Int. J. Fatigue 27 (2005) 1509-1518.

[133] R. M. Pidaparti, R. K. Patel, Investigation of a single pit/defect evolution during the corrosion process, Corros. Sci. 52 (2010) 3150-3153.

[134] K. van der Walde, B. M. Hillberry, Initiation and shape development of corrosion-nucleated fatigue cracking, Int. J. Fatigue 29 (2007) 1269-1281.

[135] K. Jones, S. R. Shinde, P. N. Clark, D. W. Hoeppner, Effect of prior corrosion on short crack behavior in 2024-T3 aluminum alloy, Corros. Sci. 50 (2008) 2588-2595.

[136] H. Kamoutsi, G. N. Haidemenopoulos, V. Bontozoglou , P. V. Petroyiannis, Sp. G. Pantelakis, Effect of prior deformation and heat treatment on the corrosion-induced hydrogen trapping in aluminium alloy 2024, Corros. Sci. 80 (2014) 139-142.

[137] K. M. Gruenberg, B. A. Craig, B. M. Hillberry, R. J. Bucci, A. J. Hinkle, Predicting fatigue life of pre-corroded 2024-T3 aluminum from breaking load tests, Int. J. Fatigue 26 (2004) 615-627.

[138] K. K. Sankaran, R. Perez, K. V. Jata, Effects of pitting corrosion on the fatigue behavior of aluminum alloy 7075-T6: modeling and experimental studies, Mate. Sci. Eng. A 297 (2001) 223-229.

[139] G. H. Bray, R. J. Bucci, E. L. Colvin, M. Kulak, Effects of prior corrosion on the S/N fatigue performance of aluminum alloys 2024-T3 and 2524-T3, in: Effects of Environment on the Initiation of Crack Growth, ASTM STP 1298, ASTM, Philadelphia, 1997.

[140] M. Khobaib, T. Matikas, M. S. Donley, Fatigue behavior of crack initiating from corrosion damage, J. Adv. Mater. 35 (2003) 3-8.

[141] G. H. Koch, E. L. Hagerdorn, A. P. Berens, Effect of corrosion on fatigue cracking of aluminum alloys 2024-T3 and 7075-T6, Report R215-04, Prepared for Flight Dynamics Directorate Wright Laboratory Materiel Command, right–Patterson Air Force Base, Ohio, 1995.

[142] C. S. Shin, K. C. Man, C. M. Wang, A practical method to estimate the stress concentration of notches, Fatigue 16 (1994) 242-256.

[143] G. C. Sih, Stress-intensity factor solutions and formulas for reference, in Handbook of stress-intensity factors, Bethlehem, Lehigh University, Institute of Fracture and Solid Mechanics (1973).

[144] Y. Murakami, Stress Intensity Factors Handbook, Volume 2, Pergamon Press (1987).

[145] S. G. Pantelakis, A. N. Chamos, D. Setsika, Tolerable corrosion damage on aircraft aluminum structures: Local cladding patterns, Theor. Appl. Fract. Mech. 58 (2012) 55-64.

[146] G. S. Chen, K. C. Wan, M. Gao, R. P. Wei, T.H. Flournoy, Transition from pitting to fatigue crack growth modeling of corrosion fatigue crack nucleation in a 2024-T3 aluminum alloy, Mater. Sci. Eng. A 219 (1996) 126-132.

[147] S. I. Rokhlin, J. Y. Kim, H. Nagy, B. Zoofan, Effect of pitting corrosion on fatigue crack initiation and fatigue life, Eng. Fract. Mech. 62 (1999) 425-444.

[148] G. E. Noether, A brief survey of nonparametric statistics, R.V. Hogg (ed.), in: Studies in statistics, Mathematical Association America (1978) 39-65.

[149] D. W. Wayne, Kolmogorov–Smirnov one-sample test, 2nd ed., Applied Nonparametric Statistics Boston: PWS-Kent., 1990, 319-330.

[150] A. K. Vasudevan, S. Suresh, Influence of corrosion deposits on near-threshold fatigue crack growth behavior in 2xxx and 7xxx series aluminum alloy, Metall. Trans. A 12 (1982) 2271-2280.

[151] P. J. Hurley, F. J. Humphreys, A study of recrystallization in single-phase aluminium using in-situ annealing in the scanning electron microscope, J. Microsc. 213 (2004) 225-234.

[152] R. Saillard, B. Viguier, G. Odemer, A. Pugliara, B. Forib, C. Blanc, Influence of the microstructure on the corrosion behaviour of 2024 aluminium alloy coated with a trivalent chromium conversion layer, Corros. Sci. 142 (2018) 119-132.

[153] Z. Huda, N. Iskandar Taib, T. Zaharinie, Characterization of 2024-T3: An aerospace aluminum alloy, Mater. Chem. Phys. 113 (2009) 515-517.

[154] ASTM E112 – 13, Standard Test Methods for Determining Average Grain Size, ASTM International, West Conshohocken, PA, 2013.

[155] D. Steglich, H. Wafai, W. Brocks, Anisotropic Deformation and Damage in Aluminium 2198 T8 Sheets, Int. J. Damage Mech. 19 (2010) 131-152.

[156] X. Wang, J.Wang, X. Yue, Y. Gao, Effect of aging treatment on the exfoliation corrosion and stress corrosion cracking behaviors of 2195 Al–Li alloy, Mater. Des. 67 (2015) 596-605.

[157] J. Kim, J. Jeun, H. Chun, Y. R. Lee, J. Yoo , J. Yoon, H. Lee, Effect of precipitates on mechanical properties of AA2195, J. Alloys Compd. 669 (2016) 187-198.

[158] Z. Zhu, J. Han, C. Gao, M. Liu, J. Song, Z. Wang, H. Li, Microstructures and mechanical properties of Al-Li 2198-T8 alloys processed by two different severe plastic deformation methods: A comparative study, Mater. Sci. Eng. A 681 (2017) 65-73.

[159] N. Nayan, S. Mahesh, M. J. N. V. Prasad, S. V. S. N. Murthy, I. Samajdar, Temperature-dependence of plasticity and fracture in an Al-Cu-Li alloy, Philos. Mag. Lett. 100 (2020) 2913-2937.

[160] J. V. de S. Araujo, A. de F. S. Bugarin, U. Donatus, C.e de S. C. Machado, F. M. Queiroz, M. Terada, A. Astarita, I. Costa, Thermomechanical treatment and corrosion resistance correlation in the AA2198 Al–Cu–Li alloy, Corros. Eng. Sci. Technol. 54 (2019) 575-586.

[161] K. S. Ghosh, Md. Hilal, S. Bose, Corrosion behavior of 2024 AlCuMg alloy of various tempers, Trans. Nonferrous Met. Soc. China 23 (2013) 3215-3227.

[162] M.-L. de Bonfils-Lahovary, L. Laffont, C. Blanc, Characterization of intergranular corrosion defects in a 2024 T351aluminium alloy, Corros. Sci. 119 (2017) 60-67.

[163] P. Visser, H. Terryn, J. M. C. Mol, On the importance of irreversibility of corrosion inhibitors for active coating protection of AA2024-T3, Corros. Sci. 140 (2018) 272-285.

[164] R. G. Buchheit, M. A. Martinez, L. P. Montes, Evidence of Cu ion formation by dissolution and dealloying the Al2CuMg intermetallic compound in rotating ring-disk collection experiments. J. Electrochem. Soc. 147 (2000) 119-124.

[165] J.F. Li, Z.Q. Zheng, S.C. Li, W.J. Chen, W.D. Ren, X.S. Zhao, Simulation study on function mechanism of some precipitates in localized corrosion of Al alloys, Corros. Sci. 49 (2007) 2436-2449.

[166] A. Boag, A. E. Hughes, N. C. Wilson, A. Torpy, C. M. MacRae, A. M. Glenn, T. H. Muster, How complex is the microstructure of AA2024-T3?, Corros. Sci. 51 (2009) 1565-1568.

[167] S. P. Ringer, K. Hono, I. J. Polmear, T. Sakurai, Nucleation of precipitates in aged Al-Cu-Mg-(Ag) alloys with high Cu:Mg ratios, Acta Mater. 44 (1996) 1883-1898.

[168] S. P. Ringer, S. K. Caraher, I. J. Polmear, Response to comments on cluster hardening in an aged Al-Cu-Mg alloy, Scr. Mater. 39 (1998) 1559-1567.

[169] E. A. Starke, J. T. Staley, Application of Modern Aluminum Alloys to Aircraft, Prog. Aerosp. Sci. 32 (1996) 131-172.

[170] S. F Zhang, W. D Zeng, W. H. Yang, C. L. Shi, H. J. Wang, Ageing response of a Al–Cu–Li 2198 alloy, Mater. Des. 63 (2014) 368-374.

[171] Q. Liu, R. H. Zhu, D. Y. Liu, Y. Xu, J. F. Li, Y. L. Chen, X. H. Zhang, Z. Q. Zheng, Correlation between artificial aging and intergranular corrosion sensitivity of a new Al-Cu-Li alloy sheet, Mater. Corros. 68 (2017) 65-76.

[172] M. H. Tosten, A. K. Vasudevan, P. R. Howell, Microstructural development in Al_2% Li_3%Cu alloy, in: Baker, C., Gregson, P.J., Harris, S.J., Peel, C.J. (Eds.), Proceedings of the Third International Conference on Aluminium_Lithium Alloys, The Institute of Metals, London, 1986, 483-489.

[173] B.-P. Huang, Z.-Q. Zheng, Effects of Li content on precipitation in Al–Cu–(Li)–Mg–Ag–Zr alloys, Scr. Mater. 38 (1998) 357-362.

[174] B. Decreus, A. Deschamps, F. De Geuser, P. Donnadieu, C. Sigli, M. Weyland, The influence of Cu/Li ratio on precipitation in Al–Cu–Li–x alloys, Acta Material. 61 (2013) 2207-2218.

[175] W. A. Cassada, G. J. Shiflet, E. A. Starke, The effect of plastic deformation on AI2CuLi (T1) precipitation, Metall. Trans. A 22 (1991) 299-306.

[176] P. Niskanen, T. H. Sanders, J. G. Rinker, M. Marek, Corrosion of aluminium alloys containing lithium, Corros. Sci. 22 (1982) 283-304.

[177] S. Ohsaki, T. Sato, T. Takahashi, Effect of ageing on pitting corrosion behavior of Al-Li alloys, J. Japan Inst. Light Met. 38 (1988) 264-269.

[178] S. P. Ringer, R. K. W. Marceau, G. Sha, R. Ferragut, A. Dupasquier, Solute clustering in Al–Cu–Mg alloys during the early stages of elevated temperature ageing, Acta Mater. 58 (2010) 4923-39.

[179] M. Araghchi, H. Mansouri, R. Vafaei, Y. Guo, Optimization of the Mechanical Properties and Residual Stresses in 2024 Aluminum Alloy Through Heat Treatment, J. Mater. Eng. Perform. 27 (2018) 3234-3238.

[180] B. Jiang, F. Cao, H. Wang, D. Yi, Y. Jiang, F. Shen, B. Wang, H. Liu, Effect of aging time on the microstructure evolution and mechanical property in an Al-Cu-Li alloy sheet, Mater. Sci. Eng. A 740–741 (2019) 157-164.

[181] J. Soltis, Passivity breakdown, pit initiation and propagation of pits in metallic materials – Review, Corros. Sci. 90 (2015) 5-22.

[182] Z. Wang, P. Chen., H. Li, B. Fang, R. Song, Z. Zheng, The intergranular corrosion susceptibility of 2024 Al alloy during re–ageing after solution treating and cold–rolling, Corros. Sci. 114 (2017) 156-168.

[183] S. Wang, F. Yang, G. S. Frankel, Effect of Altered Surface Layer on Localized Corrosion of Aluminum Alloy 2024, J. Electrochem. Soc. 164 (2017) 317-323.

[184] W. Zhang, G.S. Frankel, Transitions between pitting and intergranular corrosion in AA2024, Electrochem. Acta 48 (2003) 1193-1210.

[185] Y. Ma, X. Zhou, X. Meng, W. Huang, Y. Liao, X. Chen, Y. Yi, X. Zhang, G. E. Thompson, Influence of thermomechanical treatments on localized corrosion susceptibility and propagation mechanism of AA2099 Al−Li alloy, Trans. Nonferrous Met. Soc. China 26 (2016) 1472-1481.

[186] J. Huang, J. Li, D. Liu, R. Zhang, Y. Chen, X. Zhang, P. Ma, R. K. Gupta, N. Birbilis, Correlation of intergranular corrosion behaviour with microstructure in Al- Cu-Li alloy, Corros. Sci. 139 (2018) 215-226.

[187] C. Larignon, J. Alexis, E. Andrieu, G. Odemer, C. Blanc, The contribution of hydrogen to the corrosion of 2024 aluminum alloy exposed to thermal and environmental cycling in chloride media, Corros. Sci. 69 (2013) 211-220.

[188] T. Marlaud, B. Malki, A. Deschamps, B. Baroux, Electrochemical aspects of exfoliation corrosion of aluminium alloys: the effects of heat treatment, Corros. Sci. 53 (2011) 1394-1400.

[189] K. S. Ghosh, M. D. Hilal, S. Bose, Corrosion behaviour of 2024 Al-Cu-Mg alloy of various tempers, Trans. Nonferrous Met. Soc. China 23 (2013) 3215-3227.

[190] L. F. Mondolfo, Aluminum Alloys – Structure and Properties, Butterworth, London, 1976.

[191] I. Polmear, Metallurgy of the Light Alloys, 3rd ed., in: Light Alloys, Metallurgy and Materials Science, Arnold, Great Britain, 1995.

[192] K. Lv, C. Zhu, J. Zheng, X. Wang, B. Chen, Precipitation of T1phase in 2198 Al–Li alloy studied by atomic-resolution HAADF-STEM, J Mater Res. 34 (2019) 3535-3544.

Research Outputs

Herein, an overview of the research outputs of the present dissertation is provided.

Peer-reviewed journal publications

1) **C. Charalampidou,** Wolfgang Dietzel, Mikhail Zheludkevich, StavrosK. Kourkoulis, N. D. Alexopoulos, *Corrosion-induced mechanical properties degradation of Al-Cu-Li (2198-T351) aluminium alloy and the role of side-surface cracks*, Corrosion Science 183 (2021) 109330. https://doi.org/10.1016/j.corsci.2021.109330

2) **Christina Margarita Charalampidou**, Christiaan C.E. Pretorius, Roelf J. Mostert, Nikolaos D. Alexopoulos, *Effect of Solution Aggressiveness on the Crack Growth Resistance and Cracking Mechanism of AA2024-T3,* CORROSION (2021) 77 (9) 1029–1040. https://doi.org/10.5006/3839

3) N. D. Alexopoulos, N. Siskou, **Ch. M. Charalampidou,** S. K. Kourkoulis, *Simulation of the corrosion-induced damage on aluminum alloy 2024 specimens with equivalent surface notches*, Frattura ed Integrità Strutturale, 50 (2019) 342-353. 10.3221/IGF-ESIS.50.29

4) N.D. Alexopoulos, **C. Charalampidou**, P. Skarvelis, S.K. Kourkoulis, *Synergy of corrosion induced micro-cracking and hydrogen embrittlement on the structural integrity of aluminium alloy (Al-Cu-Mg) 2024*, Corrosion Science 121 (2017) 32-42. https://doi.org/10.1016/j.corsci.2017.03.001

International conference proceedings

1) Dimitris Georgoulis, **Christina M. Charalampidou**, Nikolaos D. Alexopoulos, *Corrosion resistance of aluminum alloy 2198 for different ageing tempers*, Procedia Structural Integrity 37 (2022) 941–947. https://doi.org/10.1016/j.prostr.2022.02.029

2) D. Georgoulis, **C. M. Charalampidou**, N. Siskou, N. D. Alexopoulos, S. K. Kourkoulis, *Corrosion behaviour of AA2198–T8 and AA2024-T3 alloy in 3.5% aqueous solution*, Procedia Structural Integrity 28 (2020) 2297–2303. https://doi.org/10.1016/j.prostr.2020.11.076

3) N. D. Alexopoulos, **C. M. Charalampidou**, P. Papanikos, S. K. Kourkoulis, *Simulation of the mechanical behavior of pre-corroded AA2024-T3 specimens with equivalent surface notches*, Materials Today: Proceedings, 32 (2019) 254–259. https://doi.org/10.1016/j.matpr.2020.05.804

4) N. Siskou, **Ch. Charalampidou**, N.D. Alexopoulos, S.K. Kourkoulis, *Effect of corrosion exposure on aluminum alloy 2024 for different artificial ageing conditions*, Procedia Structural Integrity 10 (2018) 79-84. https://doi.org/10.1016/j.prostr.2018.09.012

Conferences

1) **C. -M. Charalampidou**, G. Grammatikos, P. Papanikos, S. K. Kourkoulis and N. D. Alexopoulos, *Effect of corrosion exposure on the mechanical performance of aeronautical aluminum alloy 2024 riveted sheets*, under the auspices of the 38th Danubia–Adria Symposium on Advances in Experimental Mechanics, 38th DAS, Poros Island, Greece 20-23 September 2022.
2) **C. Charalampidou**, Carsten Blawert, Mikhail Zheludkevich, S. Kourkoulis, N. Alexopoulos, *Effect of artificial ageing on the corrosion mechanism of aeronautical Al-Cu-Li 2198 alloy*, EUROCORR 2020, Virtual Conference, under the auspices of the European Corrosion Congress, 7-11 September 2020.
3) **C.-M. Charalampidou**, N. Siskou, N. D. Alexopoulos, S. K. Kourkoulis, *Corrosion evolution on aeronautical aluminium alloy 2024 for different artificial ageing conditions,* EUROCORR 2020, Virtual Conference, under the auspices of the European Corrosion Congress 7-11 September 2020.
4) **C.-M. Charalampidou**, N. D. Alexopoulos, A. -E. Dimou, Z. S. Metaxa, S. K. Kourkoulis, I. Karatasios, *Examination of a ternary cement-based restoration paste reinforced with carbon-nanomaterials*, 1st Virtual European Conference on Fracture, VECF1, under the auspices of the European Structural Integrity Society (ESIS), June 2020.
5) **C. Charalampidou,** D. Georgoulis, S. K. Kourkoulis, N. D. Alexopoulos, *Influence of artificial ageing on the corrosion kinetics of aeronautical aluminum alloys*, Proceedings in the 7th Pan-Hellenic conference on Metallic Materials, under the auspices of the Hellenic Metallurgical Society, Athens, Greece**, 11-13 December 2019.**
6) **C. Charalampidou**, A. Proiou, S. Kourkoulis, N. Alexopoulos, *Corrosion-induced mechanical properties decrease of aeronautical Al-Li 2198 alloy for different tempers*, Proceedings in the European Conference on Fracture ECF22 « Loading and Environment

Effects on Structural Integrity», under the auspices of the European Structural Integrity Society (ESIS), Belgrade, Serbia, 26-31 August 2018.

7) **C.Charalampidou,** S. K. Kourkoulis, A. Karanika, N. D. Alexopoulos, *Corrosion-induced mechanical properties degradation of Al-Cu-Li (2198) aluminum alloy*, Proceedings in the European congress and exhibition on advanced materials and processes, EUROMAT 2017, Thessaloniki, Greece, 17-22 September 2017.
8) **C. Charalampidou,** S. K. Kourkoulis, A. Karanika, N. D. Alexopoulos, *The effect of pre-straining on the corrosion behaviour of 2024 and 2198 aluminum alloys*, Proceedings in the European congress and exhibition on advanced materials and processes, EUROMAT 2017, Thessaloniki, Greece, 17-22 September 2017.
9) **C. Charalampidou**, P. Skarvelis, S. K. Kourkoulis, N. D. Alexopoulos, *Corrosion-induced surface micro-cracking and calculation of the effective thickness in ultra-thin sheets of aluminum alloy 2024*, 6th Panhellenic Conference of Metallic Materials, under the auspices of the Hellenic Metallurgical Company and Applied Metallurgy Laboratory of the University of Ioannina, Ioannina, Greece, 07-09 December 2016.